LONDON GLOBAL'S UNIVERSITY

Development of a Doxorubicin-Loaded Dual pH- and Thermo-Responsive Magnetic Nanocarrier for Application in Magnetic Hyperthermia and Drug Delivery in Cancer Therapy

Aziliz Hervault

Supervisors

Professor Nguyễn Thi Kim Thanh (UCL)

Professor Shinya Maenosono (JAIST)

Professor Quentin Pankhurst (UCL)

A thesis submitted to University College London for the degree of Doctor of Philosophy in the Faculty of Mathematical and Physical Sciences, Department of Physics & Astronomy

2017

Declaration of Originality

“I, Aziliz Hervault, confirm that the work presented in this thesis is my own. Where information has been derived from other sources, I confirm that this has been indicated in the thesis. This thesis has not been submitted elsewhere for examination purposes.”

March, 2017.

Aziliz Hervault

Abstract

Magnetic nanocarriers have attracted increasing attention for multimodal cancer therapy due to the possibility to deliver heat and drugs locally. The enhancement of the anti-cancer effect of chemotherapy with application of concurrent hyperthermia has been noticed more than thirty years ago. However, combining magnetic nanoparticles with drug molecules in the same nanoformulation has only recently emerged as a promising tool for the simultaneous application of hyperthermia and chemotherapy.

In this work, initial experimentation was primarily focused on the synthesis of magnetic nanoparticles of high saturation magnetisation to develop efficient mediators of heat based on an iron core and a bismuth shell. However, such nanoparticles could not be obtained due to the impossibility to grow the bismuth shell on the iron nanoparticle surface. The rest of this study reports the development of a novel magnetic nanocomposites (MNCs) made of an iron oxide core and a pH- and thermo-responsive polymer shell, that can be used as both mediators of heat and drug carriers. The conjugation of the anticancer drug doxorubicin to the thermo-responsive MNCs *via* acid-cleavable imine linkers provides advanced features for the targeted delivery of doxorubicin *via* the combination of magnetic targeting, and dual pH- and thermo-responsive behaviour, which offers spatial and temporal control over the release of the drug. The nanoparticles exhibit a superparamagnetic behaviour with a saturation magnetization around 78 emu/g and good heating properties in an alternating magnetic field. Almost a complete doxorubicin release was obtained under acidic tumour pH and hyperthermia conditions. Finally, *in vitro* studies on human glioma and breast cancer cell lines and on a murine prostate carcinoma cell line confirmed that thermo-chemotherapy applied via the developed smart delivery system exhibits a substantial increase in cytotoxicity as compared to standalone therapies, and almost complete cell death was observed while applying low thermal and chemotherapeutic doses.

Table of Contents

List of Figures

Chapter 1

Chapter 2

Chapter 3

Chapter 4

Chapter 5

Chapter 6

List of Tables

Chapter 1

Chapter 3

Chapter 4

Chapter 5

Chapter 6

List of Abbreviations

°C	degree celsius
A	ampere
Å	angstrom
AC	alternating current
ACVA	4,4'-azobis(4-cyanovaleric acid)
AIBN	2,2-azobis(2-methylpropionitrile)
AM	acrylamide
AMF	alternating magnetic field
AN	acrylonitrile
APC	allophycocyanin
Ar	argon
ATR	attenuated total reflectance
ATRP	atom transfer radical polymerization
Bi	bismuth
BLI	bioluminescence imaging
CME	clathrin-mediated endocytosis
CPPA	4-cyano-4-(phenylcarbonothioylthio)pentanoic acid
CTA	chain transfer agent
C_{tr}	chain transfer coefficient
Da	dalton
DEGMA	di(ethylene glycol) methyl ether methacrylate
D_H	hydrodynamic diameter
DLS	dynamic light scattering
DMEM	Dulbecco's modified Eagle's medium
DMSO	dimethyl sulphoxide
DOX	doxorubicin
DOX-MNC	doxorubicin-loaded magnetic nanocomposite
DPBS	Dulbecco's phosphate buffered saline
DT	decanethiol
D_{TEM}	particle core size estimated by TEM
D_{XRD}	crystallite size estimated by XRD
EDS	energy dispersive X-ray spectrometry
EtOH	ethanol
f	frequency

FBS	fetal bovine serum
FDA	Food and Drug Administration
Fe	iron
FITC	fluorescein isothiocyanate
FSC	forward scattered light
FTIR	Fourier transform infra-red spectroscopy
g	gram
GPC	gel permeation chromatography
h	hour
H	amplitude of the magnetic field
Hc	coercive field or coercivity
HCl	hydrochloric acid
HDA	hexadecylamine
HDA-HCl	hexadecylammonium chloride
HPMAM	N-(2-hydroxypropyl) methacrylamide
IC_{50}	half maximal inhibitory concentration
ILP	intrinsic loss power
IO	iron oxide
IR	infrared
IUPAC	International Union of Pure and Applied Chemistry
K	kelvin
K_{CV}	apparent permeation constant
kg	kilogram
L	litre
LAM	less activated monomer
LCST	lower critical solution temperature
LRP	living radical polymerisation
LucF	firefly luciferase
M	molecular weight
m	metre
MA	methyl acrylate
MACH	magnetic alternating current hyperthermia
MADIX	macromolecular design by interchange of xanthate
MAM	more activated monomer
MEM	minimum essential medium Eagle
min	minute
mL	milliliter
MMA	methyl methacrylate

mmol	millimole
Mn	number average molecular weight
MNC	magnetic nanocomposite
mol	mole
MRI	magnetic resonance imaging
Ms	saturation magnetisation
MTT	3-(4,5-Dimethyl-2-thiazolyl)-2,5-diphenyl-2H-tetrazolium bromide
Mw	weight average molecular weight
MWCO	molecular weight cut-off
nH	nanohenry
nm	nanometer
NMP	nitroxide-mediated polymerization
NMR	nuclear magnetic resonance
NP	nanoparticle
NVC	N-vinylcarbazole
NVP	N-vinylpyrrolidone
OA	oleic acid
OAm	oleylamine
Oe	oersted
DP_n	degree of polymerization
PBS	phosphate buffer solution
pdf	powder data file
PE	phycoerythrin
PEG	polyethylene glycol
PEGMA	poly(ethylene glycol) methyl ether methacrylate
PI	propidium iodide
PS	phosphatidylserine
P/S	penicillin/streptomycin
RAFT	reversible addition-fragmentation chain transfer
rDA	retro-Diels-Alder
RDRP	reversible deactivation radical polymerization
rpm	revolutions per minute
RT	room temperature
s	second
SAL	Slide-A-Lyzer
SAR	specific absorption rate
SCC	side scattered light
SEC	size exclusion chromatography

SPION	superparamagnetic iron oxide nanoparticle
SQUID	superconducting quantum interference device
St	styrene
t	time
T	temperature
T	tesla
T_B	blocking temperature
TEA	triethylamine
TEM	transmission electron microscope
TGA	thermogravimetric analysis
THF	tetrahydrofuran
TMSPMA	3-(trimethoxysilyl)propyl methacrylate
UV	ultraviolet
UV-vis	ultraviolet-visible
V	volume
Vac	vinyl acetate
VBA	3-vinylbenzaldehyde
VSM	vibrating sample magnetometer
W	watt
XRD	X-ray diffraction
ZFC/FC	zero field cooled/field cooled

Acknowledgements

The completion of my PhD thesis has been an amazing project and challenge to me. All along, it has been strewn with obstacles, and I have tried my best to overcome them, both individually and as part of a team. During this experience as a PhD student, I have been surrounded with great people, that never hesitated to give me help and support, and encourage me to carry on with my work and ideas.

Firstly, I want to thank my supervisors Professor Nguyễn Thị Kim Thanh, Professor Quentin Pankhurst and Professor Shinya Maenosono for giving me the opportunity to carry out my PhD under the University College London/Japan Advanced Institute of Science and Technology scheme.

I would like to thank sincerely all my lab colleagues at the UCL Healthcare Biomagnetics Laboratories that were present during my first year for their warm welcome, their kindness, the time they devoted me, and the help they gave me, including Dr. Georges Frodsham, Dr. Roger Molto, Rogier Wildeboer, Dr. Cristina Blanco-Andujar and many others. More particularly, my thanks go to Valentina Mameli and Roxanne Hachani who trained me on the different characterisation techniques and laboratory equipments at the Royal Institution of Great Britain and Dr. Richard Jackson, Dr. Kristopher Page and Dr. Stephen Nesbitt who always spared their time to help me and answer my questions when I needed. My special thanks also go to Dr. Paul Southern for his valuable help on the theme of magnetism and magnetic hyperthermia, and for letting me use the magnetic alternative current hyperthermia system that he built for my experiments. I am also grateful to Alexander Dunn, who firstly synthesised the polymer I used in this first part of my research project, and then gave me precious advice to help me synthesizing it myself, just as members of his research team at the University of New South Wales, Australia, including Dr. May Lim and Dr. Cyrille Boyer that both participated to the polymer synthesis project. Finally, I would like to thank the new members of the research team at UCL Healthcare Biomagnetics Laboratories that were there during my last year as a PhD student, Georgios Kasparis, Andreas Sergides, and Fang-Yu Lin and particularly Lilin Wang and Dr. Kuan Boone Tan for their precious help and advice in cell culture and *in vitro* studies. My distinctive thanks go to Simone Famiani, for all the amazing science discussions and his incredible moral support throughout my last year of experimental works.

I would also like to thank all the people in my Japanese research team at the Japan Advanced Institute of Science and Technology, my supervisor Professor Shinya Maenosono, Dr. Derrick Mott, Pryiank Mohan, Maninder Singh, Mari Takahashi, Dr. Ngoc Anh, Dipali Ahuja, Rishika Rastogi, Ian Godfrey and Kanika Gupta. They all helped me to settle in Japan, which was not easy giving the completely different culture and the difficulty to communicate with Japanese people in the everyday life. More particularly I give my special thanks to Professor Shinya Maenosono who was always available and always willing to help when I needed his expertise, and allowed me to attend and participate in several conferences including the big international chemistry congress PACIFICHEM.

I would also like to thank everyone from the University of Bordeaux that made possible the accomplishment of the short term scientific mission undertaken at IMOTION laboratory, my supervisor for these two months Dr. Franck Couillaud, and his research team, Coralie Genevois, Dr. Isabel Ferreiro and Pauline JeanJean. I had the possibility to test another cell line, learnt about a new technique, the bioluminescence imaging and got some insight about genetic modification of cell lines and *in vivo* work. My thanks also go to Dr. Olivier Sandre that gave me access to his chemistry lab to synthesize nanoparticles for my time in Bordeaux.

I greatly appreciate the financial support of University College London and the Japan Advanced Institute of Science and Technology for my PhD scholarship. Likewise, I gratefully acknowledge the Royal Society of Chemistry, University College London, the Japan Advanced Institute of Science and Technology, the Centre for Doctoral Training in Molecular Modelling and Materials Science and the Chemical Society of Japan for their financial support that allowed me to attend national and international conferences during those three years, where I was given the opportunity to give talks, present posters, network and interact with people of incredible scientific expertise. These unforgettable experiences were very rewarding both on the professional and the personal level and helped me to build confidence in presenting my research to others. COST Action RADIOMAG (TD1402) supported by COST (European Cooperation in Science and Technology) is thanked for financial support of the short term scientific mission that allowed me to do the work presented in Chapter 6.

The last but not least, I want to thank my family and friends and particularly my parents, who supported me in my decision of doing a PhD and always had my back and kept me going when I was doubting of my choices. To Daniel Downes, who has not only been my partner but my best friend and confident especially during the last year of my PhD which was without a doubt the most difficult. You have always been there for me, listened,

cheered me up, encouraged me, stayed by my side and supported me in all my choices. You helped me more than you can realise and with you this year has been a lot easier to go through. You always believed in me when I did not and there is no word to express how grateful I am and will always be. Thank you.

Aziliz Hervault

CHAPTER 1

INTRODUCTION AND LITERATURE REVIEW

1.1 Magnetic nanoparticles in biomedical applications

Nanoparticles (NPs) are defined as particles that have one or more physical dimensions under 100 nm. Their size is a significant advantage for their use as sub-cellular size probes to study biological processes at nanoscale as cells in living animals are usually between 1 to 30 µm in diameter and cells parts and organelles are much smaller in the sub-micron range. This has strongly driven the development of nanotechnology into the fields of biology and medicine. Due to their small size, and particularly due to the increasing surface-to-volume ratio, the properties of a nano-sized material will differ from the ones of the bulk material (i.e. optic, electric, magnetic and electronic properties). Thanks to their inherent properties, magnetic nanoparticles (MNPs) have been developed as magnetic resonance imaging (MRI) contrast agents,[1,2] and potential new cancer therapies such as magnetic fluid hyperthermia,[3,4] and nanovectors for controlled drug delivery.[5,6] The possibility to manipulate the MNPs with an external magnetic field is a significant advantage to target and concentrate the NPs in specific parts of the body. Recently, research has been leaning towards the design of MNPs that can combine several therapeutic functions (hyperthermia and drug delivery),[7,8] or therapeutic and diagnostic functions (so called theranostics).[9,10] Scientists have been attempting to understand the structure and properties relationship of NPs to harness their properties.[11,12] Indeed, controlling the composition, size and shape of the NPs via syntheses would allow tailoring and tuning the desired properties.[13-16]

Among MNPs, iron oxide are the most commonly used NPs and, have attracted great interest for their applications in biomedicine due to their numerous advantages.[17] Indeed, iron oxide NPs are relatively easy to synthesize, biocompatible, non-toxic, chemically rather stable and superparamagnetic below a certain size (around 27 nm).[18] Some iron oxide nanoformulations have already been approved by the US Food and Drug Administration (FDA). The two main forms of iron oxide are ɣ-Fe_2O_3 (maghemite) and Fe_3O_4 (magnetite).

The main feature of this chapter is to present the recent advances in the development of multifunctional therapeutic nanosystems incorporating both magnetic nanoparticles and drugs, and their superior efficacy in treating cancer compared to either hyperthermia or chemotherapy as standalone therapies. The principle of magnetic fluid hyperthermia is also presented, along with a study of the different parameters influencing the heating performances of the nanoparticles.

1.2 Magnetic nanoparticles for hyperthermia therapy

1.2.1 Introduction to hyperthermia

The concept of hyperthermia was already in practice many centuries ago by Greeks, Egyptians and Romans to treat certain conditions including breast masses.[19,20] In 3000 BC, Indians medical practitioners used local and whole body hyperthermia. During the 19th century, it was observed that fever can cause tumour regression,[20] and scientific study was performed on hyperthermia to treat cervical cancer.[19] The use of hyperthermia as a treatment for cancer was taken more seriously in the 1970's, and controlled clinical trials on induced hyperthermia began to be conducted. It was then discovered that cancer cells have a greater sensitivity to hyperthermia as compared to normal cells. Indeed, healthy tissues are able to withstand temperatures of 42 – 45 °C, in contrast to cancer cells which undergo apoptosis at those temperatures.[21,22] Treatment at temperatures above 46 °C is called thermo-ablation. It leads to the necrosis of cancer cells, but may also affect healthy cells. Apoptosis, also called programmed cell death, is a distinct mode of cell death, whereby the cells in normal tissues triggered their self-destruction in response to a signal.[23] Contrary to the necrosis, there is no associated inflammation. Apoptosis also occurs spontaneously in cancer cells, thereby retarding the growth of the tumour, and can be increased when subjected to heat, irradiation or anti-cancer drugs. In contrast to apoptosis that is a natural process, necrosis is a form of cellular damage that results in the premature death of cells in body tissues and initiates an inflammatory response in the surrounding environment.[24,25] It is almost always harmful and can even be deadly (i.e. can lead to septicaemia or gangrene). Thus, thermoablation in this temperature range is not desirable due to the potentially important side effects on healthy tissues, and hyperthermia induced apoptosis is preferable.

While the specific mechanism of cell killing by hyperthermia is still unknown, the thermal energy needed for induction of cell death has been found to be close to the energy needed for protein denaturation, leading to the conclusion that the main cytotoxic effect of hyperthermia is based on the denaturation of membrane and cytoplasmatic proteins.[26,27] Membrane alteration and cytoskeletal damage such as cell rounding and blebbing, a typical feature of apoptosis, are some of the most apparent manifestations of thermal damage at the cellular level. Another important consequence of protein denaturation is the alteration of DNA synthesis and repair. A higher sensitivity to heat has been observed for cells in the mitosis phase (with damage to the mitotic apparatus),[26,27] which makes cancer cells more susceptible to heat than normal cells as they undergo faster cell division. The tumour selective effect of hyperthermia is also due to the physiological differences

between normal and tumour tissues. Indeed, the architecture of the vasculature in tumour is disorganised and abnormal compared to normal tissue, one of the principal features being the lower vessel density (Figure 1.1).

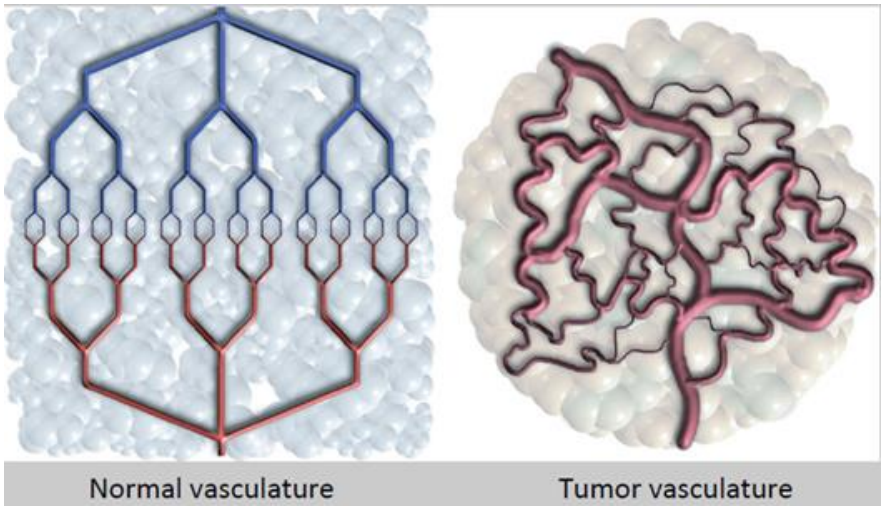

Figure 1. 1 *Schematic representation of a normal and a tumour vasculature. Figure taken and modified from ref. 28.*[28]

In many cases, tumour blood flow remains greater than in the surrounding healthy tissues, especially in small tumours (tumour blood flow generally decreases with increasing tumour size).[29] However, when hyperthermia is applied at temperatures over 42 °C, tumour blood flow tends to decrease, while in normal tissue it significantly increases. This decreased blood flow results in a lower heat dissipation rate, hence the temperature in a tumour will rise faster than in normal tissue.[29,30] This difficulty in dissipating heat may cause cancer cells to undergo apoptosis, while normal cells are more easily maintained at physiological temperature.[31] The disorganised structure of tumour vasculature also leads to oxygen and nutrient deprivation,[32] and reduction of the blood flow caused by heat exposure favours even more regions of hypoxia, energy deprivation and acidosis.[26,33] These tumour microenvironmental factors also make cancer cells more sensitive to hyperthermia,[34] in addition to its direct cytotoxicity.

In fact, hyperthermia may increase or decrease the tumour oxygenation depending on the temperature and the exposure time.[35] Hyperthermia applied at temperatures lower than 42 °C is more likely to provoke an increase in the tumour blood flow, thereby improving the oxygen supply. This phenomenon can be exploited to make cells more sensitive to radiotherapy (radiosensitivity is favored by good tissue oxygenation) or chemotherapy (drug delivery is increased by higher perfusion).[26,36] The synergistic effect of hyperthermia with radiotherapy has been demonstrated in various clinical trials,[37,38] and shows a better efficacy than either hyperthermia[39] or radiotherapy alone.[40] This synergism induces an

increase in cell death even at temperatures lower than temperatures normally applied in hyperthermia therapy. This thermal radiosensitisation is explained by the increased in blood flow, and by the fact that S-phase cells (cells undergoing DNA replication) and hypoxic cells (cells that survive the hypoxia and acidic environment of tumour), normally resistant to radiation, are highly sensitive to heat destruction.[26,41,42] The synergistic effect of hyperthermia with chemotherapy has also been demonstrated in clinical trials.[43-45] The increase in blood flow provoked by a heat treatment results in an increase in drug concentration in the tumour area, an increase intracellular drug uptake and enhanced DNA damage.[42] Moreover, heat has been found to enhance the cytotoxic effect of many anti-neoplastic drugs.[46] Consequently, hyperthermia is often used as an adjuvant therapy with radio- and/or chemotherapy.[36]

A wide range of heat sources and treatments for hyperthermia are being developed for clinical applications. There are three main types of hyperthermia: local hyperthermia, regional hyperthermia and whole-body hyperthermia. The hyperthermia technique is chosen depending on the location, the depth and staging of the malignancy. In whole-body hyperthermia, the entire body is heated up. This method is often chosen in the case of deep-seated and propagated metastases. The heating can be achieved through hot water baths, thermal chambers or infra-red radiators.[47] However, as may be expected, this treatment may lead to major side effects given the fact that the heat is not selective. Therefore, careful control of the temperatures is needed. Even if temperatures of 41.8 - 42 °C can be achieved, and the method is clinically realisable, the medical care needed to ensure a safe procedure in the case of whole-body hyperthermia is much greater than in local or regional therapy.[36] This has resulted in its limited use as a standalone procedure. Regional hyperthermia is used to deliver heat to advanced stage tumours. Thermal perfusion, external applicator or arrays of multiple applicators (microwave antennas) are example of devices used in regional hyperthermia.[47,48] Local hyperthermia is often used to treat localised tumours either superficially or in accessible body cavities. It is the less invasive technique. Local hyperthermia systems are based on applicators or antennas emitting mostly microwaves, ultrasounds or radio waves.[47,49] Recently, a new technology has been developed for local hyperthermia using MNPs as mediator of heat. This technology is called Magnetic Fluid Hyperthermia (MFH).

1.2.2 The different types of magnetism

Magnetism is a physical phenomenon in which attractive or repulsive forces are exerted by an object on other objects. All materials display to some extent a magnetic behavior, which means they are influenced by an external magnetic field. We can distinguish two

different contributions to the magnetic moment of an atom: the movement of electrons which orbit around the nucleus, known as the orbital magnetic moment, and the spin of electrons which gives an intrinsic magnetic moment, called spin magnetic moment. Therefore, the magnetic behavior of a material strongly depends on its electronic configuration. In fact, the magnetic moments of atoms or ions arise from their valence electrons. The filled electronic shells do not contribute to the magnetic moment because of their zero net orbital motion and because electrons are combined into pairs, the electron spins offset two by two (opposite intrinsic magnetic moments). There are five types of magnetism behavior: diamagnetism, paramagnetism, ferromagnetism, ferrimagnetism and anti-ferromagnetism.

Diamagnetism is a general property of atomic matter and originates from bound electrons. A diamagnetic material does not possess a permanent magnetic moment, but an induced magnetic moment which opposes the applied magnetic field. Paramagnetism is due to the presence of unpaired electrons. Every atom of a paramagnet has a magnetic moment. Because of thermal motion, those moments are randomly oriented, and therefore the average magnetization is equal to zero in the absence of any magnetic field. However, when an external magnetic field is applied, the moments of all the atoms tend to align themselves in the same direction as the applied field, thus amplifying it. If the temperature is too high, it is difficult to reach the saturation magnetization (due to the growing thermal motion). Paramagnetic materials do not retain any magnetization, which means the total magnetization drops back to zero when the external magnetic field is removed. Ferromagnetism is the property of certain material to become highly magnetized under the action of an external magnetic field, and even retain a magnetization after the removal of the applied field. A ferromagnet is formed of magnetic domains, known as Weiss domains, in which the moments of atoms are all parallel to each other to maintain a lowered-energy state. In the absence of any external magnetic field, the total magnetization of a ferromagnet is zero. However, when an external magnetic field is applied, the magnetic domains tend to align themselves in the same direction as the applied field. The saturation magnetization is reached as soon as each moment of each domain is aligned toward this direction. When the applied field is removed, the magnetization does not revert back to zero, this is the remanent magnetization. In order to reduce the magnetization to zero again, a magnetic field with a precise intensity needs to be applied, and is called coercivity (or coercive field). The magnetization curve of a ferromagnet is represented by a hysteresis loop. An antiferromagnet is also formed of magnetic domains, but the permanent magnetic moments are antiparallel per domain. Thus, the magnetization is non-existent in the absence of an external magnetic field, and a very strong magnetic field would be required to align every moment in the same direction due to strong exchange

interactions between the magnetic moments. Therefore, the magnetization curve of an antiferromagnet is a straight line with a slightly positive slope. A ferrimagnet is formed of magnetic domains with opposing magnetic moments, but the opposing moments have different amplitude. Thus, a spontaneous magnetization remains, as in the case of a ferromagnet, and the magnetization curve of a ferrimagnet is represented by a hysteresis loop. It is often difficult to tell the difference between a ferromagnetic and a ferrimagnetic material depending only on its magnetization curve. Ferro- ferri- and antiferromagnetic materials all become paramagnetic above a certain temperature due to thermal motion.

1.2.3 Superparamagnetism

Superparamagnetism is a form of magnetism that occurs in ferromagnetic or ferrimagnetic materials, when they are in the form of sufficiently small NPs. Bulk materials basically contain multiple magnetic domains due to their large size. However, below a critical size that is dependent upon the nature of the materials itself, small enough NPs becomes single-domain particles, which can be regarded as one giant magnetic moment composed of all the magnetic moments of the atoms forming the NP. Superparamagnetic NPs are preferred over ferri- and ferromagnetic NPs for biomedical applications, because they do not retain any magnetisation once the magnetic field is removed (Figure 1.2).

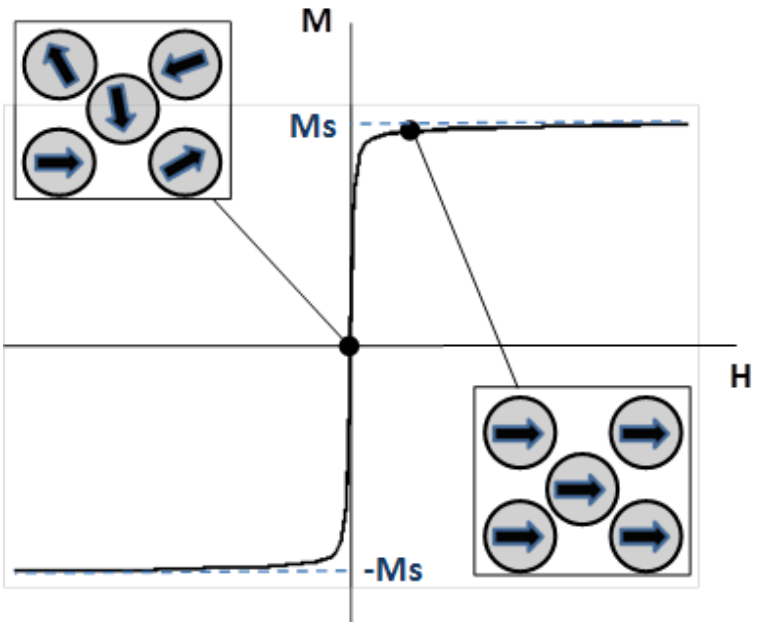

Figure 1. 2 *Typical curve for a superparamagnetic material. Squares show the orientation of the moment of single-domain nanoparticles with increasing field strength.*

Often, the magnetization aligns along one preferred direction, but the magnetization can randomly flip direction under the influence of temperature. The average time to perform such a flip is called the Néel relaxation time τ_N and is given by the following equation:[50]

$$\tau_N = \tau_0 e^{(\frac{KV}{k_B T})} \quad (1.1)$$

τ_0 is a length of time characteristic of the material. Its typical values are of a magnitude of 10^{-9} to 10^{-10} s. k_B is the Boltzmann constant, T the temperature, K the magnetic anisotropy energy density of the nanoparticle and V the volume of the nanoparticle. Thus, KV is the energy barrier the magnetization flip has to overcome by thermal energy.

In the absence of external magnetic field, depending on the timescale of the experiment τ used to measure the magnetization, the state of the nanoparticles can be identified: if $\tau >> \tau_N$, the measurement time is much longer than the average time between two flips. This means that a fluctuation state is observed, with different magnetization directions, and therefore, the magnetization appears to be in average zero. The nanoparticles are in a superparamagnetic state. In this state, an external magnetic field is able to magnetize the nanoparticles, in the same way to a paramagnet. However, their magnetic susceptibility is much larger than the one of paramagnetic materials. If $\tau << \tau_N$, the Néel relaxation time is much longer than the measurement time. This suggests the nanoparticles are in a well-defined state, the magnetisation appears static because the measured magnetization will be the same as the one at the beginning of the measurement. The system is in a blocked state. The transition between the superparamagnetic state and the blocked state occurs when $\tau = \tau_N$. The temperature for which $\tau = \tau_N$ is called the blocking temperature T_B, which is dependent upon the size and the composition of the nanoparticles.[51]

1.2.4 Magnetic hyperthermia: mechanism of heat generation

1.2.4.1 AC hysteresis losses

The conversion from magnetic energy to thermal energy in MNPs submitted to an AC magnetic field can be due to several mechanisms.

In multi-domains NPs (ferri- or ferromagnetic material), the production of heat is due to hysteresis losses, which can be seen as the amount of energy dissipated during a magnetisation cycle.[52,53] The magnetisation curve of a ferromagnet is represented by a

hysteresis loop (Figure 1.3) and the hysteresis losses can be measured by integrating the area of the hysteresis loop.

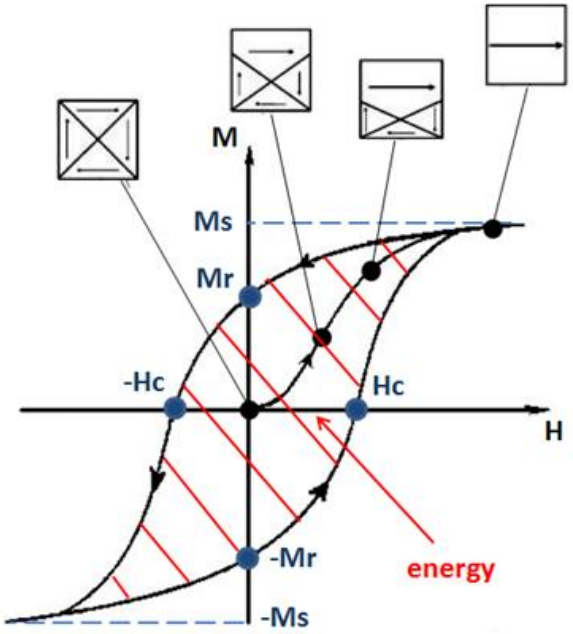

Figure 1. 3 *Hysteresis loop of a ferromagnet (squares show domain wall displacement with increasing field strength). The area of the hysteresis loop represents the energy dissipated during a magnetisation cycle.*

1.2.4.2 Relaxation losses

Single-domain NPs dissipate heat through relaxation losses which fall in two modes: Néel relaxation and Brownian relaxation. The mechanism of relaxation depends on the size of the NPs but also on the nature of the magnetic material mainly because of its anisotropy constant.[54] Néel relaxation comes from the reorientation of the magnetic moment in the same direction as the applied magnetic field with each field oscillation.[55,56] The Néel relaxation time τ_N is given by the equation 1.1:

$$\tau_N = \tau_0 \exp\left(\frac{KV}{k_B T}\right) \quad (1.1)$$

Néel relaxation is strongly size-dependent. A smaller particle requiring less energy for the rotation of its magnetic moment, the Néel relaxation mechanism will be very important.

Brownian relaxation is caused by the friction arising from the rotation of the particle itself in the carrier liquid.[55,56] The Brownian relaxation time τ_B is expressed by the following equation:

$$\tau_B = \frac{3\eta V_H}{k_B T} \quad (1.2)$$

Where η is the viscosity of the liquid carrier, V_H the hydrodynamic volume of the particle, k_B the Boltzmann constant and T the temperature. The Brownian relaxation mechanism is size-dependent too and also strongly viscosity-dependent.[57] A higher viscosity of the liquid medium will slow down the rotation of the particles. Néel and Brownian relaxation mechanisms are represented in Figure 1.4.

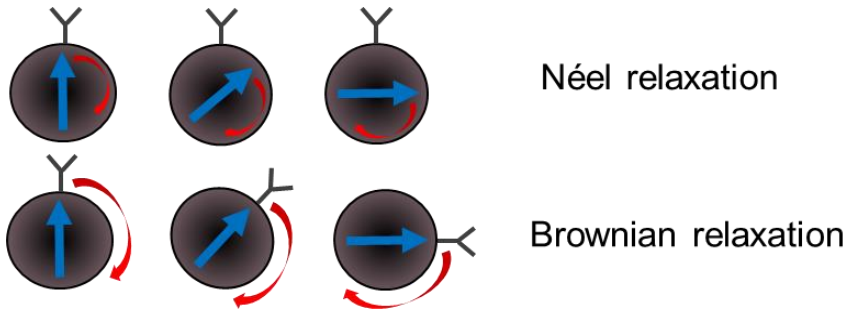

Figure 1. 4 *Schematic representation of the Néel versus Brownian relaxation. Néel relaxation: the magnetic moment rotates within each particle. Brownian relaxation: the particle rotates as a whole.*

Generally, losses by Néel relaxation prevails in small NPs while the Brownian regime dominates in larger NPs.[55,58] In fact, the Brownian losses are not exclusively found in superparamagnetic NPs.[52] For hyperthermia applications, it is better to have MNPs relaxing essentially through Néel mechanism, because when internalised in the cells, a change in the viscosity medium can happen and/or free rotation of the particles can be prevented.

A combination of the two magnetic relaxation times gives the overall effective relaxation time τ of the particles[55]:

$$\tau = \frac{\tau_B \tau_N}{\tau_B + \tau_N} \quad (1.2)$$

1.2.4.3 Quantification of heat losses

Application of an AMF oscillating faster than the relaxation time of the MNPs induces the release of heat from the MNPs caused by the delay in the relaxation of the magnetic moment.[55] The heat dissipation P is given by the following equation[59]:

$$P = \mu_0 \chi'' f H^2 \quad (1.3)$$

Where P is the heat dissipation value, μ_0 is the permeability of free space, χ'' is the AC magnetic susceptibility (imaginary part), f is the frequency of the applied AC magnetic field, and H is the strength of the applied AC magnetic field.

Quantification of the power dissipation of magnetic nanoparticles in an AMF is usually done by measuring the specific absorption rate (SAR) expressed in W/g (also referred to as specific loss power)[55]:

$$SAR = C \frac{\Delta T}{\Delta t} \quad (1.4)$$

Where C is the specific heat capacity of the sample and $\Delta T/\Delta t$ is the initial slope of the time-dependent heating curve. SAR highly depends on various parameters such as the size, size distribution, shape, chemical composition and surface modification, saturation magnetisation of the particles, frequency and amplitude of the applied magnetic field. A high heating potential is crucial for the clinical use of MFH, because it would require a smaller amount of NPs to be injected to the patient. Therefore, engineering MNPs (control their physical and chemical properties using synthesis) to obtain high SAR values is highly desirable.[60-63] For example, most ferri- and ferromagnetic materials require application of a high magnetic field to use a full loop area, which is not realisable clinically due to physiological and technical restrictions. On the other hand, superparamagnetic NPs producing heat via Néel and Brownian relaxation mechanisms are able to generate a much larger quantity of heat and thus a higher SAR at lower field amplitudes. Hergt *et al.* suggested that the optimum size to get particles with a high SAR value is near the transition from superparamagnetic to ferromagnetic behaviour.[64] Considering the equation of the heat dissipation value, it is clear that SAR values increase with the frequency *f* and the amplitude *H* of the applied field. However, to apply hyperthermia safely to patients and avoid any detrimental effect on healthy tissues due to electromagnetic radiation exposure, the *Hf* factor should not exceed a threshold which was experimentally estimated to equal 5×10^9 $Am^{-1}s^{-1}$.[65]

The comparison between SAR values obtained by different research groups can be challenging. Indeed, there is a lack of standardised protocol to measure the heating ability of the MNPs. The ideal for accurate measurement of the SAR would be an adiabatic setup, but because it is expensive and time-consuming, most research groups use non-adiabatic and often home-made setups which results in more sources of inaccuracies and increase variability of the SAR values.[66-68] Moreover, there is no standard for the frequency and

amplitude of the applied field to be used during an experiment and research groups measure nanoparticles heating capabilities under different field conditions. Because the SAR value for a given sample is not an intrinsic property of the system as it is strongly dependant on the amplitude and frequency of the field used, comparison of SAR values between different systems is almost impossible. Pankhurst *et al.* introduced a parameter allowing direct comparison of the heating efficiency of superparamagnetic nanoparticles, the intrinsic loss power (ILP).[4] The ILP is obtained by normalizing the SAR by the frequency and field amplitude, and is therefore independent of the magnetic field parameters:

$$ILP = \frac{SAR}{H^2 f} \tag{1.5}$$

1.2.5 Nanoparticle delivery to the tumour

MNPs must be delivered in a secure pathway specifically to the cancer site and should be retained in the tumour in order to avoid side effects and reach a sufficient concentration for an effective therapy whether it is for magnetic hyperthermia or for drug delivery. Three main approaches for the delivery of NPs can be distinguished: direct injection, systemic passive and active delivery.

The direct injection method consists of injecting directly the magnetic fluid into the tumour. The intratumoural injection is the simplest way to administer the NPs. It is the most commonly found in *in vivo* studies[69,70] and has even already been used in clinical trials of MFH.[38,71] The main advantage of this technique is the ease to achieve a high and localised concentration of MNPs in the tumour. However, the intratumoural injection of MNPs is only possible in localised and superficial or easily accessible tumour, thus this approach is limited in the investigation of many cancers, and particularly advanced stage cancers. Moreover, direct injection results in a non-homogeneous MNPs distribution in the tumour, which makes the complete regression of the tumour difficult.[72]

Systemic delivery is achieved by injecting MNPs intravenously that will accumulate preferentially in tumour tissue due to the enhanced permeability and retention (EPR) effect.[73,74] The EPR effect was first reported by Matsumura and Maeda in 1986,[75] and was further investigated and described in a greater extent by Maeda *et al.*[76-81] The EPR effect rests on the facts that solid tumours exhibit a defective vascular architecture and that lymphatic clearance from the interstitium of tumour tissue is impaired. The first results in an enhanced vascular permeability which facilitates nutrients and oxygen supply to satisfy the demand of growing tumours, while the second results in the retention of

macromolecules in the tumour. Therefore, solid tumours possess a leaky vasculature compared to normal tissues, which facilitates the extravasation of NPs. Consequently, when NPs are injected intravenously, they can leak out of the blood vessel to deposit in the tumour, and are retained here for a long time due to impaired lymphatic drainage (Figure 1.5).

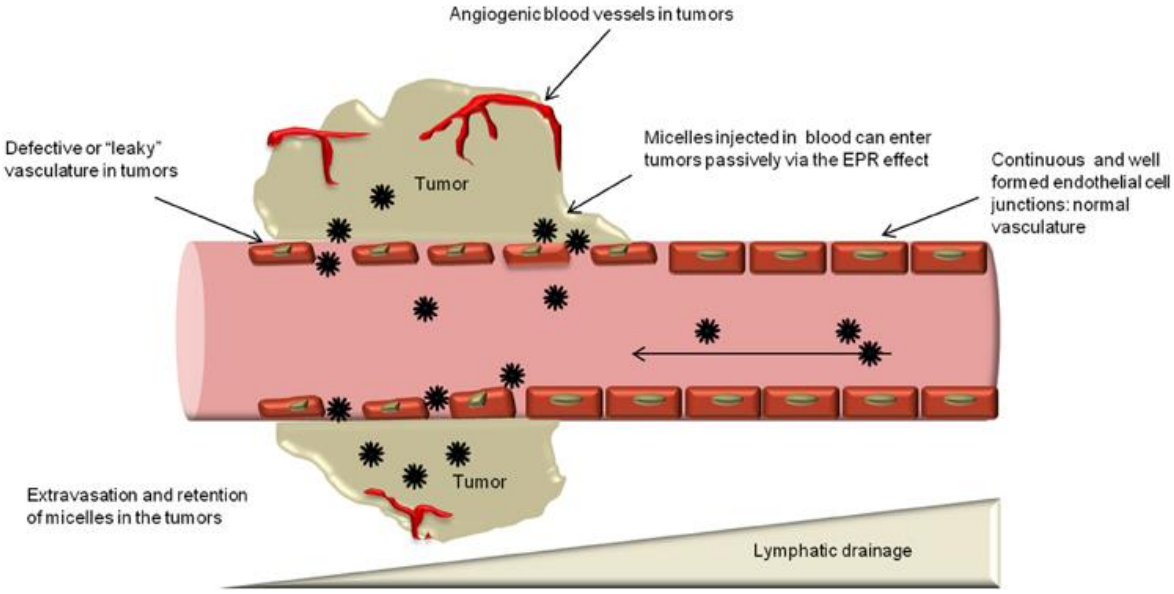

Figure 1. 5 *Passive targeting and EPR effect. Nanoparticles extravasate through vascular fenestrations of tumours and are retained there due to poor lymphatic drainage.*[82]

MNPs can also be injected in the artery supplying the blood stream to the targeted organ in order to improve the deposition of MNPs in the tumour. To take advantage of the EPR effect, the MNPs should be able to circulate long enough in the blood stream. For this purpose, NPs should have a hydrodynamic diameter smaller than 200 nm to avoid liver and spleen clearance[18] and bigger than 5 nm to avoid renal clearance.[83,84] The coating of the NPs plays an important role in the permeability and retention of the NPs in cancer cells, as well as in the blood retention time of the NPs. Ideally, NPs should be furtive to not be cleared by the reticulo-endothelial system. In a recent study, SPIONs were coated with two different polymers for MRI applications: alkali-treated dextran (ATD) and carboxymethyl dextran (CMD).[85] A much higher labeling of the macrophages was obtained with the ADT-coated NPs. After 4 h, ADT-coated NPs exhibited a labeling efficiency superior to 95% (against only 20-30% for the CMD-coated NP) as a result those NPs would be rapidly cleared by macrophages in the reticulo-endothelial system. Protein adsorption onto the surface of NPs may accelerate the clearance by the reticulo-endothelial system[86] and affect the bio-reactivity of the NPs.[87] A good coating can prevent or at least minimize proteins attachment onto the surface of NPs. An appropriate coating should also confer good colloidal stability of the nanoparticles in a biological medium, to avoid aggregation and conserve the hydrodynamic size that ensures them a long blood circulation time. The

passive delivery of NPs via the EPR effect results in a more global distribution of the MNPs in the tumour compared to an intratumoural injection and allows for the treatment of most type of cancers. However, the principal disadvantage of this method is the difficulty to reach a concentration of NPs sufficient enough for an effective treatment, yet the amount of NPs injected cannot always be further increased to avoid a non-negligible MNPs toxicity. In order to achieve higher deposition and improve tumour uptake of the NPs, they can be driven magnetically inside the body via an external magnet and/or can be functionalised with a targeting ligand for active delivery.

Active delivery consists of improving the specificity of NPs by functionalising their surface with a targeting moiety that binds to cell receptors. It usually results in a higher NPs accumulation and cellular uptake in the targeted cancer cells. Among the most commonly used targeting agents, we can find antibodies,[88,89] antibody fragments,[90,91] receptor ligands,[92,93] peptides[94,95] and aptamers.[96,97] The superiority of targeted MNPs in cancer treatments has already been proven many times. For example, in a recent study,[98] iron oxide NPs were coated with dextran and functionalised with an anti-human epidermal growth factor receptor (HER2) aptamer for targeted hyperthermia. Results showed that a 90-fold lower dose of the aptamer-functionalised NPs was necessary to produce a 60% decrease in the HER2-overexpressing cell viability compared to the non-tagged NPs.
Another targeting system that can be used to improve the accumulation of MNPs into a tumour is the magnetic targeting, also called magnetophoresis. This technique used an external static magnetic field placed near the tumour to magnetically attract the NPs toward this area and has already shown efficacy in *in vivo* studies.[99,100]

1.2.6 Magnetic nanoparticles for hyperthermia therapy

Numerous materials have been investigated for their potential use in magnetic hyperthermia, such as Fe, Co, Ni metallic NPs and their oxide. Pure metals have the highest saturation magnetisation, but have limited use in biomedical applications due to their inherent toxicity and poor chemical stability (mainly their quick oxidation process). Research into metal ferrites has shown good chemical stability, SAR values and magnetic properties, making a new class of potential candidates for magnetic hyperthermia.[60] The effects of Co or Zn dopant in metal ferrites NPs have also been investigated, showing improved SAR. 15 nm $(Zn_{0.4}Mn_{0.6})Fe_2O_4$ NPs synthesised by thermal decomposition exhibited an increased anisotropy and a saturation magnetisation of 175 emu/g resulting in a SAR value almost four times higher than that of Feridex NPs, a FDA approved iron oxide nanoparticles.[101] Despite the superior magnetic properties of metallic NPs, iron oxide NPs are still the most studied magnetic material for hyperthermia applications, due to their

low toxicity, good biocompatibility, ease of synthesis and surface functionalisation. The most used synthetic routes to make iron oxide NPs are the thermal decomposition of organometallic iron precursor and the co-precipitation of Fe^{2+} and Fe^{3+} aqueous salt in the presence of a base. Many good papers reviewing the different methods for the synthesis of MNPs for biomedical applications, the main parameters influencing the MNP properties (precursors, time and temperature of the reaction, solvent, ligand, etc) as well as MNP surface functionalisation can be found in the litterature.[17,102-105]

A number of MNP properties influence their hyperthermia potential such as the composition, shape, coating, magnetic properties, size and size distribution. Some recent studies have been carried out to investigate the influence of these properties on the magnetic hyperthermia treatment effectiveness, and Kolhatkar *et al.* reviewed parameters that can be varied to tune the magnetic properties of NPs.[106] Carrey *et al.* recently published a method to identify suitable materials for hyperthermia.[107] A new approach for the exact calculation of the hysteresis loop is presented and models for the calculation of the optimum parameters of MNPs for magnetic hyperthermia, such as the optimum anisotropy, are provided.

1.2.6.1 Influence of the size and size distribution

Sedlacik *et al.* synthesised magnetite NPs by a microwave irradiation-assisted solvothermal method, using different nucleating agent (ammonium acetate, ammonium carbonate and aqueous ammonia).[108] The highest saturation magnetisation was obtained for magnetite NPs nucleated with aqueous ammonia due to a pure cubic Fe_3O_4 spinel phase and absence of non-magnetic impurities. The lower saturation magnetisation obtained for the two other NPs was attributed to the presence of coexisting phases with different magnetic properties, such as goethite. The highest SAR value was also obtained for the NPs nucleated with aqueous ammonia, most likely caused by their higher saturation magnetisation, their smaller size and narrow size distribution compared to the particles obtained with the other nucleating agents. Gonzales-Weimuller *et al.* studied the influence of the size (range from 5 to 14 nm) and polydispersity on the SAR of iron oxide NPs subjected to an AMF (frequency = 400 kHz; amplitude = 24.5 kA/m).[14] The highest SAR value of 447 W/g (ILP = 1.86 nHm^2/kg) was obtained for the 14 nm NPs. Moreover, the lower the size polydispersity, the higher the SAR value, no matter the NPs size. For larger NPs where hysteresis losses are the main mechanism of heat, the SAR value increases as the NPs size decreases.[109] The heating power in $MgFe_2O_4$ NPs was found to be strongly size-dependant, with a maximum SAR value for particle size of 10 nm.[110] De la Presa *et al.* synthesised maghemite NPs of 8 nm, 11 nm, 13 nm and 14 nm by a co-precipitation

method, and studied the influence of NPs concentration, size, coating, liquid carrier, field amplitude and frequency on SAR value.[111] For each NP size, the concentration of NPs dispersed in water does not seem to influence the SAR in the studied iron concentration range of 6 to 300 mg/mL. Increasing the size of the NPs resulted in an increased SAR value: for 8 nm to 11 nm NPs, the SAR is increased by four times, from 10 W/g to 40 W/g. For 11 nm to 13 nm NPs, the SAR only increased from 40 W/g to 55 W/g. The influence of the medium viscosity was investigated by dispersing the NPs in either water or agar. For the smallest NPs, the viscosity has a negligible influence on the SAR, but for the biggest NPs, the SAR strongly decreases when measured in the viscous media (agar). This is due to the fact that Néel relaxation is mainly responsible of the production of heat in small NPs. With bigger NPs, both Néel and Brownian relaxation take part in the heating process. Néel relaxation, unlike Brownian relaxation, is not influenced by the carrier viscosity. As a conclusion, the optimum size for a maximized viscosity-independent SAR value was found to be around 12 nm for maghemite NPs.

1.2.6.2 Influence of the shape

The influence of the shape on the MNPs heating properties has been less extensively studied than the influence of the size. Song *et al.* synthesised magnetite NPs by thermal decomposition in octadecene in the presence of oleic acid, and varied the amount of surfactant and refluxing time to get highly monodisperse spherical (9.5 nm) and quasi-cubical (9.6 nm) MNPs.[112] The quasi cubical MNPs displayed a highest SAR value which could originate from their bigger magnetic core volume and a higher crystallinity. A significant enhancement of heating performances is observed for multi-core flower-shaped maghemite NPs of 24 nm (constituted of smaller grains of 11 nm), with a SAR of 1992 W/g.[113]

1.2.6.3 Influence of the coating

MNPs are usually coated with a hydrophilic ligand or polymer to improve their biocompatibility and their colloidal stability. Indeed, NPs aggregation would modify the NPs properties including their heating performances. The choice of the ligand is important because it can modify the magnetic properties of the NPs. Larumbe *et al.* showed that a silica coating on magnetite NPs negatively affected the magnetic properties and the SAR value, due to an enhancement of the spin disorder surface effects caused by the silica coating.[114] In a recent study, magnetite NPs with controlled particle size (9 nm, 19 nm and 31 nm) and mPEG surface coating thickness (by varying the molecular weight: 2000 Da, 5000 Da, and 20000 Da) were synthesised by thermal decomposition.[63] The heating

efficiency was observed to decrease with increasing polymer chain length, excepted for the largest NPs. Indeed, the 31 nm NPs coated with 2000 Da mPEG agglomerate, because the polymer chains were too short to provide a good colloidal stability due to strong magnetic dipole-dipole interactions between the particles. This trend was reflected by the measured SAR values for each system. The highest SAR value achieved was 930 W/g for the 19 nm NPs coated with 2000 Da mPEG and the lowest was 267 W/g for the 9 nm NPs coated with 20000 Da mPEG. The study of chitosan-coated magnetite NPs showed an improved SAR compared their bare magnetite NPs counterparts.[115] A bilayer of oleic acid has been shown to improve the hyperthermia properties of $La_{0.7}Sr_{0.3}MnO_3$ NPs,[116] arising from an improved colloidal stability of the NPs suspension at physiological pH. All these results emphasize the importance to carefully chose and optimise the surface coating for a given system to yield the highest SAR possible.

1.2.6.4 Materials for self-controlled hyperthermia

It is important to control the temperature during magnetic hyperthermia treatment, in order to avoid overheating of the surrounding healthy tissues. However, a precise control of the temperature can be difficult to achieve, and therefore, magnetic materials with a maximum self-heating temperature are very attractive for hyperthermia applications. The Curie temperature (Tc) is an intrinsic property of magnetic materials. Above this temperature, the magnetic system becomes paramagnetic (Figure 1.6) and consequently the heating stops.

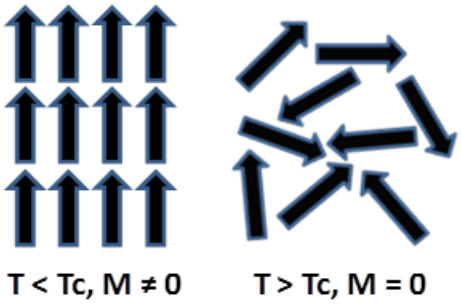

Figure 1. 6 *Schematic representation of the moments of atoms of a ferromagnet below and above its Curie temperature in the absence of an applied magnetic field.*

The Tc of a magnetic system can be modified to a certain extent with the chemical composition. By choosing a material with a Tc close to the hyperthermia temperature range and adjusting it at the desired therapeutic temperature, the heating of the tumour can be controlled and the temperature maintained at a constant desired value for a self-controlled hyperthermia treatment. For example, the Tc of Mn-ferrites can be decreased by replacing magnetic ions with non-magnetic Ti^{4+} ions ($Mn_{1+x}Ti_xFe_2O_4$), from 300 °C for x = 0 to 35 °C

for x = 0.6.[117] A Tc of 46 °C was obtained for x = 0.55. Among the magnetic materials with a tunable Tc in the therapeutic temperature range, we can find: $La_{1-x}Sr_xMnO_3$ whose Tc increases with an increasing Sr content,[118] Gd-substituted Zn-ferrite ($ZnGd_xFe_{2-x}O_4$) whose Tc increases with an increasing Gd content and was found around 45 °C for x = 0.02,[119] $Ni_{1-x}Cr_x$ whose Tc increases with a decreasing Cr content and was found equal to 44 °C for x = 5.63,[120] and $Mg_{1+x}Fe_{2-2x}Ti_xO_4$ whose Tc decreases with a decreasing Fe content and was found around 46 °C for x = 0.37.[121]

1.2.7 Examples of *in vivo* applications of magnetic hyperthermia

Basel *et al.* used specific monocytes/macrophages-like cells (Mo/Ma) to carry core/shell iron/iron oxide NPs directly into the tumour of mice injected with Pan02 cells to generate a murine model of disseminated pancreatic cancer.[122] These Mo/Ma cells have been shown to be tumour-homing cells, they infiltrate tumour site and they specifically accumulate in pancreatic tumours when injected intraperitoneally. The Mo/Ma cells loaded with MNPs were injected intraperitoneally, and 3 days after the injection, the mice were subjected to 20 min of AMF exposure. The mice subjected to the hyperthermia treatment survived significantly longer than the other mice, with a 31% increase in lifespan.

Lin *et al.* used Mn-Zn ferrite NPs coated with polyethyleneimine to evaluate the anti-cancer effect of the magnetic fluid with and without combined radiotherapy *in vitro* and *in vivo*.[123] They chose a magnetic fluid with a NP concentration of 10 g/L because the hyperthermia temperature stabilised around 43 °C under application of an AMF of 230 kHz and 1 kA/m. Tumours were grown into the right posterior limb rump of nude mice by injecting exponentially growing HepG2 cells. The magnetic fluid was injected intratumourally following a multipoint injection strategy, and the hyperthermia treatment was applied for 1 h. The volume inhibition rate and mass inhibition rate of the tumour for the combined group were 87.6 % and 88.6 % respectively, against 41.0 % and 34.2 % for the radiation-alone group, 79.9 % and 77.9 % for the hyperthermia alone group. The *in vivo* experiments revealed a good inhibition of the tumour growth, for both hyperthermia alone and the combined treatment.

Ferucarbotran (also called Resovist) consists of clinically approved SPIONs coated with carboxydextran developed for contrast-enhanced MRI of the liver. Those NPs can also be used for hyperthermia therapy as they are able to generate heat when submitted to an AMF. Araya *et al.* injected A549 cells, a human non-small cell lung cancer cell line, in

BALB/c nu/nu athymic female nude mice and studied the anti-cancer effect of ferucarbotran-mediated hyperthermia.[124] Ferucarbotran NPs were injected intratumourally and the temperature was maintained at 43 – 45 °C for 20 min by application of an AMF. Even if complete tumour suppression was not fully achieved, the tumour volume was significantly suppressed. Shetake *et al.* showed tumour regression in a fibrosarcoma tumour model after subjecting the mice to repeated magnetic hyperthermia treatment of 10 min each using iron oxide nanoparticles.[125] The tumour growth inhibition was mainly attributed to severe apoptosis and reduced tumour cells proliferation. In another study, BxPC-3-xenograft bearing mice (human pancreatic adenocarcinoma) and MDA-MB-231-xenograft bearing mice (human breast adenocarcinoma) were subjected to a magnetic hyperthermia treatment of 1 h with an AMF of 435 kHz and 15.4 kA/m using two types of dimercaptosuccinic acid-coated iron oxide nanoparticles synthesized via different routes.[126] A better response of breast cancer xenografts to the hyperthermia therapy compared to pancreatic tumours was observed. After 4 weeks, in breast MDA-MB-231 xenografts, tumours showed a significant shrinking of their relative volumes to 85% and 50% for the two different types of nanoparticles in relation to the tumour volumes before treatment. In contrast, untreated MDA-MB-231 tumours showed linear growth over the same period of time, resulting in a relative tumour volume of 305%. In pancreatic BxPC-3 xenografts, tumour growth was also significantly reduced after magnetic hyperthermia. The relative tumour volume at 4 weeks post magnetic hyperthermia was 204% and 244% compared to 507% of the untreated animal group. Interestingly, Huang and Hainfeld *et al.* reported complete regression of tumours in approximately 80% of animals using a very short 2 min dose treatment with an AMF of 980 kHz and 38 kA/m upon intravenous injection of iron oxide nanopartiches that achieved a tumour concentration of 1.9 $mg_{Fe/g}$ in a subcutaneous squamous cell carcinoma mouse model.[72] The tumours could be heated to 60 °C in 2 min, durably ablating them with millimetre precision, leaving surrounding tissue intact.

Some clinical trials have already been performed with MNPs for hyperthermia therapy and have been summarized by Thiesen & Jordan in 2008[127] and by Zhao *et al.* in 2013.[128]

1.3 Magnetic nanosystems for combined thermo-chemotherapy

1.3.1 Enhancement effect of the combined therapy

The enhancement of chemotherapy effects with application of concurrent hyperthermia is called thermo-chemosensitisation. Several mechanisms are involved in this thermal enhancement, such as an increased antineoplastic drug accumulation in tumours, and an enhanced drug cytotoxicity (improved intracellular uptake of drugs and increase sensitivity of cells to drugs).[129,130] The first one is due to the physiological effect of mild hyperthermia on tumour vasculature, including an increased blood flow, perfusion, and blood vessel pore size of the already leaky tumour vasculature. All these factors facilitate drug extravasation in tumour tissues. The mechanisms responsible for the enhanced drug cytotoxicity are not yet fully understood, but generally involve an improved intracellular uptake of drugs due to an increase cell membrane permeability, an inhibition of DNA-repair of the chemically induced lethal or sublethal damages, and an acceleration of the cytotoxic chemical reaction in the case of certain antineoplastic agents.[46] Figure 1.7 summarizes the mechanisms behind the synergistic effect of simultaneous hyperthermia and chemotherapy.

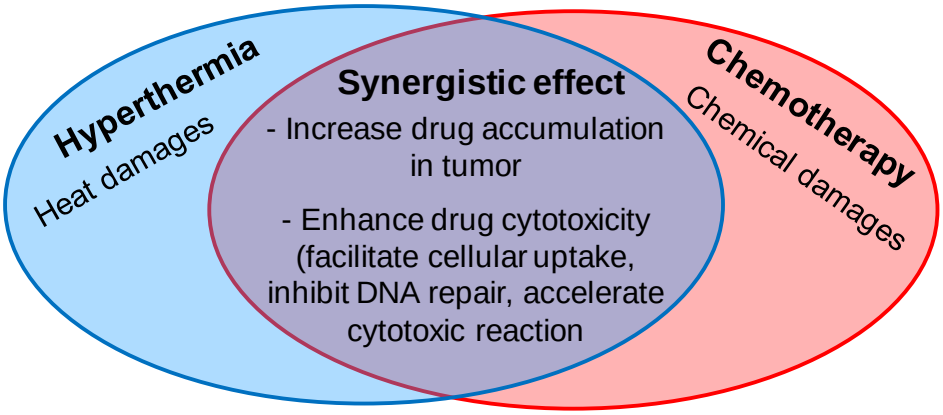

Figure 1. 7 *Mechanisms responsible for the synergistic effect of the combined thermos-chemotherapy.*

Several studies have demonstrated that the thermal enhancement of the cytotoxic activity of many anti-cancer agents is maximized at mild hyperthermia temperatures (40.5 – 43 °C).[131] Chemotherapeutic drugs can be classified into four different categories depending on the way heat affects their cytotoxicity[132]:

- Agents exhibiting a linear increase in cytotoxicity with increasing temperature: alkylating antineoplastic drugs (nitrogen mustards, nitrosoureas and thiotepa),

platinum-based chemotherapeutic drugs (i.e. cisplatin), mitoxantrone and mitomycin C are part of this category.

- Agents showing a threshold temperature effect: they do not undergo a linear increase but only a little change in cytotoxicity with increasing temperatures until a threshold of 42 °C – 43 °C. Above this threshold, a synergetic effect is observed. This is the case of adriamycin, bleomycin and actinomycin D.
- Agents not presenting any change in cytotoxicity with higher temperatures: the antimetabolites, methotrexate, 5-fluorouracil, amsacrine, and the vinca alkaloids (vincristine and vinblastine) show temperature-independent action.
- Agents that are not cytotoxic at 37 °C, but become cytotoxic with increasing temperatures. This type of cytotoxicity is characteristic of cysteamine, amphotericin B and lidocaine.

Different studies have aimed to evaluate and identify the mechanisms behind the thermal enhancement of the cytotoxic activity of some chemotherapeutic drugs. The thermal enhancement of cisplatin and adriamycin cytotoxicity was evaluated *in vitro* using a human bladder cancer cell line.[133] Mild hyperthermia alone (41 °C) and low drug concentration (20 µg/mL of cisplatin or 4 µg/mL of adriamycin) did not have any cell killing effect. However, the anti-tumour effect of the combined therapy was significantly higher than either hyperthermia or drug alone, using the same drug concentrations and hyperthermia temperature. The survival rate in the case of the combined treatment was the same as that of a 10-fold higher concentration of cisplatin or adriamycin administered alone. These results indicate that the quantity of drugs used in chemotherapy for the treatment of cancer can be effectively reduced by combination with mild hyperthermia, thereby limiting the side effects of the treatment. The mechanisms of action of the two drugs are the following: cisplatin inhibits DNA synthesis and cell division through formation of DNA intrastrand crosslink adducts (DNA platination).[134] Crosslinks causes DNA replication arrest and apoptotic cell death if the crosslink is not repaired. Adriamycin intercalates into DNA and inhibits the enzyme topoisomerase II resulting in DNA damage and cell death. Adriamycin can also generate free radicals that damage cellular membrane, DNA, proteins and lead to apoptotic cell death.[135] Consequently, mechanisms responsible for the thermal cytotoxicity enhancement of both drugs are assumed to be an increase in cellular uptake of drug and inhibition of DNA repair of drug-induced DNA damage.

Onconase is a cytotoxic ribonuclease that binds to cell surface receptors, degrades ribosomal RNA once internalised to the cell and inhibits protein synthesis causing apoptotic cell death.[136,137] Onconase also suppresses proliferation, is cytotoxic to several tumour cell lines and is synergistic with many anti-cancer agents. The thermal enhancement of onconase cytotoxic effects by mild hyperthermia was evaluated *in vitro*

on human lymphoblastoid TK6 cells.[138] The percentage of apoptotic cells was measured after treatment with onconase alone (2 or 5 µg/mL), hyperthermia alone (40 °C or 41 °C), for a treatment duration of 24 h or 48 h, and for the combined treatment. The results are presented in Table 1.1. The increased therapeutic effect of mild hyperthermia with onconase was observed at 41 °C and even at 40 °C, temperature at which the cells were not much affected. The thermal enhancement mechanism of onconase cytotoxic activity is not known with certainty. However, it is believed that an increased intracellular uptake of the drug and accelerated kinetics of ribosomal RNA degradation is responsible for the synergistic effect of the therapy.

Table 1. 1 *Percentage of apoptotic cells after 24 h and 48 h of treatment.*

Treatment duration	Onconase concentration	Temperature		
		37.5 °C	**40 °C**	**41 °C**
24h	**0 µg/mL**	6%	6%	25%
	2 µg/mL	13%	39%	> 50%
	5 µg/mL	15%	49%	> 55%
48h	**0 µg/mL**	/	7%	45%
	2 µg/mL	33%	54%	74%
	5 µg/mL	42%	77%	85%

The thermal enhancement of melphalan (alkylating agent) and oxaliplatin (platinum-based agent) cytotoxicity were studied *in vitro* using spontaneous fibrosarcoma FSa-II tumour cells, as a function of treatment time at temperatures between 37 - 44.5 °C with a constant concentration of melphalan (0.25 µg/mL) or oxaliplatin (7.5 µg/mL).[139] For both drugs, a thermal enhancement was observed, more pronounced in the case of melphalan, that became greater with increasing temperatures or increasing treatment time. The mechanism of effect of oxaliplatin has been found to be the same as cisplatin (formation of DNA intrastrand crosslink adducts which inhibits DNA replication and leads to cell death). Melphalan interacts with DNA to form interstrand crosslink adducts, also causing apoptotic cell death. At physiological temperatures, they observed a constant cell killing effect indicating that cytotoxic reactions occurred at a constant rate. With increasing temperatures, the reaction rate became faster. Thus, at mild hyperthermia temperatures (below 42 °C), the mechanisms responsible for the thermal enhancement of the drug cytotoxic activity seem to be mainly an increase rate of chemical reactions leading to cell death, the inhibition of DNA repair of drug-induced DNA damages and an enhanced intracellular uptake of drugs. Above 42 °C, hyperthermia has a direct killing effect on cells due to the denaturation of proteins induced by heat. This study also highlights the

importance of the thermal dose: the heating temperature and time of exposure greatly influence the interaction between heat and drug.

Other numerous studies showed a thermal enhancement of drug cytotoxicity. For example, the combined treatment of hyperthermia at 43 °C for 45 min and cisplatin or etoposide resulted in more apoptotic cells than hyperthermia or drug alone with a lower concentration of drug.[140] Again with cisplatin, the combined treatment was 1.7 times more effective than hyperthermia alone (43 °C, 60 min) and 1.4 times more effective than cisplatin alone.[141] Hyperthermia was in this case applied by means of iron oxide NPs injected intratumourally while cisplatin was injected intraperitoneally. BCNU (1,3-bis(2-chloroethyl)-1-nitrosourea), an alkylating agent, causes DNA interstrand crosslink which lead to cell death. The alkylation reaction rate is accelerated by hyperthermia which results in an increased cell death.[142] A comparative study of some of the clinically employed platinum-based anticancer agents (cisplatin, carboplatin and oxaliplatin) demonstrates a cytotoxic thermal enhancement for all of them.[143] However, a true synergistic effect was observed in the case of cisplatin, while only an additive effect was reported for carboplatin and oxaliplatin. All these studies reveal that the most effective treatment is achieved when hyperthermia and drug are administered simultaneously, but some exceptions exist. Thus, drug pharmacokinetics have to be investigated to be able to benefit as much as possible from the improved anti-cancer effect of the treatment using a minimum amount of drugs thereby minimizing the toxicity. For instance, gemcitabine needs a time interval of 24 h between drug administration and application of hyperthermia to obtain a synergistic effect.[46]

There is a concern about the oncogenic potential of many anti-cancer drugs. Hyperthermia combined with chemotherapy has the potential to reduce the risk of treatment-induced secondary cancer because hyperthermia lower oncogenic transformations. Indeed, hyperthermia converts sublethal damage induced by the drug to lethal damage and/or inhibits DNA repair, therefore reducing the expression of transformation. Moreover, cells in S-phase are particularly sensitive to heat, and transformation mainly occurred when cells are in S-phase. Thus, hyperthermia could reduce the frequency of transformation induced by chemotherapy. A study dedicated to the oncogenic potential of hyperthermia combined with either actinomycin D, mitomycin C or carmustine showed a reduction of the drug-induced transformation for a given level of cell killing compared to the administration of drug alone.[144] A reduction of oncogenic transformations was also reported in the case of melphalan[145] and cisplatin.[145,146]

1.3.2 Nanosystems for simultaneous hyperthermia and drug delivery

Anti-cancer agents are often highly cytotoxic for both cancer and healthy tissues. The controlled release of drugs in a localised, targeted area is a major challenge in chemotherapy, as it would allow the reduction of systemic exposure therefore minimizing the side effects, and also lower the chemotherapeutic dose used for the therapy. This becomes possible using nanosystems as vehicles for drug delivery.[9,147-151] The chemotherapeutic drug is stored and protected in the nanocarrier until it gets to the cancer site, where it is released. The drug is thus harmless to healthy tissues during its circulation in the body, and provided in high concentration at the desired location. Different nanoformulations incorporating both MNPs and drugs have been created for the purpose of thermo-chemotherapy. A growing area in drug and gene delivery is the use of stimuli-responsive compounds, and especially thermo-sensitive polymers, to trigger the release of drugs.[152]

Stimuli-responsive polymers, also called smart polymers, have the ability to change properties in response to a change in their environment such as the temperature, pH, light, magnetic field, etc.[153] Thermo-responsive polymers respond to temperature: they undergo a conformational change at a specific temperature, called lower critical solution temperature (LCST) or upper critical solution temperature. The words upper or lower indicate whether it is an upper bound or lower bound to a temperature range of partial miscibility. For example, below the LCST, the polymer is in a swollen hydrophilic state, and transforms to a shrunken hydrophobic state above the LCST by expelling the aqueous content. The most studied polymer for thermo-responsive drug delivery systems is poly(N-isopropylacrylamide) (PNIPAAm) which has a LCST of 32 °C in water. By varying the ratio of hydrophilic/hydrophobic co-monomer, the LCST of a given polymer can be tuned.[154] This behaviour is therefore used to remotely trigger the release of drug: by tuning the LCST to be in hyperthermia temperature range, a drug may be retained at physiological temperature, and released as a consequence of hyperthermia. The use of MNPs for local hyperthermia is therefore particularly relevant to this purpose. Indeed, the heat produced by the MNPs under application of an AMF will trigger the fast release of the drug, and increase the effectiveness of the treatment due to the synergistic effect of simultaneous hyperthermia and chemotherapy. The incorporation of MNPs also offers the possibility to guide the magnetic nanosystems in the body to target the tumour thanks to an external magnet. pH-responsive polymers are also often exploited for drug delivery applications because of the pH changes found in the human body. The pH in tumour environment is

often more acidic than pH in the blood or healthy tissue. pH-sensitive drug delivery systems can target the tumour site and release their payload due to the pH difference.

The approach of simultaneous thermo-chemotherapy using magnetic nanosystems is relatively new. Kumar and Mohammad recently reviewed and proposed extending of the meaning of the term hyperthermia, to cover both hyperthermia therapy and magnetically modulated controlled drug delivery through heating.[155] In this case, heat is only used as a trigger for drug release. In our context, hyperthermia and chemotherapy therapeutic functions are combined in the same nanosystem taking advantage of the great potential of MFH and controlled drug delivery in the treatment of cancer, and benefiting from the synergetic effect of the combined therapy. The most relevant organic/inorganic designs developed so far will be presented, focusing on the most encouraging results of pH- and/or thermo-sensitive systems for the triggered delivery of drugs under application of an external AMF. Among them, we can find core/shell NPs, liposomes, micelles, and polymeric carriers such as hydrogels or polymeric NPs. Figure 1.8 displays the most important biologically useful nanosystems for simultaneous thermo-chemotherapy, which are usually administered intratumourally or intravenously.

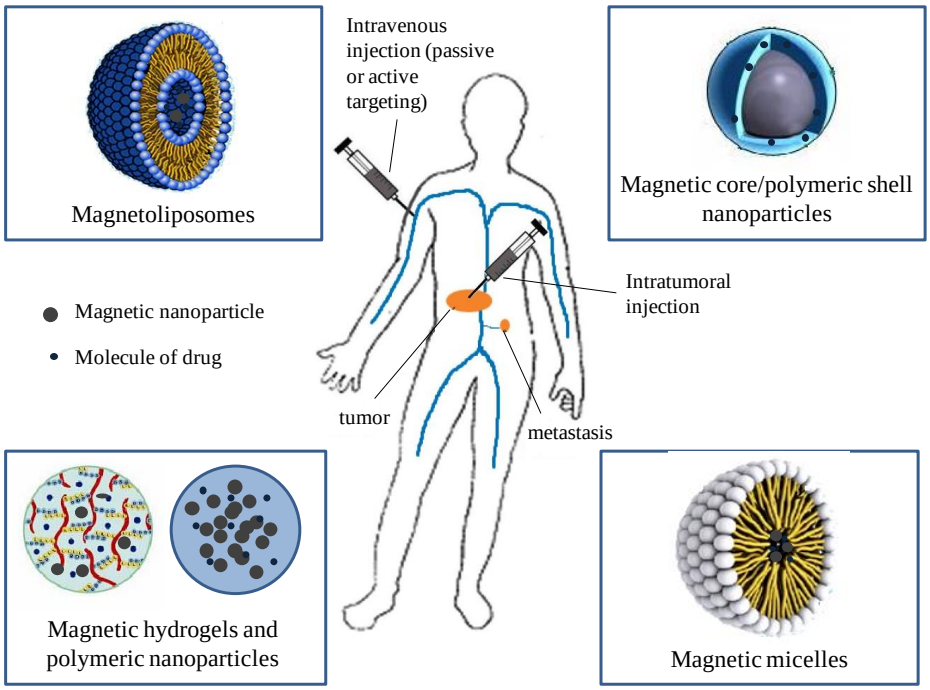

Figure 1. 8 *Type of nanosystems designed for thermo-chemotherapy commonly found in the literature.*

1.3.3 The different nanosystem designs

1.3.3.1 Liposomes

Liposomes are spherical vesicles composed of an aqueous core surrounded by a lipid bilayer. They are one of the most attractive and studied system for drug delivery. Hydrophilic chemotherapeutic drugs can be entrapped in the aqueous compartment, while hydrophobic drugs can be encapsulated in the lipid membrane. Liposomes change the pharmacokinetics of the drug and lower its systemic delivery and toxicity. With the major advancement of long circulation liposomes by incorporating PEG-chains in the lipid bilayer,[156] liposomal formulation are now able to increase the circulation time of some drugs in the body and enhance the drug deposition in the tumour via EPR effect.

Magnetoliposomes are formed by incorporating MNPs in the liposome with the molecules of drug, either in the core for hydrophilic NPs[157] or in the lipid membrane for NPs in a hydrophobic state.[158] Temperature-sensitive liposomes use specific lipid and polymers to achieve temperature-triggered release of drugs. Under the phase transition temperature of the bilayer, drugs are retained inside the liposome, until they are released in tumour tissue or vasculature as a consequence of heat causing bilayer disruption. As thermo-sensitive liposomes have been widely investigated for drug delivery, several well-documented reviews can be found in the literature.[159-161] Thermo-sensitive magnetoliposomes have shown potential efficacy for the combined treatment of cancer. For example, liposomes with MNPs encapsulated in the lipid bilayer and calcein as a model of hydrophilic drug loaded into the aqueous compartment have shown interesting “on-demand” release properties.[162] The release can be triggered repetitively, by switching on and off the AMF, with almost inexistent cargo release when the AMF is turned off. This property is due to the reversible permeability change of the lipid bilayer rather than the destruction of the liposome, and is an attractive feature to control dose, location and time of drug release, with simultaneous magnetic hyperthermia.

Kulshrestha *et al.* developed paclitaxel-loaded magnetoliposomes with a lipid bilayer formed of 1,2-dipalmitoyl-sn-glycero-3-phosphocholine (DPPC) and 1-palmitoyl-2-oleoyl-*sn*-glycero-3-phospho-*rac*-glycerol (PG) (9:1, w/w).[163] The transition temperature of DPPC is 41 °C, while the one of PG is 1 °C, but adding a small amount of PG proteins to the DPPC lipid bilayer has shown to increase the stability of the bilayer, without lowering too much the transition temperature, thereby minimizing the release of drug at physiological temperature. Magnetite NPs and paclitaxel were encapsulated into the liposome aqueous compartment. At 37 °C, only 1.2% of paclitaxel was released compared to 55.6% at 43 °C

under application of an AMF. *In vitro* experiments performed on HeLa cells showed a decrease of cell viability by 37% after magnetic hyperthermia treatment alone at 42.5 °C for 30 min and by about 50% for paclitaxel-loaded magnetoliposomes without application of an AMF, while the combined treatment resulted in 89% cell killing. Thus, this liposomal formulation shows promising potential for cancer thermo-chemotherapy, because of its good biocompatibility, the almost non-existent drug release at 37 °C, the magnetic hyperthermia-triggered burst drug release and the synergistic effect of the combined treatment.

1.3.3.2 Micelles

Surfactants are composed of a hydrophilic head group and a hydrophobic tail. When in aqueous solution, they spontaneously assemble into an aggregate with the polar heads facing the surrounding water and a hydrophobic, water-excluding core. Hydrophobic drugs can therefore be encapsulated into the micelle core. Drug molecules can also be directly conjugated to the polymer structure via a cleavable link.[164] Such as liposomes, micelles can extend the circulation time of the drugs in the body, enhance their accumulation via EPR effect in the tumour and protect them against renal and reticulo-endothelial clearance. Micelles can be engineered to be thermo-responsive via incorporation of a thermo-sensitive polymer either in the head polar group or the non-polar tail. Micelles have been widely used as drug delivery systems, and several recent good reviews can be found on the subject of polymeric micelles.[164-166] Micelles with a thermo-sensitive corona are usually used for drug delivery applications. The thermo-sensitive polymer undergoes a conformational change from hydrophilic state to hydrophobic state when it reaches its LCST, therefore destabilizing the micelle structure and allowing the release of the drug. The collapsed hydrophobic corona may interact with the cellular membrane resulting in an enhanced intracellular uptake.[167] The micelles can be loaded with MNPs and drug at the same time, to form magnetic micelles that can be used for hyperthermia with combined chemotherapy.

Kim et al. prepared iron oxide nanoparticle-conjugated polymeric micelles that encapsulate doxorubicin (DOX) and observed a significant decrease in cell proliferation under application of an AMF as compared to free DOX.[168] An enhanced apoptosis of human adenocarcinoma cells was obtained for the combined therapy than either hyperthermia or chemotherapy applied separately. Similar results were obtained for DOX and Mn, Zn doped ferrite NPs encapsulated in the hydrophobic core of magnetothermally responsive star-block copolymeric micelles with a LCST of 43 °C for application in thermo-chemotherapy.[169] The drug was found to be quickly released at 43 °C due to the

deformation of the micellar structure, and an enhanced tumour growth inhibition on human liver hepatocellular HepG2 cells was observed under application of an AMF.

1.3.3.3 Polymeric nanoformulations

Polymeric nanoparticles are of great interest for biomedical applications due to the possibility to control and tune their compositions, structures and properties (i.e. shape, size, surface charge, functionalisation) thanks to a controlled reaction of polymerisation.[170] Several MNPs and drug molecules can be encapsulated in the same polymeric NP, to be used as agents for thermo-chemotherapy. From the choice of the polymers composing the NPs as well as the different polymers ratio, can arise new or improved properties, such as thermo-sensitivity, biocompatibility, etc.

An interesting and very complete study developed a pH- and thermo-sensitive nanosystem composed of SPIONs and two anti-cancer drugs, curcumin and 5-fluorouracil (5FU), encapsulated in a poly(D,L-lactic-co-glycolic acid) (PLGA) shell for the combined therapy.[171] Curcumin causes a decrease in the mitochondrial membrane potential while 5FU inhibits the synthesis of DNA and RNA. The polymeric NPs were also functionalised with two targeting moieties, folate, whose receptors are highly displayed in several carcinomas, and transferrin, whose receptors are highly overexpressed in cancer cells to obtain a dual targeted, dual drug loaded MNPs-encapsulated PLGA nanovector. Three different cell lines were used for *in vitro* studies: a human breast cancer MCF-7 cell line, a human glial G1 cell line and a mouse fibroblast L929 cell line used to compare effects on healthy cells. The better targeting efficacy of the dual-targeted NPs was clearly evidenced by the internalization studies and cytotoxicity assays resulting in a higher specificity and uptake than single-targeted NPs. A synergistic effect of the two drugs was also observed as compared to the use of a single drug. The effect of simultaneous chemotherapy and magnetic hyperthermia was evaluated after 60 and 120 min of treatment. The use of non-targeted NPs resulted in a high reduction of the cell viability for both healthy and cancer cells, due to the lack of specificity of the nanovector, unlike the treatment performed with the dual-targeted NPs that showed a drastic cytotoxic effect on cancer cells without significant damage to healthy cells. Thanks to the dual targeting ability, both heat and drugs can be targeted to cancerous tissues. The synergistic effect of the MNPs and the combination of the drugs was found to be highly effective in destroying cancer cells within a very short period of time by initiating early and late apoptosis, with remaining cell viabilities of 7% and 4% for MCF-7 and G1 cells 24 h after the treatment.

Hydrogels consists of a three-dimensional polymer network containing large quantities of water, but remain insoluble due to their cross-linked structure. The properties of a hydrogel such as its elasticity, degradation rate or swelling ratio can be tuned by modifying the hydrogel parameters (i.e. polymer, block lengths, cross-linker ratio, etc). Nanohydrogels are commonly used as drug delivery systems through entrapment of drugs in the polymer matrix, and release via diffusion or matrix degradation. MNPs can also be incorporated in the hydrogel matrix. Thermo-sensitive nanohydrogels are formed by cross-linking thermo-sensitive polymers, and the final LCST of a nanohydrogel can be tuned by changing the different polymers ratio. Above the LCST, a nanohydrogel becomes hydrophobic and shrink, therefore expelling water and drug molecules.

A concentric layered magnetic chitosan hydrogel with controlled layer numbers and layer thicknesses was recently synthesised via a facile alternate alkali treatment method.[172] Magnetite NPs and the chemotherapeutic drug adriamycin were incorporated into the hydrogel matrix. The drug release behaviour was estimated by switching ON and OFF a low frequency AMF. An increased rate of drug release was observed when the AMF is ON. In this study, magnetic hyperthermia is not believed to be the trigger of the drug release, but rather a volume shrinkage of the hydrogel due to the magnetisation of the MNPs, which promote drug release by expelling the drug out of the hydrogel.

Jaiswal *et al.* developed a dual pH- and temperature-responsive nanohydrogels by incorporating magnetite NPs and DOX into a polymeric matrix based on poly(N-isopropylacrylamide)-chitosan, with a LCST optimised around 42 °C.[173] pH and temperature enhance release was observed under acid environment (pH 4.6) and hyperthermia temperature (42 °C). The combined treatment using the drug-loaded magnetic nanohydrogels on human breast MCF-7 cells and cervical carcinoma HeLa cells yielded up to 85% cell death, which was significantly higher than cell death achieved by hyperthermia alone. Jaiswal *et al.* also developed a DOX-loaded thermo-responsive hydrogel with embedded iron oxide nanoparticles.[174] *In vitro* studies on bladder cancer T-24 cells revealed a synergistic of the combined therapy due to enhanced apoptosis and that more than 80% cells were found dead in just 6 h post field exposure, and 95 % after 24 h. Interestingly, *in vivo* biodistribution showed a preferential accumulation of the hydrogel in the lungs, which pave the way for lung cancer treatment as well.

1.3.3.4 Core/shell nanoparticles

Core/shell NPs are particularly relevant for combined modalities of cancer therapy. The metallic core can endow the NPs with the desired magnetic properties for hyperthermia

applications, while the organic shell can provide drug loading capabilities. Moreover, the coating can also provide an increased colloidal stability, chemical stability (i.e. prevents any further oxidation), biocompatibility and reduced toxicity. The polymer can be grafted onto the MNP surface by two different approaches.[175] In the first one, called “grafting to” or “grafting onto”, an end-functionalised polymer is used with suitable terminal groups to directly bind to the MNP surface. In the second approach, called “grafting from”, the polymerisation proceeds from the surface thanks to an initiator molecule preliminary fixed on the MNP surface. Finally, simpler but less reliable, the polymer can be attached to the MNP surface by non-covalent interactions, such as electrostatic or van der Waals interactions. For drug delivery purposes, the drug can be physically loaded into the polymer shell or the drug can be covalently loaded through formation of a chemical bond between the drug and the polymer/ligand forming the shell of the MNPs. In the latter, the drug release mechanism often involves heat or pH inducing bond cleavage. In either case, it has been demonstrated *in vitro* that DOX has a higher cytotoxicity toward cancer cells when it is conjugated to iron oxide NPs covalently or electrostatically compared to free DOX, most likely due to a higher cellular uptake through endocytosis compared to passive diffusion.[176]

1.3.3.4.1 Physical drug loading

Physical drug loading is generally obtained by hydrophobic/electrostatic interactions and is generally quite simple to realise. For an efficient nanovectors, a high drug loading efficiency and a rapid “on demand” release is desirable while drug leakage through the polymer layer should be avoided. A recent study has shown promising results with a pH-responsive system in the drug release behaviour and cell killing effect with the combined therapy in the treatment of ovarian cancer.[177] Iron oxide NPs were coated with three different layers, forming a reservoir for drug loading capability: oleic acid, 1-octadecene, poly(maleic anhydride-alt-1-octadecene) (PMAO) and poly(ethylene-imine) (PEI). DOX was then encapsulated into the MNPs polymeric shell and the MNPs were further modified with a PEG layer for improved colloidal stability and increased blood circulation time. Finally, the MNPs were functionalised with a targeting ligand to human ovarian cancer cells: Luteinizing Hormone–Releasing Hormone (LHRH) peptide. This system will be called LHRH-PEG-DOX-IONP. Only 17.6% of DOX was released at pH 7.4, while 91.1% was released at pH 5.5, with a burst release within the first 2 h (44.7%). Indeed, DOX is loaded through electrostatic interactions with the negatively charged carboxyl groups of the amphiphilic polymer. The release of DOX is accelerated at acidic pH because it reduces the interaction with protonated carboxylic groups. It also increases the solubility of DOX in aqueous solution due to the protonation of the primary amine of DOX molecules.

This drug release behaviour enables a limited release of drug in the blood stream, while a quick release can be obtained at cancer sites. In order to assess the efficacy of the combined treatment *in vitro* on A2780/AD human ovarian carcinoma cell line, 15 µg Fe/mL of LHRH-PEG-DOX-IONPs were loaded with 1 µg/mL of DOX and subjected to an AMF for mild hyperthermia conditions (40 °C). The effect of chemotherapy and mild hyperthermia alone resulted in 27% and 72% cell death, respectively, while the combined treatment had a 95% cell killing effect. Thus, the combined treatment shows a superior efficacy than either chemotherapy or mild hyperthermia as stand-alone therapy and is preferable in many ways because of the lower temperature and drug concentration used, thereby minimizing side effects and damage to healthy tissues. Electrostatic interactions were also used to load DOX into $MgFe_2O_4$ magnetic nanoassemblies coated with PEG-diacid.[178] A loading efficiency of 80% was achieved and 75–80% of DOX was released under acidic pH compared to only 20-25% at physiological pH. The synergistic effect of DOX combined with hyperthermia was once more observed, with up to 90% cell death, against 45% and 65% cell death for magnetic hyperthermia or chemotherapy alone, respectively.

Barick *et al.* developed pH-responsive peptide mimic shell cross-linked magnetic nanocarriers (PMNCs) for combination therapy.[179] Magnetite NPs were functionalised with glycine and the free amine groups are utilised for further conjugation with the peptide L-arginine to obtain PMNCs with both amine and carboxylic terminal groups. The NPs were coated with a peptide, because peptides can enhance the cellular uptake, have low toxicity and are pH-responsive. The pH of zero-point charge of PMNCs was estimated at 5.4, meaning that the surface is charged positively at pH < 5.4 and negatively at pH > 5.4. The reversal of the surface charge can be exploited for the purpose of drug delivery: the drug, loaded in the shell, is retained via electrostatic interactions, and released upon the change of surface charge. DOX is used as a model of cationic chemotherapeutic agent, to study the drug loading and release behaviour at pH 4, 5 and 7.3. The DOX release studies show an increase in the release rate with a decreasing pH: only 7% of DOX was released at pH 7.3 while the release was complete at pH 4. The time needed for the release of 50% of DOX was found to be around 30 min and 45 min at pH 4 and 5, respectively. The potential of the DOX-loaded PMNCs was investigated on HeLa cells for the combined therapy, after only 10 min of AMF exposure and a DOX concentration of 4 µM. The chemotherapy treatment alone (free DOX or DOX-loaded PMNCS) resulted in a cell viability decreased by 10%, and hyperthermia alone (PMNCs subjected to AMF) had a 13% decreased effect on the cell viability. The cell killing effect was higher in the case of the combined therapy, as a 28% decrease in cell viability was observed. This system is interesting for the combined therapy giving the results obtained with a short time of AMF exposure.

Moreover, it exhibits a quasi-nonexistent drug leakage through the peptide mimic shell and the amine and carboxylic terminal groups of the nanocarriers leave many possibilities for the conjugation with targeting moieties.

While efficient, the use of pH-sensitive drug delivery systems only offers spatial control but does not allow for the remote control of the drug release. Thermo-sensitive drug delivery vehicles can be used for hyperthermia-triggered drug release, which offer spatial and temporal control over the drug release but also offer the possibility of an “ON-OFF” release by switching ON and OFF the AMF. For example, magnetite NPs coated with N-isopropylacrylamide-co-acrylamide (P(NIPAAm-co-Am)) with a LCST of about 40 °C show almost complete drug release after three AMF on–off cycles (frequency = 60 kHz; amplitude = 6.5 kA/m).[180]

1.3.3.4.2 Covalent drug loading

The advantage of conjugated drug to the MNP surface via a labile bond is that no leakage of drug through the polymer shell is possible. This design involves the cleavage of the bond used to conjugate the drug to the MNP in response to a stimulus. The drug can therefore be magnetically guided at the right location and activated at the right time, limiting systemic effects in a great extent. For the purpose of thermo-chemotherapy, heat labile bonds are particularly relevant, because the heat produced by the MNPs subjected to an AMF induces bond cleavage. For example, in the following study, the authors have designed a magnetic nanocarrier for thermo-chemotherapy composed of an iron oxide core functionalised with a ligand containing a furan ring that serves as a thermo-sensitive linker for a biologically active molecule through reversible Diels-Alder chemistry.[181] The retro-Diels-Alder (rDA) reaction generally occurs at temperatures around 90 – 110 °C. These temperatures are too high for biological purpose, but recent studies have shown the existence of local heating effect in the vicinity of MNPs leading to high temperatures at the NPs surface.[182-184] This phenomenon can be exploited to kill more effectively cancer cells without a significant increase of temperature in the biological medium, or in the case of this study, trigger the drug release by initiating a reaction occurring a high temperature. Indeed, the ligand has been designed to provide the cleavable bond close to the NPs surface, allowing the exploitation of the local heating phenomenon. The study shows that indeed, upon application of an AMF, the rDA reaction occurs, leading to the release of the conjugated molecule, and thereby this design offers possibility for thermo-chemotherapy applications.

Azo-bonds are commonly used as thermally-labile linkages.[184,185] Azo-functionalised PEG-coated core/shell iron oxide/silica nanoparticles exhibited on demand release of the covalently binded drug model upon activation of an AMF due to azo bond breakage with an elevation of temperature.[186] Riedinger *et al.* developed a drug release system in which DOX is covalently linked to PEGylated iron oxide nanoparticle through thermo-labile azo-ligands.[187] The distance between the molecules of DOX and the iron oxide nanoparticle surface was varied by using PEG spacers of different molecular weights. Results showed that upon application of an AMF, the release of the drug is distance-dependent, due to the local heating effects at the surface of the nanoparticles, which rapidly decay with increasing distance.

DNA melting as a result of temperature increase has also been exploited for drug delivery purposes. Examples include a nanoparticle capping system based on double stranded DNA that has been used as thermally sensitive gatekeepers: progressive DNA melting upon application of an AMF leads to subsequent release of the drug[188]; and a nucleic-acid duplex as a heat-labile linker that releases a drug from dextran-coated iron oxide nanoparticles trapped in a matrigel plug as *in vitro* model of tumour tissue.[189] With a nucleic acid strand covalently linked to the nanoparticle, dye-labelled single stranded DNA self-assembles on the particle's surface forming a tuneable, heat-labile linker.

Acid labile bonds are also widely used for drug delivery applications, as the pH in tumour environment is more acidic than in the blood or healthy tissue. A recent study used an acid labile imine bond to conjugate doxorubicin to magnetite NPs.[190] The mechanism by which the drug is released was assumed to be: the MNPs are taken up by the cancer cell through endocytosis, and the drug is released in acid lysosomes due to bond cleavage in acidic conditions. Other acid cleavable bonds have been used recently for drug delivery purpose and could be used for the combined therapy, such as hydrazone bonds to conjugate DOX to magnetite NPs[191,192] or nanocrystal clusters[193] or else ester bonds to conjugate paclitaxel to iron oxide NPs.[194] Finally, another possible cleavable bond that can be used for drug delivery is redox labile bond such as disulfide bonds.[195] Indeed, due to the elevated level of reductive glutathione in many tumours cells, the tumour intracellular environment enables redox bond cleavage thus releasing the drug. Acid and redox cleavable bond for use in drug delivery applications have another important advantage. It has been noticed that a high amount of glutathione is often associated to chemotherapeutic drugs-resistant cancer.[196] By releasing drugs intracellularly drug resistance can be, in a certain extent, overcome.[197]

If the drug used also have a targeting ability, no cleavage of the bond conjugating the drug molecules to the MNPs is necessary. This is the case with the drug methotrexate (MTX)

which has been used in a recent study for thermo-chemotherapy.[198] MTX was conjugated to poly(ethyleneimine)-coated magnetite NPs through an amide bond. MTX is used for its targeting ability on folate receptor, over-expressed in many types of cancers, and its therapeutic effect. The cellular uptake shows a more efficient and selective internalisation of MTX-MNPs in the cell cytoplasm as compared to non-conjugated MNPs. The relative cell viabilities for magnetic hyperthermia at 43 °C, chemotherapy alone and the combined treatment were estimated at 87.6%, 64.5% and 13.3%, respectively. A true synergistic effect between hyperthermia and MTX is observed demonstrating the efficiency of the MTX-MNP design for targeted thermo-chemotherapy applications.

1.3.4 Examples of *in vivo* applications of thermo-chemotherapy using magnetic nanoparticles

To our knowledge, there has been no clinical trial performed on drug-loaded MNPs-based nanosystems for simultaneous thermo-chemotherapy. However, the fate and effectiveness of different magnetic carriers have been tested *in vivo*. *In vivo* experiments are important because the overall effects can be observed on a living subject and it is therefore the best way to get close from the conditions found in a human body (solid tumour, complicated tumour microenvironment, etc) which can interfere in a great extent with the fate of the nano-systems (i.e. drug pharmacokinetic, NPs distribution pattern, etc).

Yoo *et al.* introduced resistance-free apoptosis-inducing magnetic nanoparticles (RAIN) based on $Zn_{0.4}Fe_{2.6}O_4$ MNPs for simultaneous hyperthermia therapy and release of geldanamycin (GM).[199] GM is a heat shock protein (HSP) inhibitors and is used to prevent thermoresistance. Thermoresistance is the development of resistance to the cytotoxic effects of heat after consecutive hyperthermia treatments that arises from the synthesis of HSPs as a response of thermal stress.[200] Indeed, the presence of HSPs has been correlated with the natural adaptation to heat of a living organism. GM is conjugated to the MNPs via a heat labile azo linker, and complete release occurs as a consequence of magnetic hyperthermia after 60 min of exposure at 43 °C while no release is observed at 37 °C. *In vitro* studies on MDA-MB-231 breast cancer cells revealed a 100% cell killing efficiency after 70 min of treatment with the RAIN, against only 25% after 80 min of treatment for magnetic hyperthermia alone. A strong expression of HSPs was observed after the heat treatment, while after exposure to RAIN hyperthermia, the expression of HSP was comparable to the control. Finally, MDA-MB-231 cells were transplanted into the

right hind legs of nude mice and 50 µg of RAIN were directly injected into the tumour. Hyperthermia at 43 °C was maintained for 30 min and while magnetic hyperthermia was not sufficient to inhibit the tumour growth, RAIN hyperthermia was found to completely suppress the tumour 8 days after single AMF exposure. *In vitro* and *in vivo* tests confirmed that HSPs are responsible for thermoresistance and that inhibition of HSPs is critical for hyperthermia induces apoptosis.

Li *et al.* developed truncated octahedral magnetite NPs coated with poly(styrene-alt-maleic acid) and further functionalised with PEG and poly-A polynucleotide.[201] PEG chains are used to bind a cancer cell targeting moiety: the anti-human epidermal growth factor receptor type 2 (anti-HER2) monoclonal antibody, while the polynucleotide has the ability to absorb the chemotherapeutic drug 5-fluorouracil (5-FU) by forming a hydrogen bond between the adenine group of the polynucleotide and 5-FU. The targeted nanosystem exhibited an enhanced cellular uptake *in vitro* on MBT-2 cells, a mouse bladder cancer cell line which over-expresses HER2 antigen, compared to the non-targeted one. MBT-2 cells were transplanted in C3H/HeN mice to induce bladder cancer in mice. NPs were injected intratumourally to assess the efficacy of the combined therapy on small size (< 50 mm^3) and large size (> 50 mm^3) tumours, and 2 h later tumours were exposed to an AMF for 15 min. In the case of small tumours, hyperthermia alone as well as the combined treatment led to almost total tumour regression. However, for large tumours, hyperthermia alone was not sufficient to significantly inhibit tumour growth, and only hyperthermia with combined chemotherapy resulted in a significant anti-cancer effect. The efficacy of the combined treatment was also evaluated using the systemic delivery method through tail-vein injection. NPs were injected once per day for four consecutive days and the hyperthermia treatment was applied 24 h after the NPs had been injected. The combined treatment resulted in a prominent cancer regression compared to either hyperthermia or 5-FU alone. Interestingly, after hyperthermia treatment, a relocation of the NPs from other organs to the tumour was observed, probably due to the change in tumour vasculature in response to hyperthermia, which facilitates NPs extravasation. This information is highly valuable in maximizing the therapeutic effect and minimizing the side effects of the treatment. It also suggests that a pre-hyperthermia treatment could be applied before injection of the NPs to increase their accumulation at the cancer site.

Many recent *in vivo* studies using thermosensitive magnetoliposomes for thermo-chemotherapy applications also demonstrated prominent tumour growth inhibition and superior survival rate over chemotherapy or magnetic hyperthermia alone.[202-204 205]

1.4 Fundamentals of RAFT polymerisation

1.4.1 Introduction to reversible deactivation radical polymerisation

Free radical polymerization is a chain polymerization in which the active centers are radicals. It is one of the most widely used polymerization techniques. However, irreversible chain transfer and chain termination reactions (bimolecular radical-radical termination reactions) are inherent to any conventional radical polymerization.

According to the International Union of Pure and Applied Chemistry (IUPAC), living polymerization is a chain polymerization from which irreversible chain transfer and chain termination are absent. The rate of chain initiation is much faster than the rate of chain propagation, so that the number of kinetic-chain carriers or active centers is essentially constant throughout the reaction.[206,207] As a result, the polymer chains grow at a constant rate and reach a similar length (narrow molar mass distribution).
Reversible addition-fragmentation chain transfer (RAFT) polymerization is one of the several techniques of reversible deactivation radical polymerizations (RDRP), others mainly being atom transfer radical polymerization (ATRP) and nitroxide-mediated polymerization (NMP). RDRP are modern methods of radical polymerization in which certain additives react reversibly with the radicals and the rate of chain initiation is much faster than the rate of chain propagation. RDRP therefore present much similarities with living polymerizations, but cannot actually be classified as such, because, even if minimized compared to conventional radical polymerization, they still display irreversible chain transfer and chain termination reactions. Many terms have been loosely used to call the RDRP, such as living radical polymerization, living free radical polymerization, controlled radical polymerization and controlled/living radical polymerization. The use of these names has been discouraged by IUPAC.[208] The term “living” cannot be used as some terminations inevitably take place. The use of “controlled” is acceptable but the type of control must be defined (i.e. control over a certain kinetic feature or structural aspect).[207] Therefore, the term RDRP is recommended.

RDRP reactions all have in common the limitation of irreversible termination reactions and chain transfer, intrinsic to conventional radical polymerization, combined with a simultaneous or quasi-simultaneous initiation of all the chains. RAFT polymerization, such as other RDRP, allows one to design functional polymers of controlled and complex architecture (linear block copolymers,[209,210] star block copolymers,[211-213] brush polymers,[214,215] etc), pre-chosen molecular weight and low polydispersity (narrow molar

mass distribution), properties which are challenging to obtain via conventional free radical polymerization processes.

In order to extend the lifetime of the propagating polymer chains, RDRP process is based on a reversible activation/deactivation equilibrium between a low concentration of active species (propagating polymer radicals) and a predominant amount of dormant species (unable to propagate or terminate).[209,216]

In NMP, this equilibrium is built on a reversible termination reaction between a growing polymer radical P_n• and a free nitroxide N• to form a macroalkoxyamine P-N (Figure 1.9).[217,218] The propagating polymer radical and the nitroxide can be regenerated by homolysis of the P-N species at high temperature (often > 70 °C). However, the equilibrium strongly favours the dormant species and therefore irreversible termination reactions are strongly lessened by preferential reaction of the polymer chain P_n• with the nitroxide radical N• (deactivation), but also with monomer M (propagation) rather than the radical-radical termination reactions.

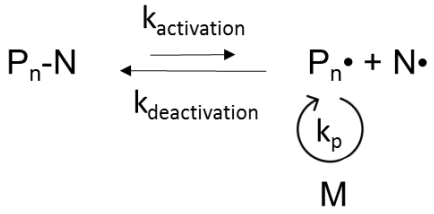

Figure 1. 9 *The reversible activation/deactivation equilibrium in NMP.*

In ATRP, the dormant species is a macromolecular alkyl halide P_n-X, and the growing polymer radicals P_n• are generated via a reversible redox process catalyzed by a transition metal complex in its lower oxidation state Mt^m/L, where Mt^m is the transition metal complex in oxidation state m and L is a ligand (Figure 1.10).[218-220] Likewise, the equilibrium strongly favours the dormant species. Various transition metals can be used for the ATRP redox catalytic process such as Cu, Ru, Fe, Co, Mn, Ni, etc.[221]

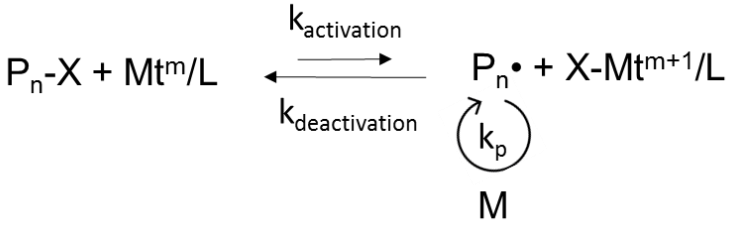

Figure 1. 10 *The reversible activation/deactivation equilibrium in ATRP.*

The RAFT polymerization mechanism differs from the one of ATRP and NMP. It rests upon a reversible degenerative chain-transfer process where the dormant species P_n-X and P_m-X equilibrate with the growing polymer radicals P_n• and P_m• (Figure 1.11).[209,218,222]

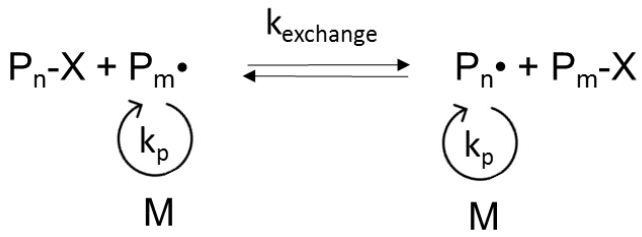

Figure 1. 11 *The reversible degenerative chain transfer equilibrium in RAFT polymerization.*

1.4.2 Generalities about RAFT polymerisation

The RAFT polymerization technique was discovered and first reported in 1998 by the Commonwealth Scientific and Industrial Research Organisation (CSIRO) of Australia.[223,224] CSIRO then published four other papers about RAFT polymerization in the two next consecutive years.[225-228] Around the same period (in 1999), a French group reported a polymerization technique as Macromolecular Design by Interchange of Xanthate (MADIX).[229,230] MADIX, such as RAFT polymerization, also works through an addition-fragmentation chain transfer mechanism and refers in fact to a specific RAFT polymerization: the one promoted by xanthates, also referred as dithiocarbonates.

RAFT polymerization is in fact nearly identical to a conventional radical polymerization, with the primary difference being the addition of a chain transfer agent. Therefore, it is not more difficult to conduct a RAFT polymerization than a radical polymerization. The same apparatus, temperatures, initiators and solvents are applicable.[231] As a consequence, RAFT polymerization retains many of the strengths derived from the inherent versatility of radical polymerization,[232] such as its compatibility with a wide range of polymerizable functional monomers, reaction media and temperatures, a relative ease of use and a high tolerance to diverse functional end groups.[231] Temperatures reported for RAFT polymerization ranged from ambient to 180 °C.[233] The really fast exchange reactions in RAFT polymerizations lead to well-controlled systems. RAFT polymerization expands the possibility to obtain polymers with targeted and controlled molecular weight and chain architectures i.e. block, brushes, stars and gradient copolymers.[234,235] Among all the RDRP methods, RAFT is most likely the most versatile and useful polymerization technique thanks to its high tolerance to a wide variety of reaction conditions, which have resulted in its increasing utilization and therefore publications about RAFT polymerization.[236] For

example, Renzo Paulus *et al.* reported the initiator-free RAFT polymerization of methyl methacrylate at high temperature in a microwave reactor.[237] Additionally, it is possible to conduct RAFT polymerization in a wide variety of solvents, including water, and biologically friendly conditions.[238,239] RAFT polymerization has also shown itself to be a particularly useful technique for the synthesis of water soluble co-polymer both in organic media or directly in aqueous media.[240] Thanks to its versatility, RAFT polymerization can be adapted to produce polymers in a sustainable manner. For instance, RAFT polymerization does not require the use of metal catalysts, and can be performed at room temperature, which is also useful for many biological applications.[222,241]

1.4.3 Mechanism and kinetics of RAFT polymerisation

The mechanism of RAFT polymerization is based on a reversible addition-fragmentation chain transfer process promoted by a thiocarbonylthio compound (ZC(=S)S-; see for example compound **1**) usually called RAFT agent or chain transfer agent (CTA).

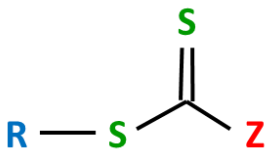

1

The **R** group initiates the growth of the polymeric chains, while the **Z** group activates the thiocarbonyl bond to give appropriate reactivity towards radical addition.

As degenerative chain transfer does not create radicals, an external source of radicals, usually an azo initiator, must be added at the beginning of the reaction, such as 2,2-azobis(2-methylpropionitrile) (AIBN) or 4,4-azobis(4-cyanovaleric acid)(ACVA).

The mechanism of RAFT polymerization can be described in 5 steps: initiation, pre-equilibrium, re-initiation, main equilibrium and termination.[224] The mechanism is presented in Figure 1.12.

- **Initiation**: The initiation is the first step of the polymerization. An initiator derived radical (I•) is created, which then react with a molecule of monomer (M) to form a propagating polymeric radical of length 1. This polymeric radical propagates with monomer (M) to give a propagating polymeric radical of length n (P_n•).

- **Pre-equilibrium**: The polymeric radical P_n• produced in the initiation step reacts with the RAFT agent **1** to give the intermediate adduct radical **2**. As RAFT agents have high

chain transfer constants, in most cases, only a couple of monomers will add to the initiator derived radical in the initiation step before adding to a RAFT agent.[240] The intermediate adduct radical **2** then fragments to yield the polymeric thiocarbonylthio compound **3** (macro-RAFT agent) and a new reinitiating radical R•, but may also fragment back to the original polymeric radical P_n• and the RAFT agent. The latter reaction is not desired and fragmentation of **2** to give **3** and R• can be favoured by choosing an appropriate CTA for the monomer being polymerized (i.e. R must be a better leaving group than P_n).

- **Re-initiation**: The radical R• derived from the leaving group R re-initiates polymerization by adding to the monomer M, initiating a new propagating polymeric radical P_m•. R• must be able to re-initiate polymerization efficiently to avoid any rate retardation. To achieve narrow molecular weight distribution, the pre-equilibrium and re-initiation steps must be completed relatively early in the reactions (RAFT agent and R• fully consumed) so that all the polymeric chains enter the main equilibrium at the same time.[209,236]

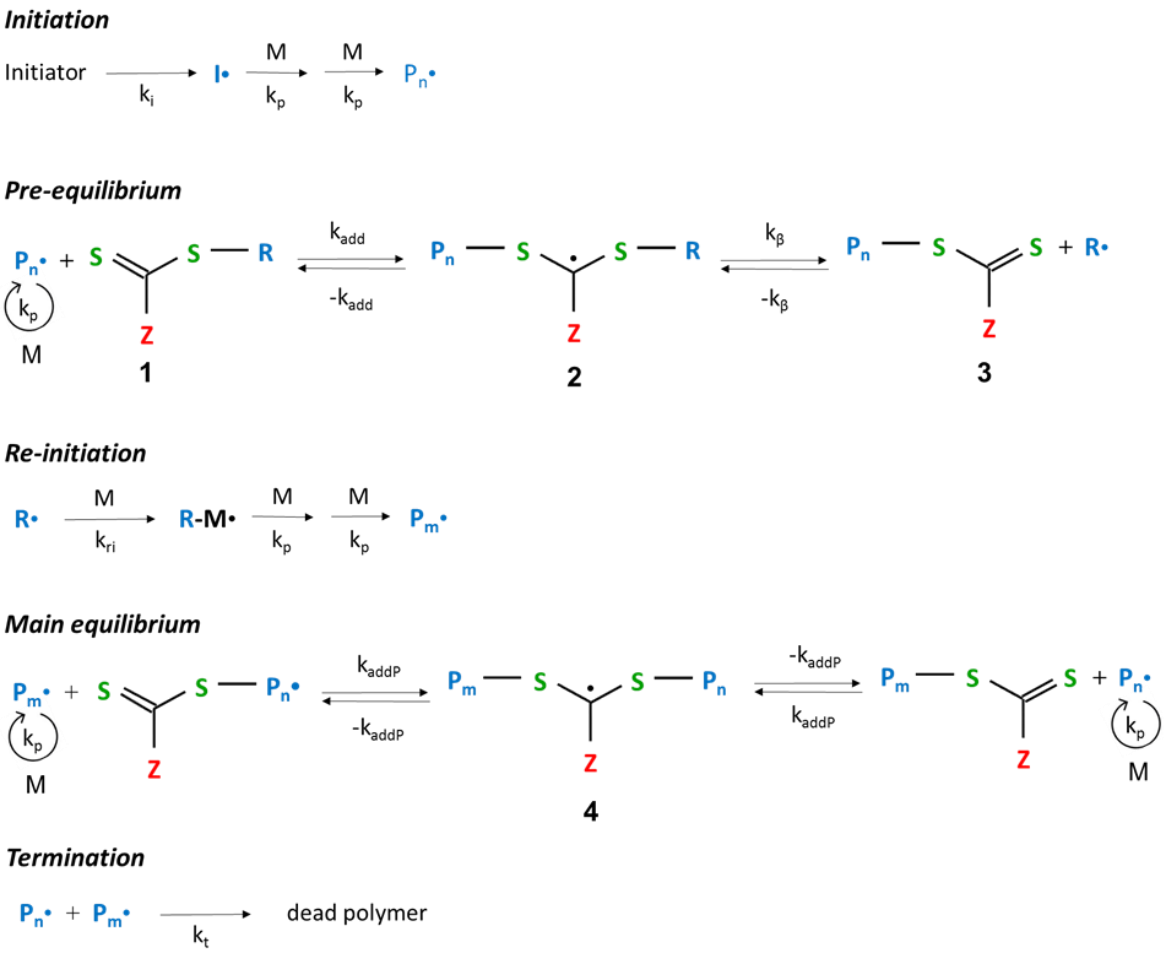

Figure 1. 12 *Mechanism of RAFT polymerisation.*[224]

- **Main equilibrium**: The main RAFT equilibrium is the most important stage of a RAFT polymerization. This step involves the propagation of polymer chains by adding monomer molecules, and the formation and fragmentation of the intermediate radical **4** via a process of rapid degenerative transfer of the thiocarbonylthio end group between the active polymeric chains P_n• and P_m•. In an ideal RAFT polymerization, due to the rapid equilibrium between the propagating polymeric radicals and the dormant thiocarbonylthio compound **4**, only a few monomer molecules are added to a chain in each addition-fragmentation cycle and probabilities for polymer chain growth are shared equally among all the existing chains that have not yet undergone termination, resulting in low polydispersity index (narrow molecular weight distribution).[242]

- **Termination**: While termination reactions are limited as compared to conventional radical polymerizations due to the rapid process of addition-fragmentation of the main RAFT equilibrium, terminations reaction still occurs, either by bimolecular combination or disproportionation. Dead polymer chains are unable to undergo further polymerization or chain extension and will therefore remain as impurities in the formed polymer (unless they can be removed via a purification process).

1.4.4 Choice of the RAFT agent

Although RAFT polymerization can be used to polymerize a wide range of polymer, choosing the CTA carefully and appropriately depending on the synthetic conditions and especially depending on the monomer, is crucial to achieve optimal control over a RAFT polymerization.[243,244] As mentioned in section 4.3.1.4, RAFT agents are thiocarbonylthio compounds of formula **1** containing two distinct groups: R a leaving group, and Z an activating group.

To achieve a well-controlled polymerization, the following requirements must be met:

- The C=S bond must be reactive towards radical addition.
- The fragmentation of the intermediate adduct radicals must be fast.
- The fragmentation must be favored towards the formation of the new reinitiating radical R• ($k_\beta > -k_{add}$).
- The radical R• must be able to reinitiates the polymerization efficiently.

There are a wide variety of RAFT agents depending on the chemical nature of R and Z.

In particular, four principal families of RAFT agents having different reactivity can be distinguished depending on the Z group. Indeed, the Z group governs the general reactivity of the thiocarbonylthio bond, and must be chosen to promote its reactivity towards radical

addition in order to increase the chance of propagating chains to add to the RAFT agent. In terms of molecular orbital energy, the Z group affects the energy level of the lowest unoccupied molecular orbital of the RAFT agent, therefore determining if radical addition is promoted.[228,232] For example, if Z allows for the delocalization of π electrons of the C=S bond, such as a phenyl group, radical addition is favored. Electron-withdrawing groups also favored radical addition while electron-donating group have the opposite effect.[244] Starting from the most active CTA, we find the dithioesters (see for example compound **5** – carbon adjacent to the thiocarbonylthio moiety), the trithiocarbonates (see for example compound **6** – sulfur adjacent to the thiocarbonylthio moiety), the xanthates (see for example compound **7** – oxygen adjacent to the thiocarbonylthio moiety) and the dithiocarbamates (see for example compound **8** – nitrogen adjacent to the thiocarbonylthio moiety).

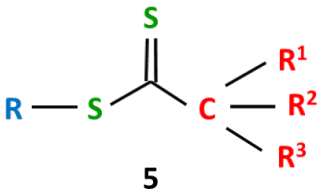

5

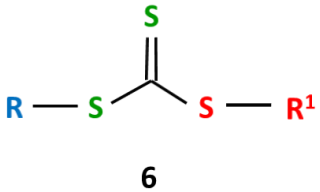

6

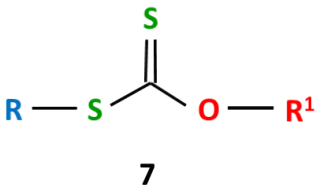

7

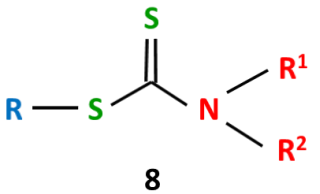

8

The Z group also plays an important role in the stabilization of the intermediate radicals. However, this stabilization must be minimized as over-stabilization can result in slow fragmentation of the intermediate radicals causing retardation of the polymerization reaction and higher probability of irreversible termination reactions.

The role of the R group is very important in the pre-equilibrium and re-initiation steps. Indeed, R must be a good homolytic leaving group, to effectively fragment from the intermediate radical and form the radical R•, which in turn, must be able to re-initiate polymerization rapidly. For that purpose, R must be a better leaving group than P_n ($k_\beta > -k_{add}$), or in other words, the stability of the radical R• must be better than the stability of P_n•, but the reactivity of R• must still be good enough to re-initiate the polymerization effectively. Steric factors, radical stability and polar factors greatly influence the leaving group ability of the R group, as more sterically hindered, more stable and more electrophilic radicals are better leaving groups.[228,243] The leaving group ability of P_n is mainly dependent on the structure of the monomer being polymerized, with $-k_{add}$ decreasing in the following order:

methacrylate ~ methacrylamide >> styrenic ~ acrylate ~ acrylamide > vinyl amide > vinyl ester.[209]

The chain transfer coefficient C_{tr}, given by the relative ratio of the rate constant for chain transfer (k_{tr}) to that for propagation (k_p), defines the reactivity of a RAFT agent for a given monomer. As RAFT polymerization involves addition-fragmentation mechanisms, the rate constant for chain transfer k_{tr} is dependent on both the rate constant for addition of the radical to the CTA (k_{add}) and the rate constant for fragmentation of the intermediate radical (k_β) as shown in equation 1.8 and 1.9:[245]

$$k_{tr} = k_{add}\phi \tag{1.8}$$

$$\phi = \frac{k_\beta}{k_{-add} + k_\beta} \tag{1.9}$$

ϕ is a partition coefficient which expresses the preference of the intermediate adduct radical to return to the starting materials or fragment to products. Ideally, R should be a better leaving group than P_n, i.e. ϕ should be > 0.5.

Chain transfer coefficients C_{tr} of several CTA have been found to vary significantly depending on the monomer being polymerized and its Z and R groups (from < 0.01 to > 1000).[228] Theoretically, to yield polymers with narrow molecular mass distribution (PDI < 1.2) and obtained a linear increase of the average molar mass with the conversion, a C_{tr} of at least 10 is required.[245]

Depending on their reactivity, radically polymerizable monomers can generally be classified into two broad groups: “more activated monomers” (MAMs) and “less activated monomer” (LAMs). MAMs usually have their vinyl group conjugated to a carbonyl group, such as methyl methacrylates, methyl acrylates and acrylamides, or conjugated to an aromatic ring, i.e. styrenes. LAMs typically have their double bond adjacent to an oxygen or nitrogen lone pair, e.g. vinyl acetate or N-vinylpyrrolidone, or to a saturated carbon, such as diallyldimethylammonium chloride.[232,245] MAMs are less active in radical addition than LAMs (lower k_p and lower k_{add}). The selection of the RAFT agent is dictated by the type of monomer being polymerized. Active CTAs such as dithiobenzoates usually lead to well-controlled polymerization of MAMs. However, active CTAs tend to inhibit polymerization of LAMs as propagation of the chains is extremely hindered by the high rate of addition of the propagating radicals to the CTA, and very slow fragmentation of the intermediate

radical due to the poor leaving group ability of poly(LAM). As a consequence, less active CTAs are used in the polymerization of LAMs, such as xanthates and dithiocarbamates.

General guidelines for the selection of the R and Z groups depending on the monomer used, adapted from previous publications, are shown in Figure 1.13.

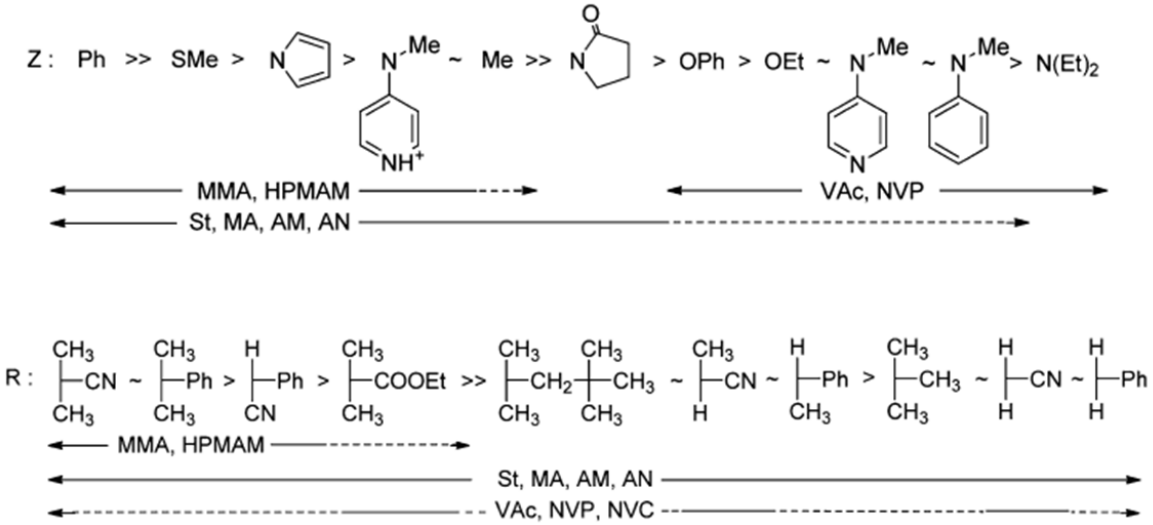

Figure 1. 13 *Guidelines for the selection of the RAFT agent Z and R groups in function of the monomer being polymerized. Dashed lines indicate partial control over polymerization. Figure adapted from earlier reviews.[235,246,247] Abbreviations: MMA: methyl methacrylate, HPMAM: N-(2-hydroxypropyl) methacrylamide, St: styrene, MA: methyl acrylate, AM: acrylamide, AN: acrylonitrile, Vac: vinyl acetate, NVP: N-vinylpyrrolidone and NVC: N-vinylcarbazole.*

1.4.5 Control of the molecular weight

The quality of control of RAFT polymerization depends on certain parameters (among these parameters is the chain transfer constant C_{tr} of the RAFT agent, already mentioned in section 4.3.1.4). The ratio of initial concentration of monomer to RAFT agent ($[monomer]_0/[RAFT]_0$) determines the average degree of polymerization DP_n at full conversion, defined as the average number of monomer unit per polymer chain. The ratio of initial concentration of initiator to RAFT agent ($[I]_0/[RAFT]_0$) affects the chain end functionalities. At one chain end, the proportion of chains being initiated with the initiator-derived radical rather than the R group of the CTA, and on the other chain end, the proportion of functional thiocarbonylthio dormant chains to dead chains. This ratio must therefore be minimized in order to have a larger amount of dormant chains rather than dead chains during the polymerization. A high ratio of RAFT agent to initiator concentration can suppress the unwanted side termination reactions. However, the initiator concentration must still be high enough to obtain an acceptable polymerization kinetics. If

initiator-derived chains are significant, the theoretical number average molecular weight (M_n^{th} in g/mol) of a RAFT synthesized polymer can be calculated as follow:[248]

$$M_n^{th} = \frac{[monomer]_0}{[RAFT]_0 + df([I]_0 - [I]_t)} * x * M^{monomer} + M^{RAFT} \quad (1.10)$$

Where $[monomer]_0$ is the initial concentration in monomer (mol/L), $[RAFT]_0$ is the initial concentration in RAFT agent (mol/L), $[I]_0$ - $[I]_t$ is the concentration of initiator consumed (mol/L), d is the number of chains formed from radical-radical termination (d ≈ 1.67 in MMA polymerization), f is the initiator efficiency, x is the monomer conversion (%), $M^{monomer}$ is the molecular weight of the monomer (g/mol) and M^{RAFT} is the molecular weight of the RAFT agent (g/mol).

Assuming that the initiator decomposition kinetic constant k_d is known, then the initiator consumption can be defined as:

$$[I]_0 - [I]_t = [I]_0(1 - exp^{(1-k_d t)}) \quad (1.11)$$

For a well-controlled RAFT polymerization, the fraction of initiator-derived chains is low, and as such, can be neglected. The theoretical average number molecular weight can then be expressed with the more commonly used following equation:

$$M_n^{th} = \frac{[monomer]_0}{[RAFT]_0} * x * M^{monomer} + M^{RAFT} \quad (1.12)$$

The molecular weight of the RAFT agent can be neglected too as it is low as compared to the other term of the equation.[248]

The average number molecular weight increases linearly with the conversion, and the obtained polymer has a low polydispersity index and carries a thiocarbonylthio moiety at its end chain, making possible a further chain extension (i.e. for the synthesis of block copolymer).

1.5 Conclusion

In this chapter, the role of magnetic nanoparticles and more particularly iron oxide nanoparticles for magnetic hyperthermia and thermo-chemotherapy application in the treatment of cancer has been reviewed.

Water colloidal dispersion of MNPs have yet shown great potential for use as heat-mediator agents, and efforts in the field have led to promising preclinical and clinical studies. However, MFH is still far from achieving its full clinical potential. Most of the research on magnetic nanoparticles-mediated hyperthermia therapy have been directed toward MNPs exhibiting good biocompatibility and improved SAR value. However, as the SAR increases with increasing frequency and amplitude of the applied field, one needs to pay careful attention as a too strong AMF may generate eddy currents and cause non-specific heating that can damage both healthy and cancer tissues.

Magnetic hyperthermia combined with drug delivery does not require working temperatures as high as those used for hyperthermia therapy alone. Indeed, as discussed in this chapter, the thermal enhancement of drug cytotoxicity is maximized at mild hyperthermia temperatures. Moreover, it has been proven many times through *in vitro* as well as *in vivo* studies that the combination therapy is far more effective than either hyperthermia or chemotherapy alone. As the combination of hyperthermia and chemotherapy in a same MNP-based nanotherapeutic system is relatively new, there are still some obstacles to tackle before clinical trials can be carried out. A high drug loading should be achieved and drug diffusion from the nanocarriers should be suppressed to limit systemic delivery. The pharmacokinetics and pharmacodynamics of the nanosystem need to be studied for a better comprehension and a possible increase in the treatment efficacy. However, thermo-chemotherapy by means of a magnetic nanosystem gathers all the numerous advantages of MFH over traditional hyperthermia and controlled drug release over traditional chemotherapy. Better anti-cancer effects at lower drug therapeutic dose and lower temperatures are achieved with the combined therapy. The possibility to trigger the drug release in cancer site owing to the use of pH- or thermo-sensitive nanocarriers is a particularly attractive feature to control the spatiotemporal release of the drug.

This chapter has established the basics and fundamentals needed to understand the motivation behind and the aim of the work presented in this thesis.

1.6 Thesis outline

This thesis reports the development of a doxorubicin-loaded dual pH- and thermo-responsive magnetic nanocarrier for application in thermo-chemotherapy of cancer and is divided among seven chapters. The first chapter deals with the introduction and wide literature review of multifunctional therapeutic nanosystems incorporating both magnetic nanoparticles and drugs, and their superior efficacy in treating cancer compared to either hyperthermia or chemotherapy as standalone therapies. The principle of magnetic fluid hyperthermia is also presented, along with a study of the different parameters influencing the heating performances of the nanoparticles. This first chapter also elaborates the necessary background of the field, including the mechanisms responsible for the synergistic effect of the combined thermo-chemotherapy. The following chapter (chapter 2) explains the principles and fundamentals of the different characterisation techniques used in this work. Chapter 3 describes initial experimentations primarily focused on the synthesis of core@shell iron@bismuth nanoparticles of high magnetic moment. These nanoparticles would have been used as the magnetic core of the nanocarrier, however, despite numerous trials, such nanoparticles could not be obtained. Iron oxide nanoparticles were chosen as a substitute and the synthesis of the nanoparticles and polymer, the functionalisation, drug loading and release studies are presented in chapter 4. The potential of the developed magnetic delivery system for thermo-chemotherapy applications was investigated in chapter 5 using two different cancer cell lines, and compared to either magnetic hyperthermia or chemotherapy as standalone treatment. The delivery system was found to be a really promising tool in the treatment of cancer, and further *in vitro* studies using the bioluminescence imaging method were performed in chapter 6. Chapter 7 concludes the entire work of this thesis.

Part of the work described in this thesis has been published or presented at different national and international conferences. These are listed in Appendix I.

CHAPTER 2

CHARACTERISATION TECHNIQUES

2.1 Introduction

Before any material can be used for biomedical applications, it is required to fully characterise it to analyse and understand its behaviour and properties. The following chapter focuses on explaining the basics and principles of all the techniques used in this work to characterise the different materials and nanosystems.

2.2 X-ray powder diffraction

2.2.1 Principle

X-ray diffraction (XRD) is a physico-chemical analysis technique used to determine the crystalline structure of a material in the form of a powder. A crystal structure is a highly ordered structure and is defined by the periodic three-dimensional repetition of an atomic pattern with interatomic distances in the Angstrom order.

X-rays are electromagnetic radiations constituted of photons with frequency within 10^{16} - 10^{19} Hz (equivalent to a wavelength in the Angstrom order). X-ray photons are generally generated during electronic transitions involving the ionisation of an electron in the inner shells of an atom. Three main ways can be distinguished in the generation of X-rays:

- Bombarding a metallic anode (often constituted of copper or molybdenum) with a beam of electron extracted from a metallic filament (generally tungsten) electrically heated, and accelerated with an electric voltage.
- The disintegration of certain radioactive sources generates X-rays.
- Exposing a material to an X-ray beam to generate a secondary fluorescent X-ray beam.

In XRD, the X-ray beam is generated by the first method, where electrons of sufficient energy collide with a metallic material. When the electrons hit the anode, X-rays can be created by two different mechanisms: (1) the braking of the electrons provoked when deflected by the electric field of the atom nucleus gives rise to a continuum spectrum of radiation, known as Bremsstrahlung, and (2) the electrons have enough energy to eject core electrons from the inner shell (K-shell) of a metal atom composing the anode. The unstable energy states are compensated by the dropping of electrons from higher energy levels to fill up the vacancy and the difference in energy may be emitted as an X-ray photon, leading to an emission spectrum of fluorescent X-rays. The second mechanism is

wanted in XRD and the wavelength of the X-ray beam will therefore depend upon the metal composing the anode and upon the electronic shell the outer electron drops from.[249]

The XRD technique requires the bombardment of a powder sample with a beam constituted of monochromatic and parallel X-rays. A monochromatic X-ray beam is needed to obtain an experimental pattern from a unique wavelength. Filtering, by foils or crystal monochromators, is used to produce monochromatic X-rays needed for diffraction. Interatomic distances and X-ray wavelengths are in the same order of magnitude. Therefore, a crystal can scatter X-rays, but the interaction between the X-rays and the matter depends upon the crystalline structure of the sample. The scattering of X-rays from atoms produces a diffraction pattern, which contains information about the atomic arrangement within the crystal. The scattered waves cancel one another in most directions, and constructive interferences are obtained only in a few specific directions determined by Bragg's law:

$$n\lambda = 2d_{hkl} \sin\theta \tag{2.6}$$

Where n is a positive integer number, λ is the X-rays wavelength, d_{hkl} is the distance between diffracting planes and θ is the incident angle. For X-rays hitting parallel planes of atoms, the path length difference between these X-rays must be a multiple of their wavelength, and as can be seen from Figure 2.1, it's a multiple of $2d_{hkl} \sin\theta$.

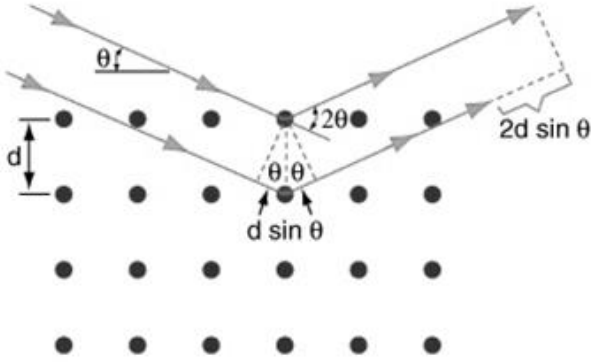

Figure 2. 1 *Diffraction of X-rays from an ordered arrange of atoms.*

In order to satisfy Bragg's law, a material of specific crystalline structure will always give rise, for a given X-ray wavelength and incident angle, to diffraction peaks in the same direction. The characteristic set of d-spacings generated in a typical X-ray scan can be considered to provide a unique fingerprint of the mineral or minerals present in the sample. A diffraction pattern is therefore characteristic of a given crystalline structure and reference powder data files (PdF) allow for the identification of the crystalline phase.

2.2.1 Instrumentation

The most commonly found geometric arrangement for X-ray powder diffractomers is known as the Bragg-Brentano parafocusing system.[250] It is built around a goniometer of fixed radius requiring that the source-to-sample distance be constant and equal to the sample-to-detector distance as can be seen in Figure 2.2. This geometry offers the advantages of high-resolution and high beam-intensity analysis at the cost of very precise alignment requirements.

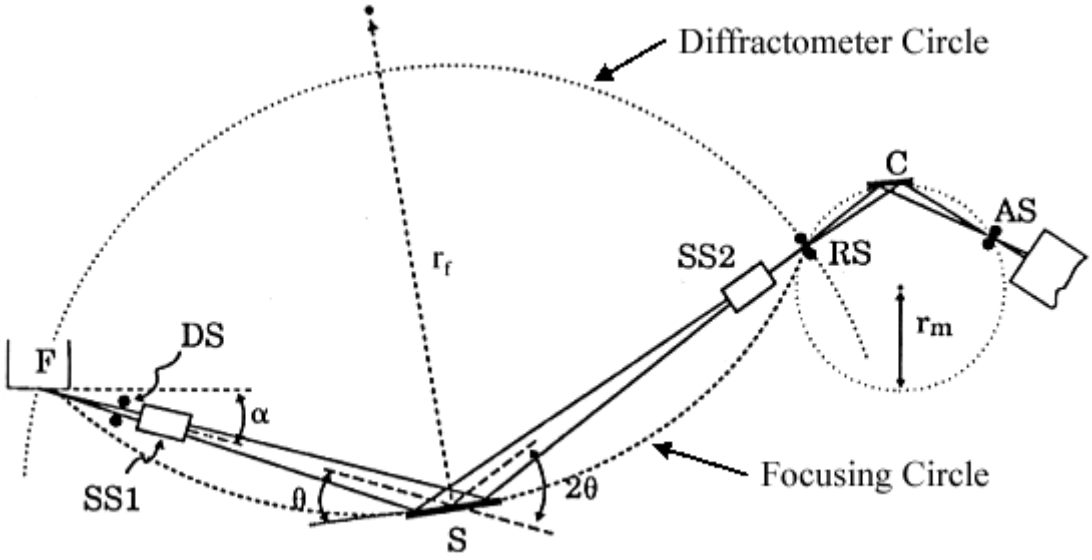

Figure 2. 2 *Schematic representation of a powder diffractometer with Bragg-Brentano parafocusing geometry, where F is the X-ray source, DS is the incident-beam divergence-limiting slit, SS is the Soller slit assembly, S is the sample, RS is the diffracted-beam receiving slit, C is the monochromator crystal AS is the anti-scatter slit.*[251]

Typically, the X-ray beam issued from the source F passes through the divergence slit DS and the Soller slit SS1 to illuminate the sample. The incident- and diffracted-beam slits move on a circle that is centred on the sample. Divergent X-rays hitting the sample at different points on its surface are diffracted. The diffracted X-rays are refocused at the receiving slit RS on the focusing circle before reaching the detector. The diffracted X-ray photons are translated into voltage pulses. Because the scanning speed of the goniometer is known, each angle 2θ can be related to its intensity and a plot of the angle 2θ versus intensity can be obtained, called a diffraction pattern or diffractogram. This geometric arrangement provides the best combination of intensity, peak shape, and angular resolution for the widest number of samples. The divergence slits are used to limit the divergence of the incident X-ray beam. Narrow divergence slits produce sharper peaks but is achieved at the expense of intensity loss as the intensity of the X-ray beam and the length of the X-ray beam hitting the sample and is reduced.

2.2.2 Sample preparation and analysis

For the work in UK, XRD diffraction patterns were obtained using an X-ray diffractometer PanAlytical with a cobalt metallic anode (λ = 1.789010 Å) in 20°-100° 2θ range for IONPs and in 20°-120° 2θ range for core@shell Fe@Bi NPs. Samples were prepared by flattening the dry powder on a zero background silicon wafer. Patterns fitting and corrections were carried out with PANalytical X'Pert HighScore Plus software.
For the work in Japan, XRD diffraction patterns were obtained using a Rigaku Miniflex600 with a copper metallic anode (λ = 1.540593 Å).

The study and interpretation of an obtained diffractogram mainly focuses on the position, the intensity and the full width at half maximum of the peaks. The diffraction pattern for a crystalline sample is characteristic of its crystalline structure, and comparison with PdF files allows for identification of the material(s) that compose the sample.

2.3 Superconducting quantum interference device – vibrating sample magnetometer

2.3.1 Principle

A superconducting quantum interference device (SQUID) is a magnetometer which allows for the measurement of weak magnetic fields. A SQUID is generally composed of two parallel Josephson junctions in a superconducting solenoid (Figure 2.3). The apparition of a current between two superconducting materials separated by a thin layer of an insulating material is called the Josephson effect. The superconducting current is carried by pairs of bound electrons, known as Cooper pairs, which travel across the junction by quantum tunnelling effect. If a superconducting ring is placed in a magnetic field, the magnetic flux penetrating the ring is quantised in units,[252] and this magnetic flux quantum is equal to 2.07 Tm^2.[253] The great sensitivity of SQUID devices is associated with measuring changes in magnetic field associated with one flux quantum. The ratio between the magnetic flux and the flux quantum determines the outcome of interference effects in SQUID devices. This interference allows highly sensitive measurements of magnetic flux and thus of magnetic field and magnetic moment linked to the flux quantum. If a constant predetermined current is maintained in the superconducting solenoid, the measured voltage oscillates with the changes in phase at the two junctions, which depends upon the change in the magnetic

flux. The flux change that has occurred is evaluated by monitoring the oscillations of the voltage.

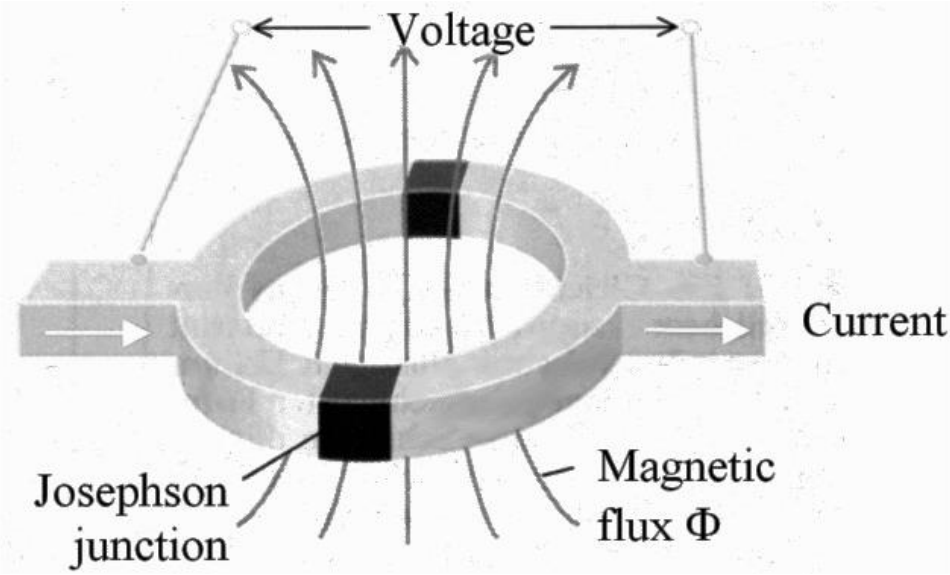

Figure 2. 3 *Superconducting solenoid with two Josephson junctions in a SQUID flux sensor.*

A SQUID device is ultra-sensitive for the detection of really small variations of the magnetic flux and it is therefore possible to measure really weak magnetic fields, but the measurement is really slow. The most common commercial use of SQUID devices is in in magnetic property measurement systems (MPMS).

A vibrating sample magnetometer (VSM) allows for the quick measurement of a sample magnetic behaviour but is not as sensible as a SQUID. Generally, the sample is positioned in the vicinity of pickup coils and subjected to a magnetic field. The voltage induced in the pickup loop is measured as the sample is vibrating sinusoidally. The vibration amplitude of the sample is dependent on its magnetic moment and thus, the measured change in voltage can be transformed into magnetic moment using a palladium calibration standard material with a known magnetic moment.

A hybrid SQUID-VSM combines the high sensitivity of a SQUID and the high speed of measurement of a conventional VSM and therefore allows for rapid measurement of weak magnetic fields.

2.3.2 Measurements

Magnetic measurements were performed with a MPMS Quantum Design hybrid SQUID-VSM. Its superconducting solenoid is made of niobium-titanium alloy.

Before starting any measurement, samples were demagnetised in order to start the measurement with a randomly oriented sample and suppress any memory effect.

2.3.2.1 Magnetisation curves

Magnetisation curves or M(H) hysteresis curves of magnetic nanoparticles were measured at 300 K and 5 K with applied magnetic field ranging from -7 T to 7 T.

2.3.2.2 Zero field cooled/field cooled curves

Zero field cooled/field cooled (ZFC/FC) curves were measured with an applied field of 100 Oe between 5 K and 400 K. In a first step, the sample is cooled at 5 K without any applied magnetic field. Then, data are recorded while heating at 5 K/min with application of a 100 Oe field, this is the ZFC curve. For the FC curve, data are recorded while cooling back to 5 K at 5 K/min with an applied field of 100 Oe.

2.3.3 Data correction

In order to get accurate values of magnetisation and coercive field, post measurement processing is necessary due to “errors” caused by flux pinning sites in the superconducting magnet. Indeed, superconductors repel magnetic field but at large applied field, field lines each carrying a flux quantum can enter the magnet and these pinned sites remain in the magnet even after removal of the field.[254,255] As a consequence, these pinned sites lead to magnet remanence and a superparamagnetic sample may appear hysteretic. The pinned sites and associated magnetic remanence are dependent on the superconducting magnet architecture. It is therefore different for each magnet and can be corrected. This remanence is reported as an offset of the magnetic field and can be calculated using a highly paramagnetic salt such as dysprosium oxide (Dy_2O_3). As $M = \chi H$, the magnetic moment follows a linear relationship, where χ, the magnetic susceptibility, is the slope of the curve. Consequently, any deviations from the linear behaviour are due to the magnet history.

For both M(H) and ZFC/FC curves, running a demagnetization sequence with a small applied field to compensate magnet remanence prior to measurement is necessary to achieve a true zero field. For M(H) curves, post processing is required to correct the recorded data using the calibration curve recorded for Dy_2O_3 and extract accurate values of the remanent magnetisation as well as of the coercive field.

2.4 Transmission electron microscopy

2.4.1 Principle

Transmission electron microscopy (TEM) is an imaging technique where an electron beam is steered onto a really thin sample. The electrons interact with the sample as they pass through. The image, whose resolution can reach 0.08 nm, is created from the interaction of the transmitted electrons through the sample. Thanks to a system of magnetic lenses, the sample image is projected onto a fluorescent screen or charge coupled device (CCD) camera, which transforms the electronic image into an optical image.

2.4.2 Instrumentation

The sample is situated between the condenser and the objective lenses. The beam of electrons can be generated by either a thermionic or a field-emission electron gun. In order to increase the mean free path of the electrons, the microscope is generally evacuated to low pressure. In the case of a field-emission source, the electrons are generated by applying an important difference of potential on a W needle tip. In the case of a thermionic source, a metallic filament (composed of W or LaB_6) with a V shape is heated to a high temperature to accelerate the movement of electrons. A small number of electrons reach the tip of the V with a so high velocity that they are ejected from the metal. The V shape ensures that the electrons are emitted from a small area. The electrons then pass through a Wehnelt, an electrode that serves as a convergent electrostatic lens for focusing and control of the electron beam. It is set to a negative voltage relative to the filament and to condense the beam of electrons. The electrons travel across an anode, and are accelerated towards the sample due to the high difference of potential that is applied. Then, the electron beam passes through a system of magnetic lenses. Firstly, the condenser lenses which control the region of the sample being illuminated, and allows for the manipulation and focusing of the beam on the sample. Secondly, the objective lenses which enables the magnification of the image. The image is then magnified again by mean of the intermediate and projecting lenses before reaching the detector and the image is finally projected on a fluorescent screen or a CDD camera (Figure 2.4).

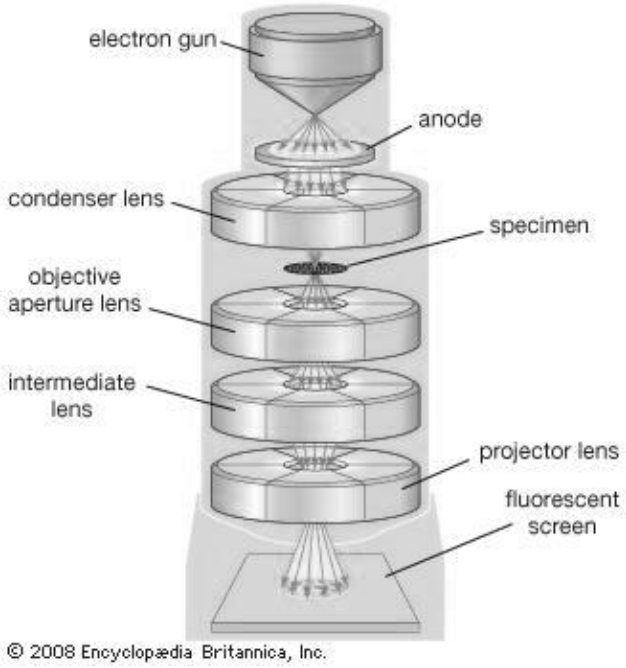

Figure 2. 4 *Schematic representation of a TEM and its components. Image taken from https://global.britannica.com/technology/transmission-electron-microscope*

2.4.3 Sample imaging

TEM was used to observe the size, size distribution, shape and in a certain extent the aggregation state of the nanoparticles. Samples were prepared by putting a drop of the nanoparticle suspension on the surface of a carbon-coated copper grid and air-dried.

For the work in UK, the TEM images of the inorganic NPs were acquired with a JEOL JEM-1200EX, with a thermionic electron gun (W filament) working at a voltage of 120 kV. The microscope also combined a Gatan Orius SC200B CCD camera giving the opportunity for real time capture images. This system allows for image resolution of 0.3 nm.
For the work in Japan, a Hitachi H-7650 transmission electron microscope with a thermionic electron gun operated at an acceleration voltage of 100 kV was used to acquire images of the NPs. This system allows for image resolution of 0.1 nm.

2.5 Dynamic light scattering

Dynamic Light Scattering (DLS) is a spectroscopic analysis technique, which allow for the determination of the hydrodynamic size of small particles in a liquid suspension. DLS uses a laser as a source of light. When the light interacts with particles animated by Brownian motion, the light is scattered in all directions. The measurement of fluctuations in the

scattering intensity over time at a given angle gives information about the velocity of the particles, related to their diffusion coefficient D. The particles size can then be calculated thanks to the Stokes-Einstein equation:

$$D_H = \frac{kT}{3\pi\eta D} \quad (2.2)$$

Where D_H is the hydrodynamic diameter of the particles, k is the Boltzmann's constant, T is the temperature, η is the liquid carrier viscosity, and D is the diffusion coefficient.

The hydrodynamic diameter of the nanoparticles was measured using a dynamic light scattering Malvern Nanosizer ZS instrument with a He-Ne laser at a wavelength of 633 nm. For hydrodynamic diameter measurements, samples were prepared by diluting a drop of nanoparticle aqueous suspension in milli-Q water into a disposable cuvette.

2.6 Attenuated total reflectance- Fourier transformed infra-red spectroscopy (ATR-FTIR)

Fourier transformed infra-red (FTIR) spectroscopy is a technique, which allow for the identification of the molecular structure of a sample. FTIR is based on the measurement of how well electromagnetic radiations whose wavelengths lie in the mid infrared region (4000-400 cm^{-1}) are absorbed by a solid, liquid, or gas sample. Rather than illuminating a sample with a monochromatic beam of light, this technique shines a beam containing many wavelengths of light at once, and measures how much of that beam is absorbed by the sample. Next, the beam is modified to contain a different combination of wavelengths, giving a second data point. This process is repeated many times. Afterward, a computer takes all this data and works backward to deduce what the absorption is at each wavelength. The name "Fourier transform infrared spectroscopy" originates from the fact that a Fourier transform is required to convert the raw data into the actual spectrum.

Infrared spectroscopy relies on the fact that molecules possess specific frequencies at which they vibrate. If the frequency of a radiation matches the vibration frequency of a molecule, this molecule absorbs the energy of the radiation and a diminution of the transmitted or reflected intensity is recorded. The absorbed frequencies are resonant frequencies and are characteristic of the molecule structure. However, for a vibrational mode to be IR active, meaning for a molecule to show infrared absorptions it must possess

a specific feature, i.e. the electric dipole moment of the molecule must change during the vibration. The dipole moment of a molecule changes as the bond expands and contracts. An example of an IR inactive molecule is a homonuclear diatomic molecule because its dipole moment remains zero no matter the length of the bond. Thus, not all the vibrations necessarily result in absorption: it depends on the geometry and symmetry of the molecule. Each vibration involves all the atoms of the molecule, but the vibration tends to be more accentuated on a specific region or functional group of the molecule. The position of the vibration bands strongly depends on the strength of the bond and the mass of the atoms. As a consequence, a sample of a given chemical structure and composition will provide a spectrum in which the position of absorption bands is characteristic of the nature, proportion, and orientation of the chemical bonds. The intensity of the absorption band is related to the concentration of the functional group responsible of the absorption.

Attenuated total reflectance (ATR) sampling is often used in conjunction with IR spectroscopy, because it makes possible the analysis of sample in the liquid or solid state without any further preparation. ATR uses a crystal with a high refractive index, so that the infra-red beam which is directed onto the crystal is totally reflected, leading to the formation of an evanescent IR wave within the crystal that extends into the sample. The evanescent waves are attenuated in the IR region and are therefore absorbed by the sample.

Solid samples must be pressed onto the ATR crystal with an appropriate force thanks to a tip to improve the penetration of the evanescent wave (and prevent air region in the case of a powder) while the surface tension of the liquid is generally enough to ensure a direct contact with the crystal.

In this work, FTIR absorption spectra were recorded with a Perkin Elmer Spectrum 100 spectrometer.

2.7 Thermogravimetric analysis

Thermogravimetric analysis (TGA) is a technique of thermal analysis, which consists in measuring the changes in chemical and physical properties of a material as a function of time with constant temperature applied, or as a function of temperature using a constant heating rate. Information about physical phenomena such as second-phase transitions can be provided, or about chemical phenomena such as oxidation or decomposition of the compound.

In our case TGA analysis is used to determine the percentage of organic compound in our NPs by measuring the weight loss of a sample of known initial mass (as the organic part burns at lower temperatures than the inorganic one). The TGA instrument continuously records the mass of the sample as it is being heated. Components decomposed with increasing temperatures resulting in a mass change, and therefore the weight percentage of each component can be calculated. TGA analysis requires very precise measurement of the mass and temperature. The instrument is generally composed of a hermetic sample chamber which can be purged with inert gas if necessary (i.e. to prevent oxidation), a programmable furnace, and a precision balance. The sample is placed in a pan, either made of aluminium for measurements at temperatures below 600 °C, or made of platinum for measurement at temperatures above 600 °C, that is positioned on the balance.

Samples under the form of a dry powder were placed on an aluminium pan and heated from 25 °C to 500 °C at a rate of 10 °C /min under N_2 atmosphere on a Seiko EXSTAR600 TG/DTA 6200 instrument. Prior to the measurement, powders were heated to 100 °C for 30 min to remove water that could be present in the sample.

2.8 Magnetic Alternative Current Hyperthermia (MACH) System

In UK, the heating potential of the synthesised MNPs for hyperthermia therapy has been assessed using an in-house patented magnetic alternative current hyperthermia (MACH) system.[256] The MACH system is able to generate an alternating magnetic field of frequency in the MHz region and high field amplitude. The magnetic field is dependent on the capacitor and the coil combination configuration, being capable to generate magnetic fields up to 20 $kA.m^{-1}$ (250 Oe) with a 100 kHz - 2 MHz frequency range.

The MACH system is composed of a 6-turn coil (inductor) and a capacitor that creates a resonance circuit allowing for the generation of very large magnetic field (Figure 2.5). Voltage from the sense coil is fed back into a control circuit that creates a pulse of current at the right frequency and at specific time points to prevent the current intensity to drop. A chiller is used as a cooling system to limit heating effects.

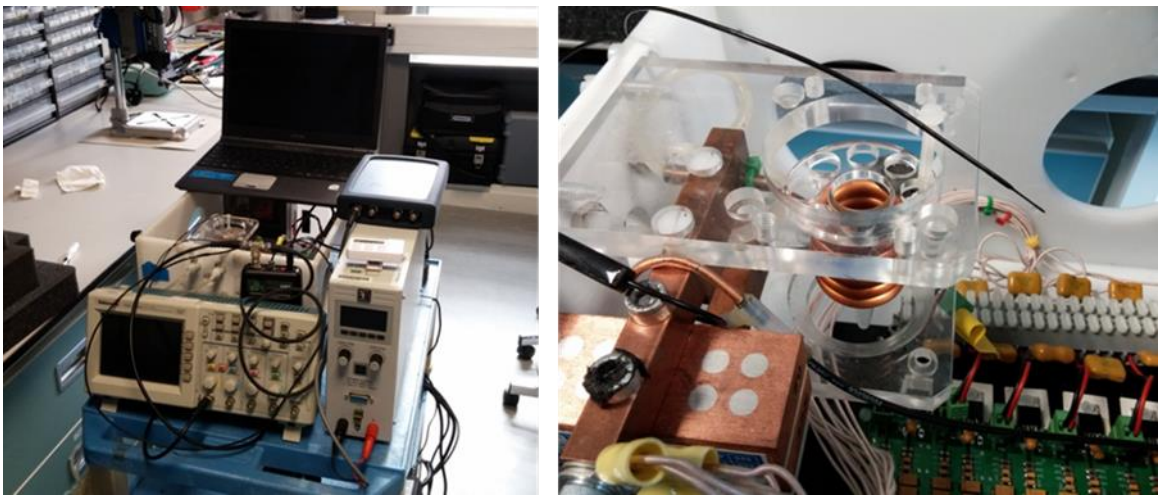

Figure 2. 5 *Photos of the MACH system.*

A 6-turn coil was employed to measure the heating performances of MNPs in suspension and for *in vitro* experiments. The 6-turn coil provides a homogeneous field distribution at the center of the coil. Glass vials with a volume of 1 mL were used as containers and positioned in the middle of the coil with the help of a support that fix the position of the vial and help for experiment reproducibility. The same volume of MNP or cell suspension (0.5 mL) was adopted for all the experiments. The increase in temperature over time was measured with fibers optic probes centered in the suspension.

For the work in France, a DM3 system manufactured by nanoScale Biomagnetics was used (Figure 2.6). The DM3 system has 4 working frequencies of 146, 217, 344.5 and 473.5 kHz and capable to generate magnetic fields up to 20 $kA.m^{-1}$. It is mainly designed for *in vivo* experiments, but can be used for the characterisation of magnetic nanoparticle suspensions and for *in vitro* experiments by positioning the vial or the petri dish at the center of the coil. The increase in temperature over time was measured with fibers optic probes centered in the suspension.

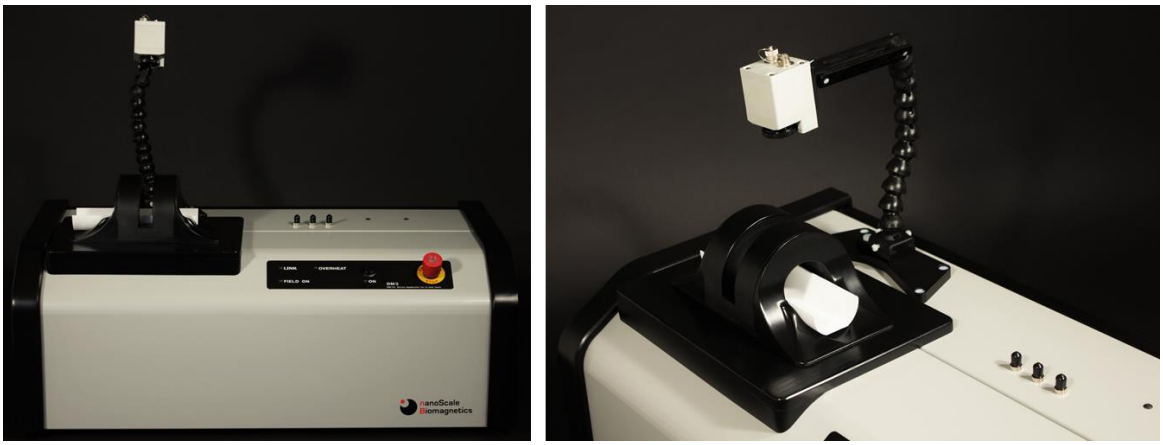

Figure 2. 6 *Photos of the DM3 setup.*

2.9 UV-visible spectroscopy

UV-visible spectroscopy is a spectroscopy technique based on the measurement of the absorption of photons whose wavelengths are within the ultraviolet (200 – 400 nm) or the visible ranges (400 – 750 nm). When a material is exposed to light in this region of the electromagnetic spectrum, molecules or ions are susceptible to undergo one or several electronic transitions. Valence electrons on the ground state are excited and passed to a state of higher energy. This transition involves π-electrons and generally occurs between a bonding orbital (highest occupied molecular orbital) and an empty anti-bonding orbital (lowest unoccupied molecular orbital). In most cases, samples are analyzed in solution.

A UV-visible spectrophotometer is usually composed of a light source, a monochromator to separate the different wavelengths, and a detector. The instrument measures the intensity of the light transmitted through a sample (I) as compared to the intensity of the light transmitted through a reference containing the same solvent as the one used for the sample to be analyzed (I_0). The ratio I/I_0 (in %) is called transmittance (T). The absorbance (A) is then expressed as follows:

$$A = -\log(T) \tag{2.3}$$

The UV-Vis spectroscopy technique is often used as a quantitative technique to measure the concentration of a given compound in solution by using the Beer-Lambert's law:

$$A = -\log\left(\frac{I}{I_0}\right) = \varepsilon l c \tag{2.4}$$

Where l is the path length (cm), c is the concentration of the absorbing compound ($mol.L^{-1}$) and ε is the molar absorptivity or extinction coefficient (in $L.mol^{-1}.cm^{-1}$). ε is a constant for a given species and wavelength. As for a given wavelength the product ***εl*** is a constant, it can be determined by plotting a calibration curve made from solutions of known concentration of the absorbing specie. It is then easy to determine the concentration of that compound in solution.

A JASCO V-630 spectrophotometer was used to determine the absorbance/concentration of DOX in aqueous solution. Absorption spectra were recorded between 350 nm and 600 nm.

The LCST of the polymer in aqueous solution was determined using a JASCO V-630 spectrophotometer equipped with an EYELA NCB-1200 temperature controller. The solution was heated from 25 °C to 47 °C whilst the transmittance was recorded at 540 nm. The LCST value was interpreted as the temperature at which the solution transmittance reached 80%.

A SpectraMax M2e multi-mode microplate reader was used to determine the absorbance/cell viability during the *in vitro* cytotoxicity studies of the nanosystems realised by MTT assay.

2.10 Nuclear magnetic resonance spectroscopy

Nuclear magnetic resonance (NMR) spectroscopy is a technique based on the NMR phenomenon and exploits the magnetic properties of some atomic nuclei. NMR spectroscopy can provide information about the molecular structure and purity of a compound. NMR is a physical phenomenon that describes a property of some atomic nuclei having a nuclear spin placed in a magnetic field. When they are subjected to a radio-frequency pulse, they can absorb the energy of the electromagnetic radiation and then re-emit it during the relaxation. This only works if the pulse is applied at a very specific frequency called the resonance frequency.[257] This resonance frequency is different for each isotope as it depends upon the magnetic properties of the isotope of the atoms and is directly proportional to the strength of the applied magnetic field. Only nuclei having a non-zero nuclear spin can give rise to the NMR phenomenon. The most commonly studied nuclei are ^{1}H and ^{13}C, although nuclei from isotopes of many other elements have been studied by NMR spectroscopy as well.

Many nuclei are magnetic, meaning that they will interact with a magnetic field. This interaction can be expressed as a magnetic moment. The larger the magnetic moment, the stronger is the interaction. When a magnetic nucleus is placed in a magnetic field, the response of the nuclear magnetic moment (due to the spin) is to retain its orientation with respect to the magnetic field, and to rotate around it. This is known as precession (Figure 2.7). The magnetic moment describes a cone with an angle that is dependent upon its initial position when the magnetic field was applied.

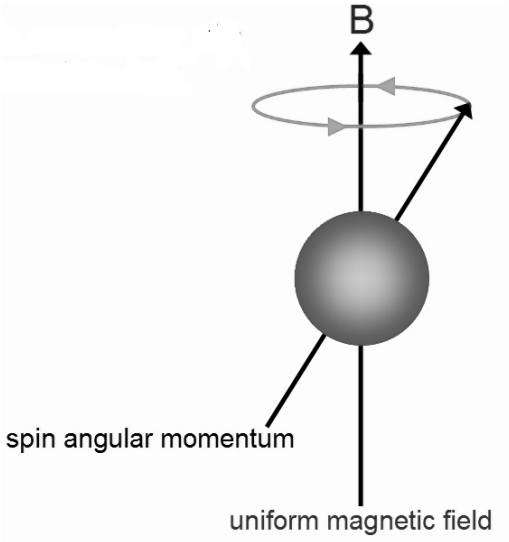

Figure 2. 7 *Precession of the magnetic moment.*

This precession movement is called Larmor precession and its angular frequency depends upon two factors, the gyromagnetic ratio γ and the strength of the magnetic field B:

$$\omega_L = -\gamma B \tag{2.5}$$

ω_L, the precession frequency of the nuclear magnetic moment otherwise known as the Larmor frequency, is the resonance frequency of the nucleus. Typical values for it are on the order of MHz. In a standard magnetic field strength of 11.7 T, the magnetization of the ^{1}H nucleus precesses at a Larmor frequency of 500 MHz (and a spectrometer with this field strength would therefore be referred to as “a 500”). The gyromagnetic ratio *γ* is literally the ratio between the “gyroscopic” (precessional) frequency and the magnetic field strength. This is a fundamental quantity that is fixed for each nuclear isotope.

NMR spectroscopy, in its most basic form, is the measurement of the precession frequency of nuclear magnetism. A bulk system composed of many nuclei will, through longitudinal relaxation, develop a net magnetization parallel to the external magnetic field (along the z-axis). In an NMR experiment, this magnetization is tipped into the x-y plane using an electromagnetic pulse and its precession frequency is measured.

NMR spectroscopy can provide detailed information on the structure and dynamics of a sample down to a molecular level. It is non-destructive and can be applied to almost any type of sample (gases, liquids, solids, heterogeneous, viscous…). Specific nuclei can be targeted, allowing local characterization of specific regions of a molecule. The information that NMR can potentially provide includes local coordination environments, molecular

structures, bond lengths and angles, motional rates, geometries and activation energies, 2D and 3D images (magnetic resonance imaging) and diffusion coefficients.

^{1}H NMR spectroscopy was used to monitor the polymerization reaction advancement and analyse the polymer composition. ^{1}H NMR spectra were recorded on a Bruker Avance III 400 MHz NMR spectrometer using chloroform-d as a solvent.

2.11 Gel permeation chromatography

Gel permeation chromatography (GPC) is a type of size exclusion chromatography (SEC). SEC is a method of chromatography in liquid phase allowing for the separation of macromolecules on the basis of hydrodynamic size. It is a widely used technique for the analysis of polymers as it can provide important information concerning the characterization of the polymer such as the polydispersity index and the average molecular weight in number, weight and size. Depending on the nature of the two phases, we can distinguish the GPC and the gel filtration chromatography.

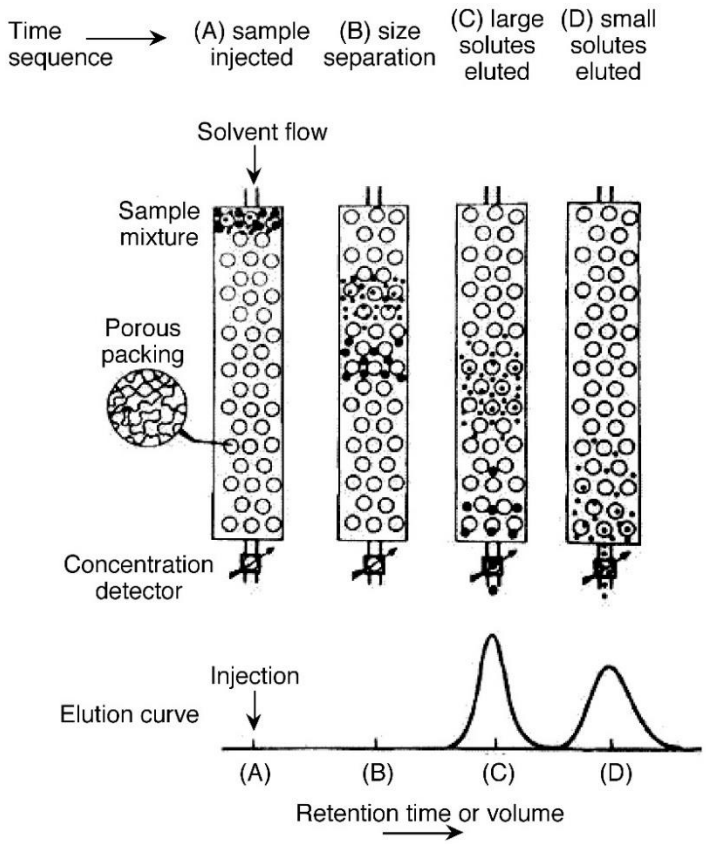

Figure 2. 8 *Schematic illustration of the principle of size exclusion chromatography. Figure taken from http://cnx.org/contents/uieDnVBC@21.1:28CLlnd_@2/Size-Exclusion-Chromatography-*

Unlike the methods of affinity chromatography which depends on the chemical affinity of the compound with the substrate, the main physical phenomenon GPC makes use of is the hydrodynamic volume of macromolecules in solution. The stationary phase of a GPC is made of porous beads packed in a column. Depending on their sizes, the molecules constituting the analyte may more or less enter the pores of the stationary phase. Thus, the smaller analytes can penetrate the pores more easily and are retained longer, increasing their retention time, while the bigger ones can barely or cannot penetrate the pores and are therefore eluted faster (Figure 2.8).

Every column has a specific range of molecular weights that can be separated: too large macromolecules will not be retained and elute with the free volume (volume outside of the beads) while too small molecules will be completely retained and elute at the end of the injection with the eluent. Macromolecules having a molecular weight in between those two limits can be separated. This is known as the fractional range. Data analysis outside this fractional range does not provide any information. In order to obtain the average molecular weight of a polymer, calibration of the GPC with standard polymers of known average molecular weight and low polydispersity is necessary. Commonly used polymers for the calibration of the GPC are polystyrene or poly(methyl methacrylate) standards.

A GPC instrument is similar to any liquid chromatography equipment. It is composed of a solvent reservoir, a pump that constantly delivers fresh eluent to the column at a precise and constant rate, an injector, a column and one or multiple detectors. The eluent should be a good solvent of the polymer as samples are dissolved in it prior to injection.

Number average molecular weight (Mn) and polydispersity (PDI = Mw/Mn) of the synthesized polymers measured by SEC were performed on a Shimazdu Prominence high-performance liquid chromatograph equipped with a LC-20AD liquid chromatograph, a RID-10A refractive index detector, a CTO-20A column oven and a DGU-20A3 degasser. Tetrahydrofuran (THF, stabilizer free) was used as the mobile phase. Samples were prepared by dissolving 5 mg of vacuum-dried polymer in 2 mL of THF. THF was constantly delivered to the column with a uniform flow of 1 mL/min. The molecular weights of the polymers were determined by a conventional calibration using polystyrene standards ranging from 5.8×10^2 g/mol to 2.0×10^4 g/mol.

2.12 Flow cytometry

Flow cytometry is a widely used technique for characterizing and analyzing particles in suspension, i.e. cells, bacteria or chromosomes. Typically, particles of size comprised between 0.2 µm to 150 µm are suitable for flow cytometry analysis. Flow cytometry can give information about biophysical properties of a sample, such as granularity or internal complexity, size and fluorescence intensity. Cytometers samples must be in the form of liquid suspensions as the properties of single particles are simultaneously measured as they flow in a fluid stream through a laser beam.

A BD Accuri C6 flow cytometer (BD Bioscences, UK) was used in this work to perform flow cytometry analyses on cells in suspension.

A flow cytometer is constituted of three main parts. The first part is the fluidic system, which transports the particles via a flow of sheath fluid into a flow chamber (also called flow cell), where a beam of light will interact with the particles. Based on laminar flow principles, the design of the flow cell is made so that the fluid stream carrying the particles is focused in the center of the laser beam and only one particle at a time pass through the laser beam, allowing for interrogation of single particles. This process is known as hydrodynamic focusing. The scattered light and the fluorescence emitted as particles move through the laser beam are measured and analyzed. The optic subsystem is made of excitation components and collection components. The excitation optics consist of the laser, prisms and lenses used to shape and focus the laser beam to the interrogation point. The optic collection components consist of lenses positioned appropriately to collect the forwarded scattered, side scattered and fluorescence light. Finally, the electronic part of a flow cytometer is composed of detectors (photodiodes and photomultiplier tubes) which convert the light intensity measured into electronic signals. More information about this technique can be found in the comprehensive book about flow cytometry published by H. M. Shapiro.[258]

2.12.1 Light scattering

When a particle passes through a beam of light, light scattering occurs. In a cell, the degree of light scattering is dependent upon its physical properties, such as its size, shape, nucleus, internal complexity and granularity. Depending on the direction the light is scattered, two types of scattered light can be distinguished: forward scattered light (FSC) and side scattered light (SSC) (Figure 2.9).

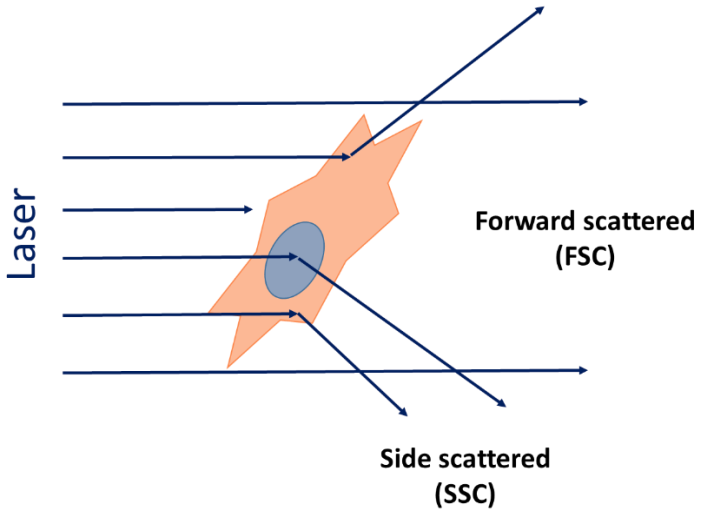

Figure 2. 9 *Light scattering of a cell passing through a beam of light.*

The scattered light in the forward direction is based on the size or surface area of the cell and the difference between the refractive indexes of the cell and the sheath fluid. Increasing size and difference between the refractive index both increases the generation of FSC. FSC is mainly due to diffracted light. The SSC is mainly dependent upon the cell granularity. The more granular a cell is the more SSC is generated. SSC is mainly due to refracted and reflected light, and is collected perpendicular (at approximatively 90°) to the laser beam. Correlated measurement of FSC and SSC can allow for differentiation of cell types in a sample of heterogeneous cell composition. Furthermore, it can also be used to study the cell uptake and internalization of nanoparticles or drugs as the SSC increases with the degree of loading.

2.12.2 Fluorescence

Fluorescence is the emission of light induced by the excitation of a molecule, generally by absorption of a photon, i.e. by absorption of light, immediately followed by a spontaneous emission. Indeed, this absorption of light energy promotes a valence electron in the ground state to an excited state of higher energy. The electron quickly relaxes back to its ground state emitting the excess energy as a photon of light, called fluorescence.

Every fluorescent compound, also called fluorophore or fluorochrome, has a characteristic absorption spectrum, which is the range of wavelengths that excites the fluorophore, and a characteristic emission spectrum, which is the range of wavelengths that can be re-emitted by the fluorophore. In most cases, the energy of the emitted photon is lower and therefore the emitted light has a longer wavelength than the absorbed radiation.

The labelling of cell with a fluorescent compound, known as cell staining, can be used for identification and cell sorting. An argon ion laser with blue emission at 488 nm is commonly used in flow cytometry, because it can excite more than one fluorophore. The Accuri C6 flow cytometer is equipped with a blue laser (emission at 488 nm) and a red laser (emission at 640 nm). Examples of common fluorochromes used in flow cytometry that can be excited at a wavelength of 488 nm are fluorescein isothiocyanate (FITC), phycoerythrin (PE), propidium iodide (PI) and allophycocyanin (APC). The detectors for fluorescent light can be made specific to a particular fluorophore by positioning optic filters, which only let through a narrow range of wavelengths in front of the detectors. More than one fluorophore can be used simultaneously to stain the cells as long as they can be excited at the same wavelength and their main peak emission are far apart enough to be measured by different detectors. With the C6 Accuri flow cytometer, four channels are used for the detection of emission: FL1 533/30 nm filter (i.e. FITC), FL2 585/40 nm filter (i.e. PE/PI), FL3 > 670 nm filter (i.e. PerCP/PerCP-Cy5.5/PE-Cy7) and FL4 675/25 nm filter (i.e. APC). The numbers give the characteristic of the range of wavelength that can reach the detector, for example, 530/30: 530 ± 15 nm. Cell staining can help in the investigation of cell events, for example, AnnexinV-FITC/PI are used for the study of cell death and cell viability, for the detection of early apoptosis and late apoptosis/necrosis.

When more than one fluorophores are used at the same time, their emission spectra may overlap, and can be detected by the detection filter for other fluorophores. For example, the emission spectra of FITC overlap with the one for PI. As a consequence, due to the spillover of FITC fluorescence into PI bandpass filter, the PI population will appear positive. This can be corrected by a process of fluorescence compensation, which ensures that the fluorescence detected in a particular detector derives from the fluorophore that is being measured.

2.13 Inductively coupled plasma atomic emission spectroscopy

Inductively coupled plasma atomic emission spectroscopy (ICP-AES) is an analytical technique which allows for the quasi-simultaneous detection and quantification of all metals present in a sample at the parts per million range. In this method, the sample is placed in an argon or helium plasma at very high temperatures (6000 - 8000 K) to generate ions and excited atoms. Samples can be in the solid or liquid state. Generally, solid samples are previously dissolved in an acid to form a solution. The solution is injected into

the centre of the plasma flame via a nebulizer that transforms the sample into a fine spray. The molecules constituting the samples are broken up into simple atoms and will in turn be ionised as they collide with the charged ions and electrons composing the plasma. The ICP-AES is based on the fact that when the released electrons resulting from the ionisation of the sample recombine, a photon is emitted in the UV/visible range, and this wavelength is characteristic of the element involved. The light emitted by the plasma is analysed and separated into its different wavelengths via one or several monochromators or a polychromator, and finally the intensity is measured thanks to photomultiplier tubes or a CCD. The intensity of the radiation is proportional to the concentration of the ions in the sample. Consequently, the concentration of the desired element can be easily determined by referring to a calibration curve previously obtained by measuring intensities of solutions of known concentration of this same element under the same conditions.

A Varian 720 axial ICP-AES has been used to determine the total iron content in the synthesized iron oxide nanoparticles. Samples were prepared by digesting 1.2 mg of dry nanoparticle powder in 0.2 mL of nitric acid and diluted with 14.8 mL of milli-Q water. The final concentration of nanoparticles in solution is 80 ppm, therefore we know that the final iron concentration will be between 0 – 80 ppm. This information indicates what range of concentration the calibration curve must cover. Solutions of known concentrations were used to obtain a calibration curve using an ICP iron standard solution of 10000 ppm. Appropriate dilutions were made to obtain the desired concentration, using the same total volume and same volume of acid as for the samples.

2.14 Optical microscopy

An optical microscope uses visible light and a set of lenses composed of an objective and a condenser to magnify images of really small sample. Optical microscopes are commonly used in biology for the observation of cells and tissues.

A Leica DMI6000 B automated inverted microscope was used for imaging of biological samples. For fluorescence microscopy, a light source of wavelength 633 nm was used. Captured images were processed and analysed with Leica Application Suite X software.

An inverted microscope is upside down compared to a conventional optical microscope. Its light source and condenser are pointing down and are located above the stage where the sample is positioned, while the objective and turret are pointing up and are located below the stage. As a consequence, one is looking at a sample from below with an inverted

microscope. It is widely used to observe living cells and organisms as it is large enough to fit large containers such as a flask which allows the specimen to be under natural conditions while in other types of microscopes the sample is under glass slide.

2.14.1 Bright field microscopy

Bright field microscopy is the oldest and simplest optical microscopy technique. The sample is illuminated with white light. The light transmitted through the sample forms the image, and the contrast is the result of transmitted light being absorbed in more or less dense areas of the sample. For biological samples, this technique usually has a low resolution and contrast. Contrast can be enhanced by staining the samples, for examples, histological samples of cells loaded with iron oxide nanoparticles can be stained with Prussian blue and nuclear fast red. Prussian blue stains the iron in blue while nuclear fast red stain the cell nucleus in pink (Figure 2.10).[259]

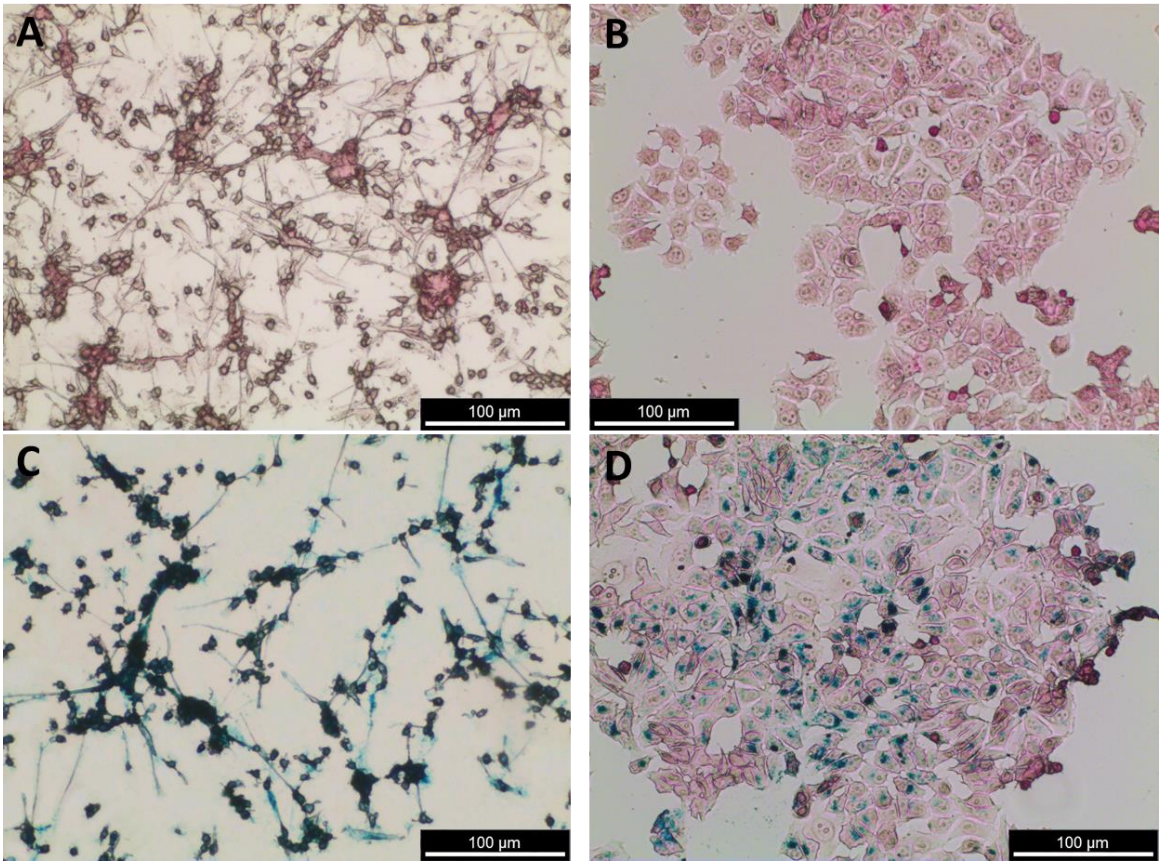

Figure 2. 10 *Images acquired with an inverted microscope using the bright field imaging technique. A) U-87 cells and B) MCF-7 cells counterstained with nuclear fast red. C) U-87 cells and B) MCF-7 cells loaded with iron oxide nanoparticles stained with Prussian blue and counterstained with nuclear fast red.*

2.14.2 Fluorescence microscopy

Fluorescence microscopy is a type of optical microscopy that uses the fluorescence phenomenon, that is the absorption and subsequent re-emission of light by a compound. A higher intensity light source as compared to conventional optical microscopy needs to be used to excite the fluorescent species in the sample of interest. In most cases, labelling of the sample with fluorescent stains is necessary to make it fluorescent. Study of cellular processes and imaging of structural components can be performed via labelling specific cell compartments or molecules. Fluorescence microscopy even allows users to determine the distribution of a single molecule species, its amount and its localization inside a cell. Colocalisation and interaction studies can be performed, and ion concentrations as well as intra- and intercellular processes like endocytosis and exocytosis can be observed. For example, DRAQ5 is a far-red DNA stain that is commonly used to counterstain the nuclei or measure DNA content. LysoTracker Green is a green stain commonly used to label acidic compartments in cells such as lysosomes. The intrinsic fluorescence of a sample or compound can also be used. For instance, the drug doxorubicin is fluorescent and therefore allows for the study of its localisation in cells.

CHAPTER 3

SYNTHESIS OF CORE@SHELL Fe@Bi NANOPARTICLES FOR HYPERTHERMIA APPLICATIONS

3.1 Introduction

In this project, efficient mediators of heat based on an iron core and a bismuth shell were aimed to be developped. Indeed, one of the major challenge in magnetic hyperthermia and thermo-chemotherapy is to obtain NPs with good heating abilities, as it would allow the reduction of the magnetic nanoparticles quantity to be injected in the patient. Pure iron NPs have a much greater heating potential than iron oxide NPs, due to their higher saturation magnetisation and magnetic anisotropy. However, such NPs are really difficult to obtain because of the quick oxidation process of iron. Iron is a hard magnetic material, which means it has a large hysteresis loop. Therefore, the NPs must have a superparamagnetic or quasi-superparamagnetic behaviour so that a high magnetisation can be reached at low applied field to be used safely for hyperthermia therapy. This project focused on the synthesis of new NPs based on pure iron in an attempt to get MNPs with high saturation magnetisation and low coercive field to get exceptional heating potential for hyperthermia therapy. Moreover, iron oxide is already well-known for its application as contrast agent for MRI. Because the saturation magnetisation of iron oxide is much lower compared to pure iron, the use of pure iron NPs would provide a better contrast at lower quantities.[260] Bismuth has been chosen as a coating to protect iron against oxidation. Such as gold, bismuth is rather chemically inert and can be used as CT-imaging agent. It has been preferred over gold, because it possesses a larger X-ray attenuation coefficient, has low toxicity and is less expensive.[261,262]

If the development of such NPs is successful, they would find applications not only in hyperthermia therapy but also in CT-imaging due to the bismuth coating and as MRI contrast agent due to the iron core. For that purpose, different synthetic routes by sequential reduction of iron and bismuth were investigated. These NPs could then be functionalised with a biocompatible polymer and used for thermo-chemotherapy applications.

3.2 Materials and methods

3.2.1 Reagents

Hexadecylamine ($C_{16}H_{35}N$, HDA, 90%), hydrochloric acid (HCl, 37%), oleylamine ($C_{18}H_{37}N$, OAm, 70%), 1-octadecene ($C_{18}H_{36}$, 90%), 1-decanethiol ($C_{10}H_{22}S$, 96%), iron pentacarbonyl ($Fe(CO)_5$, >95%) and bismuth trichloride ($BiCl_3$, >98%) were purchased from Sigma Aldrich, Japan. Ethanol (EtOH, 99.5%) was obtained from Nacalai tesque,

Japan. Iron pentacarbonyl ($Fe(CO)_5$, >95%) and hexane (C_6H_{14}, >96%) were obtained from Kanto Chemicals, Japan. All the reagents were used as purchased without any further purification.

3.2.2 Preparation of the Bi-DT complex

Bismuth-decanethiol (Bi-DT) complex was synthesized using a molar ratio of 1:4 or 1:12 (Table 3.1). Briefly, $BiCl_3$ was added to a mixture of decanethiol and octadecene (2 mL), and stirred under argon (Ar) atmosphere until full dissolution of the solid occured. The formation of the complex could be confirmed by a change in colour of the solution, from colourless to yellow.

Table 3. 1 *Quantities of $BiCl_3$ and DT used for the preparation of the Bi-DT complexes.*

$BiCl_3$:DT molar ratio	**m_{BiCl3} (mg)**	**n_{BiCl3} (mmol)**	**V_{DT} (mL)**	**n_{DT} (mmol)**
1:4	79	0.25	0.212	1
1:12	79	0.25	0.636	3

3.2.3 Synthesis of core@shell Fe@Bi nanoparticles

The iron core was synthesised by following a slightly modified previously reported procedure.[263] In a typical synthesis, oleylamine (OAm, 0.16 mL, 0.5 mmol), hexadecylammonium chloride (HDA-HCl, 0.139 g, 0.5 mmol) and 1-octadecene (10 mL) were mixed in a 50 mL three-neck flask and degassed for 30 min at 120 °C under an Ar flux and vigorous magnetic stirring. Addition of $Fe(CO)_5$ (0.35 mL, 2.5 mmol) was performed at 180°C and the solution was kept at this temperature for 30 min. Then, the Bi-DT complex was added to the flask either in one go or at a constant rate of addition (Table 3.2) using a syringe pump (KD Scientific Inc., KDS100). After addition of the Bi-DT complex, the temperature was maintained at temperature T for a time t (Table 3.2).

The NPs were collected with hexane and ethanol, and washed by centrifugation with 5 mL of hexane and 15 mL of ethanol (8500 rpm, 3 times, 10 min) and redispersed in hexane for further use. A small amount of NPs was dried under an Ar flux to obtain a dry powder.

In addition to those syntheses, core@shell $Fe@Fe_3O_4$ NPs and Bi NPs were also synthesized following the same protocol for comparison.

Table 3. 2 *Experimental conditions used for the synthesis of the core@shell Fe@Bi nanoparticles.*

Sample	$BiCl_3$:DT (molar ratio)	Rate of injection Bi-DT complex (mL/hr)	T (°C)	t (min)
AH31	1:4	/	180	30
AH38	1:4	/	180	60
AH37	1:12	/	180	60
AH43	1:4	30	180	30
AH45	1:4	15	180	30
AH48	1:4	10	180	30
AH49	1:4	10	160	30

3.2.4 Synthesis of core@shell Fe@Fe_3O_4 nanoparticles

The synthesis of core@shell Fe@Fe_3O_4 NPs was performed by following a slightly modified previously reported procedure.[263] In a typical synthesis, OAm (0.16 mL, 0.5 mmol), HDA-HCl (0.139 g, 0.5 mmol) and 1-octadecene (10 mL) were mixed in a 50 mL three-necks round bottom flask and degassed for 30 min at 120 °C under an Ar flux and vigorous magnetic stirring. Precursor $Fe(CO)_5$ (0.35 mL, 2.5 mmol) was added at 180 °C and the solution was kept at this temperature for 30 min.

The NPs were collected with hexane and ethanol, washed by centrifugation with 5 mL of hexane and 15 mL of ethanol (8500 rpm, 3 times, 10 min) and redispersed in hexane for further use. A small amount of NPs was dried under an Ar flux to obtain a dry powder.

3.2.5 Synthesis of Bi nanoparticles

The synthesis of Bi nanoparticles was carried out as follows: OAm (0.16 mL, 0.5 mmol), HDA-HCl (0.139 g, 0.5 mmol) and 1-octadecene (10 mL) were mixed in a 50 mL three-necks round bottom flask and degassed for 30 min at 120 °C under an Ar flux and vigorous magnetic stirring. The Bi-DT complex was added at 180°C and the solution was kept at this temperature for 60 min.

The NPs were collected with hexane and ethanol, washed by centrifugation with 5 mL of hexane and 15 mL of ethanol (8500 rpm, 3 times, 10 min) and redispersed in hexane for further use. A small amount of NPs was dried under an Ar flux to obtained a dry powder.

3.3 Results and discussion

3.3.1 Initial considerations

Thermal decomposition of $Fe(CO)_5$ at 180 °C in the presence of hexadecylammonium chloride and oleylamine in octadecene under inert atmosphere has been shown to give highly crystalline iron NPs.[263] Preliminary experiments were performed at UCL using this approach to synthesize the iron core. Formation of the bismuth coating was attempted by reduction of bismuth tribromide using triethylsilane:

$$BiBr_3 + 3Et_3SiH \rightarrow Bi(0) + 3/2H_2 + 3Et_3SiBr$$

Interpreting the results (not shown) was challenging but after careful analysis, the most likely conclusion was that the Bi NPs were growing independently of the Fe seeds instead of coating them. This hypothesis is consistent with the important lattice mismatch between Fe and Bi calculated from XRD patterns. Moreover, Fe and Bi crystallize in completely different system, i.e. α-Fe crystallizes in a cubic structure with a lattice parameter a = 2.8444 Å, while Bi crystallizes in a rhombohedral structure with lattice parameters a = b = 4.5460 Å and c = 11.8600 Å. This significant mismatch in lattice parameters makes the heteroepitaxial growth of Bi on the Fe seeds impossible. However, despite numerous trials with different synthetic conditions, it seemed that the non-epitaxial growth of Bi on the Fe substrates was not happening either.

After arriving at JAIST, and discussing the synthetic scheme with Prof. Maenosono, we decided not to continue with this synthetic scheme and to change the method used to form the Bi coating.

The thermal decomposition of $Fe(CO)_5$ at 180 °C in presence of HDA-HCl and OAm in octadecene under inert atmosphere was kept for the synthesis of the iron core. However, we decided to use a Bi complex formed from $BiCl_3$ and decanethiol (called Bi-DT complex) in octadecene for the formation of the Bi coating. Indeed, having a precursor in the liquid form was more convenient to add during the synthesis performed under vacuum as compared to the solid precursor $BiBr_3$. We chose a Bi-DT complex because it has been shown by Prof. Maenosono's group that decanethiol makes stable complexes with the Bi cation, which then can be effectively reduced to Bi metal while being protected from creating BiOCl crystals. This is not the case for Bi-oleylamine or Bi-oleic acid complexes.[264] Moreover, from the literature, it was found that Bi has a strong affinity with thiols, which could help in the stabilization of the particles.[265]

3.3.2 Synthesis of core@shell Fe@Fe_3O_4 nanoparticles

Fe@Fe_3O_4 nanoparticles were synthesized following the same protocol as for the synthesis of Fe@Bi NPs, but without adding the Bi-DT complex. This is really important to see what type of Fe NPs are obtained following this synthetic route and so that differences between the obtained nanoparticles with and without bismuth can be identified more easily.

The TEM images show spherical core@shell NPs (Figure 3.1). The core was composed of iron, and the shell of iron oxide. The iron oxide shell was most likely formed when the NPs were exposed to air at the end of the synthesis. The Fe@Fe_3O_4 NPs were agglomerated, but calculations from the NPs present on the edges of the agglomerates, showed an average nanoparticle size of 16.6 ± 3.0 nm (n = 100), with an average core size of 10.9 ± 2.4 nm.

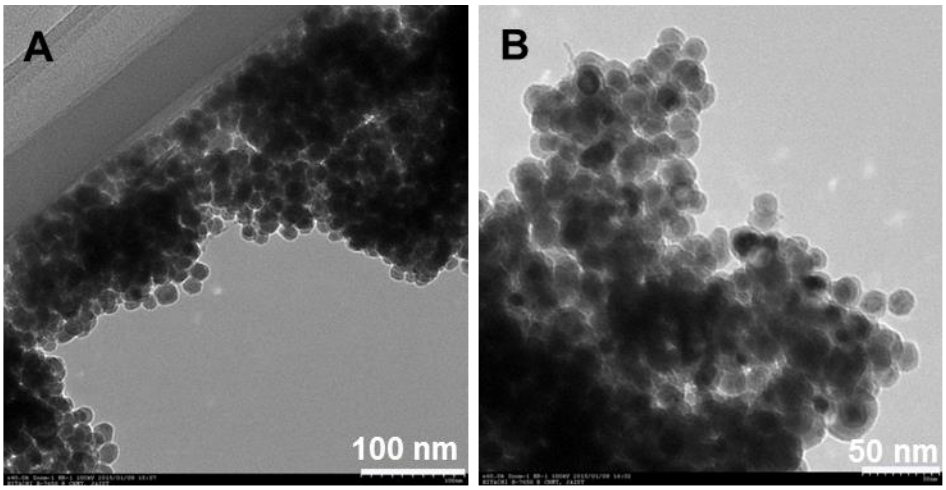

Figure 3. 1 *TEM micrographs of Fe@Fe3O4 nanoparticles A) at low magnification and B) higher magnification.*

The XRD pattern of the Fe@Fe_3O_4 NPs matched with cubic α-Fe (Figure 3.2). There was no peak characteristic of an iron oxide phase, meaning that the shell of the NPs was formed of amorphous or really small grain domain size iron oxide. From the XRD pattern, a crystallite size of 11.5 ± 0.2 nm was calculated for the iron peaks, which was in good agreement with the core size calculated from the TEM images.

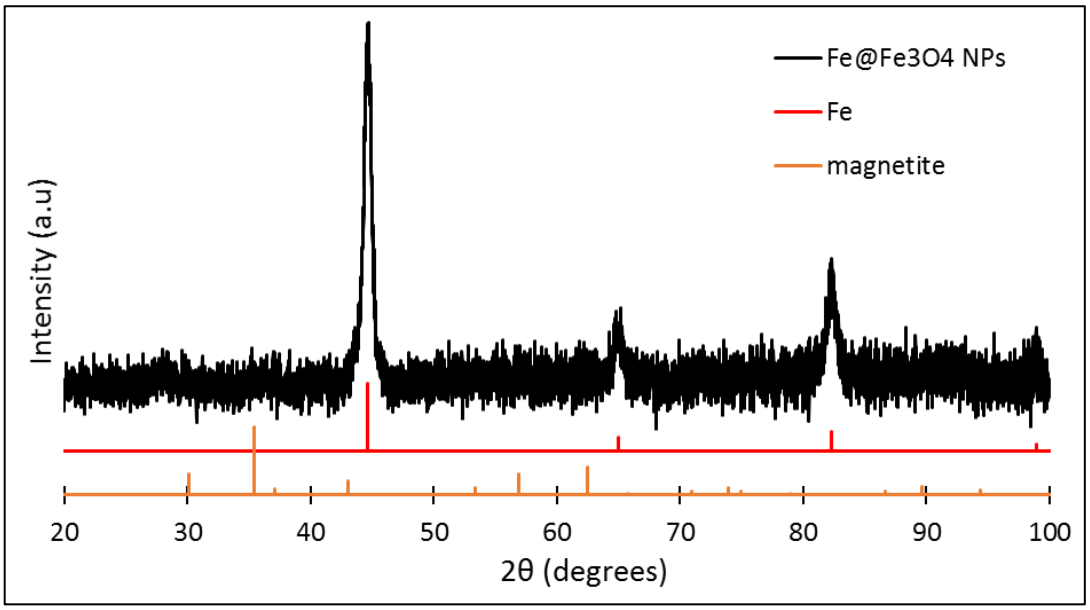

Figure 3. 2 *XRD pattern of the Fe@Fe_3O_4 NPs. Peaks were indexed according to the reference patterns for iron (pdf ref. 00-006-0696) and magnetite (pdf ref. 00-019-0629).*

The magnetic properties of the Fe@Fe_3O_4 NPs were evaluated at 300 K on the dry powder using a SQUID (Figure 3.3). The NPs had a quasi-superparamagnetic behaviour at room temperature with a saturation magnetisation of 103 emu/g (measured 16 days after the synthesis) and a coercive field of 100 Oe.

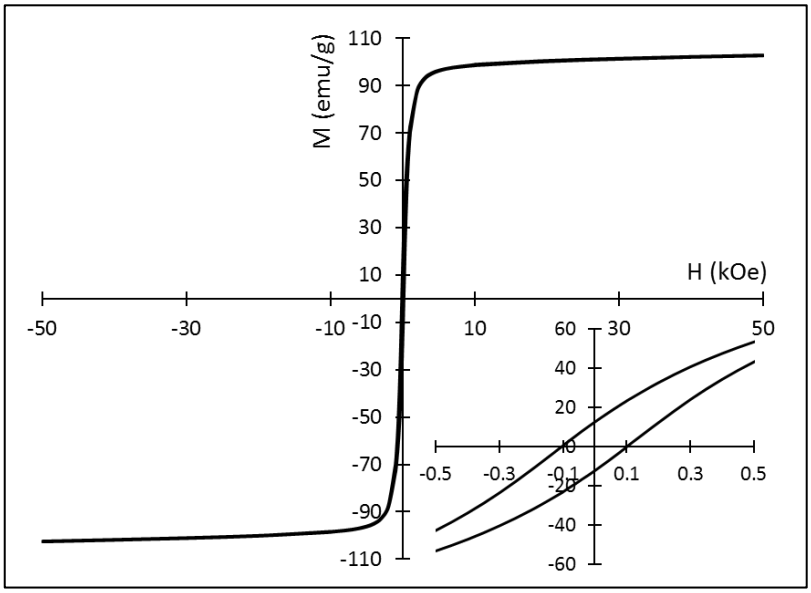

Figure 3. 3 *Magnetisation curves of the Fe@Fe_3O_4 NPs at 300K. The inset shows a zoom into the low magnetic field region.*

The difference between the saturation magnetization of bulk iron (i.e. 218 emu/g)[266] and the saturation magnetization obtained for the Fe@Fe_3O_4 NPs was mainly due to the

presence of an iron oxide shell in the NPs, which has a lower saturation magnetization (i.e. 92 emu/g)[267] than pure iron. Moreover, according to the XRD pattern, this iron oxide shell was amorphous and as a consequence would result in an even lower saturation magnetisation.

3.3.3 Synthesis of Bi nanoparticles

Bi NPs were also synthesized using the same synthetic conditions for comparison. Figure 3.4 shows the TEM images of the obtained Bi NPs. The NPs were hexagonal in shape and very polydisperse in term of size. The average NP size (measured along one diagonal of the hexagon) was found to be equal to 57 ± 17 nm (n = 110).

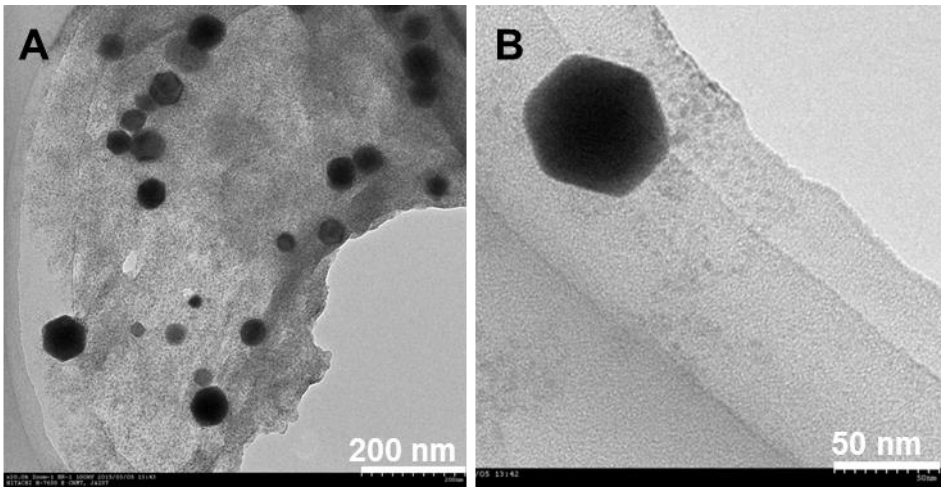

Figure 3. 4 *TEM micrographs Bi nanoparticles A) at low magnification and B) higher magnification.*

The obtained XRD pattern shows a highly crystalline structure with peaks matching with reference JCPDF of rhombohedral Bi crystalline phase (Figure 3.5). No peak corresponding to the oxide phase could be observed. The crystallite size of the Bi NPs calculated from the XRD pattern was 38.7 ± 2.1 nm, which is smaller than the size obtained from TEM images, suggesting that the NPs were polycrystalline.

No characterization of the magnetic properties of the Bi NPs was performed as bismuth is a diamagnetic material.

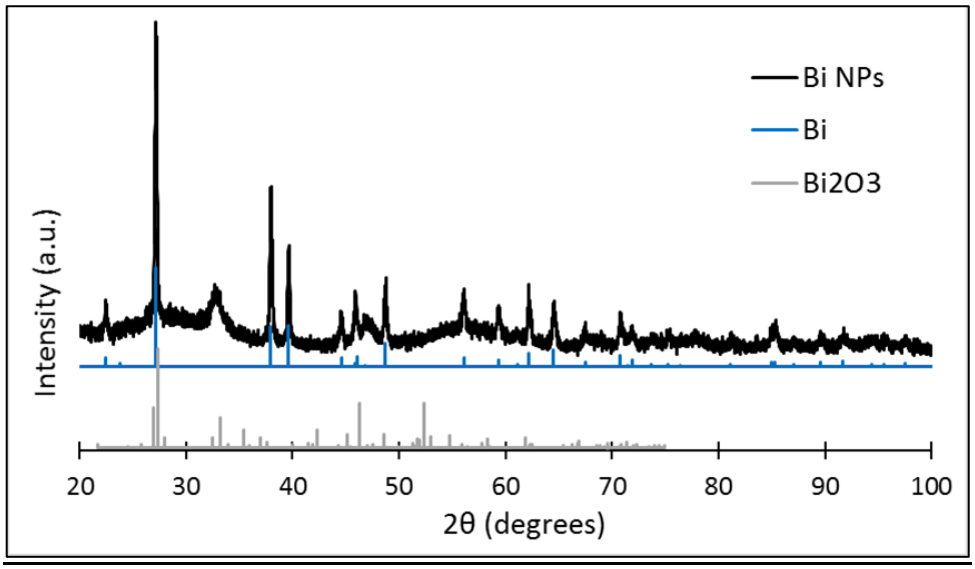

Figure 3. 5 *XRD pattern of the Bi NPs. Peaks are indexed according to the reference patterns for bismuth (pdf ref. 00-005-0519) and bismuth oxide (pdf ref. 00-041-1449).*

3.3.4 Synthesis of core@shell Fe@Bi nanoparticles

3.3.4.1 Preliminary experiment

The first experiment was performed by adding the Bi-DT complex in one go. In the rest of the document, the NPs obtained via this synthetic process will be referred as sample FeBi_A (see Table 3.2 in section 3.2.3 for the details of experimental conditions used to synthesize FeBi_A NPs).

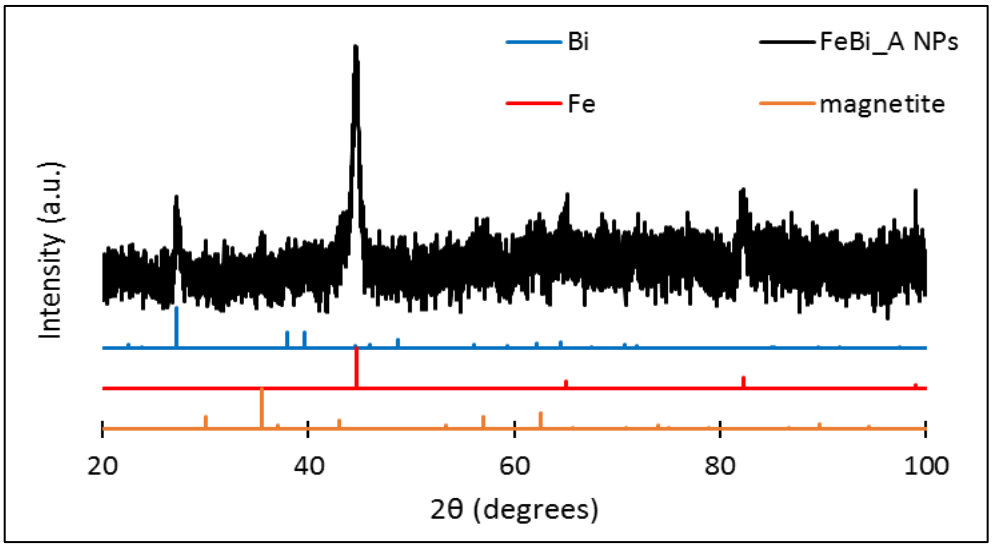

Figure 3. 6 *XRD pattern of the FeBi_A NPs. Peaks were indexed according to the reference patterns for bismuth (pdf ref. 00-005-0519), iron (pdf ref. 00-006-0696) and magnetite (pdf ref. 00-019-0629).*

XRD pattern of FeBi_A NPs shows the presence of both cubic α-Fe and rhomboedral Bi crystalline phases (Figure 3.6). The crystallite sizes calculated from the XRD pattern were D_{Fe} = 11.0 nm and D_{Bi} = 16.2 nm. The low intensity of the main bismuth peak may suggest that Bi ions had not been reduced entirely into Bi metal. However, there is a big decrease in the Bi crystallite size extracted from the XRD pattern of FeBi_A NPs as compared to the syntheses performed following the first synthetic scheme (part performed at UCL) and is more coherent with the size of the nanoparticles.

Figure 3.7 shows TEM images of the FeBi_A NPs. The NPs had a spherical core@shell morphology with an average size of 16.3 ± 2.8 nm and an average core size of 9.4 ± 1.9 nm (n = 116), which matches well with the sizes obtained from analysis of the XRD pattern. Moreover, from TEM images it did not seem possible to distinguish between two different types of nanoparticles.

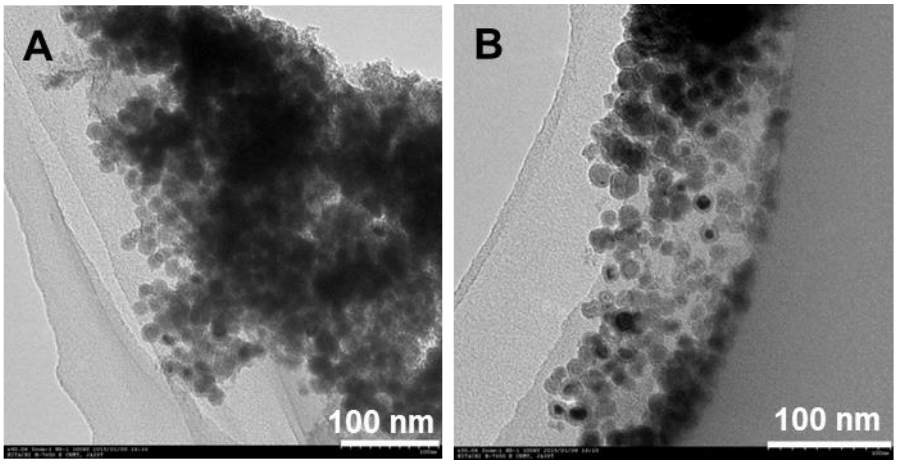

Figure 3. 7 A) and B) *TEM micrographs of FeBi_A NPs.*

The obtained NPs were not stable in hexane, and were therefore aggregated. However, it was possible in a certain extent, to stabilize them by adding an excess of OAm and sonicating the suspension for 30 min. This step was repeated several times to obtain as many stable particles as possible. Then, the stable nanoparticles were separated from the ones still sinking in the bottom of the suspension, and after rewashing the nanoparticles by centrifugation, a grid with well separated particles could be obtained (Figure. 3.8). Again, on those images, only one type of NPs can be observed which leaned towards the hypothesis of obtaining core@shell Fe@Bi NPs. From the TEM images only, it was not possible to say whether the desired Fe@Bi core@shell nanoparticles were obtained for sure, because other core@shell structures could be obtained such as Fe@Fe_3O_4 for example. Indeed, Fe@Fe_3O_4 nanoparticles are very likely to be obtained if the bismuth does not grow on the iron seeds during the reaction and these nanoparticles looked similar

to the ones obtained in the synthesis of Fe@Fe_3O_4. The lighter shell and darker core of the nanoparticles would be more consistent with an iron oxide shell and an iron core in term of electron density. Indeed, Bi has a higher electron density than Fe and should therefore appear darker than Fe on TEM images. However, exceptions with TEM contrast have already been observed, i.e. in the case of iron and gold with core@shell Fe@Au NPs, it has often been reported that the gold shell appears lighter than the iron core[268-271] This is attributed to the dominance of the mass-thickness contrast over the diffraction contrast, rendering the shell lighter despite Au having a higher electron density than Fe.[272]

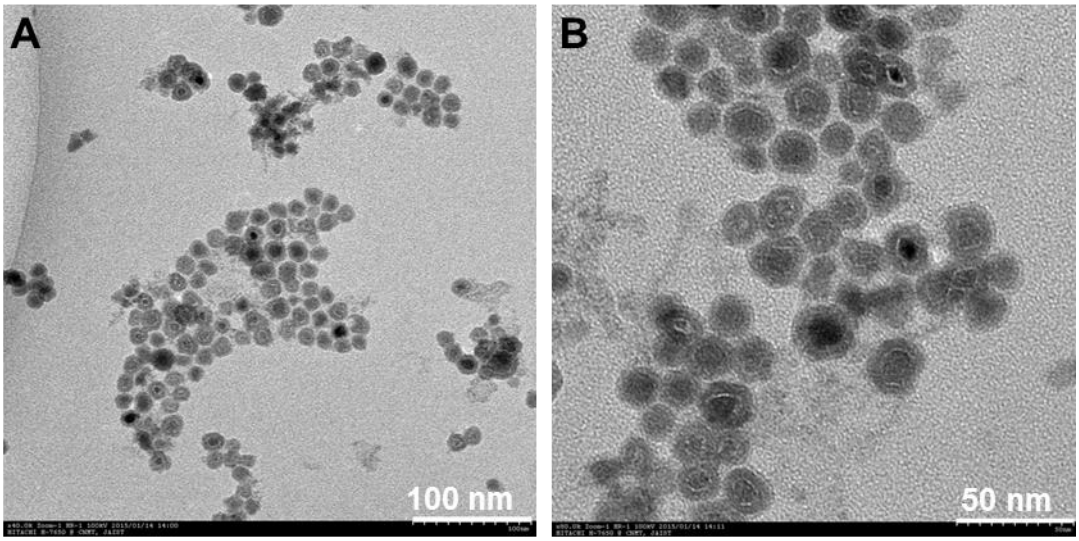

Figure 3. 8 *TEM micrographs of FeBi_A NPs after stabilisation with OAm A) at low magnification and B) higher magnification.*

A void between the core and the shell of the NPs was observed. If the core@shell NPs are made of Fe@Bi NPs, the void could be due to the galvanic replacement phenomenon[273,274] as the reduction potential of Bi is higher than the reduction potential of iron ($E_{Fe2+/Fe}$ = -0.44, $E_{Fe3+/Fe}$ = -0.037 and $E_{Bi3+/Bi}$ = 0.317). Indeed, galvanic replacement reactions rely on the different reduction potential of two metals, which combine to give a more favourable reaction. It involves the oxidation of one metal (i.e. the one having the lowest reduction potential, which in our case is iron) by the ions of another metals having a higher reduction potential (here bismuth). As a result, atoms of the iron core are oxidized and dissolved into the solution, while the bismuth ions are simultaneously reduced and plated on the outer surface of the nanoparticles, leading to the formation of a void between the iron core and the bismuth shell.

If the core@shell NPs are made of Fe@Fe_3O_4 NPs, the void could originate from the unbalanced interfacial diffusion of oxygen and iron during the oxidation process (when the NPs are exposed to air). This phenomenon is known as the Kirkendall effect: Fe metal

atoms diffuse faster outward than O diffuse inward leading to a net material flux across the spherical interface and consequent formation of a void.[273]

In order to get a better idea of the composition of the obtained core@shell NPs, EDS analysis and elemental mapping were performed on this sample. Because the composition of the sample did not seem to be homogeneous, the atomic percentage of Bi and Fe were not averaged, and will be presented area per area.

The iron and bismuth precursor were introduced with a molar ratio Fe/Bi = 10, which is equivalent to an atomic percentage of $91\%_{Fe}$ and $9\%_{Bi}$. EDS analyses show that Bi is not homogeneously distributed in the sample, however, it is hard to distinguish the bismuth-rich area (Figure 3.9).

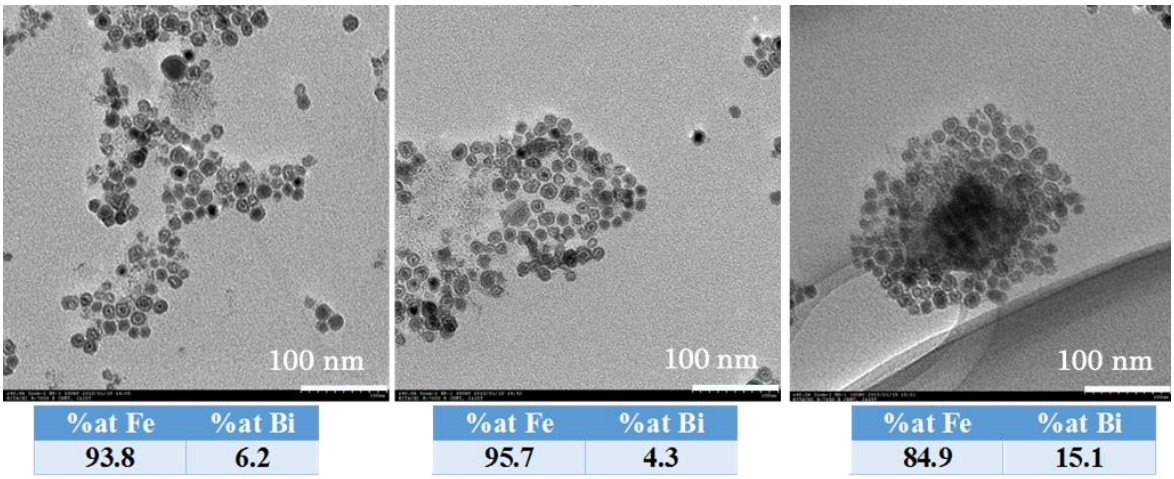

%at Fe	%at Bi
93.8	6.2

%at Fe	%at Bi
95.7	4.3

%at Fe	%at Bi
84.9	15.1

Figure 3. 9 *TEM micrographs of areas of FeBi_A sample where EDS analyses were performed, with the corresponding atomic percentage of Fe and Bi.*

Figure 3.10 presents the Fe and Bi elemental mapping data for an ensemble of three particles, and two single particles. The images provided clear evidence of an iron core, and demonstrated that iron is also present in the shell but in a lesser extent, which is consistent with a $Fe@Fe_3O_4$ core@shell structure. From the images of the two single particles, it seems that some bismuth is also homogeneously distributed in the shell of the nanoparticles. However, the quantity of bismuth in the shell does not seem enough to match the initial feeding ratio in the synthesis, maybe indicating that bismuth ions were not entirely reduced during the synthesis, or some bismuth nanoparticles nucleate separately from the iron seeds. This hypothesis would explain the non-homogeneous distribution of Bi throughout the sample observed with EDS analyses, even though no separate Bi NPs could be observed on the TEM images. Moreover, on the image showing an ensemble of

three particles, it can clearly be observed that some bismuth atoms are also located where there is not any particle.

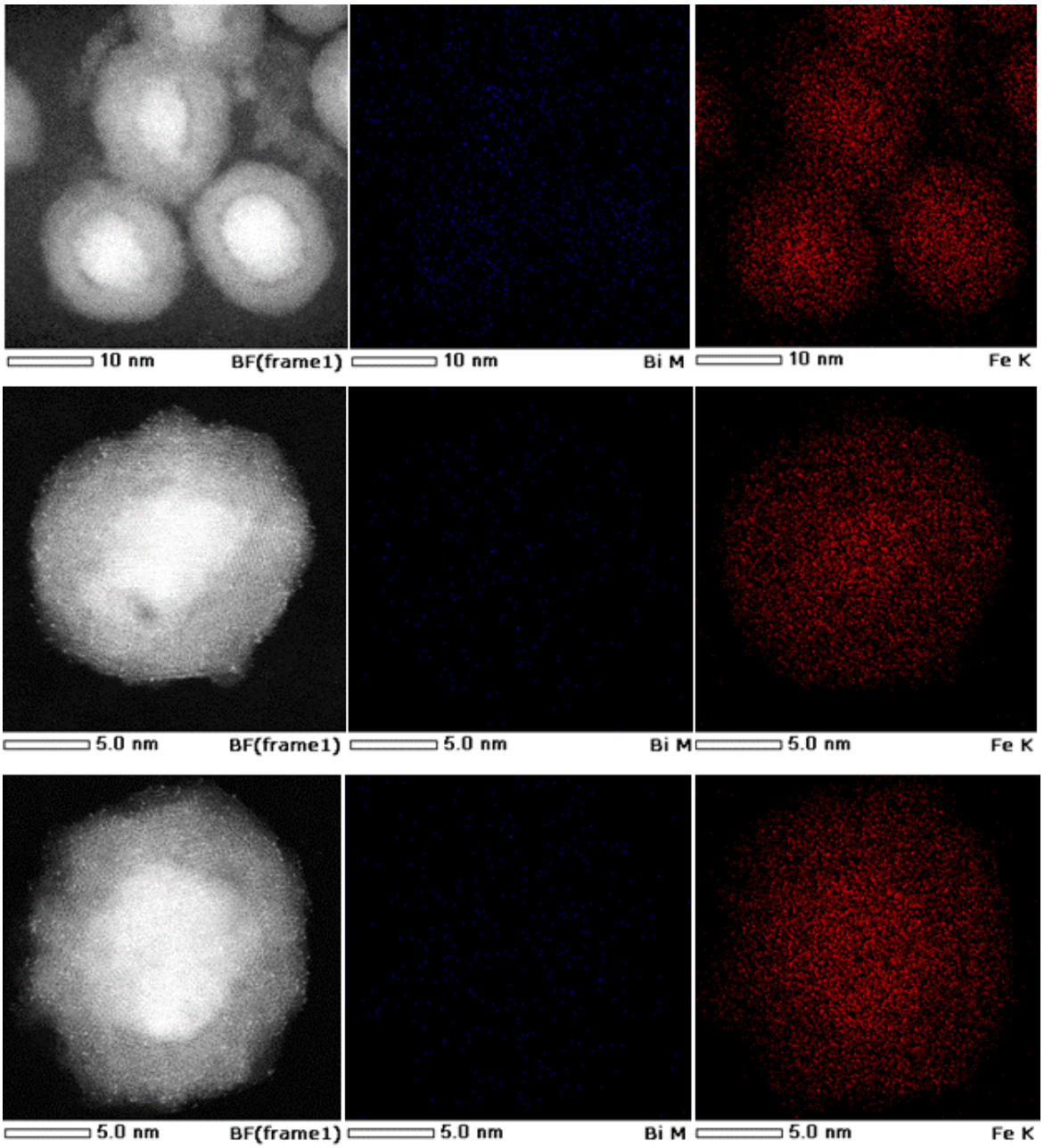

Figure 3. 10 *Local elemental mapping of FeBi_A NPs. Left: Bright field image; middle: Bi mapping; right: Fe mapping.*

Analysis of high resolution TEM images gave further information on the nature and structure of the nanodomains. Investigations of the outer shell of the particles evidence a polycrystalline shell (Figure 3.11). Lattice planes were observed in both the core and the shell of the particles. Spacing of the core lattice planes was found to be 2.0255 Å, which corresponds to the bcc crystalline structure of iron (Table 3.3). Spacing of the shell lattice

planes in two different crystalline domains were found to be 4.939 Å and 2.661 Å, which is close to the values of the cubic crystalline structure of magnetite (Table 3.3).

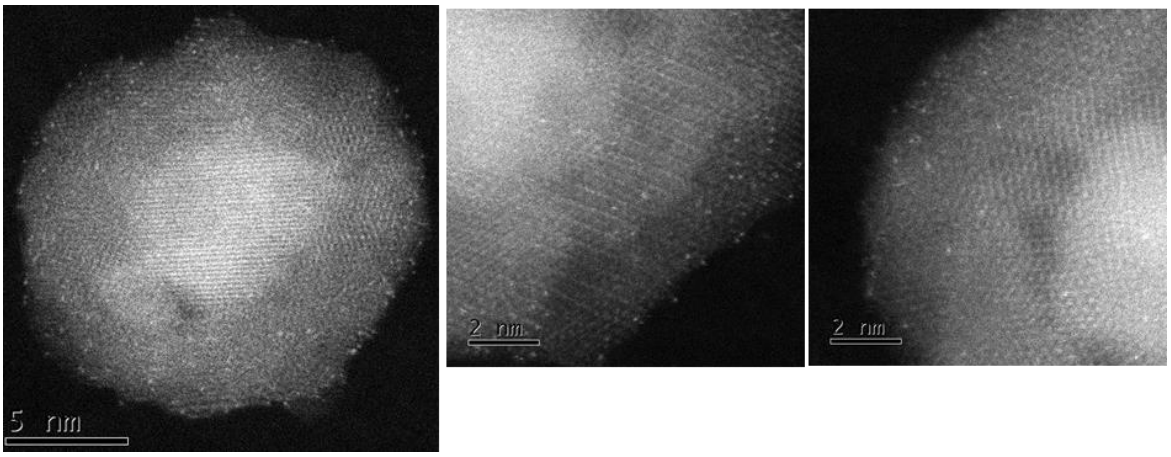

Figure 3. 11 *High resolution TEM images of FeBi_A NPs. Left: entire isolated particle; middle and right: shell.*

Table 3. 3 *Lattice fringe parameters of different materials containing Fe and/or Bi (obtained from their respective PdF card).*

Material	Plane	Lattice fringe (Å)
Fe	110	2.0268
Fe3O4	111	4.852
	222	2.426
Fe2O3	111	4.822
BiFeO3	110	2.7905
Bi	012	3.28
Bi2O3	120	3.255

By combining all those results together, the most likely hypothesis is that some bismuth atoms deposit on the surface of the iron seeds. However, at the end of the synthesis, the bismuth layer is not thick enough to protect iron against oxidation and therefore, a layer of iron oxide is formed when the nanoparticles are exposed to air. The rest of the bismuth may be nucleating in separated particles, however their observation on TEM images was not possible. Another explanation is that all the Bi ions are not entirely reduced into bismuth metal during the synthesis, and the inhomegeneous dispersion of Bi in the sample could be due to some remaining Bi-DT complex despite the washing steps.

Therefore, for the next experiments, the different synthetic conditions will be changed in order to study the influence of the reaction time after addition of the Bi-DT complex, of the decanethiol content and of the rate of addition of the Bi-DT complex.

3.3.4.2 Influence of the reaction time after addition of the Bi-DT complex

To study the influence of the reaction time after addition of the Bi-DT complex, the time was increased to 60 min as compared to 30 min used in the synthesis of FeBi_A (see Table 3.2 in section 3.2.3 for the experimental conditions used to synthesize FeBi_A and FeBi_B NPs).

XRD patterns of FeBi_B NPs and FeBi_A NPs are quite similar and show the presence of both cubic α-Fe and rhomboedral Bi crystalline phases (Figure 3.12).

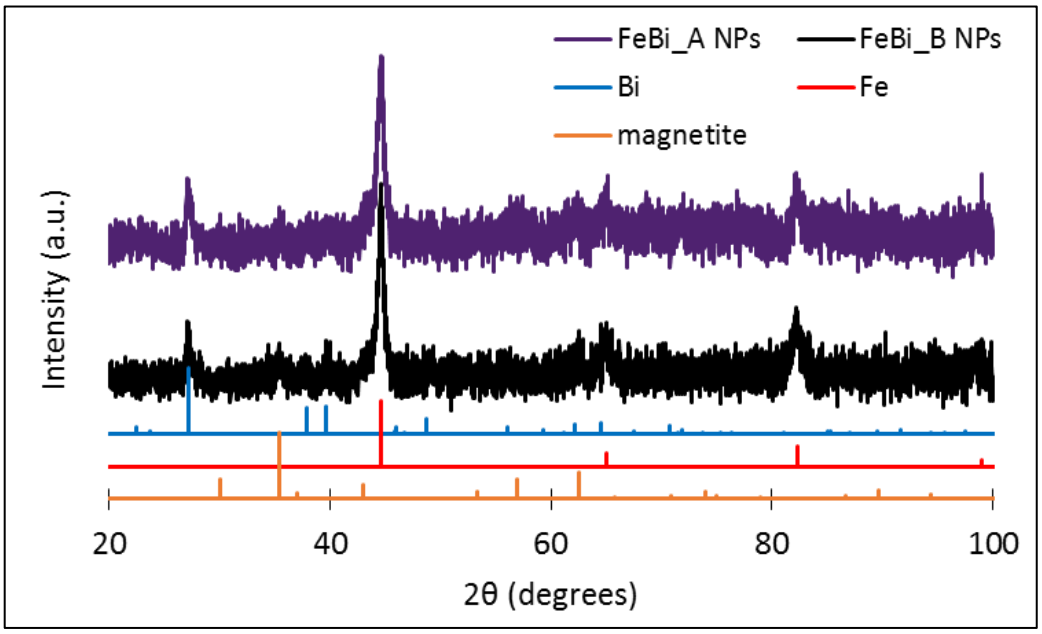

Figure 3. 12 *XRD pattern of the FeBi_A and FeBi_B NPs. Peaks were indexed according to the reference patterns for bismuth (pdf ref. 00-005-0519), iron (pdf ref. 00-006-0696), and magnetite (pdf ref. 00-019-0629).*

The crystallite size for FeBi_B NPs calculated from the XRD pattern were D_{Fe} = 12.4 nm and D_{Bi} = 16.5 nm. An increase in the crystallite size of iron as compared to FeBi_A sample was observed but the crystallite size of bismuth remained similar. Such as for FeBi_A NPs, the intensity of the main bismuth peak was very low. In fact, the XRD patterns of the two samples were very similar: no significant difference in the peak intensities or peak positions could be observed. As such, an increase in the reaction time did not seem to have any influence on the second step of the reaction (i.e. the reduction of bismuth ions into bismuth metal to form a bismuth shell on the already formed iron nanoparticles). Therefore, the hypothesis of the bismuth ions not being entirely reduced after 30 min of reaction could be

discarded, as no change is observed by increasing the reaction time. Moreover, given the high reduction potential of bismuth, it seems unlikely that the Bi ions would not be entirely reduced after 1 h of reaction at a temperature of 180 °C.

Figure 3.13 shows TEM images of the FeBi_B NPs. The NPs have a spherical morphology and a core@shell structure.

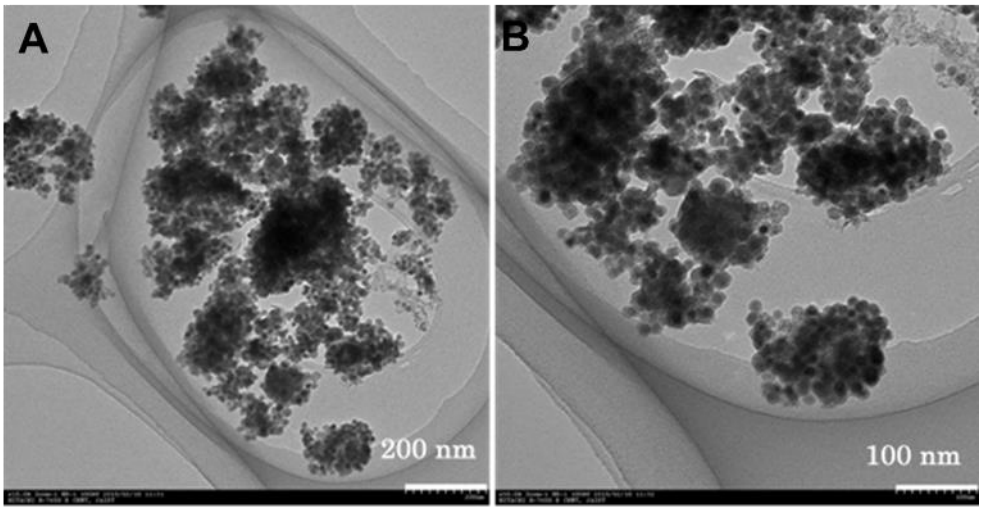

Figure 3. 13 *TEM micrographs of FeBi_B NPs A) at low magnification and B) higher magnification.*

Figure 3.14 represents the quantitative atomic percentage of iron and bismuth obtained from EDS analysis, as well as the TEM images of the areas where EDS was performed. Again, because the composition of the sample did not seem to be homogeneous, the atomic percentages of Bi and Fe were not averaged, and will be presented area per area. The distribution of bismuth in the sample was not homogeneous and considering the initial feeding ratio, was lower than the expected atomic percentage of 9%. All the results obtained for FeBi_B sample were similar to those obtained for FeBi_A sample.

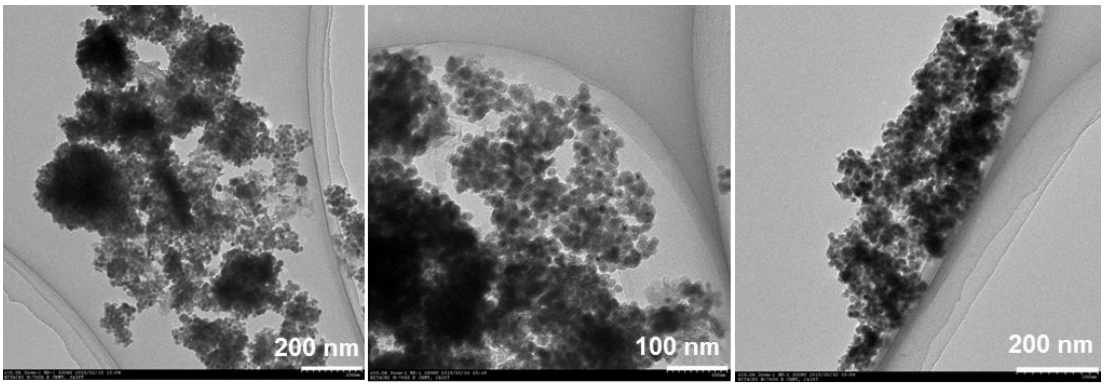

%at Fe	%at Bi
96.1	3.9

%at Fe	%at Bi
92.8	7.2

%at Fe	%at Bi
97.7	2.3

Figure 3. 14 *TEM micrographs of areas of FeBi_B sample where EDS analyses were performed, with the corresponding atomic percentage of Fe and Bi.*

We can conclude that increasing the second step time does not seem to have much influence on the synthesized nanoparticles. At this point, it is most likely that Bi nucleates into separated particles. Indeed, due to the quick reduction process of bismuth, the Bi ions do not necessarily have the time to reach the Fe nanoparticle surfaces, and therefore nucleate into separate particles. Though no particles different from the core@shell nanoparticles could be observed on the TEM images, one should keep in mind that bismuth was introduced in a lesser amount than iron, therefore meaning that the number of bismuth nanoparticles would be much lower than the iron ones, and from the crystallite size obtained by XRD, the bismuth nanoparticles would be only a few nanometers bigger than the iron nanoparticles. Therefore, as the aggregation of the core@shell nanoparticles is quite important in those samples, the bismuth particles could easily be hidden in the high aggregation area, making their observation challenging.

To conclude this section, increasing the reaction time of the second step did not change significantly the properties of the resulting particles. Therefore, the reaction time of the second step will be kept to 30 min in the next experiments.

3.3.4.3 Influence of the decanethiol concentration

As already mentioned previously, the synthesised nanoparticles were not stable in hexane suspension, which makes their observation challenging with TEM samples. In an attempt to tackle this issue, the amount of decanethiol in the formation of the Bi-DT complex was increased (molar ratio 1:12) as compared to the amount used in the synthesis of FeBi_A (molar ratio 1:4), and the effect of the decanethiol concentration on the resulting nanoparticles was studied (see Table 3.2 in section 3.2.3 for the experimental conditions used to synthesize FeBi_A and FeBi_C NPs).

XRD patterns of FeBi_A and FeBi_C NPs presented in Figure 3.15 show the presence of both cubic α-Fe and rhomboedral Bi crystalline phases.

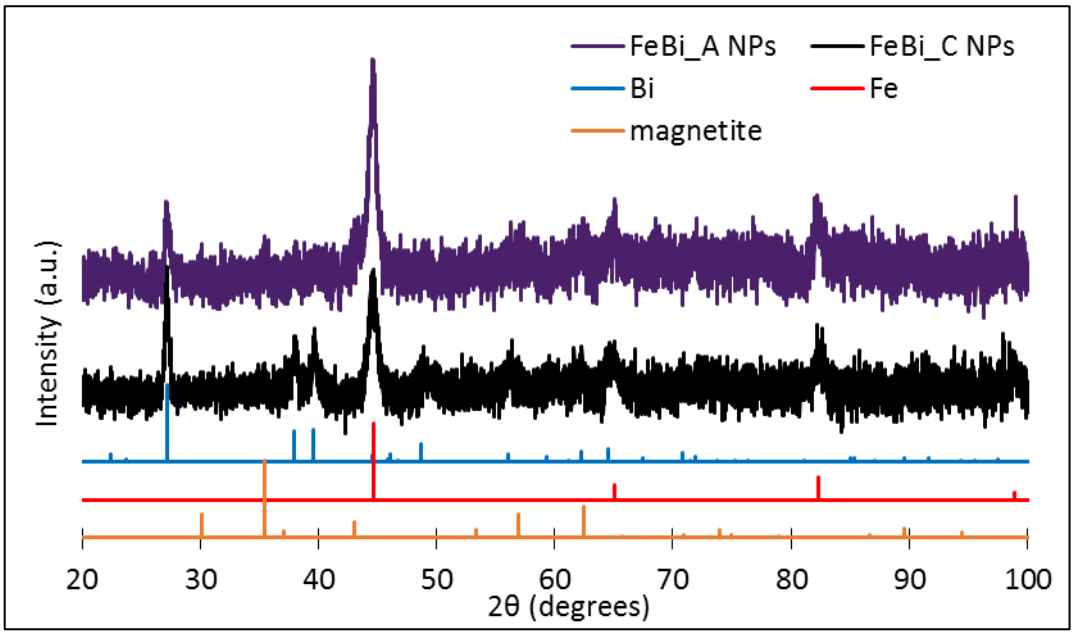

Figure 3. 15 *XRD pattern of the FeBi_A and FeBi_C NPs. Peaks were indexed according to the reference patterns for bismuth (pdf ref. 00-005-0519), iron (pdf ref. 00-006-0696), and magnetite (pdf ref. 00-019-0629).*

The crystallite size calculated from the XRD pattern for FeBi_C NPs were D_{Fe} = 10.8 nm and D_{Bi} = 23.9 nm. A significant increase in the bismuth crystallite size could be observed as well as an increase in the bismuth peak intensities. Increasing the decanethiol concentration may facilitate the reduction of bismuth ion into crystalline bismuth metal. However, such a big crystallite size cannot be representative of the shell of the NPs, therefore pointing in the directions of the formation of separated bismuth particles.

TEM images of the FeBi_C sample show the presence of dark sheets and spherical core@shell NPs (Figure 3.16).

In order to identify what the dark sheets are made of, EDS analyses were performed on the sample (Figure 3.17).

From the resulting atomic percentages, the dark sheets were identified as an iron sulfide phase with an amorphous structure as it does not appear on the XRD pattern. Indeed, decanethiol is a source of sulfur, and those sheets were not observed when using a smaller amount of decanethiol. Again the obtained atomic percentages for the different elements show an inhomogeneous distribution of bismuth throughout the sample, with high concentration areas and low concentration areas. However, it is hard to distinguish where the bismuth is located in the sample, due to particle agglomeration and the presence of the dark sheets.

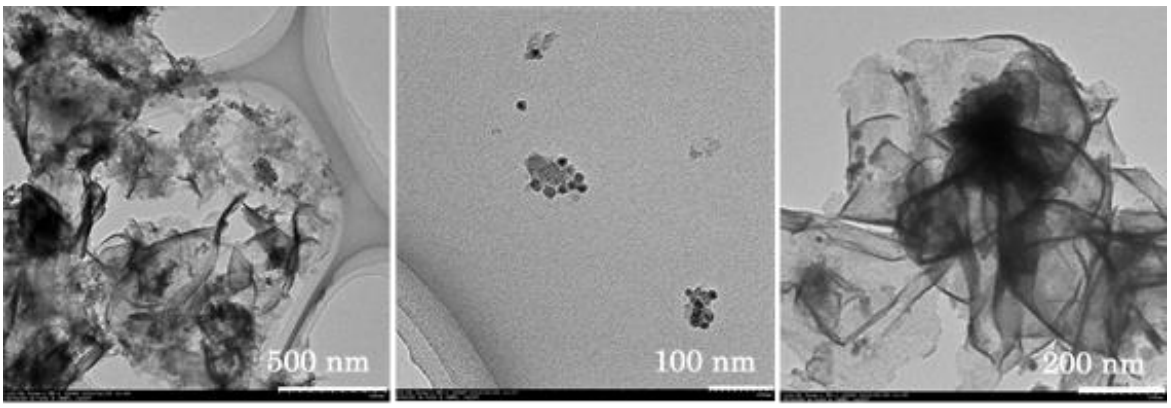

Figure 3. 16 *TEM micrographs of FeBi_C sample. Both dark sheets and nanoparticles can be observed.*

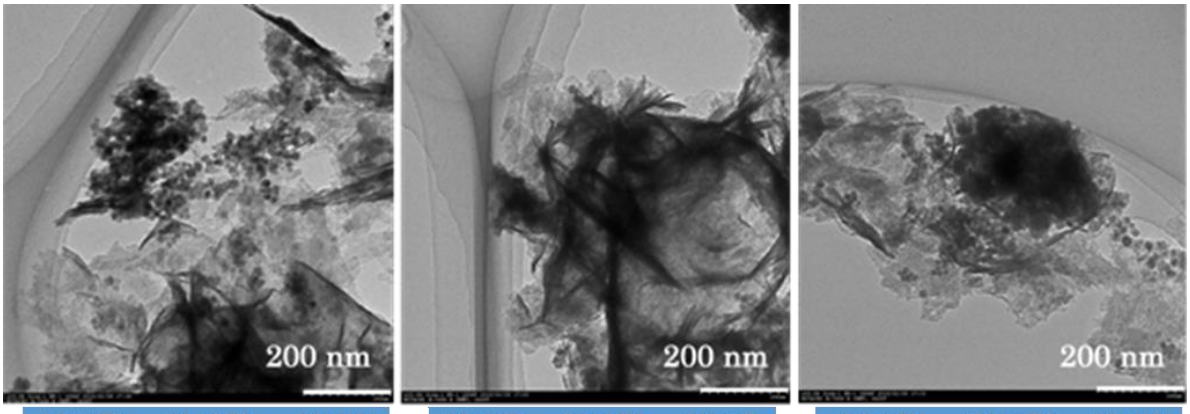

%at Fe	%at Bi	%at S
62.5	0.9	36.6

%at Fe	%at Bi	%at S
55.9	0.7	43.4

%at Fe	%at Bi	%at S
61.5	16.6	21.9

Figure 3. 17 *TEM micrographs of areas of FeBi_C where EDS analyses were performed, with the corresponding atomic percentage of Fe, Bi and S.*

Using a high amount of decanethiol in the Bi-DT complex leads to the formation of amorphous iron sulfide sheets and does not help in the stabilisation of the particles. As the formation of this iron sulfide phase is not desired, we can conclude that using a molar ratio of 1:12 for the formation of the Bi-DT complex is not an appropriate condition for the synthesis. In the next experiments, the amount of decanethiol used for the preparation of the Bi-DT complex will be kept as initially chosen (molar ratio of 1:4).

3.3.4.4 Influence of the rate of addition of the Bi-DT complex

In this section, we controlled the rate of addition of the Bi-DT complex in an attempt to suppress the separated growth of the bismuth nanoparticles, and promote the growth of a bismuth shell on the already formed Fe NPs. To that aim, the Bi-DT complex was added dropwise at different rate, using a syringe pump, to manipulate the reaction kinetic. Table 3.4 summarizes the different conditions used for the syntheses.

Table 3. 4 *Reminder of the experimental conditions used to synthesize FeBi_D, FeBi_E, FeBi_F and FeBi_G nanoparticles.*

Sample	$BiCl_3$:DT (molar ratio)	Rate of inj Bi-DT complex (mL/hr)	T (°C)	t (min)
FeBi_D	1:4	30	180	30
FeBi_E	1:4	15	180	30
FeBi_F	1:4	10	180	30
FeBi_G	1:4	10	160	30

For each synthesis, XRD patterns show the presence of both cubic α-Fe and rhomboedral Bi crystalline phases (Figure. 3.18).

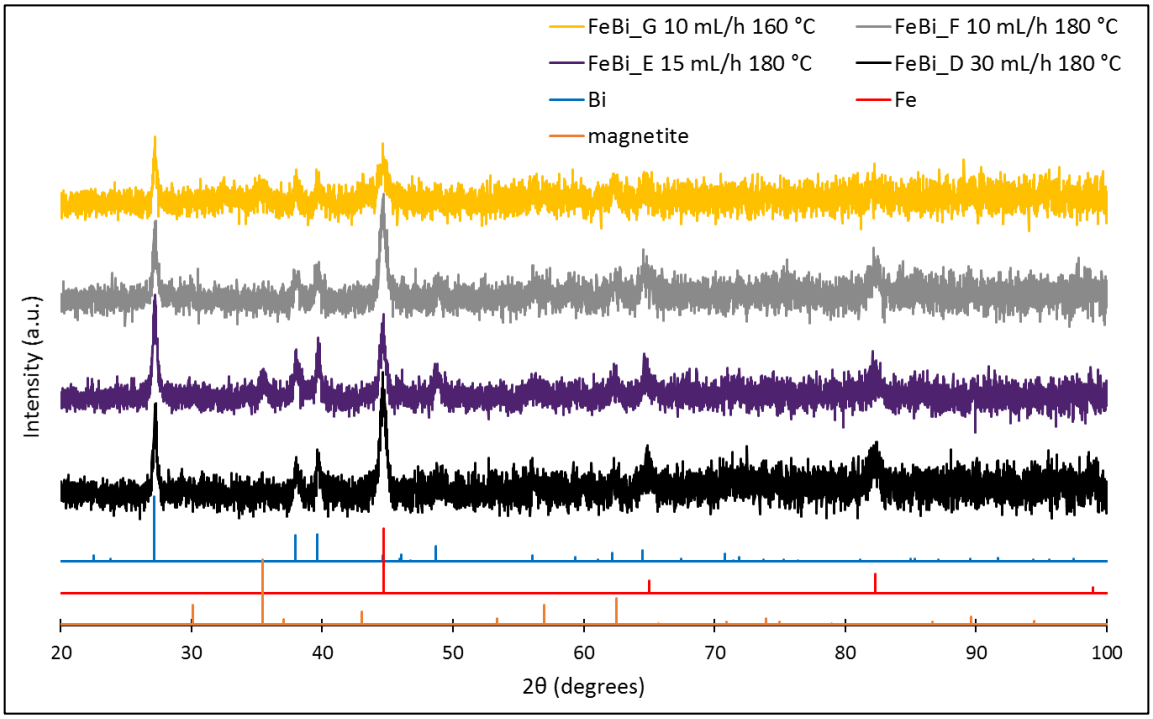

Figure 3. 18 *XRD pattern of the FeBi_D, FeBi_E, FeBi_F and FeBi_G NPs. Peaks were indexed according to the reference patterns for bismuth (pdf ref. 00-005-0519), iron (pdf ref. 00-006-0696), and magnetite (pdf ref. 00-019-0629).*

The crystallite size calculated from the XRD pattern for a rate of addition of the Bi-DT complex of 30 mL/hr, are D_{Fe} = 15.2 nm and D_{Bi} = 28.4 nm. By decreasing the addition rate to 15 mL/hr, the bismuth crystallite size decreased to D_{Bi} = 22.5 nm while the iron crystallite size increased to D_{Fe} = 16.8 nm. This result is encouraging, as a decrease in the bismuth crystallite size could indicate that a larger proportion of bismuth grows on the iron nanoparticles instead of nucleating separately. However, this trend is not followed in the two next syntheses, as decreasing further the addition rate to 10 mL/hr does not influence the resulting grain sizes (D_{Fe} = 15.6 nm and D_{Bi} = 22.2 nm). By decreasing the temperature

at which the Bi-DT complex is added to slow down the kinetic of reduction of bismuth, a decrease in the Bi and Fe peaks intensities is observed, and the Bi crystallite size seems to increase again while the one of iron decreases (D_{Fe} = 13.7 nm and D_{Bi} = 27.2 nm). Thus, no logical trend can be concluded from those results.

Figure 3.19 represents the TEM images of the different samples. The NPs look similar for all samples, they are spherical and possess a core@shell structure. The high agglomeration state of the nanoparticles makes the observation of the samples difficult.

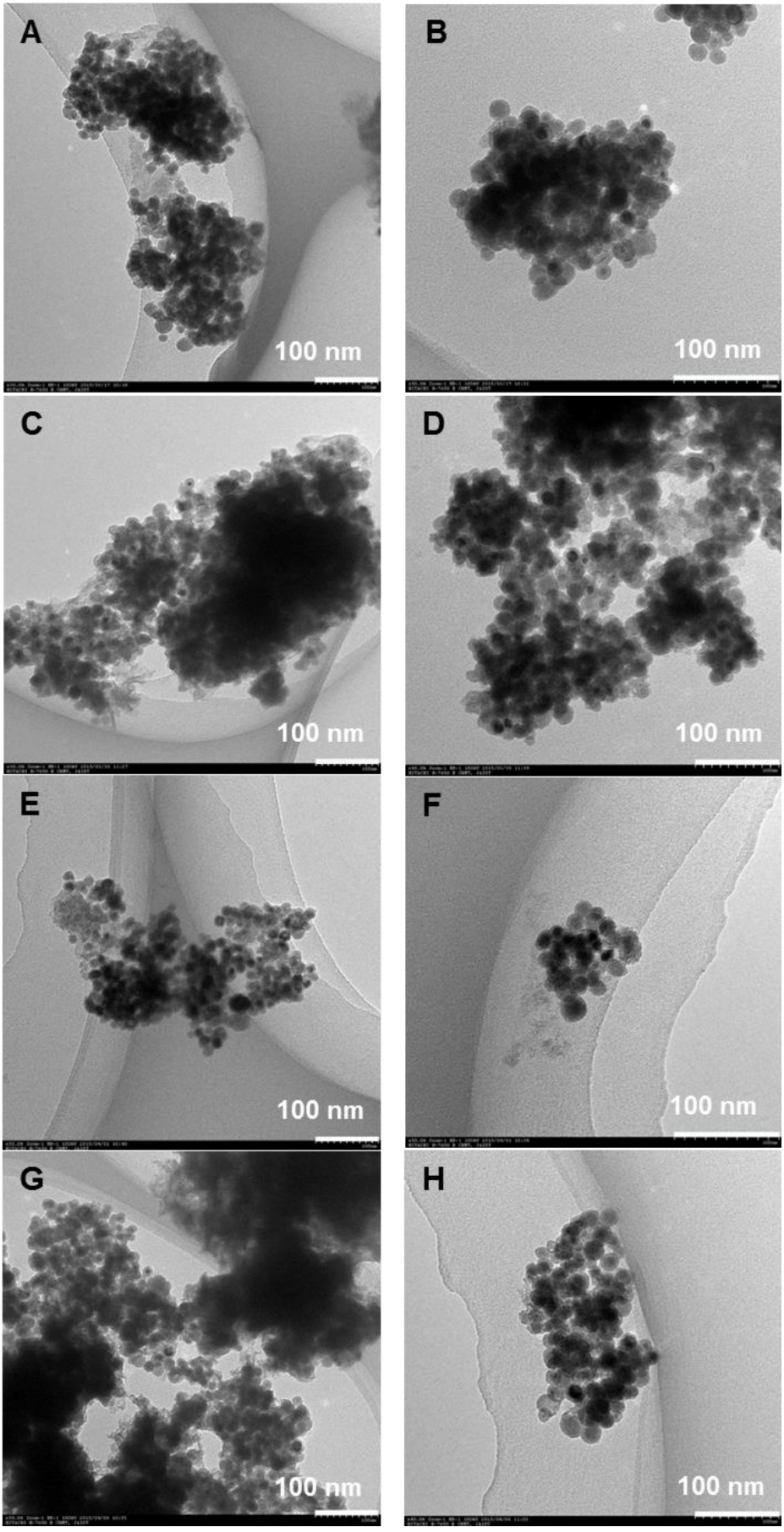

Figure 3. 19 *TEM micrographs of A), B) FeBi_D NPs, C), D) FeBi_E NPs, E), F) FeBi_F NPs and G), H) FeBi_G NPs.*

The quantitative atomic percentage of iron and bismuth were measured with EDS analysis for the samples FeBi_D, FeBi_E, FeBi,F and FeBi_G. Again, because the composition of the samples did not seem to be homogeneous, the atomic percentage of Bi and Fe were not averaged, and will be presented area per area.

EDS analysis reveals a completely inhomogeneous repartition of Bi in the sample FeBi_D (Figure 3.20). However, nothing particular or different from the rest of the sample could be observed in the image with the high Bi concentration area (left image).

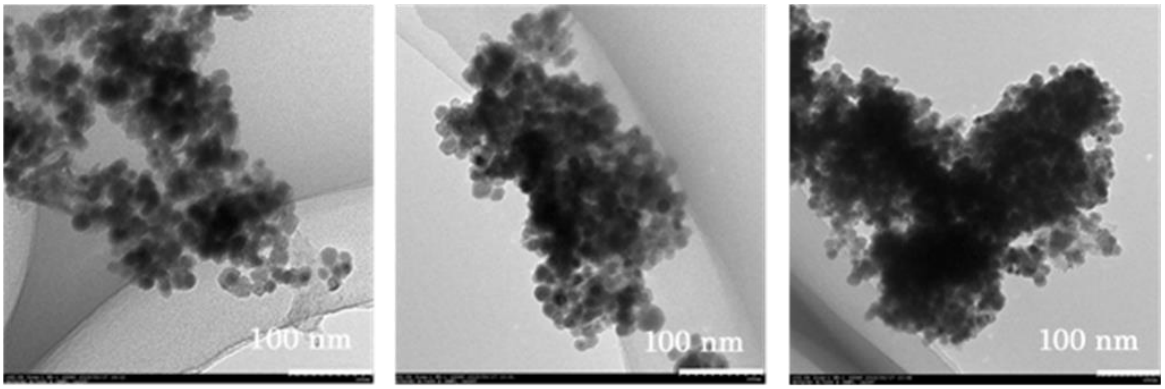

%at Fe	%at Bi
42.7	57.3

%at Fe	%at Bi
99.7	0.3

%at Fe	%at Bi
96.6	0.4

Figure 3. 20 *TEM images of areas of FeBi_D where EDS analyses were performed and their corresponding atomic percentage of Bi and Fe.*

In the sample FeBi_E, areas containing bismuth such as in the middle image which is only composed of a few nanoparticles could be observed, but no distinct bismuth particles can be identified, which could lead to think that bismuth is equally present on each core@shell nanoparticle. On the other hand, a big agglomerate such as in the right TEM image, barely contains any bismuth, which therefore is more coherent with the opposite explanation: bismuth forms separated particles (Figure 3.21).

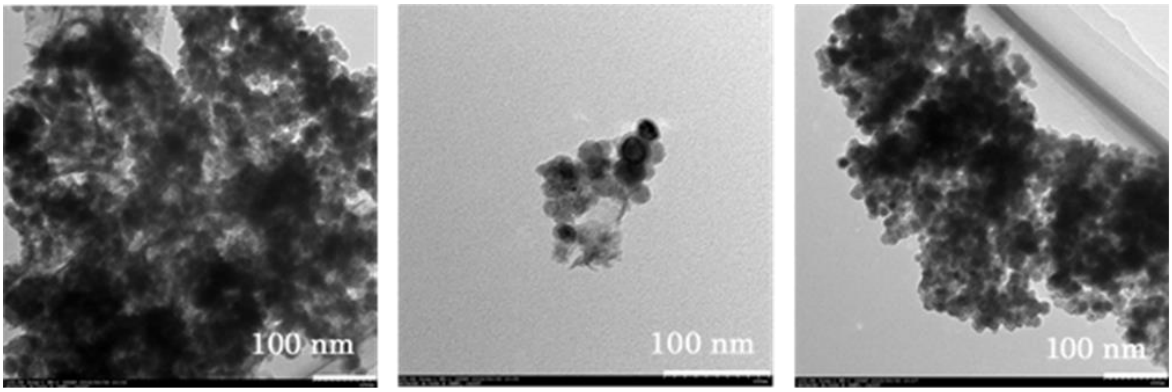

%at Fe	%at Bi
90.8	9.2

%at Fe	%at Bi
93.8	6.2

%at Fe	%at Bi
98.6	1.4

Figure 3. 21 *TEM images of the areas of FeBi_E where EDS analyses were performed, and their corresponding atomic percentage of Bi and Fe.*

Again, in sample FeBi_F, areas with high and low concentration of bismuth could be observed (Figure 3.22). In the middle image where a high atomic percentage of bismuth was obtained, a particle of hexagonal shape - similar to the shape of the nanoparticles obtained with the Bi NPs synthesis (see section 3.3.2) - can be observed (circled in red).

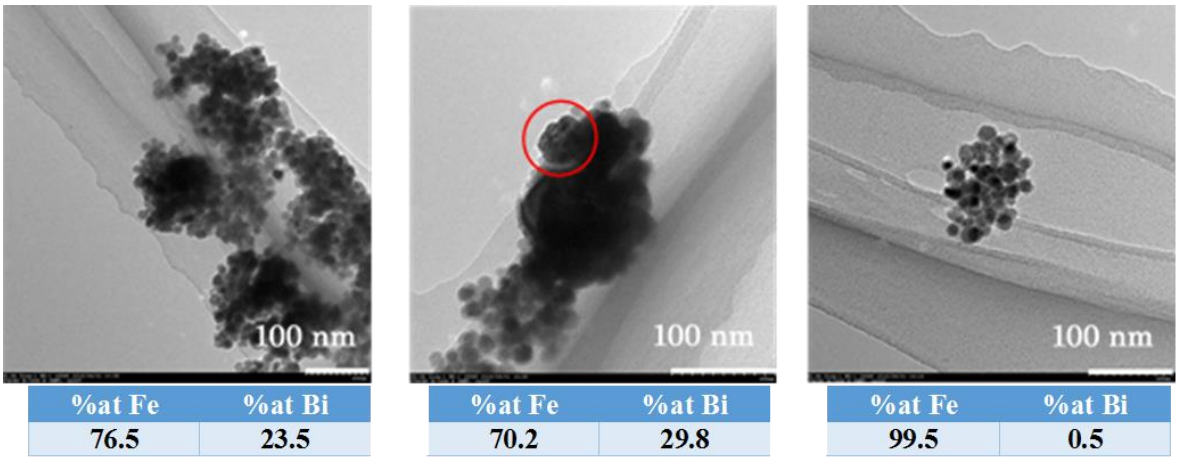

%at Fe	%at Bi
76.5	23.5

%at Fe	%at Bi
70.2	29.8

%at Fe	%at Bi
99.5	0.5

Figure 3. 22 *TEM images of areas of FeBi_F where EDS analyses were performed and their corresponding atomic percentage of Bi and Fe.*

The presence of areas with high and low concentration of bismuth were also observed in sample FeBi_G (Figure 3.23). Attempt to perform EDS analysis on a single particle was made (right image), which showed a low bismuth content.

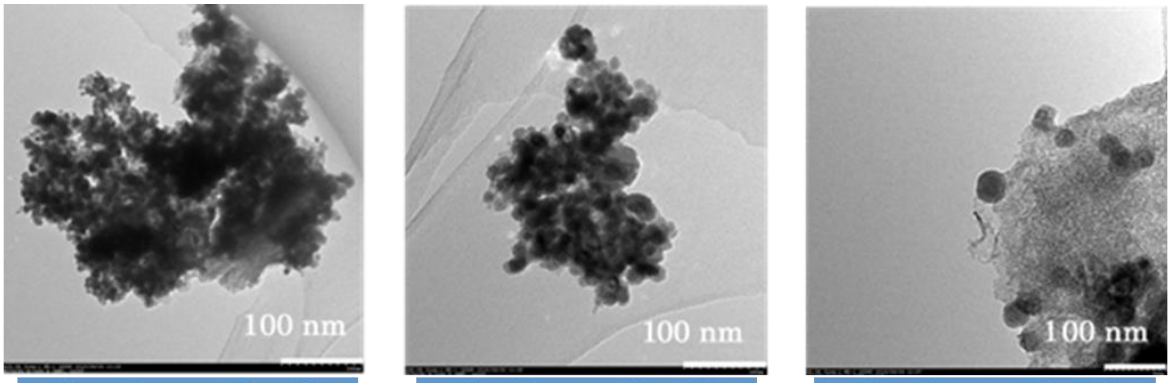

%at Fe	%at Bi
82.6	17.4

%at Fe	%at Bi
97.6	2.4

%at Fe	%at Bi
99.5	0.5

Figure 3. 23 *TEM images of the areas of FeBi_G where EDS analyses were performed and their corresponding atomic percentage of Bi and Fe.*

3.4 Conclusion

In summary, iron nanoparticles were found to be highly magnetic. This resulted in highly aggregated nanoparticles that made their observation by TEM challenging. Despite

numerous trials, the synthetic route chosen in this part of the work did not appear to be successful for the synthesis of Fe@Bi core@shell NPs. Adding the Bi precursor slowly dropwise did not help in suppressing the separated growth of Bi particles. Table 3.5 summarizes the crystallite sizes for Fe and Bi obtained with the different synthesis. In fact, the best results, (i.e. the smallest Bi grain sizes and most homogeneous distribution of Bi in the sample observed with EDS) were obtained for samples FeBi_A and FeBi_B where the Bi-DT complex was added in one go.

Table 3. 5 *Summary of Fe and Bi crystallite grain size obtained by varying the synthetic parameters.*

Sample	T (°C)	Rate inj (mL/hr)	Time (min)	$D_{XRD\ Bi}$ (nm)	$D_{XRD\ Fe}$ (nm)
FeBi_A	180	/	30	16.2	11.0
FeBi_B	180	/	60	16.5	11.8
FeBi_D	180	30	30	28.4	15.2
FeBi_E	180	15	30	22.5	16.8
FeBi_F	180	10	30	22.22	15.6
FeBi_G	160	10	30	27.2	13.7

While interpreting the results was not easy, the most likely hypothesis even in the case of samples FeBi_A and FeBi_B is that two types of particles having roughly the same sizes are obtained: Bi NPs and Fe@Fe_3O_4 core@shell NPs containing small amount of bismuth in the outer shell.

CHAPTER 4

SYNTHESIS AND FUNCTIONALISATION OF IRON OXIDE NANOPARTICLES FOR THERMO-CHEMOTHERAPY

4.1 Introduction

In the previous chapter, despite the different attempts made, the synthesis of NPs with a high magnetic moment composed of an iron core and a bismuth shell was found to be unsuccessful. In order to be able to make progress towards the main goal of the study, that is to develop a magnetic nanocarrier for hyperthermia therapy and drug delivery, it has been decided that iron oxide nanoparticles will be used to develop the desired nanocarrier. Iron oxide nanoparticles may not have as much heating potential as iron nanoparticles do for hyperthermia therapy, but yet they have many advantages for their use in biomedical applications, such as chemical stability, biocompatibility and their ease of synthesis.

In this chapter, the synthesis of iron oxide nanoparticles by a microwave-assisted co-precipitation method previously developed in our lab was adapted for the purpose of this work. The thermo-responsive polymer composed of four main blocks p(DEGMA-co-PEGMA-b-[TMSPMA-co-VBA]), was synthesized by RAFT polymerisation and then grafted onto the iron oxide nanoparticle surface via a silanisation reaction using a modified Stöber method. The functionalisation protocol was optimized by varying the MNPs to polymer ratio and the pH of the solution. The nanoparticles were characterized by XRD, TEM, DLS, FTIR and TGA and their potential as agents for magnetic hyperthermia was evaluated. Finally, doxorubicin was loaded into the nanosystem via formation of pH-cleavable imine bonds between the amine group of doxorubicin and the aldehyde group of the polymer. The drug release kinetics were carefully studied as a function of the pH and the temperature.

4.2 Materials and methods

4.2.1 Reagents

Iron(II) chloride tetrahydrate ($FeCl_2 \cdot 4H_2O$, purity 99%), iron(III) chloride hexahydrate ($FeCl_3 \cdot 6H_2O$, >99%), sodium carbonate (Na_2CO_3, 99%), hydrochloric acid (HCl, 37 vol%), poly(ethylene glycol) methyl ether methacrylate (PEGMA, $H_2C=C(CH_3)CO_2(CH_2CH_2O)_nCH_3$, Mn = 300 g/mol), di(ethylene glycol) methyl ether methacrylate (DEGMA, $H_2C=C(CH_3)CO_2(CH_2CH_2O)_2CH_3$, 95%), 3-(trimethoxysilyl)propyl methacrylate (TMSPMA, $C_{10}H_{20}O_5Si$, 98%), 3-vinylbenzaldehyde (VBA, C_9H_8O, 97%), 4,4'-azobis(4-cyanovaleric acid) (ACVA, $C_{12}H_{16}N_4O_4$, ≥75%), 4-cyano-4-(phenylcarbonothioylthio)pentanoic acid (CPPA, $C_{13}H_{13}NO_2S_2$, 97%), chloroform-d NMR solvent ($CDCl_3$, 99.8 atom % D), triethylamine (TEA,

$C_6H_{15}N$, 98%), acetonitrile (C_2H_3N, 99.8%), toluene (C_7H_8, 99.8%), petroleum ether, sodium phosphate monobasic (NaH_2PO_4, 99%) and sodium phosphate dibasic (Na_2HPO_4, ≥99%) were purchased from Sigma Aldrich. Tetrahydrofuran (THF, C_4H_8O, stabilizer free, 99.8%) was provided from Wako Chemicals. Ethanol (EtOH, 99.5 % or 100%) was obtained from Nacalai Tesque Japan or from Hayman, UK. All the reagents were used as purchased without any further purification. The Spectra/Por Biotech grade dialysis membranes were obtained from SpectrumLabs and the Slyde-A-Lyzer (SAL) dialysis cassettes were obtained from Thermo Fischer Scientific.

4.2.2 Experimental methods

4.2.2.1 Synthesis of the copolymer P(DEGMA-*co*-PEGMA-*b*-[TMSPMA-*co*-VBA])

The P(DEGMA-*co*-PEGMA-*b*-[TMSPMA-*co*-VBA]) polymer was synthesized by reversible addition fragmentation chain transfer (RAFT) polymerization according to a previous publication with some modifications.[275]

4.2.2.1.1 Step 1: copolymerization of the two PEG chains

The PEGMA and DEGMA monomers were mixed in different molar ratios (for the study of the LCST) with the CPPA as the RAFT chain transfer agent and ACVA as the initiator (molar ratio CPPA:ACVA 5:1). Under Ar atmosphere, anhydrous acetonitrile was added to the flask and the mixture was degassed by bubbling Ar for 30 min. After degassing, the mixture was heated to 70 °C and maintained at this temperature for 5 h. The resulting polymer was then washed several time using petroleum ether and dried under vacuum overnight.

4.2.2.1.2 Step 2: chain extension

A chain extension was then carried out by mixing the dry P(DEGMA-*co*-PEGMA) polymer used as macro-RAFT agent with ACVA initiator (ratio 5:1), TMSPMA and VBA in toluene. The two monomers were added in a molar ratio of 1:4. This mixture was then degassed under Ar and heated to 90 °C for 4 h. The resulting polymer was again purified by precipitation in petroleum ether, and dried under vacuum.

4.2.2.1.3 Measurement of the LCST

The LCST of the polymer in aqueous solution was determined by UV-Vis spectroscopy using a JASCO V-630 spectrophotometer equipped with an EYELA NCB-1200 temperature controller. The solution was heated from 25 °C to 47 °C whilst the transmittance was recorded

at 540 nm. The LCST value was interpreted as the temperature at which the solution transmittance reached 80%.

4.2.2.2 Synthesis of bare iron oxide nanoparticles

IONPs were synthesized following a modified procedure consisting of microwave-assisted co-precipitation of Fe(II) and Fe(III) salts with Na_2CO_3 and the aid of a SP-Discovery Microwave (CEM, USA).[276] In a typical synthesis, $FeCl_2 \cdot 4H_2O$ (0.4 mmol, 0.0795 g) and $FeCl_3 \cdot 6H_2O$ (0.8 mmol, 0.2162 g) were dissolved in 20 mL of Milli-Q water (Millipore, 18.2 MΩ/cm), transferred into a 35 mL microwave vial and sealed with a pressure cap. The solution was heated to 60 °C (300 W, power max on), and Na_2CO_3 aqueous solution (4 mL, 1 M, 0.4240 g) was added drop wise at a rate of 2 mL/min using a syringe pump. The solution was kept at this temperature for 20 min before allowing to cool down to room temperature. The NPs were then washed three times with ultrapure water by magnetic separation (Figure 4.1) and redispersed in ultrapure water for further use.

Figure 4. 1 *Photo of the washing step of the iron oxide nanoparticles by magnetic separation.*

4.2.2.3 Grafting of the copolymer onto the iron oxide nanoparticle surface

Functionalisation of the MNPs with the polymer P(DEGMA-*co*-PEGMA-*b*-[TMSPMA-*co*-VBA]) was carried out via a silanisation reaction between the trimethoxysilane groups of the polymer and the hydroxyl groups naturally present on the surface of the bare IONPs, forming a covalent Si-O-Fe bond. The functionalisation parameters were optimized to find the best conditions. Typically, freshly synthesized naked IONPs were sonicated for 20 – 30 min in order to break all the aggregates that could have been formed. The IONPs were then mixed straightaway with the P(DEGMA-*co*-PEGMA-*b*-[TMSPMA-*co*-VBA]) copolymer dissolved in 20 mL of ethanol with different ratio w/w (Table 4.1). The mixture was acidified to a certain pH (Table 4.1) by

adding HCl 37%. The NPs suspension was then sonicated for 10 min and vigorously stirred at room temperature for 24 h. The copolymer-functionalized IONPs, hereafter referred to as magnetic nanocomposites (MNCs) were washed by magnetic separation twice with ethanol and once with ultrapure water before being redispersed in ultrapure water at a concentration of 10 mg/mL for further use.

Table 4. 1 *Experimental conditions used for the functionalisation of the iron oxide nanoparticles.*

Sample	pH	NPs:polymer ratio (w/w)
P-IO4,1:1	4	1:1
P-IO2,1:1	2	1:1
P-IO2,1:3	2	1:3
P-IO2,1:5	2	1:5
P-IO2,1:7	2	1:7

4.2.2.4 In vitro hyperthermia of the magnetic nanocomposites

Magnetic heating measurements were performed to assess the heating performances of the different nanocomposites using a magnetic alternating current hyperthermia (MACH) system (Resonant Circuit Ltd, UK). Preliminary experiments to assess which nanomaterials had the best heating potential were performed at an operating frequency f = 970 kHz and field amplitude H = 6.8 kA/m. Samples made of 0.5 mL of MNCs dispersed in water with a concentration of 3 mg/mL were placed in the middle of the coil. The increase in temperature was continuously logged using fibres optic probes centred in the suspension. Two probes were used in order to limit possible errors coming from a non-homogeneous spatial heating of the suspension. The measurement was started when the temperature of the suspension was stabilised to room temperature, and the measurement time was limited to 10 min. Both the SAR and ILP parameters were calculated.

Once the nanomaterials with the best heating performances was identified, the SAR of the MNCs was also measured in biological media. In order to have conditions closer than what will be used for magnetic hyperthermia on cells, samples made of 0.5 mL of MNCs dispersed in biological media, i.e. Dubelcco's modified Eagles medium (DMEM) supplemented with 10% fetal bovine serum (FBS), at a concentration of 1 mg/mL were placed in the middle of the coil maintained at 37 °C, and subjected to an AMF of frequency f = 950 kHz and field amplitude H = 10.5 kA/m. These field conditions were used so that a higher temperature could be reached in a shorter amount of time. In order to verify that the

change of conditions do not influence the ILP, the same experiment was performed with the original frequency and field amplitude conditions of f = 970 kHz and H = 6.8 kA/m.

4.2.2.5 Preparation of the phosphate buffer solutions

Phosphate buffer solutions 0.01 M (PBS) at pH = 7.4 and pH = 5.7 were used in many experiments. A pH of 7.4 was used to mimic physiological condition while the pH of 5.7 was used to mimic acidic tumour environment.

Firstly, stock solutions of Na_2HPO_4 (base) and NaH_2PO_4 (acid) at a concentration of 0.1 M were prepared. For a volume of 100 mL, the stock solution of Na_2HPO_4 requires 1.42 g of Na_2HPO_4 to be dissolved in 100 mL of ultrapure water, and the stock solution of NaH_2PO_4 requires 1.20 g of NaH_2PO_4 to be dissolved in 100 mL of ultrapure water.

Preparation of 100 mL of PBS at pH = 7.4 was carried out as follows: 7.70 mL of Na_2HPO_4 (0.1 M) were mixed with 2.30 mL of NaH_2PO_4 (0.1 M) and diluted 10 times with ultrapure water. Similarly, 100 mL of PBS at pH = 5.7 was prepared as follows: 0.60 mL of Na_2HPO_4 (0.1 M) were mixed with 9.40 mL of NaH_2PO_4 (0.1 M) and diluted 10 times with ultrapure water.

The pH of both PBS solutions was then checked with a pH meter, and adjusted to the right pH values with diluted NaOH or HCl aqueous solutions if needed.

4.2.2.6 Colloidal stability of the magnetic nanocomposites

Colloidal stability of the MNCs in an aqueous dispersion over time was investigated by monitoring the hydrodynamic size of the MNCs using the dynamic light scattering technique throughout 14 days after being synthesised. Effect of pH on the stability of the MNCs was also assessed as well as the colloidal stability of the MNCs in phosphate buffer solutions and in biological media in the presence of serum.

4.2.2.7 Working with DOX: risks and safety precautions

DOX is an antineoplastic agent classified as anthracycline antibiotic that has been used to treat many cancers such as leukaemia, breast, ovarian, bladder, lung cancers and more. DOX can have severe side effects such as acute and chronic toxic effects (cardiotoxicity, dermatitis, anemia, skin and eye tissue vesication, and it is also embryotoxic, carcinogenic, teratogenic

and mutagenic. Therefore, protective equipment when handling DOX must be worn such as gloves, safety goggles, lab coat and complete coverage of skin

4.2.2.8 Determination of DOX calibration curves for UV-vis and study of the photodegradation of DOX with time

To be able to find the concentration of DOX in PBS at pH = 5.7 and PBS at pH = 7.4 by UV-vis, calibration curves of DOX in each media must be determined. The absorption of DOX solution of known concentration in each media (i.e. 1, 2, 8, 12, and 16 μg/mL) at a wavelength of 480 nm, which is the typical absorption for DOX, was measured. The absorption as a function of DOX concentration was recorded to generate the calibration curves.

DOX is a light-sensitive chemical. In order to study the photodegradation of DOX with time, the absorption of the DOX solutions of known concentrations in PBS at pH = 7.4 were recorded again 3 days later. The absorption as a function of DOX concentration was recorded and compared to the calibration curve to study the time-dependency of the absorbance of DOX.

4.2.2.9 Dialysis of free DOX

Because dialysis is the method used for the determination of the drug release behaviour, dialysis of free DOX was performed as preliminary experiments. Dialysis rests on the principle of diffusion of solutes, which is that substances in solution tends to naturally move from an area of high concentration to an area of low concentration to make a homogeneous system. Dialysis also uses the principle of ultrafiltration, where the concentration gradients lead to a separation through a semipermeable membrane. In dialysis, the donor solution containing the solutes is placed in the dialysis membrane, which is soaked in the receiver phase (Figure 4.2). Due to the concentration gradients, the solutes in the donor phase will pass through the membrane. By choosing appropriately the molecular weight cut-off (MWCO) of the dialysis membrane used during the dialysis experiment, solutes of higher molecular weights than the MWCO are retained in the dialysis bag, while lower molecular weight ones can pass through the membrane.

The main advantage of using dialysis to study the release behaviour of a drug from a nanosystem as compared to other conventional methods such as ultracentrifugation or magnetic separation, is that no additional step of separating nanoparticles from the free drug molecules at various time points is necessary. Indeed, by choosing the dialysis membrane judiciously, the nanoparticles are retained in the dialysis bag while only the

drug molecules can pass through. The concentration of the drug in the receiver phase can be analyzed at different time points to get the drug release profile.

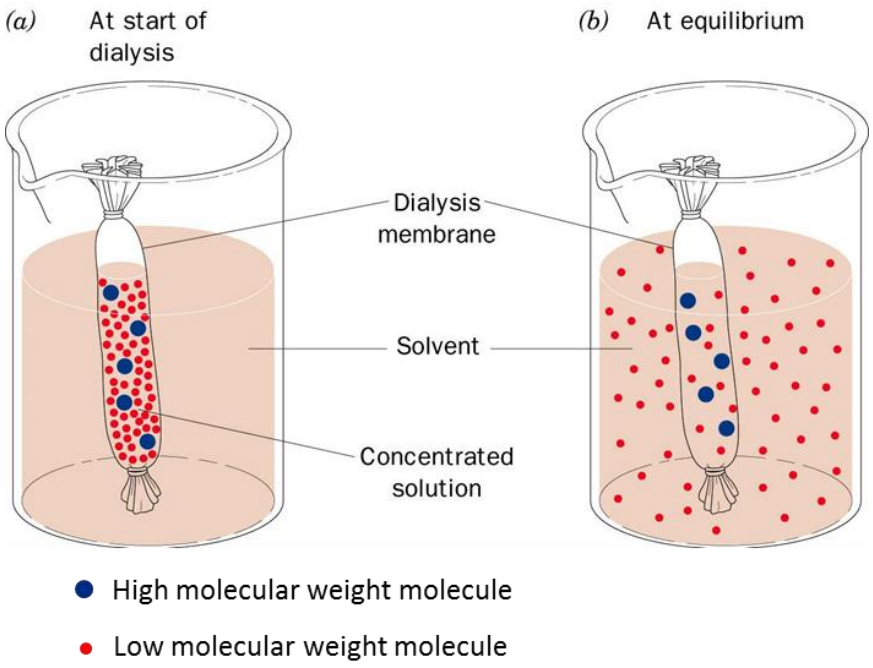

Figure 4. 2 *Schematic representation of a dialysis set-up (image taken and modified from* http://schoolworkhelper.net/selective-permeability-of-dialysis-tubing-lab-explained/*).*

However, with dialysis, one has to keep in mind that the apparent release rate is the net results of drug transport across two barriers: diffusion from the nanoparticles followed by diffusion across the dialysis membrane.[277,278] Therefore, the drug release profile obtained may not necessarily represent the rate of drug release from the nanoparticles, and it is important to assess in what extent the rate of drug transfer from the donor phase to the receiver phase is affected by the dialysis membrane. For that purpose, dialysis of free DOX was performed prior to the drug release experiments. Two parameters greatly influence the transport of the drug across the dialysis membrane: the solubility of the drug in the media and the MWCO of the membrane.[279] Indeed, the dialysis set up must respect sink conditions, meaning that as the drug dissolves, it is essential that the presence of the already dissolved drug in solution should not affect the ability of more drug to be dissolved in any way. The MWCO of the dialysis membrane must be at least high enough to permit drug transport. The higher the MWCO of the membrane, the easier is drug transport across the membrane.

According to Gupta *et al.*, the apparent permeation constant K_{CV} of the drug through the membrane can be determined by monitoring the DOX concentration in the receiver phase as a function of time, using the following equations:[280]

$$ln\ \left(m_0 - C_1(V_1 - V_2)\right) = ln\,(m_0) - K_{CV}t \quad (4.7)$$

With:

$$K_{CV} = \frac{kA(V_1 - V_2)}{V_1 V_2 \varepsilon} \quad (4.8)$$

Where m_0 is the total amount of drug in the system, C_1 is the drug concentration in the receiving phase, V_1 is the volume of the receiver phase, V_2 is the volume of the donor phase, k is the drug permeability constant of dialysis membrane, A is the surface area of the membrane and ε is the thickness of the membrane.

Thus, a plot of $ln\ (m_0 - C_1(V_1 + V_2))$ versus time would give a straight line with a slope equal to - K_{CV} and an intercept of $ln\ (m_0)$.

4.2.2.9.1 Dialysis of free DOX and determination of K_{CV} using a dialysis bag

This dialysis of DOX was performed using a dialysis membrane in regenerated cellulose with a 10 000 Da MWCO. A MWCO of 10 000 Da was found to be suitable for our system as the polymer used to functionalize the MNPs has a molecular weight higher than 10 000 Da, while DOX has a molecular weight of 543 Da. It is therefore small enough to retain the MNCs while letting the DOX molecules through the membrane easily.

Prior to the experiment, the dialysis membrane was immersed in the dialysis buffer for 48 h, and was replaced three times with fresh buffer, to remove the sodium azide preservative. One extremity of the membrane was tight up with elastic bands to make sure no solution could be leaking. A 4 mL solution of DOX in PBS (pH 7.4) at 16 µg/mL was introduced in the membrane, and the other extremity of the membrane was sealed with rubber bands to prevent any leak. The dialysis bag was soaked and dialyzed against 40 mL of PBS at pH = 7.4 under mild stirring in a polypropylene container. A receiver phase volume of 10 times that of the dialysis bag was chosen to ensure sink conditions for the DOX, while the absorbance of DOX in solution remains in the UV-vis detectable range. The dialysis setup was covered with foil to avoid any light degradation of the drug during the experiment. At predetermined time points (*i.e.* 0.25, 0.5, 0.75, 1, 2, 4, 8 and 10 h), 3 mL of dialysate were taken out for UV-visible spectroscopy, and replaced with 3 mL of fresh PBS to keep the total volume constant and preserve sink conditions. The DOX content of the extracted solution was measured by UV-visible spectrophotometry and the diffusion profile of DOX through the dialysis membrane was determined.

4.2.2.9.2 Dialysis of free DOX and determination of K_{CV} using a Slyde-A-Lyzer dialysis cassette

The dialysis of DOX was performed using a SAL dialysis cassette composed of a low-binding regenerated cellulose membrane with a 10 000 Da MWCO. The SAL cassette provides high surface-area to volume ratio that maximizes diffusion rate (Figure 4.3).

Figure 4. 3 *Photo of a Slyde-A-Lyzer dialysis cassette.*

In a typical procedure, the dialysis cassette was soaked in the dialysis buffer for 24 h prior to the experiment to hydrate the membrane. 6 mL of DOX solution (in PBS at pH = 7.4) at 16 µg/mL were inserted in the cassette through the gasket via one of the corner ports, and the excess of air was withdrawn with a syringe to insure that the DOX solution was in contact with all the surface area of the membrane. The dialysis cassette was soaked and dialyzed against 60 mL of PBS at pH = 7.4 under mild stirring in a polypropylene container. A receiver phase volume of 10 times that of the dialysis cassette was chosen to ensure sink conditions for the DOX, while the absorbance of DOX in solution remains in the UV-vis detectable range. The dialysis setup was covered with foil to avoid any light degradation of the drug during the experiment. At predetermined time points (*i.e.* 0.25, 0.5, 0.75, 1, 2, 4, 8 and 10 h), 3 mL of dialysate were taken out for UV-visible spectroscopy, and replaced with 3 mL of fresh PBS to keep the total volume constant and preserve sink conditions. The DOX content of the extracted solution was measured by UV-visible spectrophotometry and the diffusion profile of DOX through the SAL dialysis membrane was determined.

4.2.2.10 Drug conjugation to the magnetic nanocomposites

Conjugation of DOX with the MNCs was achieved through formation of imine bonds, also called Schiff base bonds, between the primary amine group of DOX and the aldehyde group of the P(DEGMA-*co*-PEGMA-*b*-[TMSPMA-*co*-VBA]) polymer. DOX and MNCs were mixed in PBS at pH = 7.4 with a ratio 1:10 w/w. The mixture was shaken gently in the dark for 24 h at room temperature, thereby leading to the conjugation of DOX *via* imine linkage. The DOX-loaded MNCs (DOX-MNCs) were retrieved by magnetic separation and washed thoroughly with PBS until no DOX was detected in the supernatant (at least 10 washing

cycles). The drug conjugation efficiency (%) is calculated by measuring the absorbance of the supernatant at 480 nm of the free DOX remaining in solution, and after each washing cycle, using the following equation:

$$Drug\ conjugation\ efficiency\ (\%) = \frac{M_{conjugated}}{M_{feed}} * 100 = \frac{M_{feed} - M_{excess}}{M_{feed}} * 100 \quad (4.9)$$

Here M_{feed} is the initial mass of DOX used for the conjugation, $M_{conjugated}$ is the mass of DOX actually conjugated to the MNCs, and M_{excess} is the total mass of DOX found in the supernatants after the drug loading and each washing step. The DOX content in DOX-MNCs (%) was also evaluated, and is defined as follow:

$$Drug\ content\ (\%) = \frac{M_{conjugated}}{M_{carrier}} * 100 \quad (4.10)$$

where $M_{carrier}$ is the total mass of the nanosystem DOX-MNCs.

4.2.2.11 In vitro drug release behaviour in the absence of an AMF

In order to study the pH and temperature dependence of the drug release kinetics in the absence of an AMF, 6 sets of experiments were performed. The drug release was studied at 25 °C (room temperature), 37 °C (physiological temperature, <LCST) and 50 °C (hyperthermia temperature, >LCST). For each temperature, one sample was held at pH = 7.4 (physiological pH) and another at pH = 5.7 to mimic acidic tumour pH. Typically, 3.3 mg of DOX-MNCs dispersed in 6 mL of PBS with the appropriate pH (7.4 or 5.7) were inserted in a SAL dialysis cassette (MWCO 10 kDa) and dialyzed against 60 mL of PBS with the appropriate pH under mild stirring in a polypropylene container. A receiver phase volume of 10 times that of the dialysis cassette was chosen to insure sink conditions for the DOX. This volume was required for the dialysis cassette to be fully immersed in the medium, while the absorbance of DOX in solution remained in the detectable range of UV-Vis. Dialysis setups were either maintained to room temperature, or placed into preheated water baths at 37 °C and 50 °C. They were also covered with foil to protect them against light and avoid photodegradation of DOX as much as possible during the all duration of the experiments. At predetermined time points (*i.e.* 0.25, 0.5, 0.75, 1, 2, 4, 8, 24 and 48 h), 3 mL of dialysate were taken out for UV-Visible spectroscopy, and replaced with 3 mL of fresh PBS of the appropriate pH to keep the total volume constant and preserve sink conditions. The DOX content of the extracted solution was determined from the

absorbance measured by UV-Visible spectrophotometry at 480 nm and the DOX cumulative release was calculated.

4.2.2.12 Drug release kinetics

In order to determine the mechanism of drug release and the release rate, the data obtained from the drug release studies were fitted with the most relevant kinetic models for our system, such as first order, Higuchi and Korsmeyer-Peppas models.[281]

The first order kinetic release is concentration dependant and can be expressed as:

$$M_t = M_\infty[1 - \exp(K_1 t)] \quad (4.11)$$

where M_t is the amount of drug released at time t, M_∞ is the amount of drug release at infinite time, and K_1 is the first order rate constant.

The Higuchi model describes drug release from solid matrices, and is described as:

$$M_t = K_h\sqrt{t} \quad (4.12)$$

where K_h is the dissolution constant.

The Korsmeyer-Peppas model consists in a simple relationship, which describes drug release from a polymeric matrix, and is written as:

$$M_t = M_\infty K_{kp} t^n \quad (4.13)$$

where K_{kp} is the rate constant which is characteristic of the drug delivery system and n is the exponent. The value of n changes depending on the release mechanism. In order to determine the drug release mechanism, first 60% of the drug release data was fitted with the Korsmeyer-Peppas model.

By comparing the regression coefficient (R^2) of the different model, the accuracy of each fitting could be verified. For each pH and temperature conditions, the model that gives the highest R^2 was considered as the best fit of release data.

4.2.2.13 In vitro drug release behaviour in the presence of an AMF

In order to study the drug release behaviour in the presence of an AMF, 4 sets of experiments were performed. Four identical samples containing 1 mg/mL of DOX-MNCs

were prepared. Two samples were held at pH = 7.4 (physiological pH) and the two others were held at pH = 5.7 to mimic acidic tumour pH. The drug release was studied at room temperature for one sample of each pH, while one sample of each pH was exposed to an AMF (H = 10.5 kA/m, f = 950 kHz). After either 15 min, 30 min or 1 h, the MNCs were separated from the supernatant by magnetic separation. The DOX content of the supernatant was determined from the absorbance measured by UV-Visible spectrophotometry at 480 nm and the DOX cumulative release was calculated.

4.3 Results and discussion

4.3.1 Polymer characterisation

4.3.1.1 Polymer synthesis

The P(DEGMA-*co*-PEGMA-*b*-[TMSPMA-*co*-VBA]) polymer is presented in Figure 4.4.

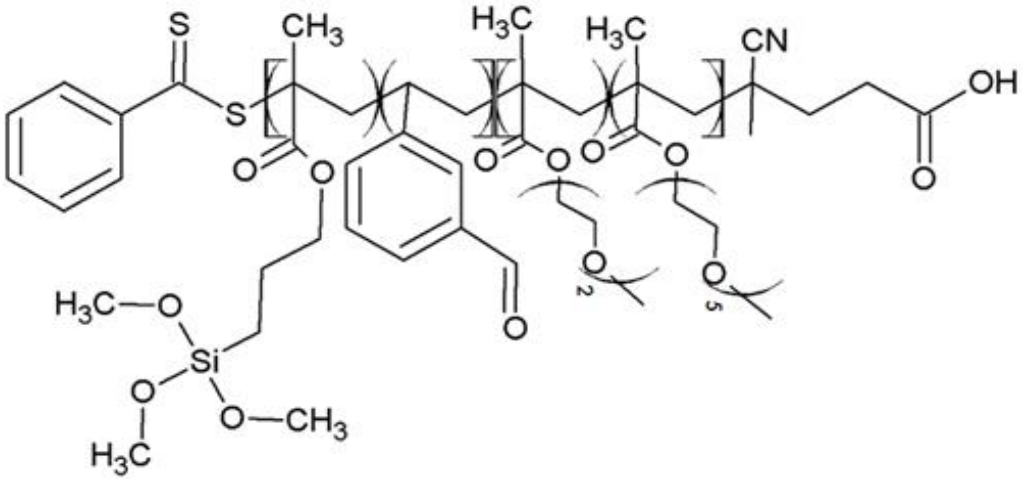

Figure 4. 4 *Chemical structure of P(DEGMA-co-PEGMA-b-[TMSPMA-co-VBA]) polymer.*

The polymer is composed of four mains groups: two PEG chains of different lengths, a benzaldehyde group and a trimethoxysilane group. PEG is FDA-approved and is widely used for biomedical applications, as it is non-toxic to cells and biocompatible with both blood and tissue. Therefore, PEG chains in the P(DEGMA-*co*-PEGMA-*b*-[TMSPMA-*co*-VBA]) polymer provide biocompatibility and water dispersibility to the nanosystem. PEG also reduces protein adsorption and thus confers prolonged blood circulation time in the body.[282] Finally, the two PEG chains of different length confer a temperature-responsivity to the polymer. The benzaldehyde group is the drug storage unit and by reacting the

aldehyde group with a primary amine a pH-labile imine bond can be formed. The trimethoxysilane group is the grafting group and will be used to attach the polymer onto iron oxide nanoparticle surfaces *via* the formation of covalent Si-O-Fe bond.

The first step in the synthesis of the polymer involves the co-polymerisation of the two PEG chains via RAFT polymerisation. CPPA was chosen as RAFT agent because it is especially suited for the polymerisation of methyl methacrylate monomers. The ACVA initiator was chosen so that the radical I• derived from the initiator is the same as the reinitiating radical R• derived from the RAFT agent.

In a first step, the polymerisation reaction advancement was followed by NMR spectroscopy. To that aim, the reaction was left on for 24 h. The reaction medium was sampled at predetermined time point and subsequently analysed by NMR to monitor the disappearance of the vinyl protons of the two PEGMA and DEGMA monomers. Because the initial ratio of PEGMA:DEGMA is known, the initial number of vinyl protons is also known, and the percentage of conversion can be calculated. The conversion was plotted as a function of time (Figure 4.5).

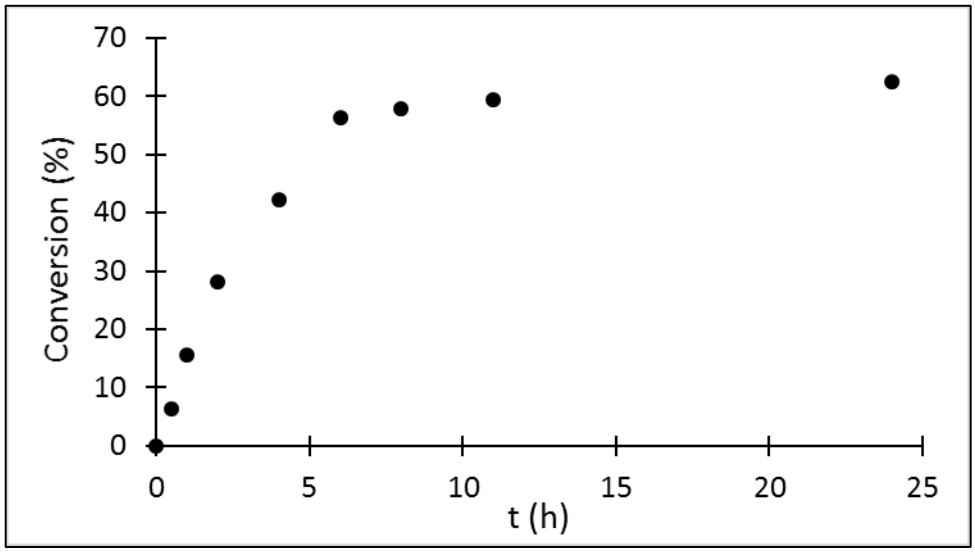

Figure 4. 5 *Follow up of the RAFT polymerisation reaction by NMR spectroscopy.*

The percentage of conversion increases linearly at the beginning of the reaction and reaches a plateau after 6 h. For that reason, the reaction time was limited to 5 h.
The quantities of RAFT agent and monomers were calculated to obtained the desired final polymer molecular weight according to the following equation:

$$M_n^{th} = \frac{[monomer]_0}{[RAFT]_0} * x * M^{monomer} \quad (4.13)$$

After this first step, M_n of the polymer is around 12000 g/mol (PDI = 1.10) as determined by SEC. Calculation of the theoretical molecular weight of the polymer by NMR was in close accordance with SEC results. Subsequently, a chain extension was carried out with the TMSPMA and VBA monomers (molar ratio TMSPMA:VBA = 1:4), using the synthesized P(DEGMA-*co*-PEGMA) polymer as macro-RAFT agent. The successful chain extension was confirmed by NMR, dominantly shown by the new signal at 10 ppm corresponding to the proton of the aldehyde group (Figure 4.6). An increase in the molecular weight of the polymer from 12 000 g/mol to 14 000 g/mol (PDI = 1.15) further confirms the polymer was chain extended.

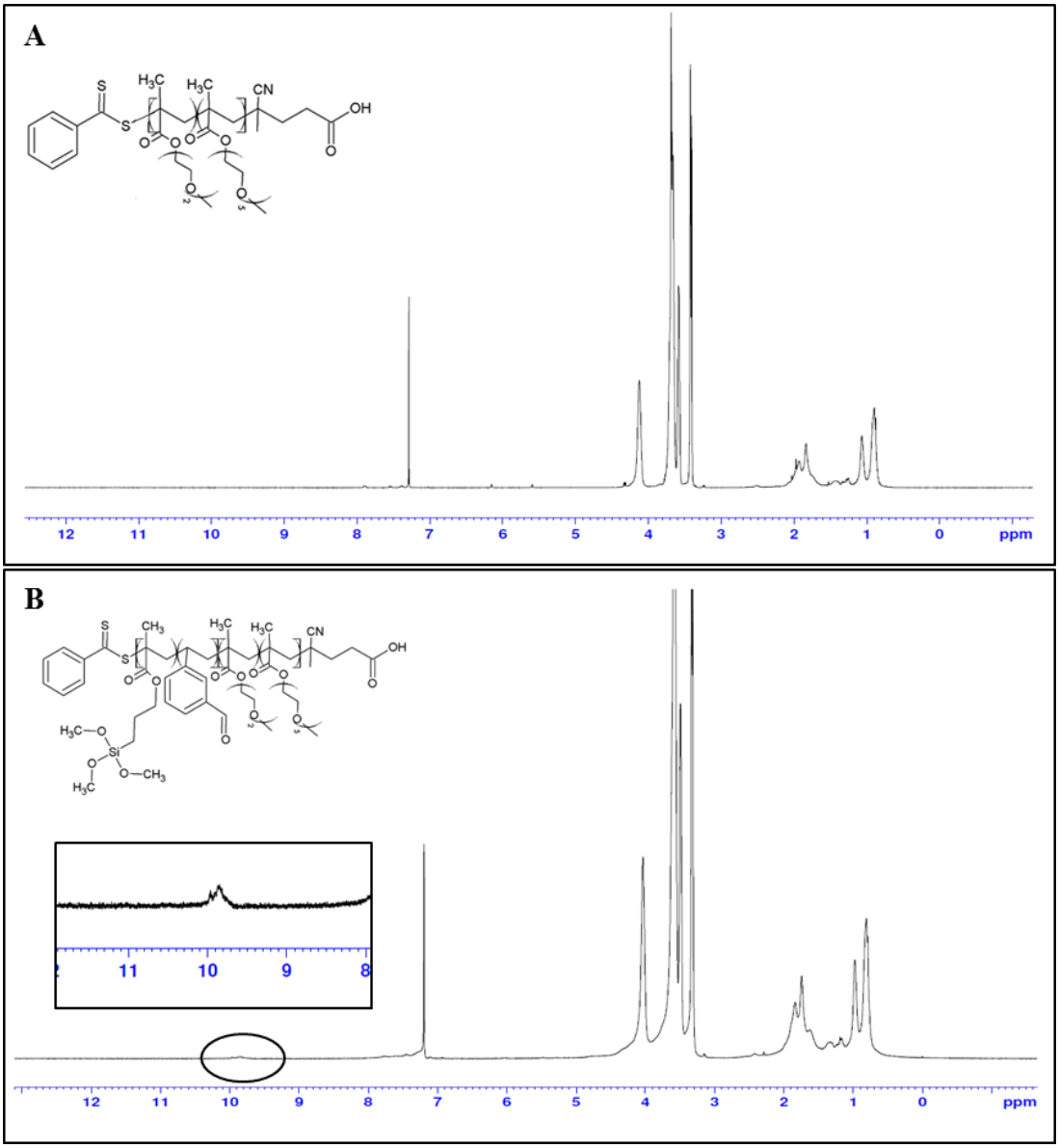

Figure 4. 6 *^{1}H-NMR spectra of A) P(DEGMA-co-PEGMA) and B) the chain extended polymer P(DEGMA-co-PEGMA-b-[TMSPMA-co-VBA]). Inset shows the peak at 10 ppm corresponding to the aldehyde.*

4.3.1.2 Tuning of the LCST of the polymer

Copolymerizing two PEG chains of different length provides temperature-responsive behaviour to the polymer, with the possibility to tune the LCST by varying the molar ratio PEGMA:DEGMA (Figure 4.7). Indeed, by varying the ratio of hydrophilic/hydrophobic co-monomer, the LCST of a given polymer can be tuned.[149,154] Generally, increasing the content of hydrophobic co-monomer lowers the LCST, while increasing the content of hydrophilic co-monomer increases the LCST. PEGMA is more hydrophilic than DEGMA due to its higher number of ethylene glycol units, consequently, increasing its content during the synthesis also increases the LCST of the final copolymer.

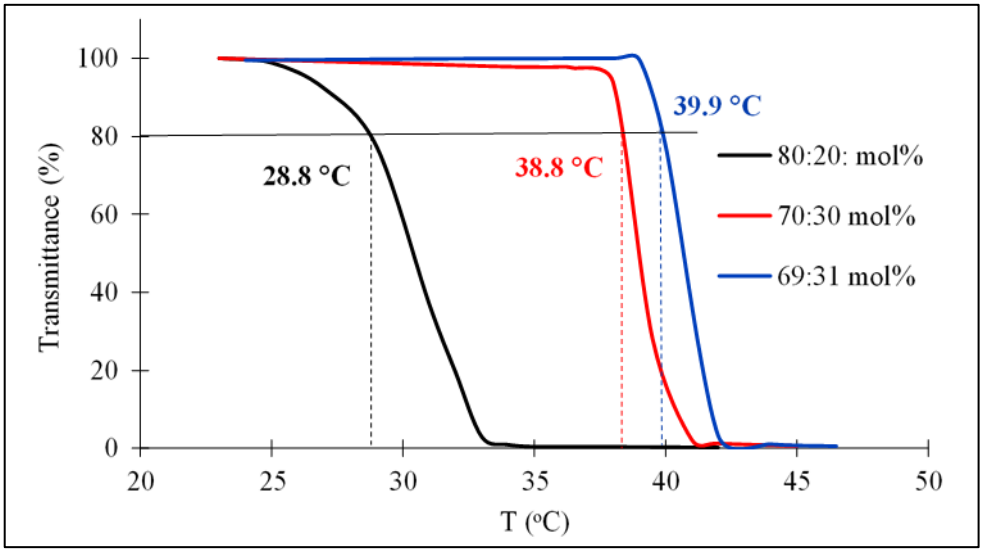

Figure 4. 7 *LCST of P(DEGMA-co-PEGMA-b-[TMSPMA-co-VBA]) as measured by UV-vis spectroscopy at 540 nm depending on the DEGMA:PEGMA molar ratio.*

A molar ratio of DEGMA:PEGMA of 1:2.2 (corresponding to 69:31 mol%) was selected for this work as it yields a polymer with a sharp LCST at 40 °C. This LCST is ideal because it is higher than the physiological temperature of 37 °C and can be easily reached via magnetic hyperthermia.

4.3.2 Characterization of the naked iron oxide nanoparticles

Figure 4.8 shows TEM images of the bare IONPs. The IONPs are spheroidal in shape with an average size of 13.3 ± 2.2 nm calculated from TEM images (n = 305). Some extent of aggregation can be observed on the TEM micrographs, which could be due to the absence of any stabilizing ligand on the surface of the nanoparticles and the drying effects that cause the accumulation and aggregation of particles on the TEM grid.

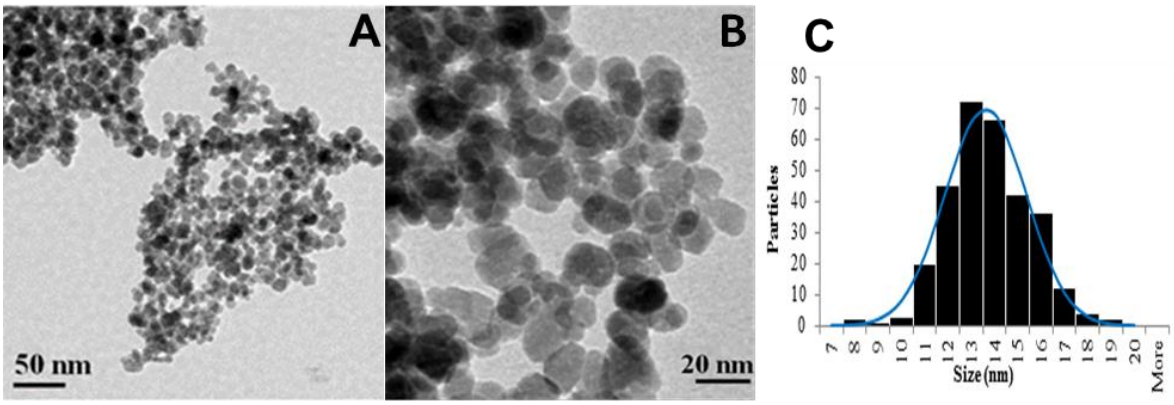

Figure 4. 8 *A) TEM micrographs of the as-synthesized IONPs at low magnification, B) at higher magnification and C) their size distribution histogram.*

Sharp and clearly defined peaks can be observed in the XRD pattern of the IONPs (Figure 4.9), which indicates a high degree of crystallinity of the particles.

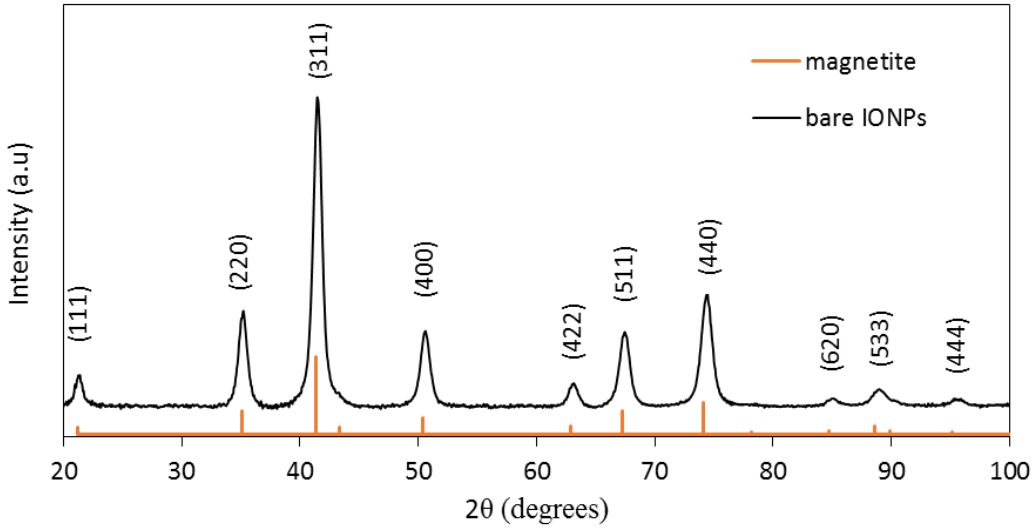

Figure 4. 9 *XRD pattern of the as-synthesized IONPs. Peaks were indexed according to the reference pattern for magnetite (JCPDS PDF No. 00-019-0629).*

Diffraction peaks matching with a Fe_3O_4 magnetite phase seems to indicate that the IONPs are primarily constituted of magnetite. A mean crystallite size of 11.1 nm was calculated from the XRD pattern, which is slightly lower than the particle size measured from the TEM images.

The magnetic properties of the IONPs were evaluated at 5 K and 300 K (Figure 4.10). Superparamagnetic behaviour was observed at 300 K with a saturation magnetisation around 78 ± 4 emu/g and a very low coercive field of 8 ± 3 Oe. At 5 K, a hysteresis cycle can be observed due to the transition to a low temperature blocked state, that comes with an increase of the saturation magnetisation to 92 ± 5 emu/g and of the coercive field to 275 ± 30 Oe.

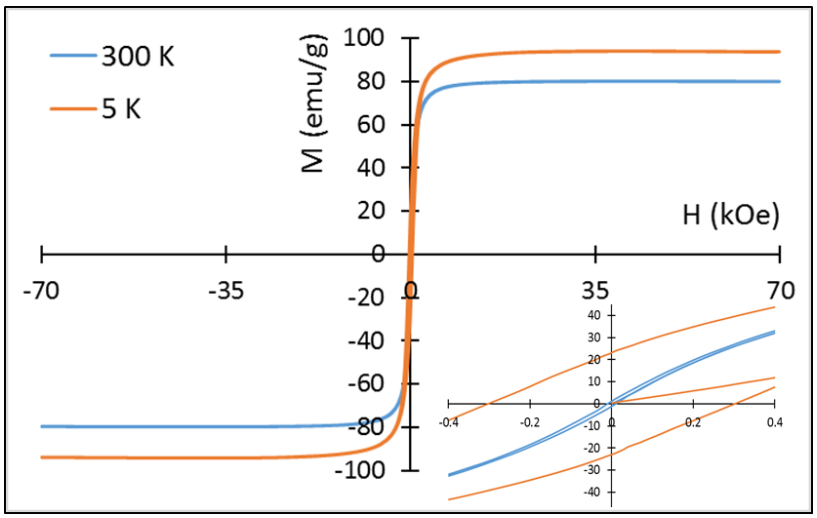

Figure 4. 10 *Typical magnetisation curves of IONPs at 300 K (blue line) and 5 K (orange line). The inset shows a zoom into the low magnetic field region.*

The magnetic properties of the bare IONPs were measured again at 300 K three months after the first MH curves were recorded, which roughly is equivalent to three months after the synthesis (Figure 4.11).

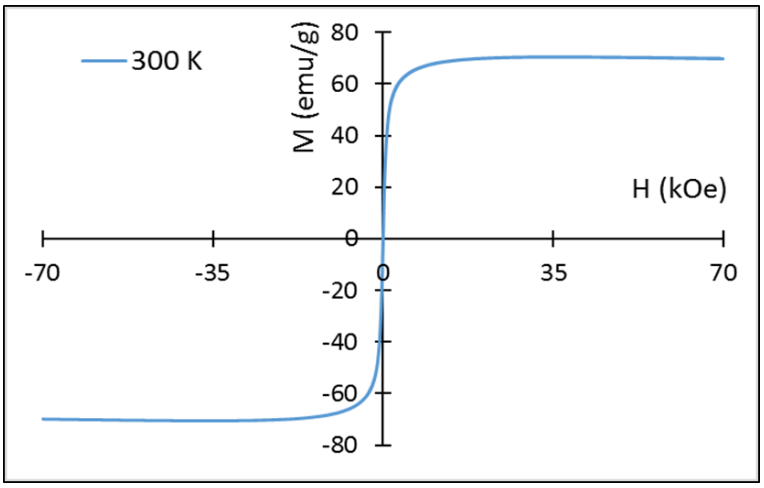

Figure 4. 11 *Typical magnetisation curves of IONPs at 300 K three months after the synthesis.*

Again, a superparamagnetic behaviour was observed at 300 K with a saturation magnetisation around 70 ± 3 emu/g and a coercive field of 12 ± 3 Oe. The drop of the saturation magnetisation over time is due to the oxidation of the nanoparticles. However, this drop remains quite small over a three-months period, most likely due to the high crystallinity of the particles. The coercive field seems to slightly increase, and can be attributed to a slight agglomeration of the particles, as aggregates of superparamagnetic nanoparticles can behave as a ferromagnetic material.

Inductively coupled plasma atomic emission spectroscopy revealed an average iron percentage of 64.2 % in the bare iron oxide nanoparticles.

4.3.3 Functionalisation of the IONPs with the polymer

Coating the IONPs with a polymer can usually be done either during the polymerization process, referred as in-situ functionalization, or separately, once the IONP has already been synthesized prior to the functionalization. In our case, *in-situ* functionalization was not an option as the nanoparticle synthesis is performed in water and the two steps of the polymerization reaction are performed in organic solvents. Moreover, the presence of the polymer during the synthesis of the nanoparticles can impede with the nucleation and growth of the particles and often results in magnetic nanoparticles with smaller sizes and saturation magnetisation than the equivalent nanoparticles prepared in the absence of polymer.[283] For those reasons, a post-synthetic functionalization protocol has been preferred.

The grafting of the polymer onto the IONP surface was realized through a silanisation reaction between the hydroxyl groups naturally present on the surface of the naked IONPs and the trimethoxysilane groups of the polymer, to form covalent Si-O-Fe bonds. The pH of the medium as well as the NP to polymer ratio (w/w) were found to have a significant impact on the functionalization step, and as such, had to be optimized (see Table 4.1 in section 4.2.2.3 for the details of the experimental conditions tested).

4.3.3.1 Influence of the pH during the functionalization step

Surface functionalization of the IONPs was assessed by ATR-FTIR spectrum. The presence of the polymer on the nanoparticle surface was confirmed by the presence of characteristic absorption peaks at 1750 cm^{-1}, 1450 cm^{-1}, 1110 cm^{-1} and 1050 cm^{-1} which were assigned to carbonyl ester bonds C=O, a small aromatic peak C=C, Si-O bonds and ether bonds C-O-C in PEG chains (Figure 4.12).[284,285] The absorption bands observed around 3100 – 3500 cm^{-1} may correspond to OH groups from the polymer, but is mainly associated to OH groups from the physisorbed water molecules on the nanoparticle surface.[276] The stretching band at 1635 cm^{-1} present for each sample also shows the presence of residual physisorbed water molecules.[285]

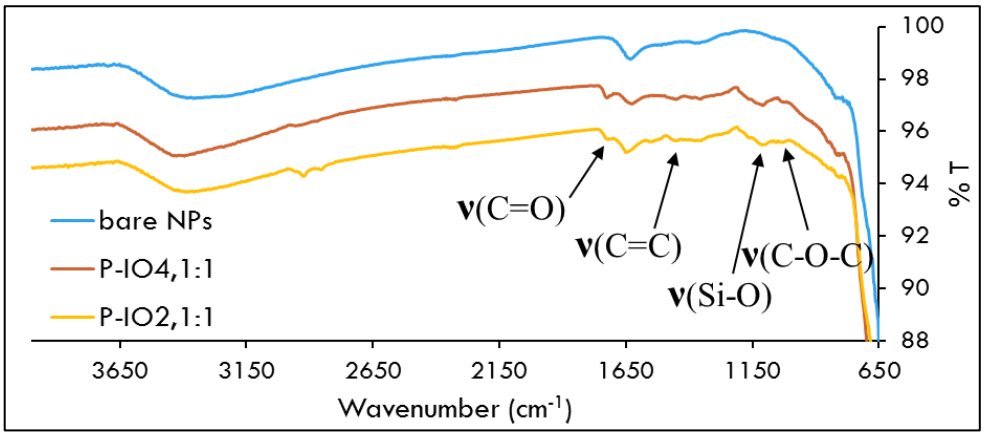

Figure 4. 12 *ATR-FTIR spectra of the functionalised IONPs with a NPs to polymer ratio of 1:1 at pH 4 (P-IO4,1:1 sample) and pH 2 (P-IO2,1:1 sample). Spectra of the as-synthesised bare IONPs was included for reference.*

The organic content of each sample could be determined by TGA analysis in the temperature range from 25 °C to 500 °C. Figure 4.13 shows the weight loss of bare IONPs, P-IO4,1:1 and P-IO2,1:1 samples as a function of temperature. Polymer thermal decomposition occurs between 240 °C and 420 °C with a weight loss of 3.7 wt% and 4.5 wt% for sample P-IO4,1:1 and P-IO2,1:1 respectively, therefore corresponding to the polymer content in each sample.

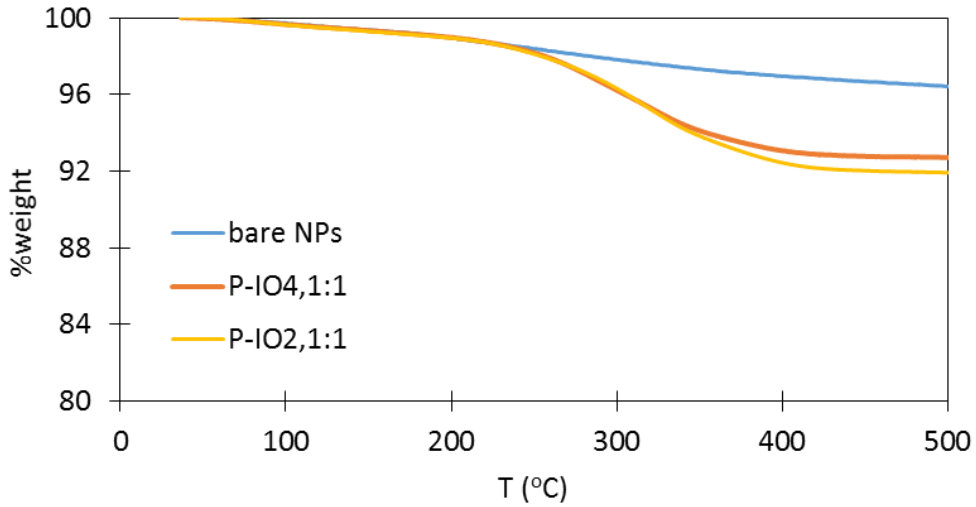

Figure 4. 13 *Weight loss curves as a function of temperature of the as-synthesized bare IONPs, P-IO4,1:1 and P-IO2,1:1 samples.*

It is well known that silanisation reactions are catalysed by an acidic pH, thus two acidic pH (i.e. pH 2 and pH 4) were studied. Indeed, the silanisation reaction is comprised of two steps: first, hydrolysis of the trimethoxysilane group and then condensation with the hydroxyl groups present on the surface of the IONPs as follows:

1) Hydrolysis : $-Si(OMe)_3 + H_2O \rightarrow -Si(OMe)_2(OH) + MeOH$
2) Condensation : $-Si(OMe)_2(OH) + Fe\text{-}OH \rightarrow -Si(OMe)_2\text{-}O\text{-}Fe + H_2O$

An acidic pH has been shown to catalyze both the hydrolysis and the condensation reaction.[286] For the functionalisation of the iron oxide nanoparticles, an acidic pH of 2 resulted in a better grafting density than a pH of 4. Therefore, the grafting of the polymer on the nanoparticle surface will be performed at pH 2 for all the next experiments.

TEM images of samples P-IO4,1:1 and P-IO2,1:1 are presented in Figure 4.14. The IONPs are clearly more dispersed in the case of P-IO2,1:1 as compared to P-IO4,1:1 which is consistent with a higher grafting density, therefore preventing particles agglomeration in a greater extent. The grafting density is an important criterion to ensure the colloidal stability of the iron oxide nanoparticles. Low polymer grafting densities may not form a coating structure compact enough to prevent the formation of aggregates. For both samples, the particle stability was compromised with the appearance of particle flocculation within a few days.

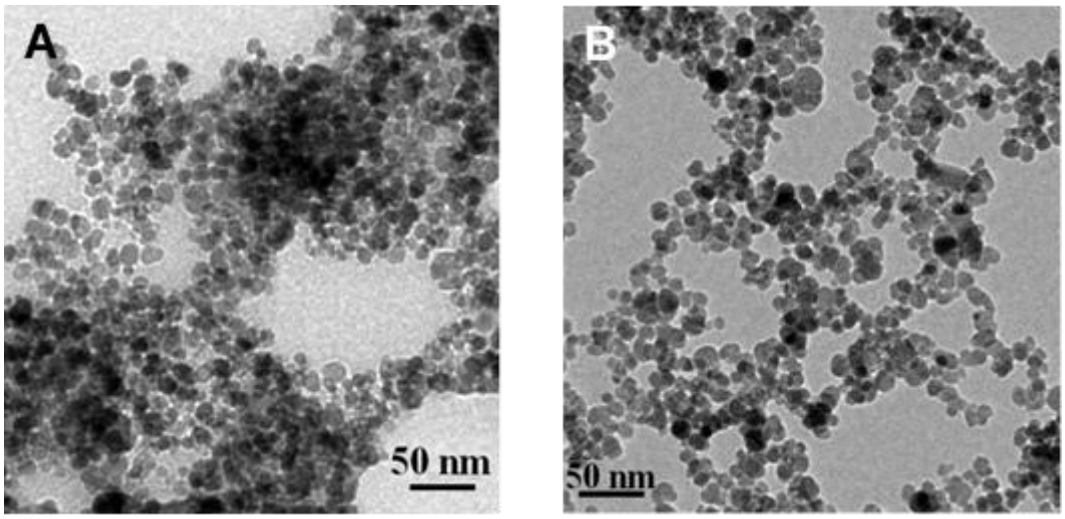

Figure 4. 14 *TEM micrographs of A) P-IO4,1:1 and B) P-IO2,1:1 samples.*

4.3.3.2 Influence of the NP:polymer ratio w/w

Likewise, surface functionalization of the IONPs was assessed by ATR-FTIR spectrum. The presence of the polymer on the nanoparticle surface was confirmed by the presence of the same characteristic absorption peaks at 1750 cm^{-1}, 1450 cm^{-1}, 1110 cm^{-1} and 1050 cm^{-1}, assigned to carbonyl ester bonds C=O, a small aromatic peak C=C, Si-O bonds and ether bonds C-O-C in PEG chains (Figure 4.15).[284,285]

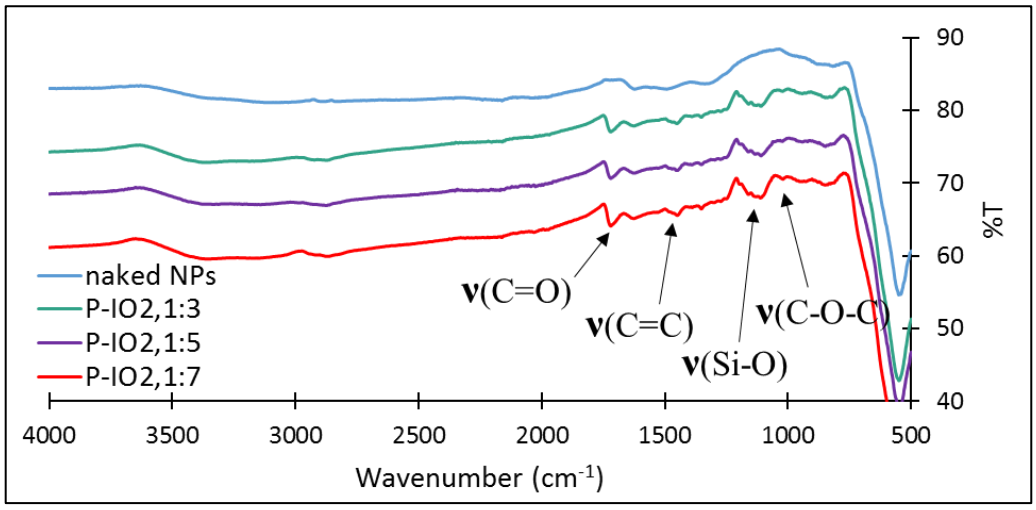

Figure 4. 15 *ATR-FTIR spectra of the functionalised IONPs at pH 2 with a NPs to polymer ratio of 1:3 (P-IO2,1:3 sample), 1:5 (P-IO2,1:5 sample) and 1:7 (P-IO2,1:7 sample). Spectra of the as-synthesised bare IONPs was included for reference.*

The absorption bands observed around 3100 – 3500 cm^{-1} may correspond to OH groups from the polymer, but is mainly associated to OH groups from the physisorbed water molecules on the nanoparticle surface.[276] The stretching band at 1635 cm^{-1} present for each sample also shows the presence of residual physisorbed water molecules.[285]

The organic content of each sample could be determined by TGA analysis in the temperature range from 25 °C to 500 °C. Figure 4.16 shows the weight loss of bare IONPs, P-IO2,1:1, P-IO2,1:3, P-IO2,1:5 and P-IO2,1:7 samples as a function of temperature.

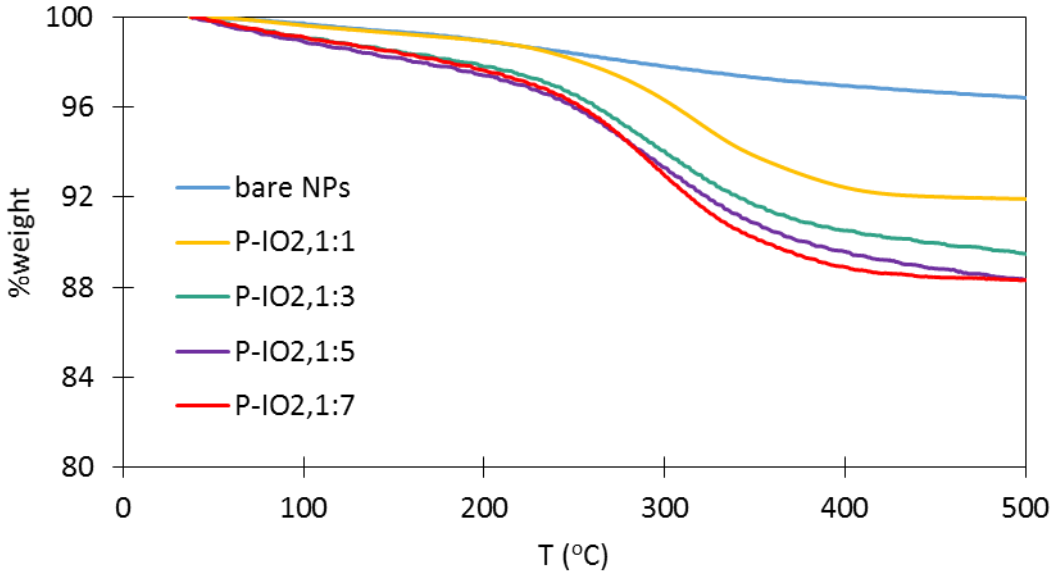

Figure 4. 16 *Weight loss curves as a function of temperature of the as-synthesized bare IONPs, P-IO2,1:1, P-IO2,1:3, P-IO2,1:5 and P-IO2,1:7 samples.*

Polymer thermal decomposition occurs between 240 °C and 420 °C with a weight loss increasing with an increasing ratio of NP to polymer, i.e 4.5 wt% at ratio 1:1, 6.9 wt% at ratio 1:3, and 8.1 wt% at ratio 1:5 and 1:7, respectively, therefore corresponding to the polymer content in each sample. No increase in the polymer content constituting the nanoparticles is observed between the ratio 1:5 and 1:7, which is most likely because no more polymer chain can reach the surface of the nanoparticles.

The grafting density used in the synthesis of P-IO2,1:3 to P-IO2,1:7 is enough to confer the nanoparticles a good colloidal stability as no flocculation was observed even after a few months. Assuming the nanoparticles are spherical, and using the magnetite density, the nanoparticle size and the molecular weight of the polymer, a number of 25 polymer chains/nanoparticle can be calculated. This corresponds to a low grafting density of 0.05 polymer chain/nm^2. The strategy adopted for the grafting of the polymer chains onto the nanoparticle surface is a major factor influencing the grafting density. There are two commons approaches for the functionalisation of nanoparticles with a polymer, the “grafting from” and “grafting to” approach.[287] Here, a “grafting to” approach was used, that involves chemical binding of already formed polymer chains to the surface of the nanoparticles. This method usually results in low grafting densities as the diffusion of polymer chains to the surface is obstructed once a certain number of chains has already attached. On the other hand, with the “grafting from” method polymer chains are grown from initiators already bound to the nanoparticle surfaces. While this technique usually results in higher grafting density, it could not be envisaged to apply it to our system considering polymerisation conditions were not compatible with this technique. De Gennes described two polymer conformations depending on whether the grafting density is low or high,[288] that are called mushroom and brush conformation. At high grafting density, the polymer chains adopt a brush structure, with the chain extending from the NP surface, while at low grafting density, the polymer chains acquire a mushroom structure.[289,290] Here, the mushroom conformation is most likely the conformation obtained considering the low grafting density calculated after functionalisation of the particles. If polymer segments attractively interact with the nanoparticle surface, a pancake-like structure can also be obtained at low grafting density.[291]

TEM images of samples P-IO2,1:3, P-IO2,1:5 and P-IO2,1:7 show that the nanoparticles are well dispersed, even in area of high concentration (Figure 4.17).

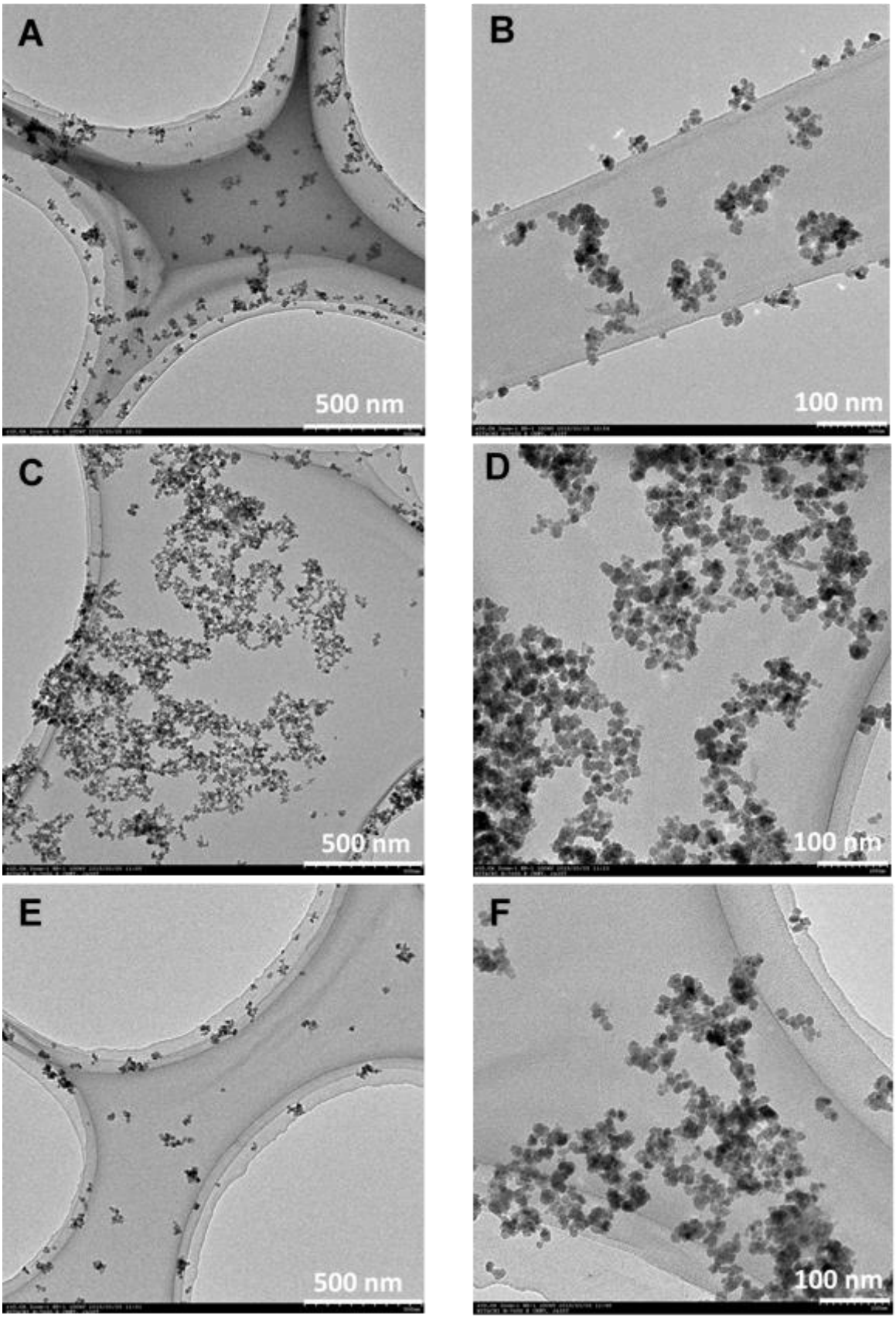

Figure 4. 17 *TEM micrographs of A) P-IO2,1:3 NPs at low magnification and B) higher magnification, C) P-IO2,1:5 NPs at low magnification and D) higher magnification and E) P-IO2,1:7 NPs at low magnification and F) higher magnification.*

4.3.4 Magnetic heating measurements - MACH

In vitro heating behaviour of the different nanoparticle suspensions were evaluated with a MACH system. Heat dissipation power measurements were performed on aqueous suspensions of concentration of 3 mg/mL subjected to an AMF of frequency f = 970 kHz and field amplitude H = 6.88 kA/m. The generated heat was characterized in terms of the ILP parameter, defined by Q. Pankhurst *et al.*,[4] as an alternative to the more widely used SAR parameters. The SAR is commonly employed to quantify the heat dissipation rate of a given ferrofluid, even though it is not an intrinsic property of the system as it is strongly dependent upon the frequency and field amplitude used during the measurement. On the contrary, the ILP can be considered as an intrinsic property of the NPs because it is obtained by normalizing the SAR by f and H (equation 4.14). Hence one can directly compare the heating efficiency between different nanosystems measured under different experimental conditions using ILPs. The heating power of each nanoparticle suspension will therefore be characterized with the ILP value, but the SAR will be given as indication.

$$ILP = \frac{SAR}{H^2 f} \tag{4.14}$$

The calculated ILP and SAR values from the respective experimental heating curves of the studied suspensions are shown in Table 4.4.

Table 4. 2 *SAR and ILP values of the P-IO sample series measured at a frequency of 970 kHz and a field amplitude of 6.88 kA/m.*

Sample	*SAR (W/g)*	*ILP (nHm²/K)*
P-IO4,1:1	31.6 ± 2.5	0.7 ± 0.05
P-IO2,1:1	67.8 ± 3.6	1.5 ± 0.09
P-IO2,1:3	94.1 ± 5.3	2.1 ± 0.10
P-IO2,1:5	91.9 ± 7.0	2.0 ± 0.15
P-IO2,1:7	85.5 ± 6.8	1.9 ± 0.18

The heating efficiencies vary significantly between the samples, ranging from 0.7 nHm²/K to 2.1 nHm²/K for sample P-IO4,1:1 and P-IO2,1:3 respectively.

After analysis of the results, it seems that the ILP values reflect the colloidal stability of the suspensions. Indeed, a good colloidal stability is necessary to ensure a constant homogeneous magnetic heating. P-IO2,1:7, P-IO2,1:5, and P-IO2,1:3 are equally stable and, as can be seen from their respective TEM images, are well dispersed (Figure 4.17).

The slight decrease in the ILP from 2.1 nHm²/K to 1.9 nHm²/K for P-IO2,1:3 and P-IO2,1:7 respectively, can be attributed to the increase organic content for the fabrication of the nanoparticle polymeric shell. However, the colloidal stability of P-IO2,1:3 > P-IO2,1:1 > P-IO4,1:1 and so is their ILP values. This is mainly due to the change in dipolar interactions. Indeed, it is well-known that Néel relaxation is strongly dependent upon dipole-dipole interactions.[292,293] The role of interparticle dipole-dipole interactions still remains an open question. Some investigations showed that dipolar interactions can lead to an increase of the SAR while others showed a decrease. G.T. Landi reports that dipole-dipole interactions can be used to increase the SAR of nanoparticles made of soft magnetic materials as it increases the anisotropy energy barrier. On the other hand, he also reports a decrease of the SAR for nanoparticles made of hard magnetic materials caused by a larger freezing of the magnetic spins that hampered the particles.[294] However, once needs to be careful and distinguish the effect of nanoclustering and single particle in suspension. Indeed, nanoclustering acts to reduce the SAR while a peak against concentration is obtained for well-dispersed suspensions.[295] It is therefore clear the dipolar interaction can both decrease or increase the SAR. For a given nanoparticle, interparticle dipole-dipole interactions vary with the nanoparticle concentration. The SAR increases for increasing concentration, reaches a maximum, and then decreases for higher concentration.[295,296] An aggregated state means particles form clusters and are very close from each other, increasing their dipolar magnetic moment interaction inside the cluster in presence of an AMF. The higher the dipole-dipole interaction, the longer Néel relaxation time, and the lower the SAR. C. Blanco-Andujar *et al.,* demonstrated that a better magnetic heating is associated with less core-to-core magnetic interactions.[276] In the same way, D. Cabrera *et al.* showed that the aggregate compactness plays a major role in the decrease of the ILP. An increase aggregate compactness leads to a drastic decrease of the ILP as magnetic dipolar interactions between NPs in the aggregates are maximized.[297] P-IO4,1:1 is the sample where the highest nanoparticle agglomeration is found as could be seen in the TEM images presented in Figure 4.14 in section 4.3.3.1, which explains its lower ILP value.

According to the magnetic heating measurements, the ideal conditions for the functionalisation of the iron oxide nanoparticles were found to be at pH 2 with a NPs:polymer ratio w/w of 1:5 to obtain the highest ILP and grafting density. From now one, the experiments will be conducted with NPs prepared according to this protocol and the magnetic nanocomposites will be referred to as MNCs in the rest of the thesis.

The MNCs exhibited a temperature rise of 16 °C in only 10 min, sufficient to reach hyperthermia temperatures, and yielding an ILP of 2.1 nHm²/K, that translated into a SAR of 94.1 W/g (Figure 4.18). Considering the percentage of polymer and iron that compose

the MNCs, a SAR of 159.5 W/g_{Fe} and an ILP of 3.5 nHm²/K can be calculated. This ILP value compares favourably to other ILP values obtained for iron oxide magnetic materials specially synthesized for hyperthermia applications,[298] and commercially available ferrofluids with ILP values ranging from 0.15 nHm²/K to 3.1 nHm²/K.[4]

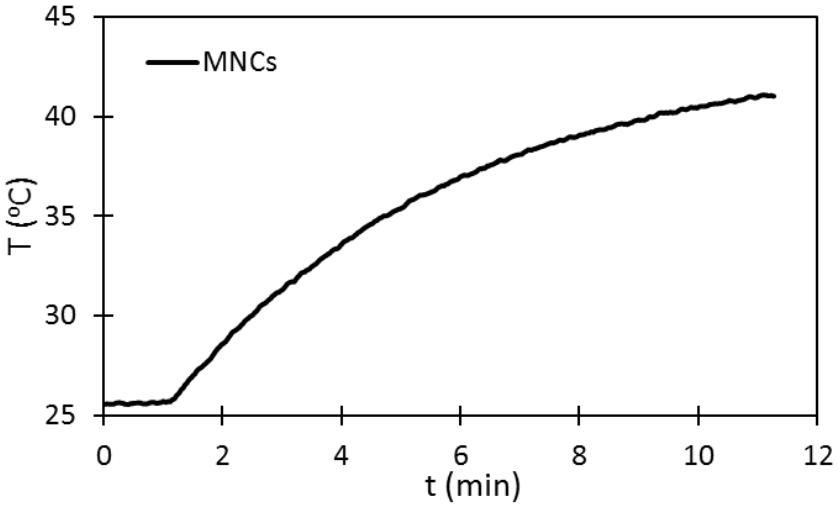

Figure 4. 18 *Typical heating curve of the MNCs dispersed in water with a concentration of 3 mg/mL and subjected to an AMF (f = 970 kHz and H = 6.88 kA/m) using the MACH instrument.*

The concentration of MNCs of 3 mg/mL used to determine their heating abilities, is lower than that used by most other research groups, and the average concentration of 112 mg_{Fe}/mL used by Jordan *et al.* for clinical trials.[37,38,299,300]

Heat dissipation power measurements were also performed on suspensions in biological media (DMEM) supplemented with fetal bovine serum with a concentration of 1 mg/mL, maintained at physiological temperature (37 °C) and subjected to an AMF of frequency *f* = 970 kHz and field amplitude *H* = 6.88 kA/m. A lower concentration of MNCs in solution was used in order to be closer from the conditions that will be used later for magnetic hyperthermia on cells. Under these conditions, the MNCs exhibited an ILP of 2.4 nHm²/K, which translated into a SAR of 108.5 W/g. The field conditions were changed to *f* = 950 kHz and *H* = 10.5 kA/m to obtain a quicker rise of the temperature (Figure 4.19).

Under these field conditions, a quick temperature rise is indeed obtained, from 34 °C to 50 °C in 12 min. The ILP was still found to be 2.4 nHm²/K, which is coherent as the ILP parameter is independent of the AMF conditions, but translated into a SAR of 247.2 W/g It can be noted that a slight increase of the ILP is obtained in biological media (2.4 nHm²/K) as compared as in water (2.1 nHm²/K).

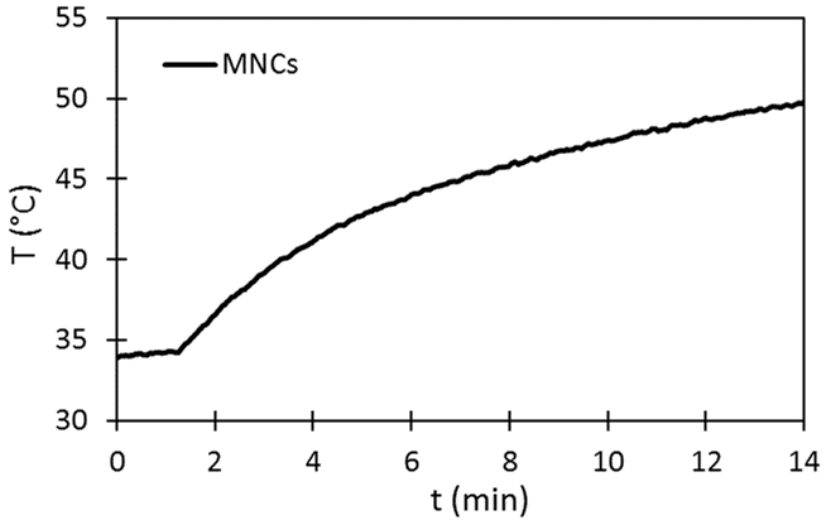

Figure 4. 19 *Typical heating curve of the MNCs dispersed in DMEM supplemented with 10% FBS with a concentration of 1 mg/mL and subjected to an AMF (f = 950 kHz and H = 10.5 kA/m) using the MACH instrument.*

4.3.5 Colloidal stability of the magnetic nanocomposites

The colloidal stability of nanoparticles over time and in different media is of significant importance for biomedical application purposes. The stability in aqueous suspension of the MNCs over time was estimated by measuring the change in hydrodynamic diameter D_H of the MNCs. No significant changes in hydrodynamic radius was determined by DLS over two weeks, indicating that the MNCs remain well dispersed in water (Figure 4.20A). Moreover, after a month, the MNCs are still well dispersed in aqueous suspension as can be seen from the picture (Figure 4.20B). The obtained D_H of 120 nm indicates that the MNCs possess a multicore structure.

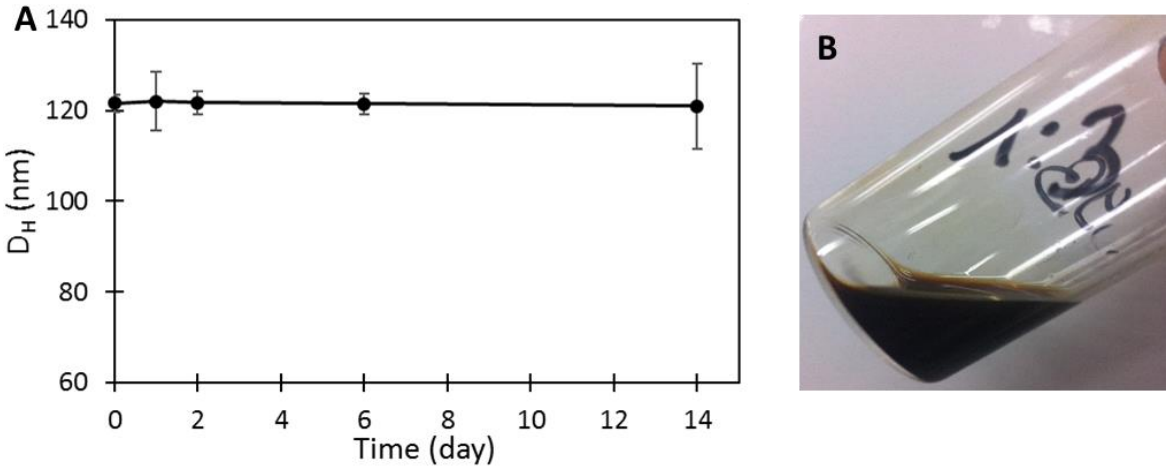

Figure 4. 20 A) *Hydrodynamic diameter of MNCs as a function of time and B) photo of the MNCs aqueous suspension after one month.*

As the pH in the human body can vary considerably, the D_H of the MNCs was measured in aqueous suspension with a pH varying from 2 to 12. The D_H of the MNCs remained constant at each different pH condition, suggesting that the pH does not have any impact on the colloidal stability of the MNCs (Figure 4.21). Finally, the D_H of the MNCs was measured in biological media (DMEM supplemented with 10% FBS) yielding a D_H of 147 nm, representing a 27 nm increase as compared to MNCs in water. The increase in D_H is most likely due to the formation of a protein corona around the MNCs that is formed instantaneously.[87] The MNCs remain stable in DMEM + 10% FBS for several weeks before any aggregation of the MNCs could be observed.

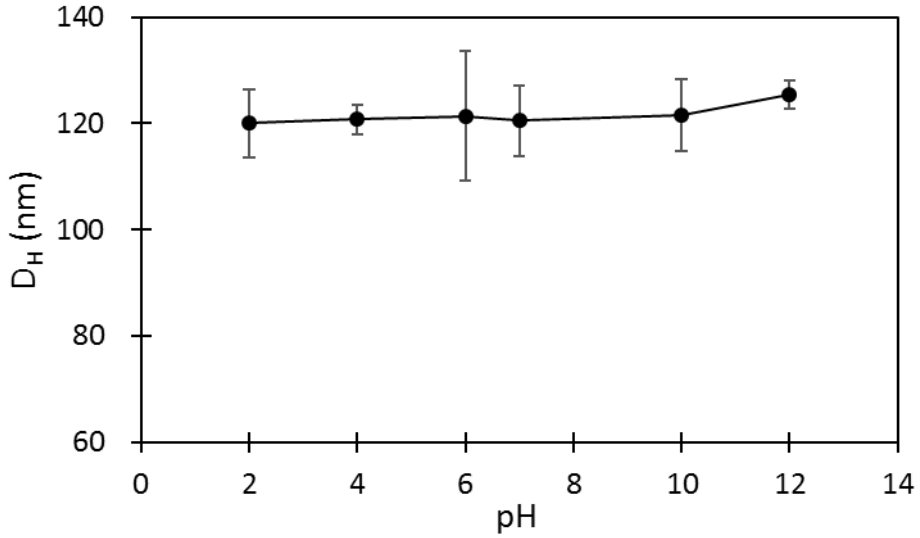

Figure 4. 21 *Hydrodynamic diameter of MNCs as a function of pH in aqueous suspension.*

4.3.6 Evolution of the magnetic behaviour from the bare iron oxide nanoparticles to the MNCs

The evolution of the magnetic behaviour from the bare IONPs to the MNCs was evaluated by recording the MH curves of both the IONPs and the MNCs under the same conditions (Figure 4.22). After functionalisation of the bare IONPs with the polymer, only a small drop of 5 emu/g is observed in the saturation magnetisation both at 300 K and 5 K. In general, silane-coated IONPs still maintains the physical properties of bare IONPs with high saturation magnetisation, the decrease value of saturation magnetisation being often less than 5 or 10 emu/g.[301,302] The coercive field slightly decreases from 8 Oe to 5 Oe at 300 K, and from 275 Oe to 200 Oe at 5 K, respectively. After stabilization of the IONPs with a polymer layer, the aggregates have been broken down to smaller aggregates, therefore resulting in a lower coercive field.

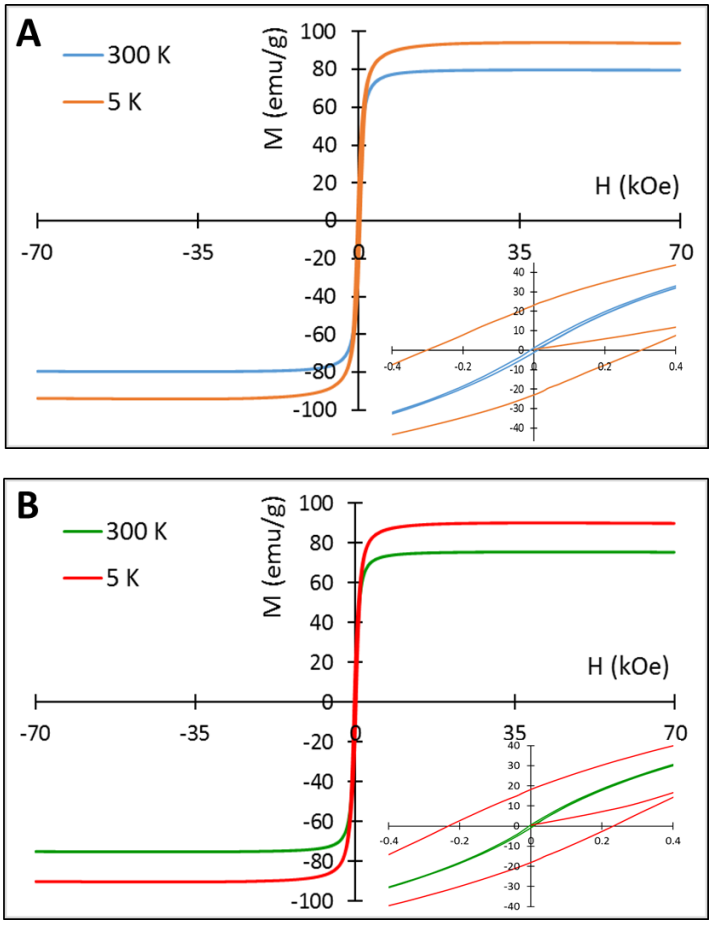

Figure 4. 22 *Typical magnetisation curves of A) bare IONPs at 300 K (blue line) and 5 K (orange line) and B) MNCs at 300 K (green line) and 5 K (red line). The insets show a zoom into the low magnetic field region.*

Zero Field Cooled/Field Cooled (ZFC/FC) magnetisation curves for both the bare IONPs and IONPs after functionalisation were obtained by cooling the sample without any applied magnetic field (ZFC curve), and in a second step by heating the sample under a low magnetic field of 100 Oe (Figure 4.23). The ZFC curves do not indicate any sharp transition for both samples. Increasing the nanoparticles size polydispersity widens the blocking temperature range due to an increase on width of the anisotropy energy barrier.[303] This phenomenon is clearly observed for the bare IONPs. Due to the absence of any stabilizing ligands, many aggregates of different sizes are present in the sample. Though after functionalisation of the IONPs with the polymer the blocking temperature range remains wide, a clear improvement in the nanoparticle polydispersity is observed, with a sharper transition. It is crucial to consider that the nanoparticles were stabilized by the formation of multicore structures, as revealed by the previous DLS measurements. The fast decrease of the magnetisation in the ZFC curves at low temperature is due to the presence of surface spin.[304] Interparticle interactions due to particle agglomeration will cause surface spins,

which rearrange much slower than interior spins. As expected, this effect is more apparent for bare IONPs.

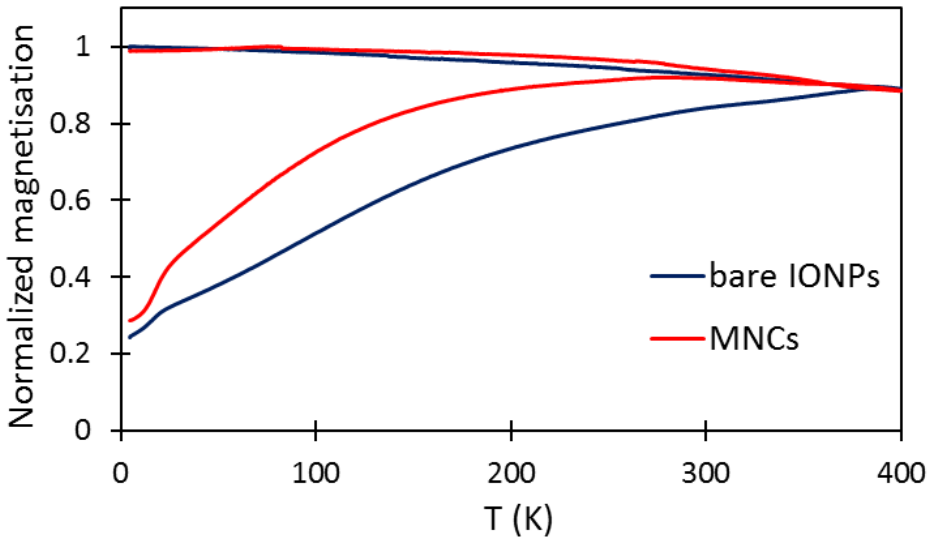

Figure 4. 23 *ZFC/FC magnetisation curves of the bare IONPs (blue line) and the MNCs (red line) recorded between 5 K and 400 K.*

4.3.7 DOX calibration curve and DOX photodegradation

The calibration curves of DOX in PBS at pH = 7.4 and in PBS at pH = 5.7 could be plotted by recording the absorbance of DOX solution of known concentration at a wavelength of 480 nm, which is the typical absorption for DOX, by UV-vis. The calibration curves are shown in Figure 4.24.

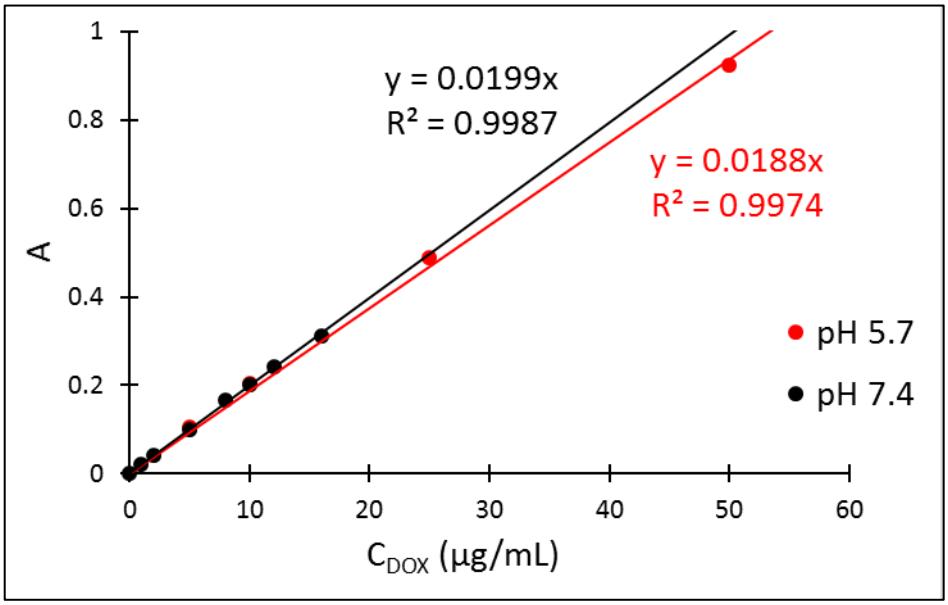

Figure 4. 24 *Calibration curves of DOX in PBS at pH 7.4 (black curve) and at pH 5.7 (red curve) obtained by UV-vis spectroscopy.*

Because DOX is light-sensitive and was to be used in very small concentrations, the photodegradation of DOX as a function of time was studied over a 3-day period. The samples prepared for the calibration curve of DOX in PBS at pH = 7.4 were kept in the dark for three days and their absorbance measured again 3 days later. The results can be observed in Figure 4.25.

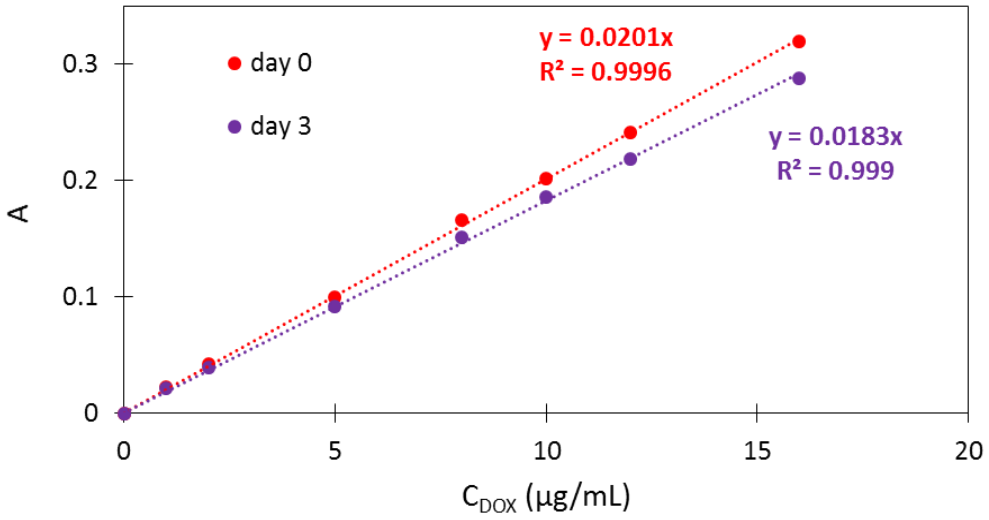

Figure 4. 25 *Absorbance of DOX solutions in PBS at pH = 7.4 (red curve) and measured again 3 days later (purple curve).*

Depending on the DOX concentration, a decrease of 7% to 10% of the original absorbance value can be observed for the absorbance of the DOX solutions measured 3 days later, which is most likely due to light degradation of DOX. Wood *et al.* reported that the photodegradation of DOX follow a first-order kinetic and is dependent on both the concentration and the pH of the solution.[305] Low concentrated solutions (in the range of the low microgram and nanogram quantities in solution) may be degraded by light rapidly and acidic pH tends to slow down the photodegradation process. The authors also mentioned that another possible cause for the decrease of the absorbance, especially on low concentration solutions, is the loss of drug due to the adsorption of DOX onto the walls of the container. It is said that adsorption of DOX can be best minimized by using polypropylene containers, which is in good accordance with other reports.[306-308]

According to those conclusions, all the experiments involving DOX, such as the dialysis of DOX and the drug release experiments, were carried out in polypropylene containers and protected from light as much as possible by using foil to cover the setups.

4.3.8 Dialysis of free DOX

Dialysis experiments of a solution of free DOX of known concentration were performed prior to the drug release experiments in order to determine the influence of the dialysis membrane on the diffusion of free DOX from the donor phase to the receiver phase.

4.3.8.1 Dialysis of free DOX and determination of K_{CV} using a dialysis bag

The first experiment was performed with a common dialysis membrane of MWCO 10 kDa. Plot of the concentration of DOX retrieved in the receiver phase as a function of dialysis time is presented in Figure 4.26.

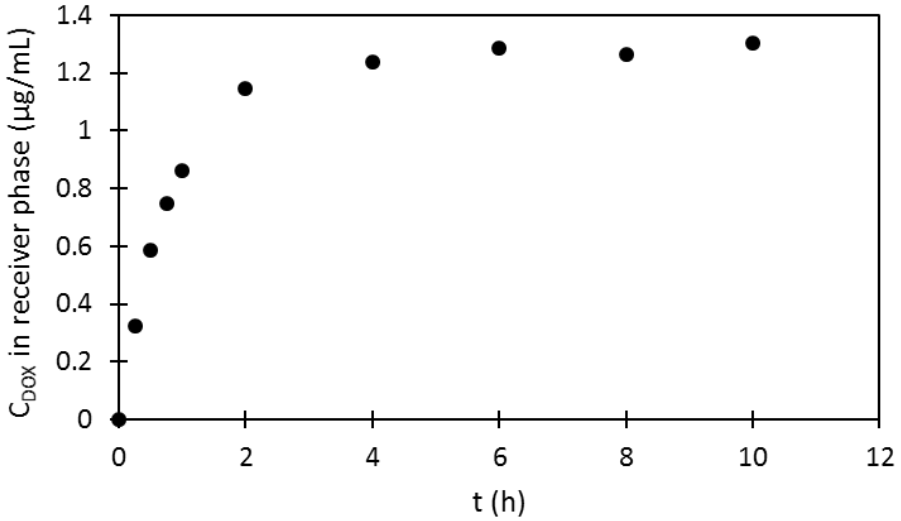

Figure 4. 26 *Cumulative DOX release in the receiver phase as a function of dialysis time using a dialysis membrane of MWCO 10 kDa.*

The plot indicates that the equilibrium between the donor phase and the receiver phase is reached after 2 - 4 h. However, the experimental equilibrium concentration (taken at the concentration of DOX in the receiver phase after 10 h of dialysis time) is equal to 1.28 µg/mL. Knowing that the total volume is 44 mL (i.e. 4 mL of donor phase and 40 mL of receiver phase), and the initial amount of DOX dissolved in the donor phase was 64 µg, the equilibrium concentration should be 1.45 µg/mL. The reason behind the disappearance of DOX could be explained by the adsorption of DOX onto the dialysis membrane.

The apparent permeation constant K_{CV} of DOX for that membrane was determined by plotting $ln\ (m_0 - C_1(V_1 + V_2))$ versus dialysis time as previously explained in section 4.2.2.8 (the equilibrium section was not considered).

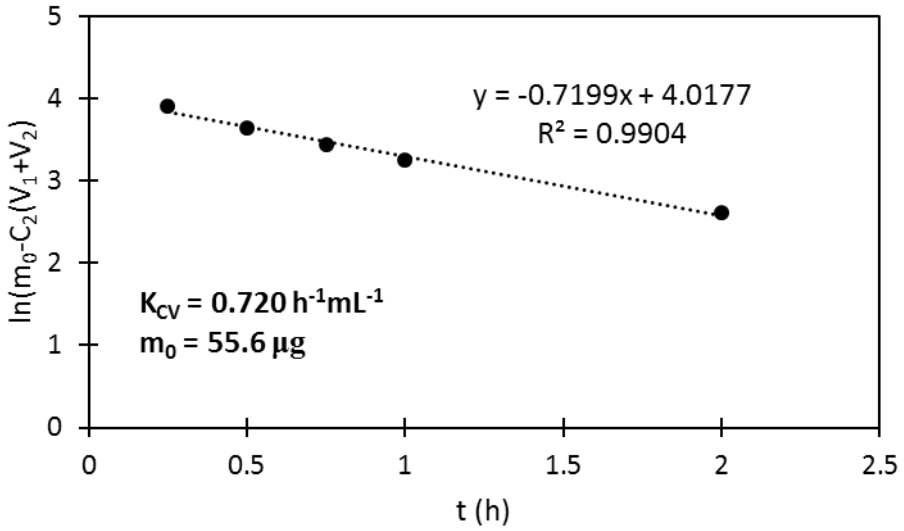

Figure 4. 27 *Plot of* $\boldsymbol{ln}\ (\boldsymbol{m_0} - \boldsymbol{C_1(V_1 + V_2)})$ *versus different dialysis time for the dialysis of free DOX using a dialysis membrane of MWCO 10 kDa.*

As can be observed in Figure 4.27, the initial amount of DOX dissolved in the donor phase m_0 obtained from the plot was found to be 55.6 µg, while the actual initial amount of DOX was 64 µg. This result suggests that a non-negligible 13.1% of DOX is lost during the dialysis process, which might be caused by its adsorption on the membrane. The value of the permeation constant K_{CV} was found to be 0.720 $h^{-1}mL^{-1}$.

To conclude, DOX seems to adsorb onto this dialysis membrane, and therefore cannot be used for the drug release experiments. Indeed, the adsorption of DOX onto the membrane is non-negligible when using small concentration in the range of the µg and for experiments with duration of 48 h.

In order to solve that issue, the experiment was repeated with another dialysis membrane that seemed more suitable for our system, the SAL dialysis cassette.

4.3.8.2 Dialysis of free DOX and determination of K_{CV} using a dialysis cassette

As the first membrane used was proven to be unsuitable for the study of the drug release behaviour due to non-negligible adsorption of DOX onto the membrane, the dialysis of DOX was repeated with a SAL dialysis cassette. This dialysis cassette was chosen because it is composed of a low binding regenerated cellulose membrane of MWCO 10 kDa and its design provides high surface-area to volume ratio that maximizes diffusion rate and ensure the maximum contact between the donor phase and the membrane.

Plot of the concentration of DOX retrieved in the receiver phase as a function of dialysis time is presented in Figure 4.28.

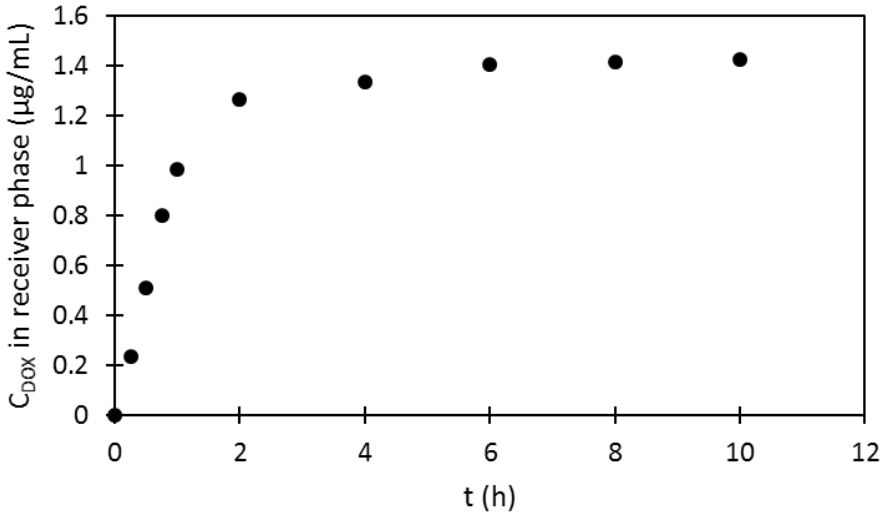

Figure 4. 28 *Cumulative DOX release in the receiver phase as a function of dialysis time using a dialysis cassette composed of a low binding membrane of MWCO 10 kDa.*

The plot indicates that the equilibrium between the donor phase and the receiver phase is reached after 2 – 4 h of dialysis. The experimental equilibrium concentration (took at the concentration of DOX in the receiver phase after 10 h of dialysis time) is equal to 1.42 µg/mL. Knowing that the total volume is 66 mL (i.e. 6 mL of donor phase and 60 mL of receiver phase), and the initial amount of DOX dissolved in the donor phase was 96 µg, the theoretical equilibrium concentration should be 1.45 µg/mL, which is really close from the determined experimental equilibrium concentration. The apparent permeation constant K_{CV} of DOX for that membrane was determined by plotting $ln\ (m_0 - C_1(V_1 + V_2))$ versus dialysis time as previously explained in section 4.2.2.8 (the equilibrium section was not considered).

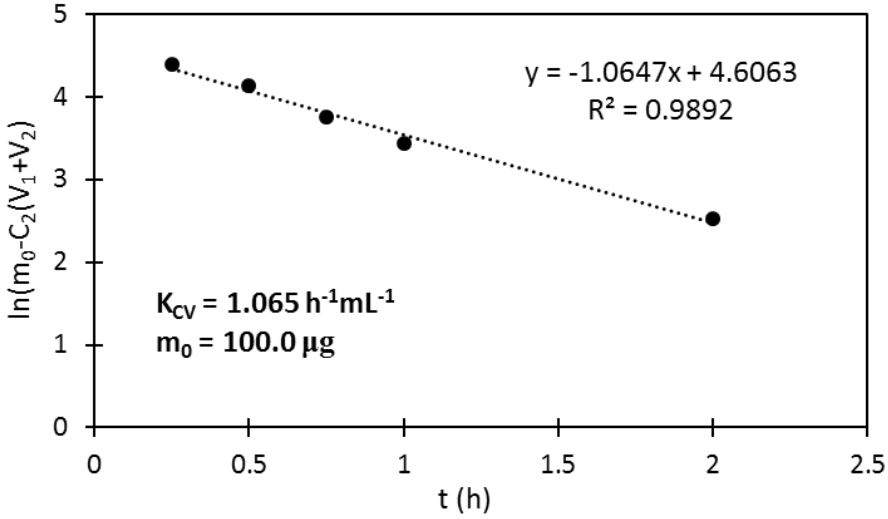

Figure 4. 29 *Plot of* $\boldsymbol{ln\ (m_0 - C_1(V_1 + V_2))}$ *for the dialysis of free DOX using a SAL dialysis cassette composed of a low binding membrane of MWCO 10 kDa.*

The value of m_0 (initial amount of DOX dissolved in the donor phase obtained from the plot) was found to be 100.0 µg (Figure 4.29), which is in close accordance with the actual initial amount of DOX of 96 µg. This result suggests that DOX does not absorb on the membrane of the SAL dialysis cassette. The value of the permeation constant K_{CV} was found to be 1.065 $h^{-1}mL^{-1}$, which is higher than the value of K_{CV} obtained with the previous tested membrane.

The SAL dialysis cassette were therefore suitable for the drug release experiments, as negligible adsorption of DOX onto the membrane was found by using the SAL dialysis cassette.

4.3.9 Drug loading – Dox conjugation efficiency

In this work, DOX was chosen as anti-cancer drug because of its primary amine group, which can react with an aldehyde to form a Schiff base bond, releasing one molecule of water. Under acidic conditions, DOX can then be released by hydrolysis of the Schiff base bond without any damage to its chemical structure (Figure 4.30).

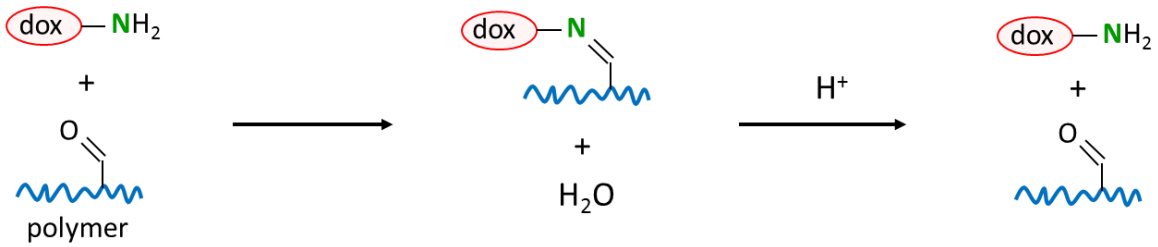

Figure 4. 30 *Schematic representation of the drug loading and drug release mechanisms.*

DOX is one of the most widely used chemotherapeutic drugs because of its efficacy against an extensive range of cancers.[309] Its major mode of action is as a toiposomerase II inhibitor: it intercalates into DNA and inhibits the enzyme topoisomerase II, which is necessary for cell division and growth, therefore resulting in DNA damage and cell death.[135,310] DOX can also generate free radicals (reactive oxygen species) that damage the cellular membrane, DNA, and proteins and lead to apoptotic cell death [135] and form adducts with DNA which enhances the cytotoxic response.[311]

However, its use as anti-cancer agent is still limited by its detrimental side effects, and especially its cardiotoxicity.[135,309] DOX encapsulation and targeting to the desired site, is therefore a very attractive solution to alter the pharmacokinetics and biodistribution of DOX toward its specific accumulation in tumour tissue, therefore reducing side effects and the

therapeutic dose needed for an efficient therapy. Ideally, the drug would be harmless to healthy tissue while circulating in the body because it is stored and protected in the MNCs until it enters the tumour, where it would be released in high concentrations. Two methods can be used to encapsulate a drug in an inorganic core/organic shell NPs: physical loading and chemical conjugation *via* labile bonds. The second method being more reliable, as chemical binding of the drug limits the leakage in a great extent through the polymer shell. In this study, DOX was efficiently encapsulated in the MNCs *via* heat- and acid-cleavable amine linkage with a conjugation efficiency of 82%, demonstrating a high efficacy of the drug loading process. The DOX content of the nanocarrier was calculated to be 7.6 wt%. A weight ratio of DOX to MNC of 1:10 was used, as a higher amount of DOX did not lead to significant increase in the conjugation efficiency.

4.3.10 *In vitro* drug release profiles

4.3.10.1 Drug release profiles as a function of pH and temperature

Plots for cumulative DOX release as a function of time without application of an AMF but at different temperatures, *i.e.* 25 °C, 37 °C and 50 °C, in PBS at pH = 7.4 or 5.7 are represented in Figure 4.31. While 50 °C may seem slightly high temperature to simulate hyperthermia, it was chosen because the existence of local heating effects in the vicinity of magnetic NPs has been demonstrated, leading to high temperatures at the magnetic NP surface without necessarily observing a significant increase in the surrounding medium.[182-184] For example, T. T. T. N'Guyen and co-workers demonstrated that by subjecting magnetic NPs to an AMF, they could initiate a retro-Diels-Alder reaction in the polymer layer functionalizing the magnetic NPs, which generally requires temperatures up to 90 – 110 °C.[181] Kim *et al.* showed that the amount of drug released from a thermo-sensitive micelle a 43 °C was found at least three times higher when the micelles were subjected to an AMF than when heated with a water bath, due to the direct thermal energy transfer from the SPIONs to the lipid layer.[312] Therefore, as the temperature was maintained *via* a water bath, we chose to use 50 °C to simulate magnetic hyperthermia conditions instead of the more widely used temperature of 45 °C.

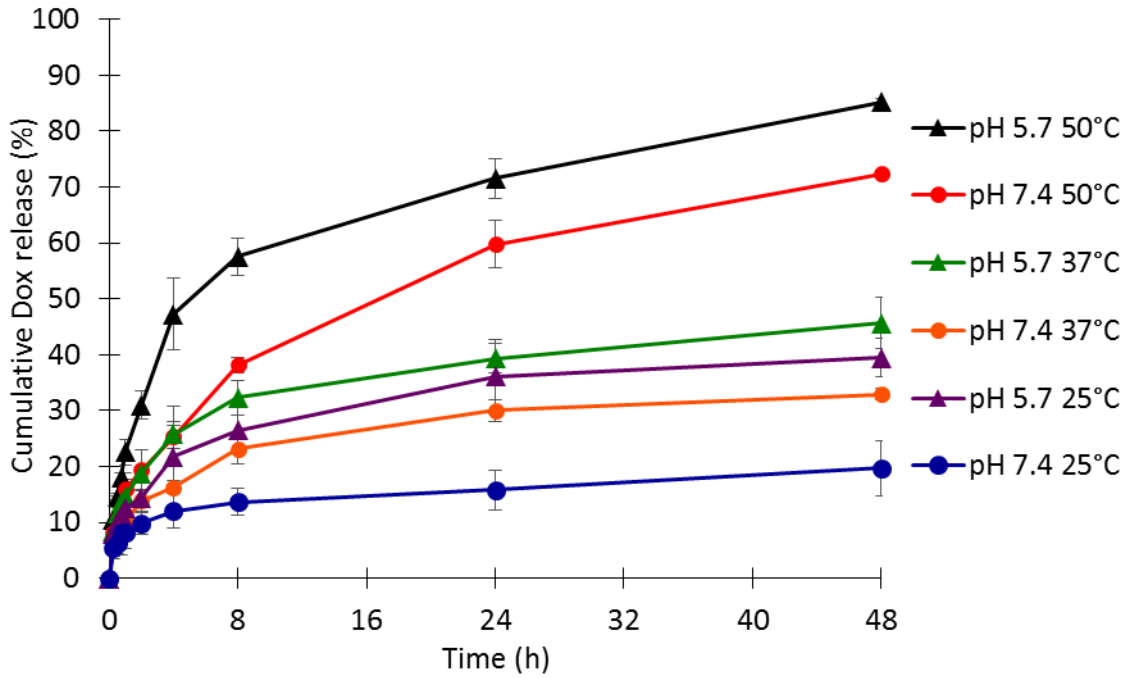

Figure 4. 31 *In vitro cumulative drug release profiles of DOX-MNCs dispersed in PBS at pH = 7.4 or pH = 5.7 at 25 °C, 37 °C and 50 °C.*

The drug release profiles of DOX-MNCs under each condition show two stages: a rapid release of DOX is obtained within 8 h followed by a slower rate of release. This behaviour is more pronounced at pH = 5.7 and 50 °C with 57.8 % of DOX released after 8 h and 85.2 % after 48 h, while at pH = 7.4 and 25 °C, 13.6 % of DOX is released after 8 h and 19.7 % after 48 h. However, with dialysis, one has to keep in mind that the apparent release rate is the neat results of drug transport across two barriers: diffusion from the nanoparticles followed by diffusion across the dialysis membrane.[277,278] As such, the release of the DOX is actually faster than what is shown with the results obtained from dialysis. This was proven by performing the dialysis of free DOX in section 4.3.8.

The pH and the temperature greatly influence the release behaviour of DOX. The minimal release of DOX is obtained at pH = 7.4 and 25 °C (followed by pH = 7.4 and 37 °C), because at room temperature and physiological pH the imine bond is quite stable and its hydrolysis kinetic is really slow. The initial small burst release of DOX at pH = 7.4 and 25 °C is probably due to physically adsorbed DOX on the outer shell of the polymer layer, despite the numerous washing of the DOX-MNCs. By using a pH stimulus, the amount of DOX released at 25 °C is doubled, with 26.5 % of DOX released after 8 h and 39.4 % after 48 h. This is because acidic pH facilitates the release of the drug by promoting the hydrolysis of the Schiff base bond (pK_a of imine bond is usually around 4). When only the temperature stimulus was used (pH = 7.4 and 50 °C), 38.1 % of DOX was released after 8 h and 72.3 % after 48 h. The maximal release of DOX was found at pH = 5.7 and 50 °C,

when the DOX-MNCs were exposed to both pH and temperature stimuli. The temperature has two different effects: first, it accelerates the rate of the hydrolysis reaction. Second, the polymer being thermo-responsive, upon reaching the LCST, the polymer becomes hydrophobic and shrinks, expelling its aqueous content and pushing the DOX molecules out at the same time. It should also be noted that at acidic pH, the primary amine group of free DOX is protonated (pK_a = 8.3), therefore increasing its solubility in aqueous medium and facilitating its expulsion out of the polymer layer. Thus, by combining both the effect of the pH and the temperature, a controlled release of the DOX can be obtained. A summary of the percentage of DOX released after 8 h and after 48 h for each temperature and pH conditions can be found in Table 4.5.

Table 4. 3 *Cumulative DOX released after 8 h and 48 h at the different temperature and pH conditions.*

Temperature (°C)	pH	Cumulative DOX released after 8 h (%)	Cumulative DOX released after 48 h (%)
25	7.4	13.6	19.7
25	5.7	26.5	39.4
37	7.4	23.1	33.0
37	5.7	32.3	45.6
50	7.4	38.1	72.3
50	5.7	57.8	85.2

4.3.10.2 Drug release kinetic and mechanism of release

In this system, the DOX molecules are chemically bound to the polymer shell of the MNCs. The drug release is therefore mainly dependant on two mechanisms; firstly, the cleavage of the imine bond to release the DOX molecules of the bond, and secondly diffusion of DOX molecules from the polymer matrix to the surrounding dialysis medium.

The use of mathematical models is necessary to predict the drug release kinetics of a particular system. In this study, different kinetic models *i.e.* first order kinetic, Higuchi and Korsmeyer-Peppas were used to fit the release data obtained for each pH and temperature condition applied. The release kinetic and mechanism of DOX from the DOX-MNCs nanosystem were therefore determined according to those mathematical models. The release parameters for each model (K_1, K_h, K_{kp} and n) are shown in Table 4.6 as well as the correlations values (R^2).

Table 4. 4 *Correlation coefficients and drug release parameters based on drug release data for each temperature and pH conditions.*

Temperature (°C)	pH	1st order		Higuchi		Korsmeyer-Peppas		
		K_1	R^2	K_h	R^2	K_{kp}	n	R^2
25	7.4	0.794	0.8188	2.352	0.8523	8.181	0.277	0.9918
25	5.7	0.288	0.8861	5.510	0.9204	12.530	0.361	0.9893
37	7.4	0.293	0.8821	4.589	0.9179	10.548	0.363	0.9911
37	5.7	0.353	0.9039	6.232	0.9040	14.841	0.378	0.9981
50	7.4	0.127	0.9385	10.585	0.9844	14.520	0.451	0.9913
50	5.7	0.259	0.9536	12.282	0.9177	22.175	0.475	0.9875

The first order kinetic model does not fit well with experimental data as manifested by low R^2 values, though an increasing of R^2 can be observed with increasing temperature and decreasing pH, suggesting a more concentration-dependant release kinetic. The Higuchi model also does not fit well with experimental data, even though it has better R^2 values than the first order model. The highest R^2 value is obtained with the Korsmeyer-Peppas model. Values for the release exponent *n* were found to be lower than 0.5 indicating a Fickian diffusion mechanism. However, an increase in the *n* values with the increasing temperature and decreasing pH can be observed, such as at pH = 5.7 and 50°C, the n value reached 0.475, which becomes close to the limit with anomalous diffusion. This can be attributed to the involvement of the imine bond cleavage, which becomes more and more important as the pH becomes more acidic and the temperature increases.

4.3.10.3 Drug release profiles in the presence of an AMF

The study of the drug release as a function of pH in the presence of an AMF was performed differently as the study of the drug release profiles as a function of pH and temperature. Indeed, it was not possible to introduce a dialysis setup in the MACH system, therefore the magnetic separation method was chosen. For each pH, one sample was held at 25 °C, and the other was exposed to an AMF of f = 950 kHz and H = 10.5 kA/m for either 15 min, 30 min or 1 h. Samples that were exposed to acidic pH and AMF were found to release DOX more rapidly than samples exposed to only one stimulus (Figure 4.32)

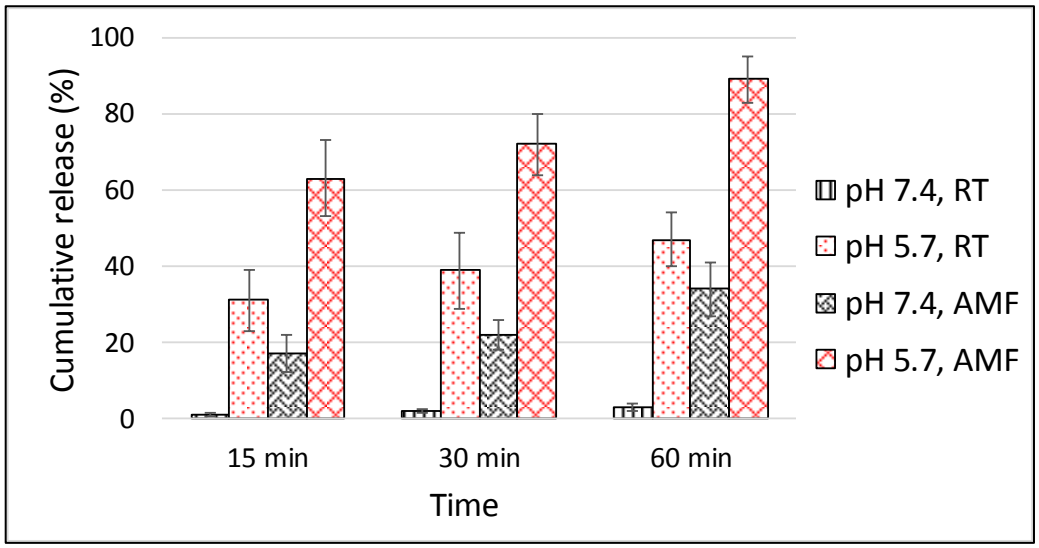

Figure 4. 32 *In vitro cumulative DOX release of DOX-MNCs dispersed in PBS at pH = 7.4 or pH = 5.7 with or without application of an AMF.*

After 1 h of hyperthermia at pH 5.7, 89% of DOX has been released, which is even more than the DOX released when the DOX-MNCs were heated with a water bath at 50 °C (85.2% after 48 h of dialysis). This might be due to the fact that the thermal energy is directly transferred from the SPIONs to the polymer layer.

4.4 Conclusions

In summary, a thermo-responsive polymer with a LCST around 40 °C has been synthesised via RAFT polymerisation. Highly crystalline iron oxide nanoparticles of 13 nm were obtained through a microwave-assisted co-precipitation method. These nanoparticles were superparamagnetic at room temperature with a high average saturation magnetisation of 78 emu/g. The magnetic properties of the nanoparticles were retained for long periods of time, with almost no loss of the saturation magnetisation three months after the synthesis. The as-synthesized IONPs were functionalized with the thermo-responsive polymer via a silanisation reaction. The functionalisation governing factors, i.e. the pH and the NPs:polymer ratio, were optimized to yield highly stable aqueous colloidal suspensions over time, under different pH conditions and in biological media. Considering the polymer content of the MNCs, it is likely that the polymer chains adopt a mushroom conformation.

Magnetic heating measurements performed with the MACH revealed that the MNCs exhibit an ILP of 2.1 nHm²/K. *In vitro* heating behaviour of the different samples showed

that the SAR is negatively affected by the presence of compact aggregates of nanoparticles in solution due to the increase of magnetic dipolar interactions within the aggregates.

High conjugation of the anticancer drug DOX to the MNCs was achieved through formation of heat- and acid-labile imine bonds using a weight ratio of DOX to MNC of 1:10. The DOX release behaviour was studied using the dynamic dialysis method. After careful choice of the dialysis membrane, plots for cumulative DOX release were obtained by studying the release of DOX as a function of time at different temperatures and pH conditions, *i.e.* 25 °C (room temperature), 37 °C (physiological temperature) and 50 °C (hyperthermia temperature), in PBS at pH = 7.4 (physiological pH) or 5.7 (tumour microenvironment/cellular organelles acidic pH). As expected, a minimum of DOX was released at physiological pH and room temperature, with less than 20% of DOX being released. The imine bond is stable under these conditions and therefore this was attributed to physisorbed DOX molecules on the outer shell of the polymer. A maximum of DOX was released under acidic pH and hyperthermia conditions, with more than 85% of DOX being released due to the dual stimuli-responsive features of the DOX-MNCs. An acidic pH facilitates the release of the drug by promoting the hydrolysis of the imine bond. Moreover, the primary amine group of free DOX molecules becomes protonated under acidic conditions, increasing its solubility in aqueous medium and facilitating its expulsion out of the polymer layer. Upon reaching the LCST, the polymer becomes hydrophobic and shrinks, expelling its aqueous content and pushing the DOX molecules out of the polymer due to squeezing effects. The temperature also accelerates the hydrolysis reaction rate. Study of the DOX release kinetic revealed that it follows the Korsmeyer-Peppas model and displays Fickian diffusion mechanism. Finally, samples that were exposed to acidic pH and an AMF were found to release even more DOX with 89% of DOX released after 1 h of hyperthermia.

The dual temperature-and pH-responsive behaviour of the nanocarrier is an important feature of the nanosystem to control where and when the drug is released. A burst release of the drug can be achieved under hyperthermia and tumour acidic pH conditions, as high temperature and acidic pH were shown to act as triggers for the release of the drug. At physiological pH and temperature, the amount of released drug is low; that is the drug is correctly retained in the nanocarrier, which is desirable in clinical applications to limit distribution of the drug to healthy tissues and unwanted side effects. The nanosystem developed here is therefore promising for thermo-chemotherapy applications.

CHAPTER 5

CELLULAR STUDIES ON CHEMOTHERAPY, MAGNETIC HYPERTHERMIA AND COMBINED THERMO-CHEMOTHERAPY FOR THERAPEUTIC APPLICATIONS

5.1 Introduction

In the previous chapter, a magnetic delivery system was developed for magnetic hyperthermia and drug delivery applications. Its good heating performances, high drug loading capability and on demand release properties as a result of pH and temperature stimuli make this nanocarrier an ideal candidate for thermo-chemotherapy applications.

The next step towards therapeutic applications of the DOX-MNCs for thermo-chemotherapy of cancer requires their testing in cellular systems. As discussed in the introductory chapter, hyperthermia has the potential to target cancer cells because healthy tissues are able to withstand elevated temperatures at which malignant cells undergo apoptosis.[21,22] Hyperthermia has also the potential to make cancer cells more sensitive to the effects of certain anti-cancer drugs,[42,46] and chemotherapy applied with concurrent hyperthermia can result in a synergistic effect.

This chapter focuses on the suitability of the DOX-MNCs for the killing of human glioma and breast cancer using U-87 and MCF-7 cell line models by thermo-chemotherapy. Firstly, the MNCs were tested for their biocompatibility. The IC_{50} values of free DOX and DOX-MNCs were evaluated on both cell lines for different incubation time. The cellular uptake of the nanoparticle as well as the fate of DOX in cells were investigated. Finally, the effect of magnetic hyperthermia, chemotherapy and the combinatorial treatment was assessed for both cell lines using two different treatment methods so that the effect of nanoparticle internalisation and hyperthermia temperature in the synergistic effect of the combined therapy could be studied.

5.2 Materials and methods

5.2.1 Reagents

Trypan blue solution (0.4%, sterile-filtered), accutase solution (sterile-filtered, for molecular biology), dimethyl sulfoxide (DMSO, for molecular biology, ≥ 99.9%), hydrochloric acid (HCl, 36.5%-38%, for molecular biology), potassium hexacyanoferrate trihydrate ($K_4Fe(CN)_6.3H_2O$) and nuclear fast red solution (0.1% w/v) were obtained from Sigma-Aldrich, UK. 3-(4,5-Dimethyl-2-thiazolyl)-2,5-diphenyl-2H-tetrazolium bromide (Thiazolyl Blue tetrazolium bromide, MTT, 98%) was obtained from Alfa Aesar, UK. Dulbecco's phosphate buffered saline (DPBS, no calcium, no magnesium, sterile) and trypsin (0.5%,

with ethylenediaminetetraacetic acid, no phenol red, sterile) were obtained from Gibco by Thermo Fisher Scientific. Ethanol (EtOH, 100%) was obtained from Hayman, UK.

Cell culture reagents: Minimum Essential Medium Eagle (MEM, with Earl's salt, non-essential amino-acids and sodium bicarbonate, no L-glutamine, sterile), was obtained from Sigma, UK. Dulbecco's modified Eagle's medium (DMEM, with 4.5 g/L D-glucose, 0.11 g/L sodium pyruvate, no L-glutamine, sterile) and Fetal Bovine Serum (FBS, sterile-filtered), L-glutaMAX (sterile) and antibiotics Penicillin/Streptomycin (P/S, sterile) were obtained from Gibco by Thermo Fisher Scientific, UK.

Unless stated, all reagents were used as purchased, without any further modifications.

5.2.2 Cell culture media

DMEM was supplemented with 1% penicillin/streptomycin used to prevent bacterial contamination of cell culture, 10% FBS and 1% L-glutaMAX. In the rest of the document, this will be referred to as complete DMEM. In this work, L-glutaMAX was used instead of L-glutamine. This is because L-glutaMAX is an improved cell culture supplement that can be used as a substitute of L-glutamine. Indeed, L-glutamine is a vital nutrient for cells to generate energy as well as for the synthesis of proteins and nucleic acids. However, L-glutamine spontaneously degrades in cell culture media, producing ammonia and pyrrolidone carboxylic acid as by-products. L-glutaMAX is more stable and is suitable for both adherent and suspension mammalian cell cultures. Cells cleave the dipeptide bond to release L-glutamine as needed. This system prevents waste build-up and maintains a fresh supply of L-glutamine during long-term culture.

MEM was supplemented with 1% P/S, 10% FBS and 1% L-glutaMAX. In the rest of the document, this will be referred to as complete MEM.

5.2.3 Buffers and stains

Prussian blue stained was always prepared fresh before use, by using a ratio 1:1 v/v of 4% HCl solution in Milli-Q water and 4% $K_4Fe(CN)_6.3H_2O$ solution in Milli-Q water.

Paraformaldehyde fixation buffer was prepared with the following percentage: 4% paraformaldehyde in DPBS.

FITC Annexin V apoptosis detection kit I (contains Annexin V-FITC, propidium iodide staining solution and Annexin V binding buffer) was obtained from BD Pharmingen, BD Biosciences, UK.

5.2.4 Experimental methods

5.2.4.1 Cell culture

5.2.4.1.1 U-87 human glioblastoma cell line and L929 mouse fibroblast cell line

Human glioblastoma cell line U-87 was cultured in 10 mL of complete DMEM medium in a T-75 culture flask and incubated at 37 °C under 5% CO_2 in a humidified atmosphere. When the cells reached 80% – 90% confluence, adherent cells were detached by trypsinization (see section 5.2.4.2) and seeded on a new tissue culture plate for subculture (cells passaging) or frozen and stored (see section 5.2.4.3), or used directly for experiments.

Mouse fibroblast cell line L929 was cultured in the same way as the U-87 cells (but in JAIST - Japan).

5.2.4.1.2 MCF-7 human breast cancer cell line

Human breast cancer cell line MCF-7 was cultured in 10 mL of complete MEM medium in a T-75 culture flask and incubated at 37 °C under 5% CO_2 in a humidified atmosphere. When the cells reached 80% – 90% confluence, adherent cells were detached by trypsinization (see section 5.2.4.2) and seeded on a new tissue culture plate for subculture (cells passaging) or frozen and stored (see section 5.2.4.3), or used directly for experiments.

5.2.4.2 Trypsinization of adherent cells

The cell culture medium was discarded and the cell layer washed with DPBS. 2 mL of pre-warmed trypsin at 37 °C was added to the cell layer. Trypsin is an enzyme that breaks down protein, to detach adherent cells from the flask they are being cultured. The culture flask was then returned to the incubator (37 °C, 5% CO_2) for 3 min. 8 mL of complete medium was added for a T-75 culture flask to inactivate the trypsin. The cells, now suspended in the medium, were centrifuged at 1200 rpm for 3 min to obtain a cell pellet. The supernatant was discarded and the cells were redispersed in 4 mL of fresh medium. The average number of viable cells in suspension was determined with the aid of a

hemocytometer and the trypan blue exclusion method. Trypan blue is a dye used to colour dead cells. The cell viability should be at least 90% for a healthy log-phase culture. After determining the number of cells/mL, the cells were either passaged and returned to culture in a new culture flask with approximately 1.10^6 cells in 10 mL of complete medium for a T-75 flask, or frozen for cryoconservation (see section 5.2.4.3), or used directly for experiments.

5.2.4.3 Cryoconservation of viable cells

5.2.4.3.1 U-87 human glioblastoma cell line

After trypsinization and counting of the U-87 cells as explained in section 5.2.4.2, the cell pellet obtained after centrifugation was re-suspended in the freezing media, composed of 95% complete DMEM and 5% DMSO. In the freezing media, DMSO is a cryoprotective agent. It is used to reduce the freezing point of the medium and to allow a slower cooling rate, therefore greatly reducing the risk of formation of ice crystals, which can damage cells and cause cell death. 1 mL aliquots containing a minimum of 1.10^6 cells/mL in cryovials were firstly placed in a freezing chamber partially filled with isopropanol to gradually freeze the cells to -80 °C at a rate of -1 °C/min. The next day, cryovials containing the cells were stored in liquid nitrogen for long conservation.

5.2.4.3.2 MCF-7 human breast cancer cell line

After trypsinization and counting of the MCF-7 cells as explained in section 5.2.4.2, the cell pellet obtained after centrifugation was re-suspended in the freezing media, composed of 90% complete MEM and 10% DMSO. 1 mL aliquots containing a minimum of 1.10^6 cells/mL in cryovials were firstly placed in a freezing chamber partially filled with isopropanol to gradually freeze the cells to -80 °C at a rate of -1 °C/min. The next day, cryovials containing the cells were stored in liquid nitrogen for long conservation.

5.2.4.4 Cells thawing from frozen storage

Cells stored in liquid nitrogen for cryoconservation were returned to culture by thawing the cryovial in a water bath maintained at 37 °C. The thawed cells were transferred to a centrifuge tube and pre-warmed complete medium at 37 °C (DMEM for U-87 cells and MEM for MCF-7 cells) was added dropwise into the cell suspension for a 10-fold dilution, while gently mixing the cells. In order to remove the cryoprotective agent DMSO that is harmful to cells in a non-frozen medium, the cell suspension was centrifuged at 1200 rpm for 3 min to obtain a cell pellet. The supernatant was discarded and the cells were

redispersed in 2 mL of fresh medium. The average number of viable cells in suspension was determined with the aid of a hemocytometer and the trypan blue exclusion method. The cell viability should be at least 90% to start a new culture from a frozen sample. After determining the number of cells/mL, the cells were cultured in 10 mL of complete medium in a T-75 culture flask is the number of viable cells was greater than 6.10^5 and in 5 mL of complete medium in a T-25 culture flask if the number of viable cells was lower than 6.10^5. The cells were then culture as explained in section 5.2.4.1, and were allowed to grow for one or two weeks (at least two passages) before being used for experiments.

5.2.4.5 Biocompatibility study of the MNCs on L929 cells by MTT assay

This experiment was performed in Japan and was the only *in vitro* experiment which was performed in JAIST. All the other studies were performed at UCL.

L929 cells were cultured as explained in section 5.2.4.1. After trypsinization, counting of the cells and confirmation that the cell viability was superior to 90% by trypan blue exclusion (section 5.2.4.2), cells suspended in a 0.1 mL complete DMEM medium at a concentration of 1.0 x 10^3 cells/well were plated in 96 well, flat-bottomed culture plates. After 72 h of incubation at 37 °C, 0.1 mL of medium containing different concentrations of sterile MNCs was added to the cells, followed by 48 h incubation at 37 °C. To evaluate the cell viability, 0.1 mL of MTT solution at a concentration of 300 µg/mL in complete DMEM medium was added to the cultured cells. After 4 h of incubation at 37 °C, the medium was removed, and 0.1 mL DMSO was added to each well to dissolve the purple formazan precipitate. The resulting color intensity, which is proportional to the number of viable cells, was measured using a microplate reader (VersaMax, Molecular Devices, USA) at 540 nm. The percentage of viable cells for each concentration of MNCs was determined based on the absorbance readings, and expressed as a percentage of the vehicle control as follows:

$$cell\ viability = \frac{absorbance_{test} - absorbance_{blank}}{absorbance_{control} - absorbance_{blank}} \quad (5.1)$$

Where $absorbance_{test}$ is the absorbance reading for a given concentration of MNPs, $absorbance_{control}$ is the absorbance reading of the control wells (containing only cells, not exposed to MNCs) and $absorbance_{blank}$ is the absorbance reading of the blank wells (containing only culture medium, no cells and no MNCs). MTT assay for the biocompatibility study of the MNCs on healthy cells was performed in duplicate.

5.2.4.6 Determination of the IC_{50} of free doxorubicin in MCF-7 and U-87 by MTT assay

MCF-7 and U-87 cells were cultured as explained in section 5.2.4.1. After trypsinization, counting of the cells and confirmation that the cell viability was superior to 90% by trypan blue exclusion (section 5.2.4.2), cells suspended in 0.2 mL complete culture medium (DMEM for U-87 cells and MEM for MCF-7 cells) at a concentration of 5.0 x 10^3 cells/well were plated in 96 well, flat-bottomed culture plates. Cells were allowed to adhere and grow by incubation at 37 °C for 24 h before exposure to drug treatment. Briefly the medium was removed from each well, and the cells were exposed to 0.2 mL of complete medium containing various fixed concentration of DOX for 24 h, 48 h or 72 h at 37 °C in the 5 % CO_2 incubator. DOX solution at 2.5 mg/mL was firstly prepared in DMSO and then diluted into the culture medium to obtain the desired concentration, as DOX solubility is low in cell culture medium. However, DMSO is toxic to cells and therefore the final percentage of DMSO in the well should not exceed 0.5 % of the total volume. Dilution from the most concentrated solution of DOX were made, meaning that the wells containing the highest concentration of DOX were also the ones containing the highest volume of DMSO (kept below 0.2% for each cell line). Control wells were therefore prepared to contain the highest percentage of DMSO used in the medium, in order to verify that DMSO had no toxic effect to cells at that percentage. At the end of incubation, culture medium was removed from each well. To evaluate the cell viability, MTT solution was added to the cells at a final concentration of 200 µg/mL in complete medium. After 4 h of incubation at 37 °C, culture medium was removed from each well, and 0.15 mL of DMSO was added to each well to dissolve the purple formazan precipitate. The resulting color intensity, which is proportional to the number of viable cells, was measured using a microplate reader (SpectraMax M2, Molecular Devices, USA) at 570 nm. The percentage of viable cells for each concentration of DOX was determined based on the absorbance readings, and expressed as a percentage of the vehicle control following Equation 5.1. All assays were performed in triplicate. Data obtained from the MTT assay were subject to median effect analysis using the CompuSyn® software to determine the half maximal inhibitory concentration (IC_{50}) of DOX on both MCF-7 and U-87 cell lines for each incubation period.

5.2.4.7 Determination of the IC_{50} of DOX-MNCs in MCF-7 and U-87 by MTT assay

MCF-7 and U-87 cells were cultured as explained in section 5.2.4.1. After trypsinization, counting of the cells and confirmation that the cell viability was superior to 90 % by trypan

blue exclusion (section 5.2.4.2), cells suspended in 0.2 mL complete culture medium (DMEM for U-87 cells and MEM for MCF-7 cells) at a concentration of 5.0 x 10^3 cells/well were plated in 96 well, flat-bottomed culture plates. Cells were allowed to adhere and grow by incubation at 37 °C for 24h before exposure to drug treatment. Briefly the medium was removed from each well, and the cells were exposed to 0.2 mL of complete medium containing various fixed concentration of DOX-MNCs for 24 h, 48 h or 72 h at 37 °C in the 5 % CO_2 incubator. At the end of incubation, culture medium was removed from each well. To evaluate the cell viability, MTT solution was added to the cells at a final concentration of 200 µg/mL in complete medium. After 4 h of incubation at 37 °C, culture medium was removed from each well, and 0.15 mL of DMSO was added to each well to dissolve the purple formazan precipitate. The resulting color intensity, which is proportional to the number of viable cells, was measured with the help of a microplate reader (SpectraMax M2, Molecular Devices, USA) at 570 nm. The percentage of viable cells for each concentration of DOX-MNCs was determined based on the absorbance readings, and expressed as a percentage of the vehicle control following Equation 5.1. All assays were performed in triplicate. Data obtained from the MTT assay were subject to median effect analysis using the CompuSyn® software to determine the IC_{50} of DOX on both MCF-7 and U-87 cell lines for each incubation period.

5.2.4.8 Histology and visualization of MNCs internalization in cells

MCF-7 and U-87 cells were cultured, trypsinized and counted as explained in section 5.2.4.1 and 5.2.4.2. For histology study and visualization of nanoparticles internalization in both MCF-7 and U-87 cancer cells, cells suspended in 1 mL of complete medium were seeded in 24 well, flat-bottomed culture plates containing glass coverslips, at a density of 50,000 cells/well. Cells were incubated at 37 °C for 72 h to be allowed to reach confluence. After growing the cells to confluence, the medium was removed from each well and 1 mL of complete medium containing different concentration of sterile MNCs (i.e. 1 mg/mL, 0.5 mg/mL, 0.1 mg/mL, 0.05 mg/mL, 0.01 mg/mL and 0.00 mg/mL) was added to the wells. The cells were then incubated for either 4 h or 24 h at 37 °C. The culture medium was then removed from each well, and the cells were washed three times with pre-warmed complete medium (37 °C) and twice with pre-warmed DPBS (37 °C) to remove the nanoparticles not internalized or attached to the cells. Cells were then fixed with paraformaldehyde buffer (400 µL, 30 min, room temperature), and rinsed twice with DPBS. Cells were stained for iron content by Prussian blue staining (310 µL, 2 min), rinsed twice with Milli-Q water, and counterstained with nuclear fast red (400 µL, 2 min). Stained cells were then rinsed twice with Milli-Q water, and dehydrated with ascending alcohol, 70% EtOH (2 min) and 100%

EtOH (5 min) and mounted onto microscope slides. Stained cells were observed by light microscopy using an inverted microscope (DMI6000B, Leica, UK).

5.2.4.9 Quantification of the cellular uptake of MNCs using a SQUID magnetometer

Cells were cultured, trypsinised and counted as explained in section 5.2.4.1 and 5.2.4.2. For the quantification of nanoparticles internalization in both MCF-7 and U-87 cancer cells, cells suspended in 2 mL of complete medium were seeded in 12 well, flat-bottomed culture plates at a density of 100,000 cells/well. Cells were incubated at 37 °C for 72 h to be allowed to reach confluence. After growing the cells to confluence, the medium was removed from each well and 1 mL of complete medium containing different concentration of sterile MNCs (*i.e.* 1 mg/mL, 0.5 mg/mL, 0.1 mg/mL, 0.05 mg/mL, 0.01 mg/mL and 0.00 mg/mL) was added to the wells. The cells were then incubated for either 4 h or 24 h at 37 °C. The culture medium was then removed from each well, and the cells were washed three times with pre-warmed complete medium (37 °C) and twice with pre-warmed DPBS (37 °C) to remove the nanoparticles not internalized or attached to the cells. Cells were then detached by trypsinization (0.4 mL, 3 min, 37 °C), re-suspended in 2 mL of complete media and centrifuged (1200 rpm, 3 min, 4 °C). The supernatant was discarded and the cell pellet was re-dispersed in 0.5 mL of complete media. The cell density was counted with the aid of a hemocytometer and the cells were pelletized again by centrifugation (1200 rpm, 3 min, 4 °C). The cell pellet was transferred into powder polycarbonate sample holder for SQUID-VSM as a suspension, and dried in a low temperature oven at 37 °C overnight before carrying out the magnetic measurements.

5.2.4.10 Fluorescence imaging of free DOX and DOX-MNCs in cells

MCF-7 and U-87 cells were cultured, trypsinized and counted as explained in section 5.2.4.1 and 5.2.4.2. For fluorescence study and visualization of DOX internalization in both MCF-7 and U-87 cancer cells, cells suspended in 1 mL of complete medium were seeded in 24 well, flat-bottomed culture plates containing glass coverslips, at a density of 50,000 cells/well. Cells were incubated at 37 °C for 72 h to be allowed to reach confluence. After growing the cells to confluence, the medium was removed from each well and 1 mL of complete medium containing different concentration of free DOX or DOX-MNCs (i.e. 4 µg and 2 µg) was added to the wells. The cells were then incubated for either 3 h or 24 h at 37 °C. The culture medium was then removed from each well, and the cells were washed

four times with pre-warmed complete medium (37 °C) to remove the free DOX or the nanoparticles not internalized in the cells. Cells were then washed twice with DPBS and fixed with paraformaldehyde buffer (400 µL, 30 min, room temperature), and rinsed twice again with DPBS. Cell nuclei were stained with DRAQ5 in the dark (5 µM, 15 min, room temperature). Stained cells were then rinsed once with Milli-Q water, and mounted onto microscope slides with either FluorSave or FluorPreserve mounting medium. Stained cells were observed by fluorescence microscopy using an inverted microscope (DMI6000B, Leica, UK) with an excitation wavelength of 488 nm for both DOX and DRAQ5. Fluorescence emissions of DOX and DRAQ5 were observed using a rhodamine (N3 ET, 600/40 bandpass filter, Leica) and a far-red (Y5 ET, 700/75 bandpass filter, Leica) filter sets, respectively. Images were captured using LAS X software.

5.2.4.11 In vitro anticancer studies by trypan blue dye exclusion assay

For *in vitro* anticancer studies, two methods were employed: hyperthermia treatment after internalization of the nanoparticles in the cells and direct hyperthermia treatment.

5.2.4.11.1 Treatment after internalization

The treatment after internalization consists in using only the nanoparticles internalized in the cells for the hyperthermia treatment. To that aim, cells and MNCs are incubated together for 24 h. The cells are then washed before being subjected to the hyperthermia treatment.

MCF-7 and U-87 cells were cultured, trypsinized and counted as explained in section 5.2.4.1 and 5.2.4.2. Cells suspended in 1 mL of complete medium were seeded in 12 well, flat-bottomed culture plates, at a density of 150,000 cells/well. Cells were incubated at 37 °C for 24 h before replacing the medium from each well with 1 mL of fresh complete medium only or containing MNCs or DOX-MNCs. The cells were then incubated for an additional 24 h at 37 °C. Six groups were formed: control- (media only, no AMF), control+ (media only, AMF), MNCs- (media containing MNCs, no AMF), MNCs+ (media containing MNCs, AMF), DOX-MNCs- (media containing DOX-MNCs, no AMF) and DOX-MNCs+ (media containing DOX-MNCs, AMF). Therefore, the group MNCs+ corresponds to hyperthermia treatment, DOX-MNCs- corresponds to chemotherapy treatment, and DOX-MNCs+ corresponds to thermo-chemotherapy treatment. A concentration of MNCs of 1 mg/mL was used for each group. After the 24 h incubation period, the three AMF positive groups (control+, MNCs+ and DOX-MNCs+ groups) were exposed to an AMF (H = 10.5

kA/m and f = 950 kHz) for 1 h using the MACH instrument. To that aim, the supernatant in each well was discarded to keep only the nanoparticles internalized or adsorbed on the cell surface. The cells were trypsinized with 0.4 mL trypsin (3 min, 37 °C) and 2 mL of fresh complete media was added. The cells were centrifuged (1200 rpm, 5 min, 4 °C), and the obtained pellet was redispersed in 0.5 mL complete media, and transfer into a vial for hyperthermia treatment. The cells in the three AMF negative groups (control-, MNCs- and DOX-MNCs- groups) were subjected to the same protocol, without being subjected to an AMF, in order to remove any environmental effect on cell death. After hyperthermia treatment, the cell suspension was properly mixed and separated in two, so that it could be seeded in two different 12 well, flat-bottomed culture plates. The volume of the cell suspension was adjusted to 1 mL for each well and the cells were incubated at 37 °C. One plate was analyzed 24 h later while the other one was analyzed after 48 h. Cell viability was determined using trypan blue dye exclusion method. Cells were trypsinized with 0.4 mL trypsin (3 min, 37 °C) and 1 mL of fresh media was added. 50 µL of cell suspension was mixed with 50 µL of sterile-filtered trypan blue. Cells were counted with the aid of a hemocytometer. Values of viability of treated cells were expressed as a percentage of that from corresponding control cells. All experiments were repeated at least three times.

The combined effect of the thermo-chemotherapy treatment was evaluated by the Valeriote's method. With (A), (B) and (A + B) representing the percentage of cell viability for treatments A (hyperthermia) and B (chemotherapy) and A + B (thermo-chemotherapy treatment). Combined effects were defined as follows:[313,314]

- synergistic: (A + B) < (A) × (B)/100
- additive: (A + B) = (A) × (B)/100
- sub-additive: (A) × (B)/100 < (A + B) < (A) if (A) < (B)
- interference: (A) < (A + B) < (B), if (A) < (B)
- antagonistic: (B) < (A + B), if (A) < (B).

5.2.4.11.2 Direct hyperthermia treatment

The direct hyperthermia treatment consists in using only nanoparticles that are not internalized in the cells, but are in the surrounding medium for the hyperthermia treatment. To that aim, the hyperthermia treatment is applied directly after mixing the cells with the MNCs. The same protocol as for the treatment after internalisation method was used, excepted that the nanoparticles were added only right before the exposure of the cells to an AMF for hyperthermia treatment.

MCF-7 and U-87 cells were cultured, trypsinized and counted as explained in section 5.2.4.1 and 5.2.4.2. Cells suspended in 1 mL of complete medium were seeded in 12 well,

flat-bottomed culture plates, at a density of 150,000 cells/well. Cells were incubated at 37 °C for 24 h before replacing the medium from each well with 1 mL of fresh complete medium and the cells were then incubated for an additional 24 h at 37 °C. The cells were trypsinized with 0.4 mL trypsin (3 min, 37 °C) and 2 mL of fresh complete medium was added. The cells were centrifuged (1200 rpm, 5 min, 4 °C), and the obtained pellet was redispersed in a volume of 0.5 mL of fresh complete media only, or containing the desired amount of MNCs or DOX-MNCs, and transferred into a vial for hyperthermia treatment. Again, six groups were formed as previously described in section 5.2.4.11.1. The concentration of MNCs in solution was adapted to obtain the desired temperature. A concentration of 75 µg/mL was used for the hyperthermia treatment at 40 °C, that was also calculated as the concentration of nanoparticle being internalized after exposure of U-87 cells for 24 h with a solution of 1 mg/mL of MNCs. A concentration of 200 µg/mL and 300 µg/mL were used for the hyperthermia treatment at 42 °C and 44 °C, respectively. The three AMF positive groups (control+, MNCs+ and DOX-MNCs+ groups) were exposed to an AMF (H = 10.5 kA/m and f = 950 kHz) for 1 h using the MACH instrument. The cells in the three AMF negative groups (control-, MNCs- and DOX-MNCs- groups) were subjected to the same protocol, without being subjected to an AMF, in order to remove any environmental effect on cell death. After hyperthermia treatment, the cell suspension was properly mixed and separated in two, so that it could be seeded in two different 12 well, flat-bottomed culture plates. The volume of the cell suspension was adjusted to 1 mL for each well and the cells were incubated at 37 °C. One plate was analyzed 24 h later while the other one was analyzed after 48 h. Cell viability was determined using trypan blue dye exclusion method as previously explained in section 5.2.4.11.1. All experiments were repeated at least three times.

The combined effect of the thermo-chemotherapy treatment was evaluated by the Valeriote's method as described in section 5.2.4.11.1.

5.2.4.12 Statistical analysis

Statistical analysis was performed using the Student's t-test for unpaired data and the results are presented as mean ± standard deviations. Statistical significance was accepted at a level of $p < 0.05$.

5.3 Results and discussion

5.3.1 Biocompatibility of the MNCs

The first experiment to be performed *in vitro*, is to verify that the nanoparticles are biocompatible. Indeed, a good biocompatibility is fundamental for *in vivo* use and further clinical use. A good biocompatibility is achieved when a material interacts with the body and its biological environment without inducing intolerable degree of toxic, carcinogenic, immunogenic and thrombogenic responses. It is well-known that the biocompatibility of a material is affected by their physical and chemical properties, such as composition, shape, size, surface chemistry and charge, and stability.[290,315] Therefore, surface engineering of nanoparticles to find an appropriate surface coating is required. The coating plays an important role in the biocompatibility as it determines the physicochemical properties of the surface, hydrophilicity/hydrophobicity degree, the surface charge and influence the colloidal stability.[316] The surface coating of the MNCs is made of a hydrophilic polymer mainly composed of PEG chains. PEG is one of the most promising coating materials for biomedical applications due to its good biocompatibility, and its ability to provide a steric barrier to protein adsorption, resulting in reduced uptake by macrophages of the reticulo-endothelial system, and therefore increases the blood circulation lifetime of the nanoparticle.[317] PEG was also demonstrated to diminish cell adhesion, and materials coated with PEG do not show antigenic activity. PEG also suppresses platelet adhesion, reducing risk of thrombus formation and tissue damage.[318]

As such, biocompatibility studies on a L929 mouse fibroblast cell line was performed by MTT assay to assess the biocompatibility of the MNCs with healthy cells after 48 h of exposure with various concentration of MNCs (Figure 5.1).

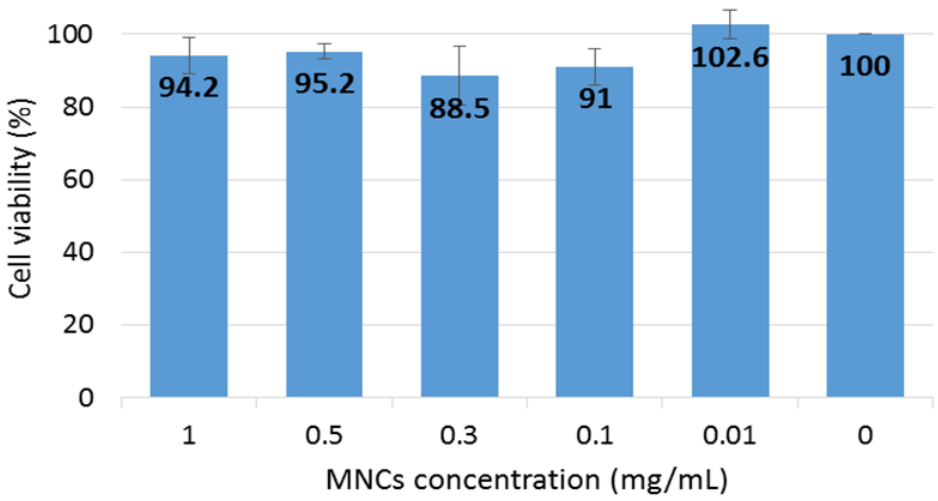

Figure 5. 1 *Biocompatibility study on L929 cells in the presence of MNCs for concentration ranging from 0.0 mg/mL to 1.0 mg/mL.*

No apparent cytotoxicity of the MNCs towards healthy cells was observed for concentration up to 1.0 mg/mL, indicating a good biocompatibility of the nanosystem.

5.3.2 Nanoparticle cellular uptake

The cell plasma membrane is the interface regulating any exchange between the intracellular and extracellular environment. For example, cellular internalization of vital small molecules such as sugars, water or amino-acids occurs via membrane diffusion or through membrane channels.[319] The internalization of larger entities such as nanoparticles occurs via endocytosis. During the endocytic process, membrane-bound vesicles called endosomes are formed. They engulf the nanoparticles and carry them into the cells. The main intracellular endocytic mechanisms are briefly described here, and more detailed information can be found elsewhere.[319-321] Endocytosis takes place by multiple pathways and can be divided into two broad categories, phagocytosis (the uptake of large particles) and pinocytosis (the uptake of fluids and solutes).

Phagocytosis is primarily used by specialized cells, such as macrophages and monocytes, whose role is to clear dead cells, cell debris and pathogens. Phagosomes formation starts with cup-shaped membrane protrusions, which gradually surround and enclose the particles (Figure 5.2). Different modes of phagocytosis can be observed dependent on the receptor that recognizes the particles to be ingested and the particle itself. The size of a phagosome depends on the size of the particle, and can range from hundreds of nanometers to dozens of micrometers.[320]

Pinocytosis, unlike phagocytosis, exists in all type of cells. Pinocytosis can further be classified into at least four basic mechanisms: macropinocytosis, clathrin-mediated endocytosis, caveolae-mediated endocytosis, and clathrin- and caveolae-independent endocytosis.

Macropinocytosis involves the formation of membrane ruffles that protrude to engulf a large amount of extracellular fluid and particles. The membrane ruffles then close by fusing with the plasma membrane, generating vacuoles called macropinosomes (Figure 5.2). The macropinosomes are the larger vesicles that can be formed during a pinocytosis process, with size ranging from 0.5 to 10 µm.

Clathrin-mediated endocytosis (CME) is the common pathway of cellular entry in all mammalian cells. It carries out the constant supply in nutrients to the cells. CME is triggered by transmembrane receptor-ligand binding, which are then engulfed through the formation of coated pits, formed by the assembly of clathrin cytosolic proteins (Figure 5.2).

The pits self-assemble into polygonal cages, to form clathrin-coated vesicles of size around 120 nm.

Caveolae-mediated endocytosis can particularly be found in endothelial cells. It is triggered by the binding of the cargo to caveolin membrane proteins. The cargo is engulfed in flask-shaped caveolae of size ranging from 50 to 80 nm (Figure 5.2).

Clathrin- and caveolae-independent endocytosis occurs in cells lacking clathrin and caveolin proteins. There are multiple entry pathways, which are likely to depend on many parameters, including the nature of the cargo molecule. However, mechanisms behind clathrin- and caveolae-independent endocytosis are still poorly understood.

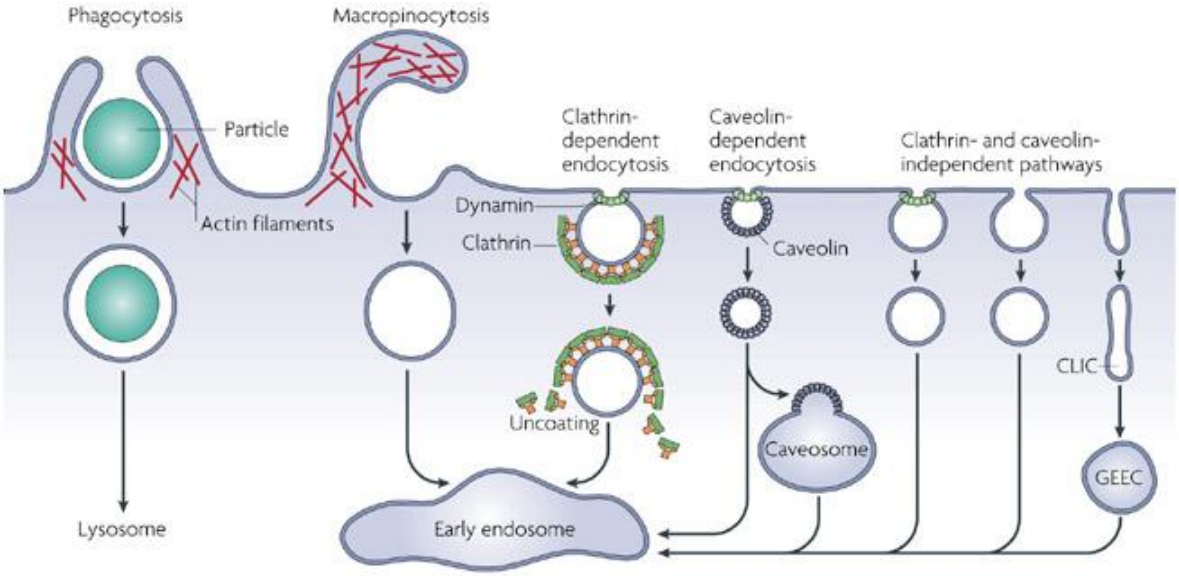

Figure 5. 2 *Schematic representation of the different endocytic pathways.*[322]

The nature of a nanomaterial, including its structure and physicochemical properties (composition, size, morphology, surface charge and chemistry and degree of hydrophobicity/hydrophilicity), greatly influence the endocytic process by which it will be internalized in the cells.[320,321,323-325] Usually, each type of particles exhibits a preferential uptake pathway. For example, in nonphagocytic cells, the internalization of charged iron oxide nanoparticles is favoured as compared to their uncharged counterparts, and the positively charged ones seem to be preferred over the negatively charged particles.[323] Positively charged particles appears to be mainly internalized through CME or macropinocytosis, while negatively charged particles were shown to be more likely internalized via caveolae-mediated endocytosis and clathrin- and caveolae-independent endocytosis.[320,325] But exceptions exist, and some charged/uncharged particles can also be taken up through multiple endocytosis pathways. In term of size, it is commonly believed that particles need to have a diameter between 10 to 100 nm to enter cells. However, these small particles may be internalized faster but studies revealed that

particles up to 5 µm in size can enter cells through macropinocytosis.[320] Nanoparticle suspensions often have a size distribution and not a specific size, mainly depending on the aggregation and polydispersity of the nanoparticles. Thus, a given type of nanoparticle can enter cells using different pathways depending on its size. In the case of non-specific adhesion to cells, small nanoparticles of diameters less than 10 nm are not internalized via endocytosis, but can enter cells through other routes such as diffusion through the membrane.[321] In the case of specific interactions, small nanoparticles coat the plasma membrane before being taken up by cells, while bigger particles are internalized immediately.[324] This may be due to the insufficient interaction with receptors of the cell membrane to trigger an endocytic response. The concentration of nanoparticles at which cells are exposed can also influence the uptake pathway. A study showed that at a low concentration, nanoparticles may have cross the membrane individually through diffusion process, while at higher concentrations, nanoparticles were taken up as clusters, enclosed inside vesicles, which is sign of an endocytic pathway.[326] As a consequence, the uptake of nanoparticles may not be proportional to the concentration. In term of morphology, the highest uptake seems to be obtained for spherical-shaped nanoparticles as compared to nanoparticles of other shape. This behaviour has been observed for gold nanoparticles, where spherical nanoparticles enter cells more easily than rods.[325] Molecular simulations predict that the fastest internalization rate is obtained for spherical nanoparticles, followed by cubic, rod and then disk nanoparticles.[327] For rod-like particles, the aspect ratio plays an important role: a high aspect ratio leads to the particles being internalized with their long edge parallel to the membrane therefore requiring longer membrane wrapping time due to high wrapping fraction, while rods with low aspect ratio enter cells tip first.[328]

Finally, the uptake of nanoparticle is also highly dependent on the cell or tissue type. Different internalization pathways for a same particle have already been observed between healthy and cancer cells. This may help to selectively target cancer cells. For example, a polymeric micelle was shown to selectively be cytotoxic to cancer cells. The micelles were not entering healthy endothelial cells even after 24 h, while they were reaching lysosomes in 30 min in cancer cells.[329] As a consequence, it is critical to evaluate the suitability of a given nanomaterial on different cell types.

5.3.2.1 Histology and visualization of MNCs internalization in cells

The ability of a cell or tissue to uptake nanoparticles can vary between different cells or tissue types. Therefore, it was important to investigate the cellular uptake of the MNCs was on both MCF-7 and U-87 cell lines. Different concentration of MNCs ranging from 0.0

mg/mL to 1.0 mg/mL and different incubation time of the cells in contact with the MNCs (i.e. 4 h and 24 h) were studied. Iron oxide nanoparticles were stained with Prussian blue, and the cells counterstained with nuclear fast red before observing by light microscopy. No significant morphological changes were observed after incubation of the MNCs with both cancer cell lines, even with the highest concentration of MNCs and 24 h of incubation. The cellular uptake of the MNCs is clearly dependent on both the nanoparticle concentration and the exposure time for both cell lines (Figure 5.3 and Figure 5.4). The presence of Prussian blue staining inside the cells is due to the presence of iron oxide nanoparticles, therefore confirming the cellular internalization of the MNCs. A higher MNCs concentration as well as a longer incubation times lead to an increase in the cellular uptake as exhibited from the increase Prussian blue staining for the iron. However, because cell images obtained by light microscopy are only 2D images, nanoparticles internalized in the cells and nanoparticles only adsorbed on the cell membrane cannot be distinguished. U-87 cells seem to take up more MNCs as compared to the MCF-7 cells as can be seen from the higher amount of Prussian blue staining for a same nanoparticle concentration and incubation time (Figure 5.3 and Figure 5.4). Only images acquired after incubation with media only (negative control), or with a solution containing 0.1 mg/mL, 0.5 mg/mL and 1.0 mg/mL of MNCs are shown in Figure 5.3 and Figure 5.4. Smaller tested concentrations of 0.01 mg/mL and 0.05 mg/mL are not presented as almost no particles can be observed in the cells.

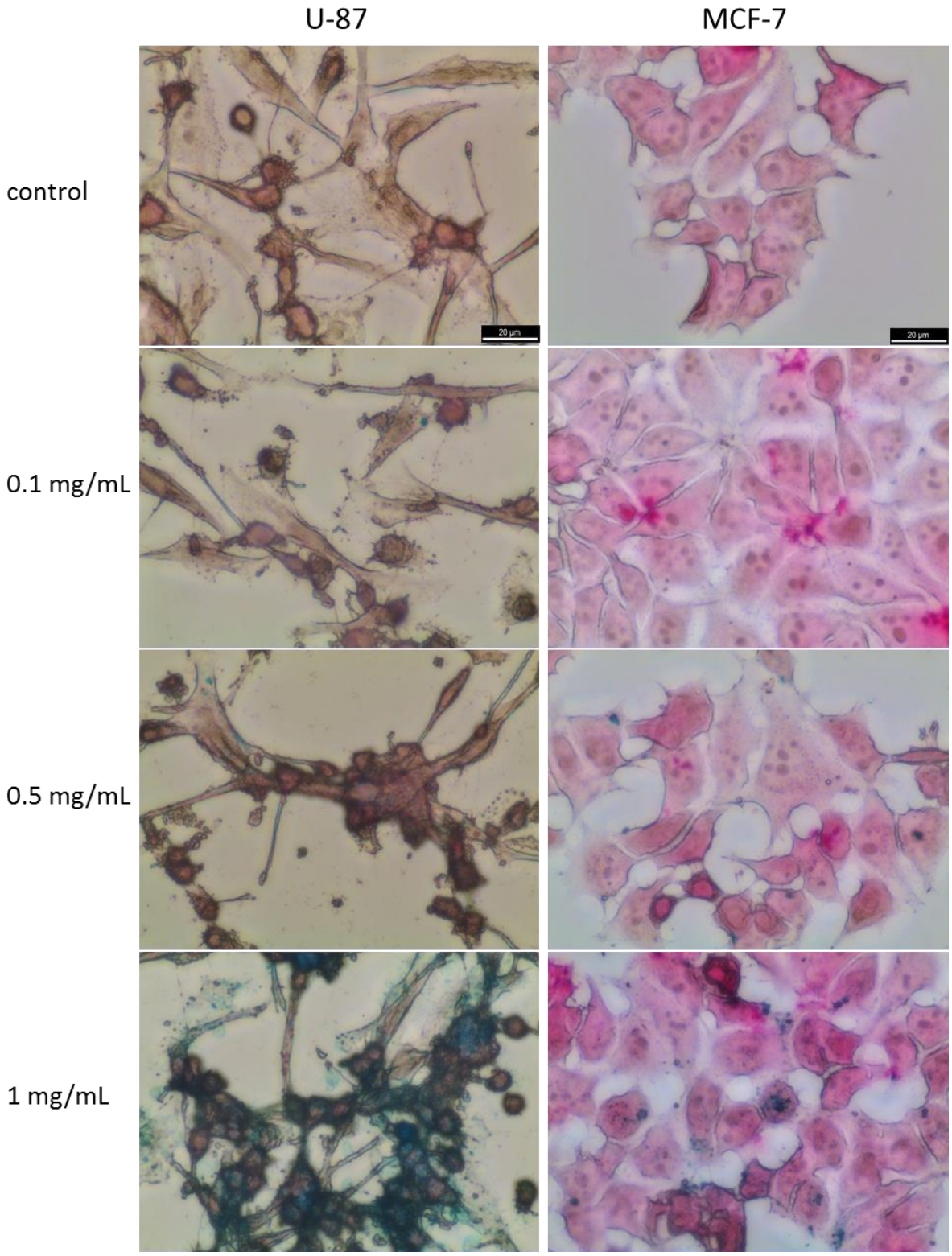

Figure 5. 3 *Microscope images of human glioblastoma U-87 cells and human breast adenocarcinoma MCF-7 cells loaded with MNCs after 4 h of incubation with a solution containing different concentration of MNCs, i.e. no particles, 0.1 mg/mL, 0.5 mg/mL and 1.0 mg/mL. Cells were stained with Prussian blue and counterstained with nuclear fast red. Scale bar: 20 µm.*

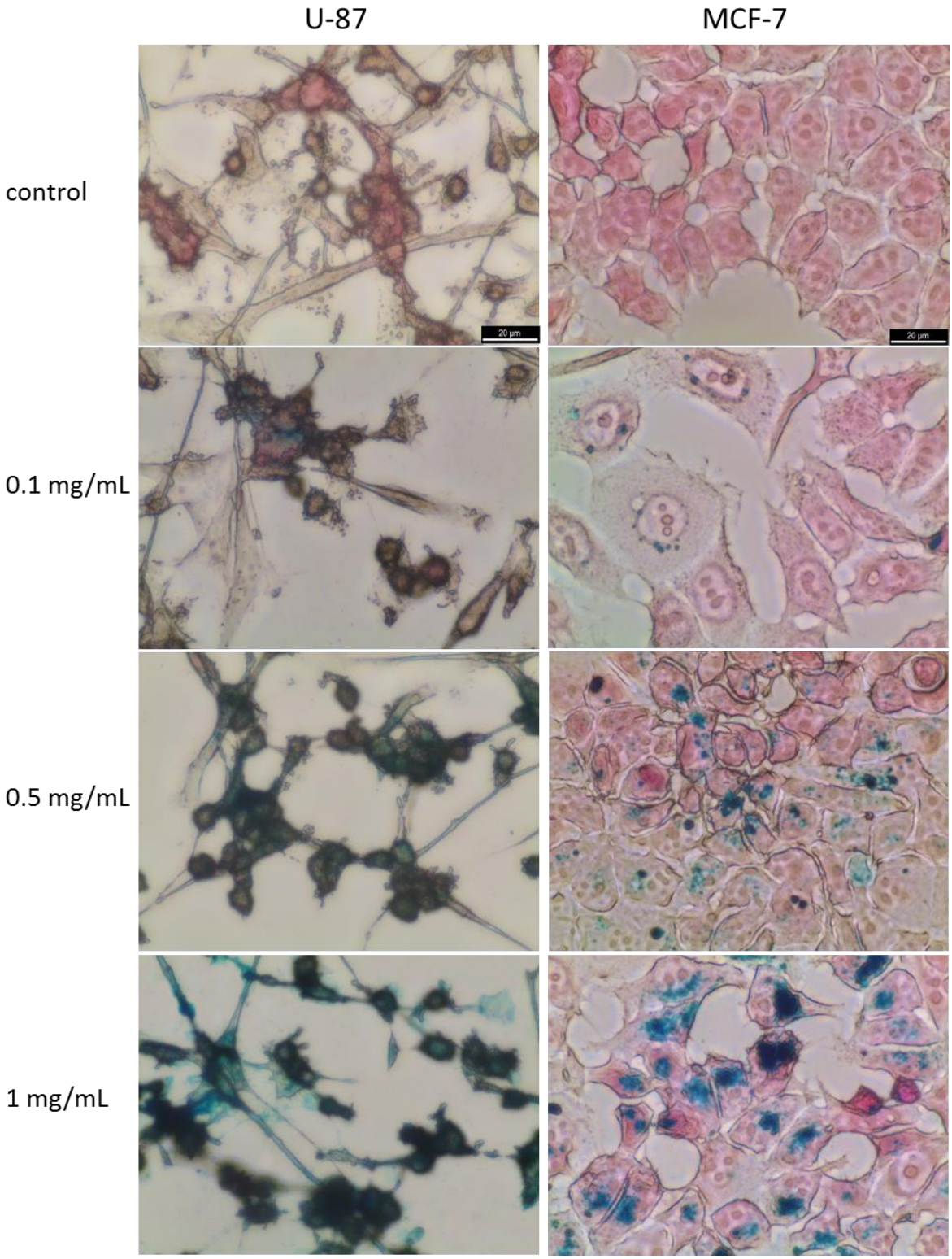

Figure 5. 4 *Microscope images of human glioblastoma U-87 cells and human breast adenocarcinoma MCF-7 cells loaded with MNCs after 24 h of incubation with a solution containing different concentration of MNCs, i.e. no particles, 0.1 mg/mL, 0.5 mg/mL and 1.0 mg/mL. Cells were stained with Prussian blue and counterstained with nuclear fast red. Scale bar: 20 µm.*

5.3.2.2 Quantification of MNCs cellular uptake

Cellular internalisation of the MNCs could be observed by flow cytometry in both U-87 and MCF-7 cell lines (Figure 5.5). An increase of the SSC when cells have been incubated with MNCs can be observed as compared to cells culture in media only. As the side scattered light increases with the degree of loading due to a change in cell granularity upon internalisation of nanoparticles, it can be concluded that both cell line internalized the MNCs in some extent. The increase in side scattered light compared to non-loaded cells seems to be greater in the case of U-87 cells, indicating that U-87 cells internalize more MNCs than MCF-7 cells.

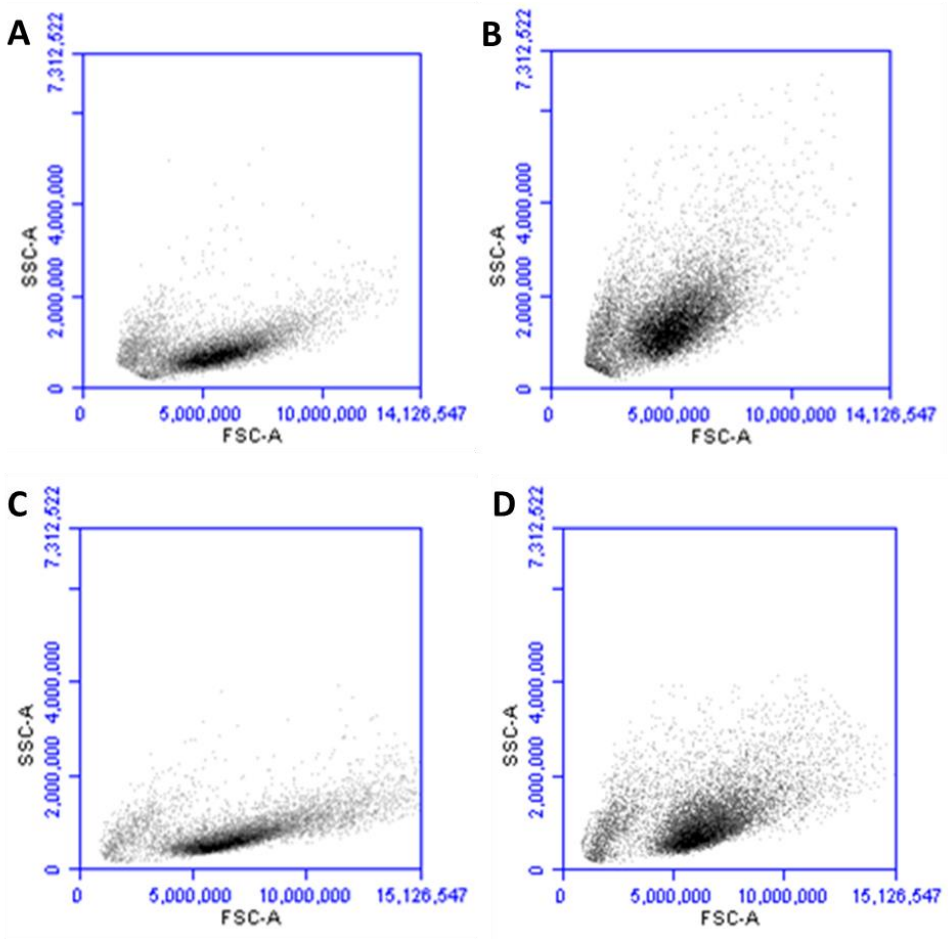

Figure 5. 5 *Side scatter as a function of forward scatter flow cytometry dot plots of A) human glioma U-87 cells loaded with no particles, B) loaded with MNCs and of C) human breast cancer MCF-7 cells loaded with no particles and D) loaded with MNCs. Cell debris have been removed for simplification.*

Cell uptake was quantitatively determined by magnetic measurements using the SQUID magnetometer on cell samples loaded with MNCs. Table 5.1 summarizes the different results obtained for each tested conditions. The results confirm what was observed by cell staining and flow cytometry, cell uptake increased with the concentration of MNCs in

solutions and a clear variation of cell uptake with cell type is observed. U-87 cells uptake the MNCs in larger quantity with a maximum non-targeted cell uptake of 125 pg(Fe_3O_4)/cell as compared to only 13 pg(Fe_3O_4)/cell for MCF-7 cells in the same conditions.

Table 5. 1 *MNCs uptake expressed in pg(Fe_3O_4)/cell from magnetic measurements on MCF-7 and U-87 cells for incubation time of 4 h and 24 h with the MNCs and concentrations ranging from 0.01 mg/mL to 1.00 mg/mL in solution.*

Cell line	*Time (h)*	*MNC concentration (mg/mL)*				
		0.01	0.05	0.10	0.50	1.00
MCF-7	4	/	/	1	3	6
	24	/	/	2	5	13
U-87	4	/	2	7	15	32
	24	2	6	12	55	125

5.3.3 Determination of the IC_{50} of free DOX and DOX-MNCs in MCF-7 and U-87

The MTT metabolic activity assay was performed to examine and compare the cytotoxicity of free DOX and DOX-MNCs and determine the IC_{50} values of the drug on both cell lines. The concentration effect of DOX in both formulations as well as the exposure time on the cell viability were investigated. Incubation time points of 24 h, 48 h, and 72 h were chosen. For each condition, the IC_{50} values were calculated. IC_{50}, the half maximal inhibitory concentration, is the concentration of drug at which only 50% of the cells remains viable. It is therefore in this case, an assessment of the effectiveness of the drug for those particular two cell lines. The IC_{50} values for each condition were determined by constructing a dose-response curve according to the results obtained from the MTT viability assays. The IC_{50} values are summarized in Table 5.2. For both the breast cancer cells and glioma cells, the cytotoxicity of free DOX was dependent on concentration and exposure time (Figure 5.6A and 5.6B). The IC_{50} values decrease as the exposure time increases. The IC_{50} values for U-87 cells exposed to free DOX are 0.13 µg/mL, 0.06 µg/mL and 0.04 µg/mL for an incubation period of 24 h, 48 h and 72 h, respectively. The IC_{50} values for MCF-7 cells exposed to free DOX are 0.95 µg/mL, 0.29 µg/mL and 0.16 µg/mL for an incubation period of 24 h, 48 h, and 72 h, respectively. By comparing the IC_{50} values for U-87 cells and MCF-7 cells for a same incubation time, it is clear free DOX is more cytotoxic towards the glioma cell line than the breast cancer cell line.

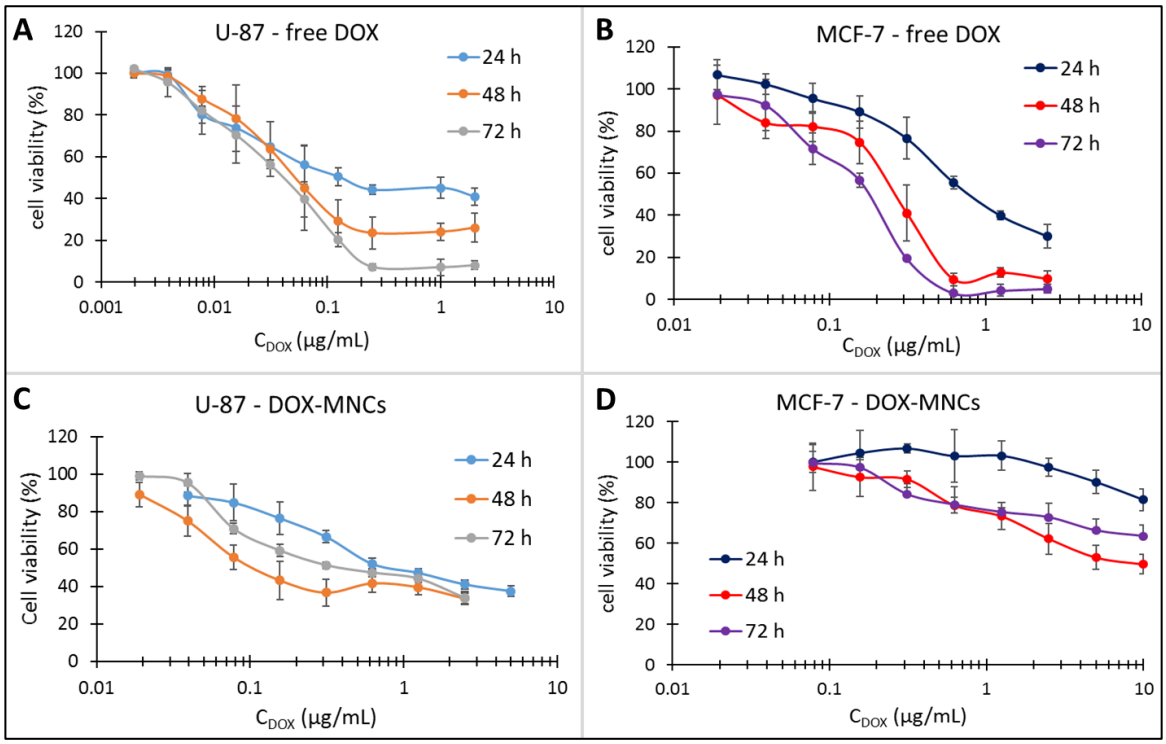

Figure 5. 6 *Dose response curves. Cell viability of U-87 cells incubated with DOX concentrations of either A) free DOX or C) DOX-MNCs and cell viability of MCF-7 cells incubated with DOX concentrations of either B) free DOX and D) DOX-MNCs for incubation period of 24 h, 48 h and 72 h.*

The IC_{50} values for U-87 cells exposed to DOX-MNCs are 0.90 µg/mL, 0.12 µg/mL and 0.50 µg/mL for an incubation period of 24 h, 48 h and 72 h, respectively. The IC_{50} values for MCF-7 cells exposed to DOX-MNCs are >10 µg/mL, 7.91 µg/mL and >10 µg/mL for an incubation period of 24 h, 48 h, and 72 h, respectively. The IC_{50} values of DOX-MNCs are higher than those of free DOX for both cell lines, meaning that the DOX-MNCs are less cytotoxic towards cells than free DOX. This effect is particularly present in the MCF-7 cells, which can be explained by the fact that they internalised less MNCs than the U-87 cells (as demonstrated in section 5.3.2.1 and 5.3.2.2), and are therefore less exposed to the drug. The lower cytotoxicity of DOX-MNCs as compared to free DOX, mainly due to the drug being partially retained in the MNCs, is desired in order to reduce side effects on healthy cells. Another interesting point is that for both cell line, the IC_{50} of DOX-MNCs is higher after 72 h of incubation than after 48 h (Figure 5.6C and 5.6D). This might be as a result of the release regimes of the drug from the MNCs. Whether the MNCs are internalized in the cells or still in the media, it was shown in section 4.3.11 that the drug release reaches a plateau after 24 h. If no more drug is released from the DOX-MNCs, cells might be able to recover and grow faster, resulting in an increase in cell viability.

Table 5. 2 *IC_{50} values of free DOX and DOX-MNCs for U-87 and MCF-7 cell lines after exposure time of 24 h, 48 h and 72 h.*

		IC_{50} (μg/mL)		
		24 h	48 h	72 h
U-87	Free DOX	0.13	0.06	0.04
	DOX-MNCs	0.90	0.12	0.50
MCF-7	Free DOX	0.95	0.29	0.16
	DOX-MNCs	>10	7.91	>10

5.3.4 The fate of DOX in cells

The intracellular internalization of DOX plays an important role in its anticancer activity. As explained in section 4.3.10, DOX acts by binding to DNA and inhibiting the topoisomerase II enzyme,[135,310] and therefore localizes into the cell nucleus. However, in nanoparticle-based drug delivery systems, endocytosis is often the main cell penetration pathway, which is particularly interesting to overcome drug resistance in drug resistant cancer. Indeed, when a cancer developed drug resistance, efflux of the drug from the cancer cell cytoplasm is observed.[330] Nanoparticle-based drug delivery systems can avoid the activation of the efflux pump in the cells due to internalization pathways and the triggering of processes which are different from those of free DOX,[331] therefore circumventing the mechanisms of drug resistance.

Free DOX and DOX-MNCs internalization in U-87 and MCF-7 cells was studied by fluorescence microscopy based on the intrinsic red fluorescence of DOX. The drug localization in the cells was efficiently monitored by incubating the cells either with free DOX or with the DOX-MNCs for different period of time. DRAQ5, a far-red fluorescing DNA dye, was employed as a nuclear stain for labelling of the cell nucleus. LysoTracker Green, a green fluorescent dye, was introduced to stain acidic compartments in cells (i.e. lysosomes). Unfortunately, the fluorescence of this dye was greatly hindered after fixing the cells with paraformaldehyde buffer, and substantial spillover of DOX fluorescence in the green filter made the use of LysoTracker Green not appropriate. Free DOX solution and DOX-MNCs were added to the cells with an equivalent amount of DOX (4 μg and 2 μg), and fluorescence images were acquired 3 h or 24 h later. As expected DOX fluorescence was more visible when using 4 μg than 2 μg, but the obtained results were the same. Consequently, only images acquired using a DOX amount of 4 μg under the

form of free DOX or DOX-MNCs are presented in Figure 5.7, Figure 5.8, Figure 5.9 and Figure 5.10.

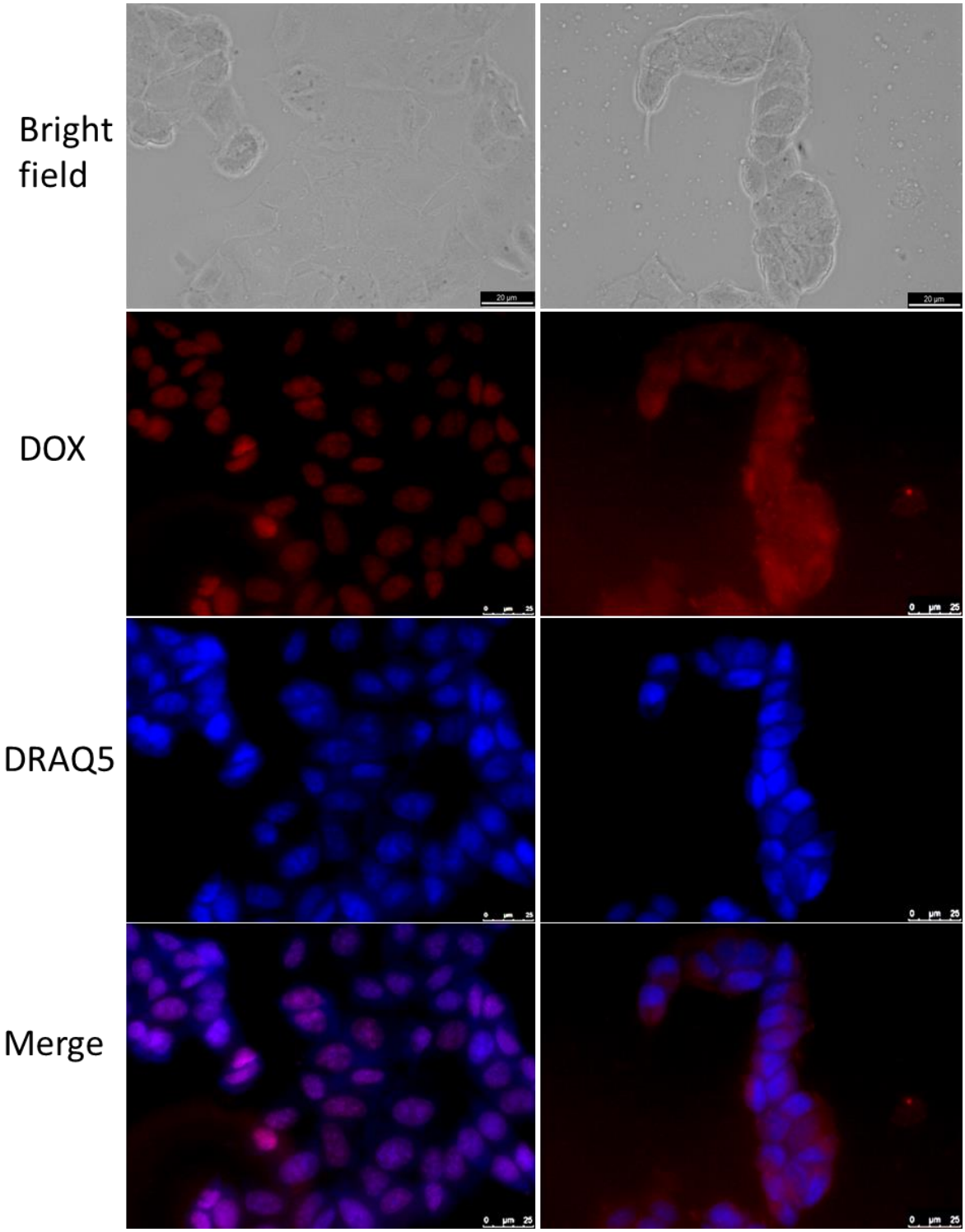

Figure 5. 7 *Fluorescence images of MCF-7 cells after 3 h of incubation with either free DOX (left) or DOX-MNCs (right). Cells were counterstained with DRAQ5. Scale bar: 20 µm.*

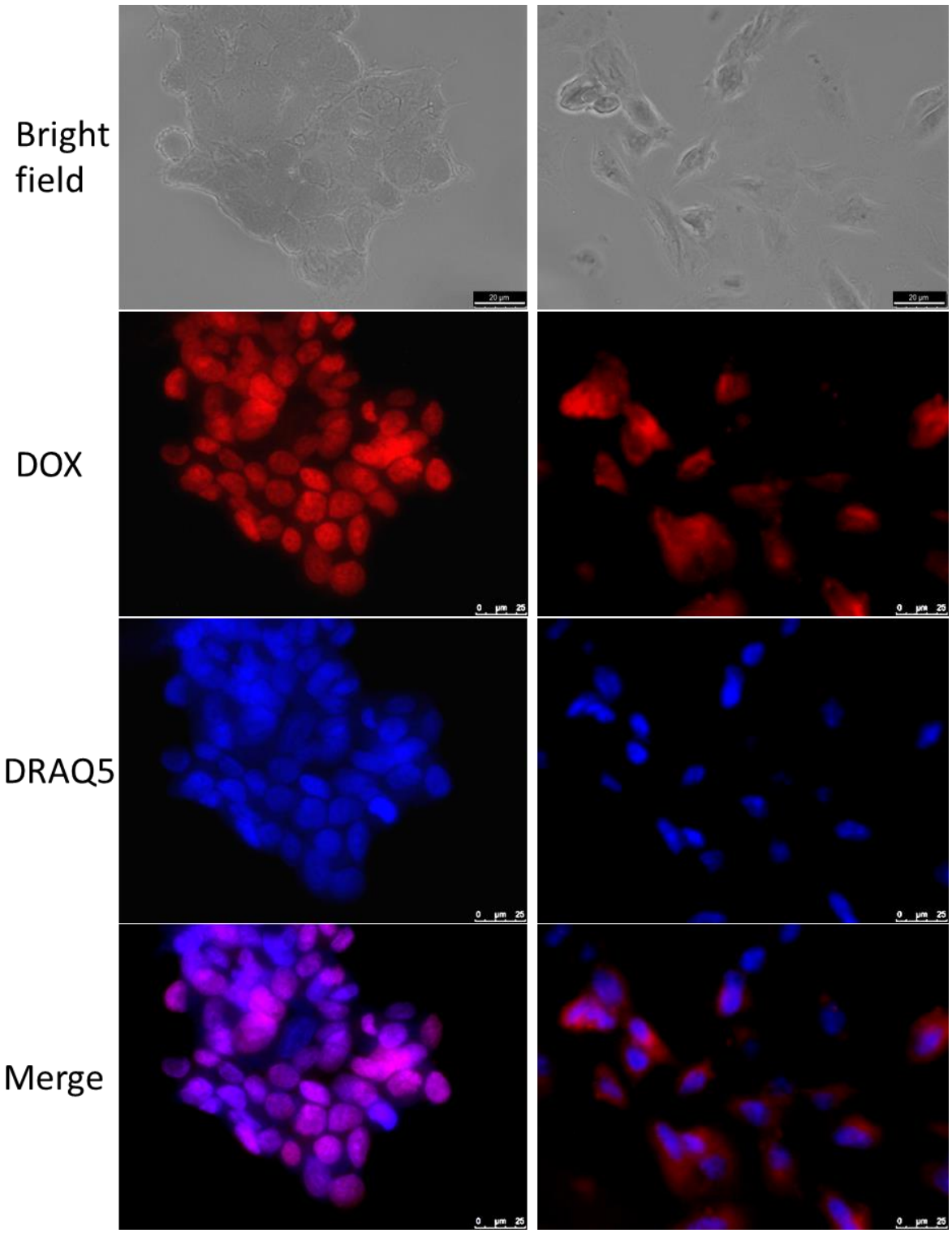

Figure 5. 8 *Fluorescence images of MCF-7 cells after 24 h of incubation with either free DOX (left) or DOX-MNCs (right). Cells were counterstained with DRAQ5. Scale bar: 20 µm.*

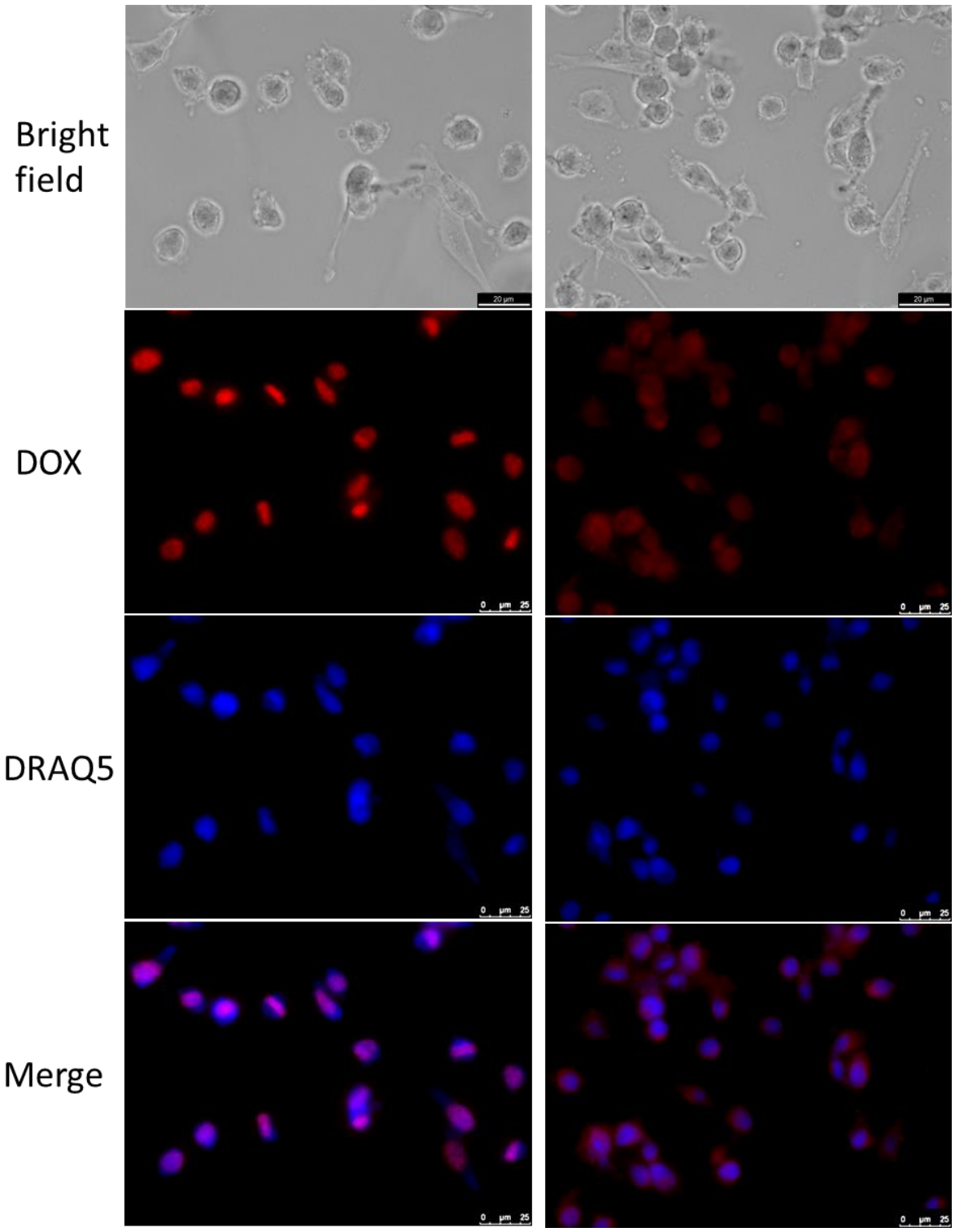

Figure 5. 9 *Fluorescence images of U-87 cells after 3 h of incubation with either free DOX (left) or DOX-MNCs (right). Cells were counterstained with DRAQ5. Scale bar: 20 µm.*

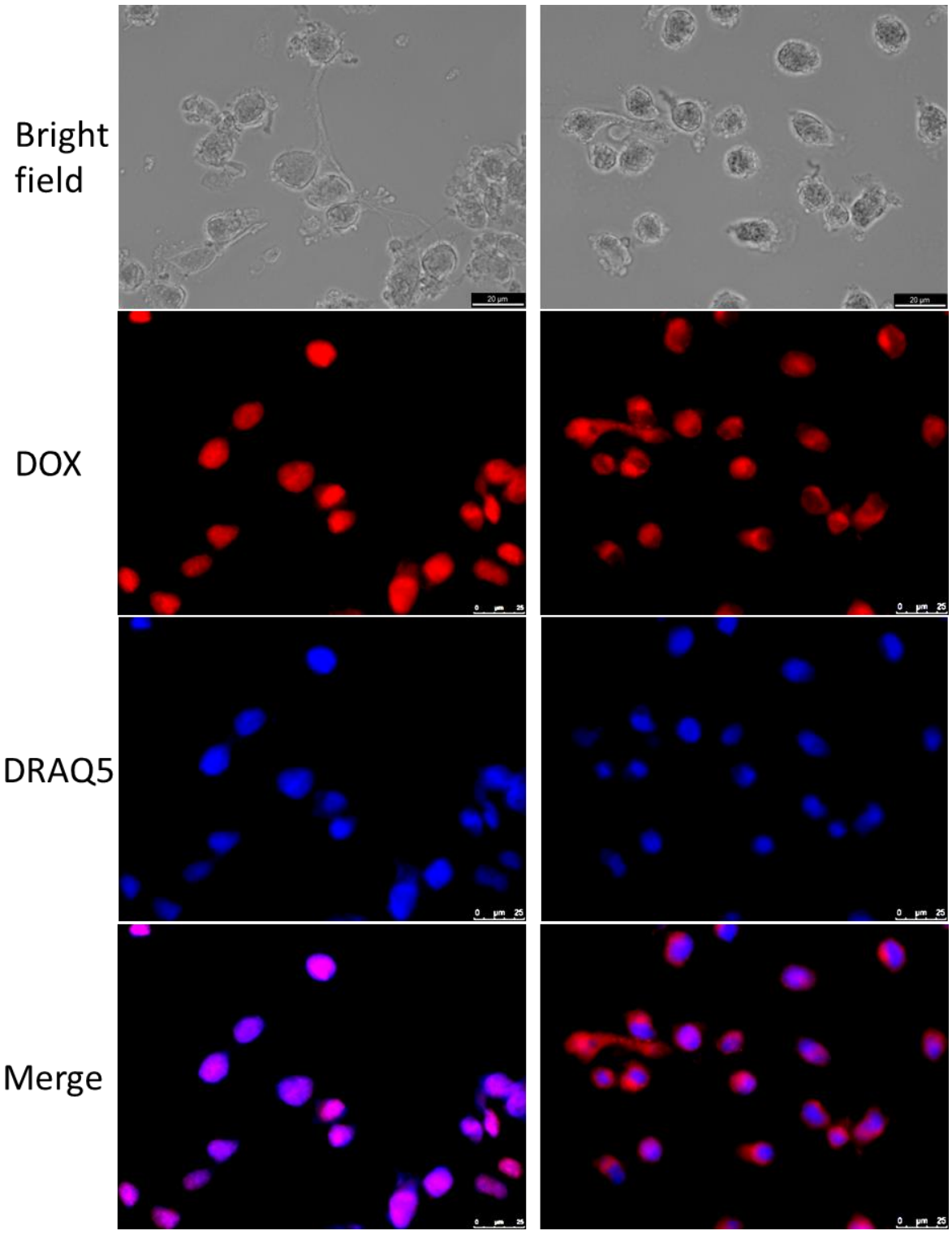

Figure 5. 10 *Fluorescence images of U-87 cells after 24 h of incubation with either free DOX (left) or DOX-MNCs (right). Cells were counterstained with DRAQ5. Scale bar: 20 µm.*

In both MCF-7 and U-87 cells, the fluorescence signal of DOX for both free DOX and DOX-MNCs is more visible 24 h than 3 h later, that is because more DOX has penetrated into the cells after 24 h of incubation. The fluorescence signal of DOX for DOX-MNCs is stronger in U-87 cells than in MCF-7 cells, which confirm again that U-87 cells internalize the MNCs in a larger quantity as compared to MCF-7 cells. The fluorescence signal of

DOX for free DOX was also found stronger in U-87 cells than in MCF-7 cells, which might explain why the IC_{50} values of free DOX against U-87 cells is much lower than for MCF-7 cells.

Unlike with confocal microscopy, it cannot be concluded for certain whether DOX is localised inside the cells or only on their surfaces because the images obtained by fluorescence microscopy are 2D images. Therefore, the following hypotheses are only true if DOX is indeed localised inside the cells.

Drug intracellular distribution of DOX-MNCs is quite different from that of free DOX. After 3 h of incubation with free DOX solution, the strong co-localisation of DOX and DRAQ5 fluorescence indicates that free DOX only localised in the cell nuclei in both MCF-7 (Figure 5.6) and U-87 cells (Figure 5.9), suggesting that free DOX permeates cellular and nuclear membrane by passive diffusion and rapidly accumulate in the cell nuclei and intercalate to the chromosomal DNA. This phenomenon is well-known and has been previously reported many times.[177,190,332,333] In contrast, DOX-MNCs were expected to be taken up by malignant cells through endocytosis, followed by some extent of drug release in the cytoplasm due to acidic pH of endosomes/lysosomes organelles and subsequent DOX diffusion to the nucleus. The endocytic pathway and mechanism of drug release result in a much slower process than passive drug diffusion and consequent slower delivery of DOX to the cell nuclei and was reported elsewhere many times.[177,190,334] This hypothesis seem to be confirmed by the fluorescence images revealing that DOX-MNCs were initially trapped in endosomal compartments after cellular uptake. Indeed, DOX molecules delivered by the MNCs are predominantly distributed in the cytoplasm after 3 h of incubation for both MCF-7 (Figure 5.6) and U-87 cells (Figure 5.9). After 24 h of incubation, in the case of MCF-7 cells, fluorescence attributed to DOX is still dominantly seen in the cytoplasm (Figure 5.8), while for U-87 cells, DOX molecules are located in the cytoplasm but have also diffused in the nuclei (Figure 5.10). These data not only demonstrated that the internalisation pathway of DOX-MNCs differs from that of free DOX, but also that MNCs are efficient vectors to carry the DOX molecules into the cytoplasm and later in the nuclei. These data also explain why the conjugation of DOX molecules to the MNCs results in lower *in vitro* anticancer activity than that of free DOX. Indeed, it was shown in section 5.3.3 that the IC_{50} values of DOX-MNCs were much higher than the IC_{50} values of free DOX for both U-87 and MCF-7 cells. In culture conditions, DOX conjugation to the MNCs is less cytotoxic than free DOX due to longer time required for drug nuclear transportation. The slow release of DOX from the MNCs can be realised in a controlled manner from inside endosomes and lysosomes, to potentially increase the cytotoxicity of drugs with long-term effect, which is more desirable for chemotherapy than the use of drug with acute

cytotoxicity. Such a delivery system also reduces the amount of available free drug molecules present in the extracellular environment therefore reducing unwanted side effects, which is one of the major drawbacks of chemotherapies nowadays. Finally, the MNCs have also the potential to bypass multidrug resistance mechanisms because they enter the cells through endocytosis and avoid p-glycoprotein pumps responsible for fast drug efflux.[335-337]

5.3.5 *In vitro* anticancer studies by trypan blue dye exclusion assay

5.3.5.1 Preliminary experiments

In this chapter, cell viability has been investigated by trypan blue dye exclusion assay. Two methods of treatment were employed: the direct treatment and treatment after internalization methods as explained in section 5.2.4.11. Preliminary experiments of hyperthermia, chemotherapy and the combined thermo-chemotherapy after internalization were realized on U-87 cells and MCF-7 cells with a concentration of MNCs or DOX-MNCs of 1 mg/mL. This MNCs concentration, previously shown to be not cytotoxic to cells, was chosen so that enough nanoparticles could be internalized in the U-87 and MCF-7 cells after an incubation period of 24 h to have a cytotoxic effect under application of an AMF.

The typical heating curves obtained by recording the temperature during the *in vitro* hyperthermia treatment of U-87 and MCF-7 cells after nanoparticle internalisation are shown in Figure 5.11.

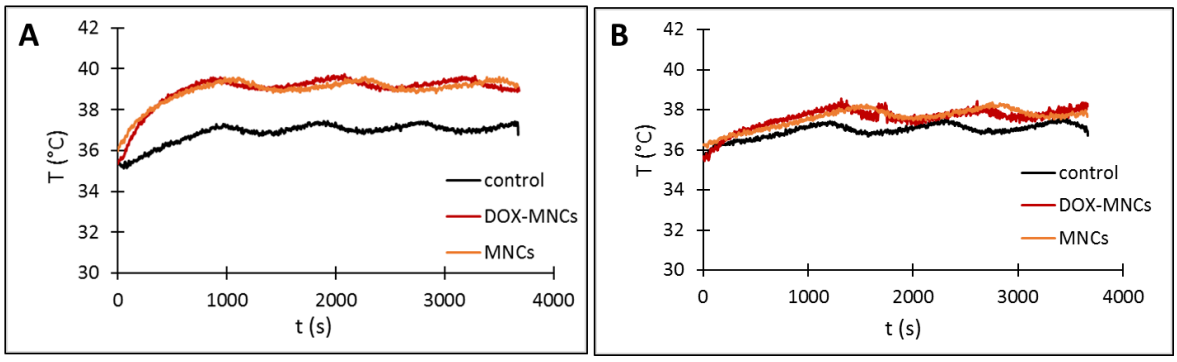

Figure 5. 11 *Local environment temperature of A) U-87 cells and B) MCF-7 cells suspensions dispersed in DMEM supplemented with 10% FBS after internalisation of MNCs or DOX-MNCs and subjected to an AMF (f = 950 kHz and H = 10.5 kA/m). Control cells were not treated with nanoparticles.*

The oscillations of the temperature observed in every curve is due to the water running through the inductor coil used to maintain the temperature to 37 °C. The chiller temperature was set to 37 °C so that the coil was maintained at physiological temperature and so was the cell sample.

The control experiments for both MCF-7 and U-87 cells show that under application of an AMF of f = 950 kHz and H = 10.5 kA/m, the local temperature of the suspensions do not exceed 37.6 °C. The local temperature of U-87 cell suspensions for cell samples that have been treated with either MNCs or DOX-MNCs stabilizes around 39.2 °C with a maximum at 39.5 °C. In the case of MCF-7 cells, only a slight increase of the temperature as compared to the control can be observed. The temperature stabilizes around 37.7 °C with a maximum of 38 °C. These types of heating curves were expected as it was shown previously in section 5.3.2 that, unlike U-87 cells, MCF-7 cells do not internalise the MNCs in a high amount.

The resulting cell viabilities 24 h and 48 h after treatment for both MCF-7 and U-87 cells are presented in Figure 5.12.

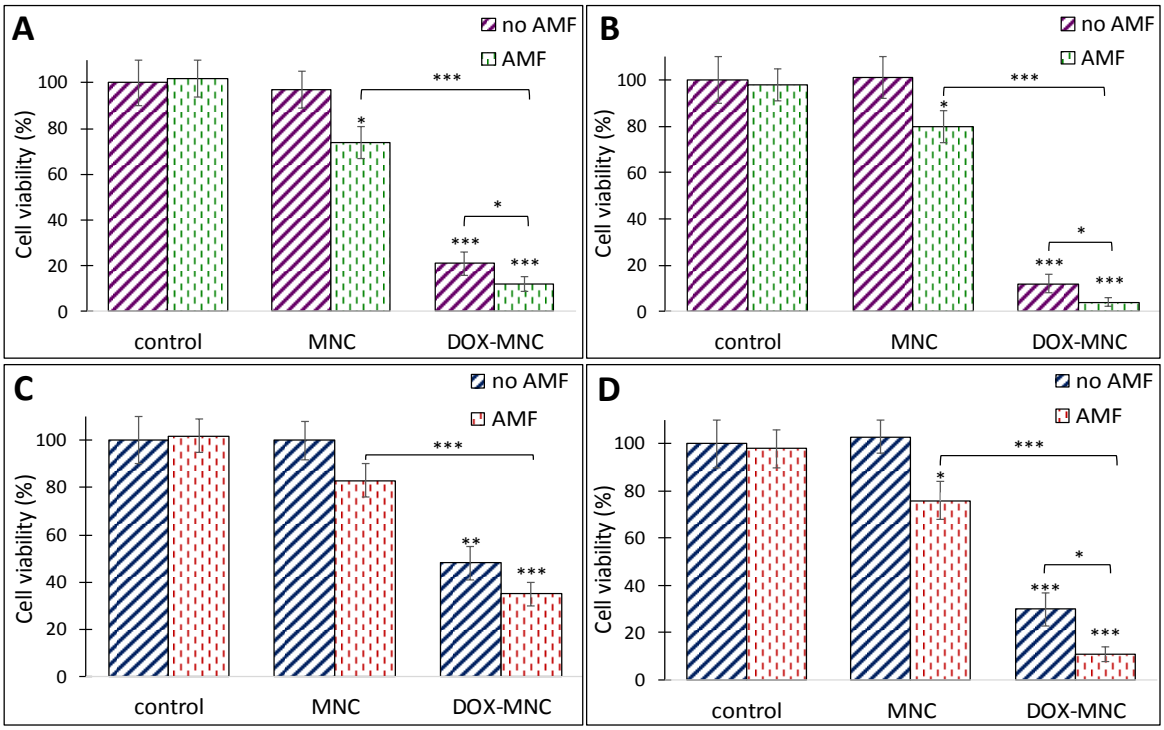

Figure 5. 12 *Treatment after internalisation method, cell viabilities of A) U-87 cells 24 h, B) U-87 cells 48 h, C) MCF-7 cells 24 h and D) MCF-7 cells 48 h following treatment with or without a 1 h exposure to an AMF (f = 950 kHz and H = 10.5 kA/m) after nanoparticle internalisation with media alone (control cells), MNCs or DOX-MNCs. The asterisks refer to significant levels compared to the corresponding control experiment or the combined therapy; p < 0.05 (*), p < 0.01 (**) and p < 0.001 (***).*

For both cell lines, the effect of the MNCs only and the magnetic field alone have no detrimental effect on the cell viability. Control experiments of free DOX in presence of an AMF to assess the effect of the magnetic field on free DOX cytotoxicity were not carried out. It has been shown in many studies that free DOX treatment with or without application of a magnetic field does not result in significant changes in viability.[168,178,190,338,339] Another study showed that pre-exposure of cells to a static magnetic field does not sensitize the cells to free doxorubicin treatment either.[340]

For both cell lines, the combinatorial treatment (DOX-MNCs, AMF) is the most effective treatment. In the case of MCF-7 cells, the relative cell viabilities 24 h after treatment were 83% for hyperthermia, 48% for chemotherapy and 35 % for thermo-chemotherapy; 48 h after treatment, cell death increases, with the relative cell viabilities being 76% for hyperthermia, 30 % for chemotherapy, and 11 % for thermo-chemotherapy.

In the case of U-87 cells, the relative cell viabilities 24 h after treatment were 74 % for hyperthermia, 21 % for chemotherapy and 12 % for thermo-chemotherapy. 48 h after treatment, the relative cell viabilities are 80 % for hyperthermia, 12 % for chemotherapy and 4 % for thermo-chemotherapy. U-87 cells seem to start recovering from the hyperthermia treatment as an increase of the cell viability is observed after 48 h.

Interestingly, even though it was demonstrated that U-87 cells internalize a higher quantity of MNCs as compared to MCF-7 cells, hyperthermia treatment results in about the same percentage of cell death for both cell lines, indicating that MCF-7 cells are more sensitive to the effect of heat released from internalised nanoparticles than U-87 cells.

For both cell lines, the cytotoxic effect of the combinatorial treatment achieved with the developed delivery system after cellular uptake of the nanoparticles is superior to each of the two treatments applied separately, and an evaluation using Valeriote's formula showed that the combined effects were synergistic in nature (Table 5.3).

Table 5. 3 *Evaluation of the combined effect of the thermo-chemotherapy treatment after nanoparticles internalisation for both MCF-7 and U-87 cell lines according to Valeriote's formula.*

		(A)*(B)/100 (%)	**(A+B)** (%)	**Effect**
MCF-7	**24 h**	40	35	synergistic
	48 h	23	11	synergistic
U-87	**24 h**	16	12	synergistic
	48 h	10	4	synergistic

5.3.5.2 Combined effect of DOX and magnetic hyperthermia on U-87 cells

5.3.5.2.1 Initial considerations

Numerous studies have already demonstrated that the combination of hyperthermia with a number of conventional anticancer agents results in additive or synergistic effects.[298] Therefore, the aim of this work was not to kill the tumour cells with high concentrations of chemotherapeutic drug or high temperature, but rather to show an efficacy of the combined thermo-chemotherapy achieved at lower therapeutic doses of chemotherapeutic drug and MNCs. For that purpose, experiments with a lower DOX concentration were performed by mixing the MNCs with DOX-MNCs to obtain the desired nanoparticle concentration and the desired DOX concentration. Indeed, in the preliminary experiments presented in the above section and especially in the case of the U-87 cells, while the nanoparticle concentration is appropriate, the DOX concentration is too high and the chemotherapy treatment alone results in almost complete cell death. Using the IC_{50} values of DOX-MNCs for U-87 cells obtained from the dose-response curves determined by MTT assay in section 5.3.3, a DOX concentration of 0.15 µg/mL was chosen for the current study.

Another aim of this study was to compare the direct treatment method with the treatment after internalisation method for the cell lines used in this work, as both methods are widely found in the literature.[341,342] Comparing both methods allows to answer whether a heat treatment is more effective in the case of heat being released from the inside of the tumour cells, or in the case of the surrounding medium being heated, and in which case the combinatorial treatment is the most effective. To be able to compare both treatment methods, the concentration of nanoparticles used during the hyperthermia treatment must be the same. In order to determine what is the amount of nanoparticle being internalised by the cells after 24 h, the number of cells at the time of the hyperthermia treatment, i.e. 48 h after seeding the cells, must be known. Under optimal conditions, a cell population in a culture will increase exponentially. Exponential growth of a cell population N at the growth rate r, as time t goes on in discrete intervals can be expressed by equation 5.2:

$$N(t) = N_0(1 + r)^t \tag{5.2}$$

Where N_0 is the number of cells at time 0. The growth rate could be easily determined from counting cells from one cell passaging to the next one. Therefore, the cell number at the time of the hyperthermia treatment could be calculated and was found to be equal to 600,000 cells. Previously cellular uptake of the MNCs using a SQUID magnetometer was

quantified in section 5.3.2.2. Under the same conditions, it was shown that an average of 125 pg(Fe_3O_4)/cell was internalised. Thus, it can be concluded that a total of 75 µg of MNCs is internalised in the cells.

In order to be able to compare the direct treatment method with the treatment after internalisation method, a total of 75 µg of MNCs was chosen for the direct treatment. Other experiments with 200 µg and 300 µg of MNCs were also realized to assess the effect of the temperature on the effectiveness of the thermo-chemotherapy treatment.

5.3.5.2.2 Treatment after internalisation U-87 cells

Experiments of hyperthermia, chemotherapy and the combined thermo-chemotherapy after internalization were repeated on U-87 cells with a concentration of nanoparticles of 1 mg/mL. However, this time the concentration in DOX was kept low, i.e. 0.15 µg/mL, by mixing MNCs and DOX-MNCs (ratio 454:1 w/w) to obtained the desired final concentration in DOX and in nanoparticles. The obtained cell viabilities 24 h and 48 h after treatment are presented in Figure 5.13.

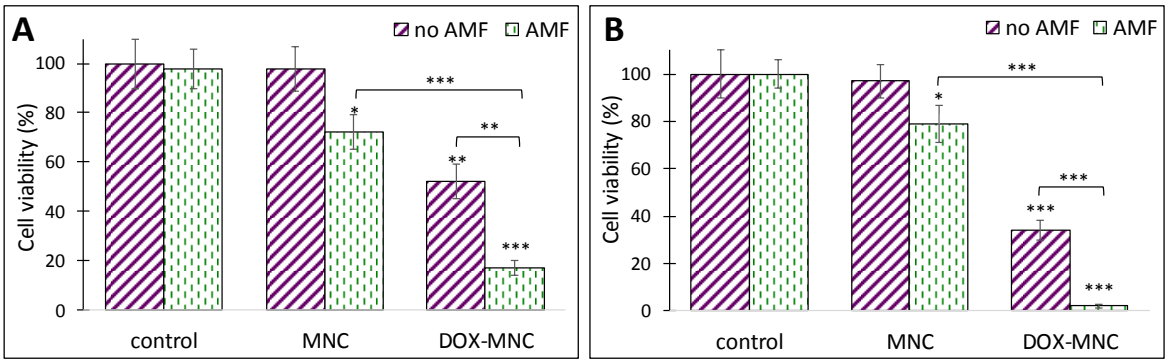

Figure 5. 13 *Treatment after internalisation method, cell viabilities of U-87 cells after A) 24 h and B) 48 h incubation following treatment with or without a 1 h exposure to an AMF (f = 950 kHz and H = 10.5 kA/m) after nanoparticle internalisation with media alone (control cells), MNCs or DOX-MNCs containing 0.15 µg of DOX. The asterisks refer to significant levels compared to the corresponding control experiment or the combined therapy; p < 0.05 (*), p < 0.01 (**) and p < 0.001 (***).*

The relative cell viabilities 24 h after treatment were 72% ($p < 0.05$) for hyperthermia, 52% ($p < 0.01$) for chemotherapy and 17% ($p < 0.001$) for thermo-chemotherapy; 48 h after treatment, the relative cell viabilities were 79% ($p < 0.05$) for hyperthermia, 34% ($p < 0.001$) for chemotherapy and 2% ($p < 0.001$) for thermo-chemotherapy. As already observed in the preliminary experiments, U-87 cells start recovering from magnetic hyperthermia 24 h after the treatment as an increase of the cell viability is observed after 48 h.

Again, the cytotoxic effect of the combinatorial treatment achieved with the developed delivery system after cellular uptake of the nanoparticles was found superior to either hyperthermia ($p < 0.001$ after 24 h and 48 h) or chemotherapy ($p < 0.01$ after 24 h, and $p < 0.001$ after 48 h) applied separately. An evaluation using Valeriote's formula showed that the combined effects were synergistic in nature (Table 5.4).

Table 5. 4 *Evaluation of the combined effects of the thermo-chemotherapy treatment after nanoparticle internalisation with 0.15 µg of DOX for U-87 cells according to Valeriote's formula.*

		(A)*(B)/100 (%)	**(A+B)** (%)	**Effect**
U-87	**24 h**	37	17	Synergistic
	48 h	27	2	Synergistic

Several factors play a role in the synergism of the combined therapy. Here, the delivery system employed is both pH- and thermo-sensitive. We have shown previously that the DOX-MNCs are internalized through endocytosis. The main components of the endocytic pathway are lysosomes, early and late endosomes. Many research groups have reported that these intracellular organelles have an acidic pH, ranging from pH 4 to pH 6.[343,344] This acidic pH combined with the local heat generation promoted the release of DOX. Moreover, mild hyperthermia was shown to inhibit the DNA repair of lethal and sublethal damages induced by the anticancer agent and to accelerate the cytotoxic reaction rate of the drug resulting in an increased anti-tumour activity of the chemotherapy.[133]

5.3.5.2.3 Direct treatment U-87 cells

Experiments of hyperthermia, chemotherapy and the combined thermo-chemotherapy using the direct treatment method were realized on U-87 cells at different hyperthermia temperature obtained by varying the total nanoparticle concentration in solution. However, the concentration of DOX was kept constant for each experiment, *i.e.* 0.15 µg/mL, by mixing MNCs and DOX-MNCs (ratio 33:1 w/w, 90:1 w/w and 135:1 w/w for a total amount of nanoparticles of 75 µg, 200 µg and 300 µg, respectively) to obtain the desired final concentration of DOX and of nanoparticle.

The typical heating curves obtained by recording the temperature during the *in vitro* direct hyperthermia treatment of U-87 cells are shown in Figure 5.14.

The obtained cell viabilities 24 h and 48 h after treatment are presented in Figure 5.15. Control experiment of the effect of application of the AMF on the viability of U-87 cells were not repeated as it was already shown it had no harmful effect.

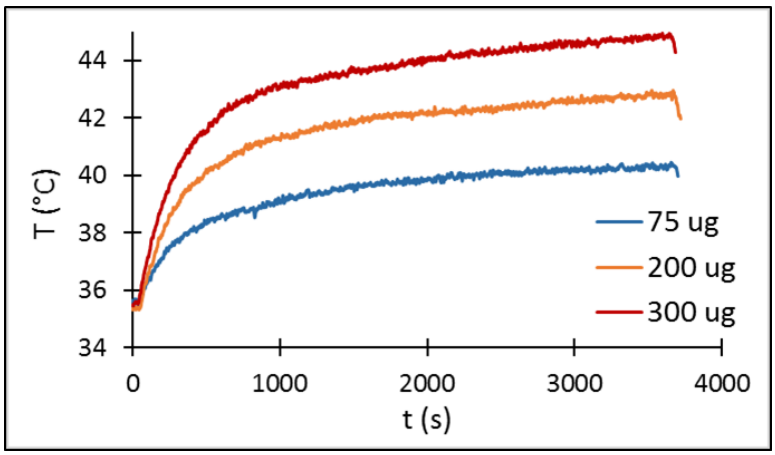

Figure 5. 14 *Local environment temperature of U-87 cells suspensions dispersed in DMEM supplemented with 10% FBS containing 75 µg, 200 µg or 300 µg of MNCs and subjected to an AMF (f = 950 kHz and H = 10.5 kA/m).*

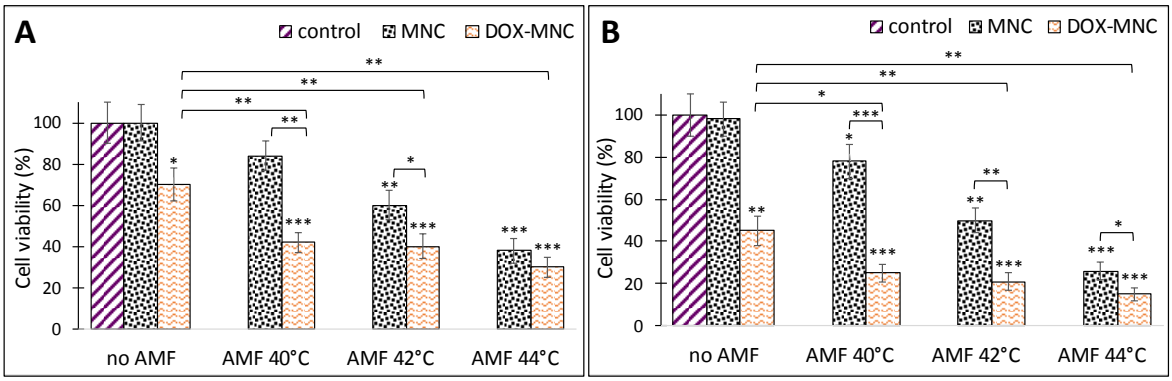

Figure 5. 15 *Direct treatment method, cell viabilities of U-87 cells A) 24 h and B) 48 h following direct treatment with or without a 1 h exposure to an AMF (f = 950 kHz and H = 10.5 kA/m) with media alone (control cells), MNCs or DOX-MNCs containing 0.15 µg of DOX. The asterisks refer to significant levels compared to the corresponding control experiment or the combined therapy; p < 0.05 (*), p < 0.01 (**) and p < 0.001 (***).*

The relative cell viabilities 24 h after treatment were 70% ($p < 0.05$) for chemotherapy, 84 % for hyperthermia and 42% ($p < 0.001$) for thermo-chemotherapy at 40 °C; 60% ($p < 0.01$) for hyperthermia and 40% ($p < 0.001$) for thermo-chemotherapy at 42 °C; 38% for hyperthermia ($p < 0.001$) and 30% ($p < 0.001$) for thermo-chemotherapy at 44 °C. 48 h after treatment, the relative cell viabilities were 45% ($p < 0.01$) for chemotherapy, 78% ($p < 0.05$) for hyperthermia and 25% ($p < 0.001$) for thermo-chemotherapy at 40 °C; 50% ($p < 0.01$) for hyperthermia and 21% ($p < 0.001$) for thermo-chemotherapy at 42 °C; 26% for hyperthermia ($p < 0.001$) and 15% ($p < 0.001$) for thermo-chemotherapy at 44 °C.

For each hyperthermia temperature, the cytotoxic effect of the combinatorial treatment achieved with the developed delivery system with the direct treatment method was also found to be superior to each of the two treatments applied separately. For each

hyperthermia temperature, the difference in cell death between hyperthermia and thermo-chemotherapy is higher 48 h after the treatment than 24 h after and translates into a decrease of p, while the difference in cell death between chemotherapy and thermo-chemotherapy is smaller 48 h after the treatment than 24 h after and translates into an increase of p. It is at mild hyperthermia temperature (40 °C) that the thermo-chemosensitisation effect is the biggest. The difference in cell death between hyperthermia alone and the thermo-chemotherapy treatment decreases with increasing magnetic hyperthermia temperature. An evaluation of the combined effects using Valeriote's formula reflects this trend, as with increasing hyperthermia temperature (A)*(B)/100 decreases and becomes inferior to (A+B) at 44 °C (Table 5.5). As a consequence, the combined effects were found to be synergistic in nature at 40 °C and 42 °C, and sub-additive at 44 °C.

Table 5. 5 *Evaluation of the combined effects of the direct thermo-chemotherapy treatment with 0.15 µg of DOX at different hyperthermia temperatures for U-87 cell line according to Valeriote's formula.*

			(A)*(B)/100 (%)	**(A+B)** (%)	**Effect**
U-87	**40 °C**	**24 h**	59	42	synergistic
		48 h	35	25	synergistic
	42 °C	**24 h**	42	40	synergistic
		48 h	23	21	synergistic
	44 °C	**24 h**	27	32	sub-additive
		48 h	12	15	sub-addtive

The delivery nanosystem used in this experiment is both pH- and thermo-sensitive. The direct treatment method does not allow any time for the nanoparticles to be taken up by the cells, as such the nanocarrier is not in contact with an acidic environment and therefore only the temperature promotes the release of the DOX. However, mild hyperthermia has been shown to increase cell membrane permeability, thus promoting nanoparticles and drugs accumulation into tumour cells.[129] Remarkably, Peller *et al.* showed that after intravenous application of DOX-loaded thermo-sensitive liposome, heating of the tumour above 40 °C for 1 h using laser light resulted in highly selective DOX uptake.[345] The DOX-concentration in the heated tumour tissue compared to the non-heated tumour showed an almost 10-fold increase.

Mild hyperthermia also inhibits DNA repair of lethal and sublethal damages induced by the anticancer agent and accelerates the cytotoxic reaction rate of the drug resulting in an

increased anti-tumour activity of the chemotherapy.[133] This direct treatment experiment proves that an appropriate thermal dose is critical for the synergy of the combined therapy.

5.3.5.2.4 Comparison of the direct treatment and treatment after internalisation methods

In the case of a cell line that internalised the desired nanoparticles in a high amount, such as the U-87 cells with the MNCs, the treatment after internalisation results in higher cell death than the direct treatment method. Indeed, the cell viabilities for the combined therapy after nanoparticle internalisation were 17% and 2%, 24 h and 48 h after the treatment, respectively. It was calculated that the total amount of nanoparticle internalised in the cells was equal to 75 µg. This amount of MNCs was used for the direct treatment in order to be able to compare the two treatments. The cell viabilities for the direct combined therapy at 40 °C are 40% and 25%, 24 h and 48 h after the treatment, respectively.
The mechanisms responsible for the synergy of the combined therapy are not yet fully understood, but generally involve:

- Improve intracellular uptake of nanoparticles or drug molecules due to increase cell membrane permeability
- Inhibition of DNA repair of the chemically induced lethal or sub-lethal damages
- Acceleration of the cytotoxic chemical reaction

Both methods show a synergistic effect of the combined therapy, which suggest that the best method could actually be a mix of the two methods tested in this chapter, i.e. some nanoparticles internalised in the cells and some in the surrounding environment. Indeed, the different mechanisms behind the synergistic effects of the combined therapy may be more or less triggered and thus play a more or less important role depending on the treatment method used.

Finally, because the MNCs are pH- and thermo-sensitive, a maximized drug release will be obtained with both stimuli at the same time, and therefore a better synergism of the combined therapy. To that aim, the MNCs need to be internalised in cell acidic compartments. However, from an *in vivo* point of view, tumour extracellular environment is often more acidic than normal tissue, with a pH ranging from 5.7 to 7.8,[344] that would facilitate the release of the drug from MNCs that have not been yet internalised, and subsequent quick accumulation in the cell nuclei of released DOX molecules through cellular membrane diffusion.

5.3.5.3 Combined effect of DOX and magnetic hyperthermia on MCF-7 cells

5.3.5.3.1 Initial considerations

The same initial considerations as for U-87 cells were made for MCF-7 cells. Experiments with a lower DOX concentration were performed by mixing the MNCs with DOX-MNCs to obtain the desired nanoparticle concentration and the desired DOX concentration. Using the IC_{50} values of DOX-MNCs for MCF-7 cells obtained from the dose-response curves determined by MTT assay in section 5.3.3, a DOX concentration of 5.25 µg/mL was chosen for the current study.

Because one of the aims of this study was to compare the direct treatment method with the treatment after internalisation method for the two cell lines used in this work, both experiments should have been performed on the MCF-7 cells. However, MCF-7 cells were shown to not internalise the MNCs to a great extent. Instead, we chose to realise the direct treatment with the same concentration of nanoparticles used for U-87 cells so that the effects of hyperthermia on both cell lines using the direct treatment method could be compared.

The treatment after internalisation was planned to be repeated with the lower concentration of DOX, unfortunately contamination of cells happened two weeks before the end date of my PhD. Because I had to go to Bordeaux for a short term scientific mission funded by EU COST TD1402 Action it was impossible to perform this experiment. However, the preliminary experiments performed on both U-87 and MCF-7 cell lines showed that the treatment after internalisation method is more efficient for U-87 cells (section 5.3.5.2.1). This was expected due to the low internalisation of MNCs by MCF-7 cells. This preliminary experiment also indicates that MCF-7 cells are more sensitive to the effect of heat released from internalised nanoparticles than U-87 cells, as cell death occurs in the same extent for both cell lines.

Consequently, only the results issued from the direct treatment experiments on MCF-7 cells are presented in this section. The same hyperthermia temperatures were tested using 75 µg, 200 µg and 300 µg of MNCs to assess the effect of the temperature on the effectiveness of the thermo-chemotherapy treatment for the MCF-7 cell line. The concentration of DOX was kept constant for each experiment, *i.e.* 5.25 µg/mL, by mixing MNCs and DOX-MNCs (ratio 0:1 w/w, 1.7:1 w/w and 3:1 w/w for a total amount of

nanoparticles of 75 µg, 200 µg and 300 µg, respectively) to obtain the desired final concentration of DOX and of nanoparticle.

5.3.5.3.2 Direct treatment MCF-7 cells

The obtained cell viabilities 24 h and 48 h after treatment are presented in Figure 5.16.

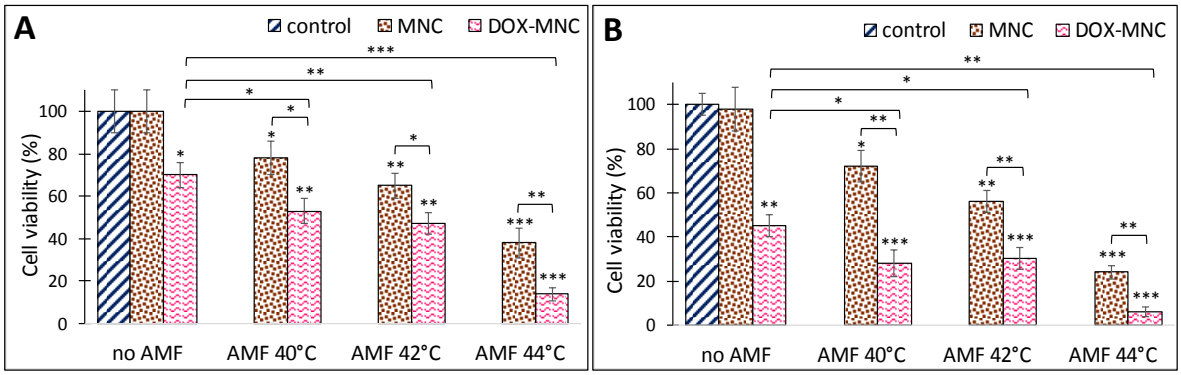

Figure 5. 16 *Direct treatment method, cell viabilities of MCF-7 cells A) 24 h and B) 48 h following direct treatment with or without a 1 h exposure to an AMF (f = 950 kHz and H = 10.5 kA/m) with media alone (control cells), MNCs or DOX-MNCs containing 5.25 µg of DOX. The asterisks refer to significant levels compared to the corresponding control experiment or the combined therapy; p < 0.05 (*), p < 0.01 (**) and p < 0.001 (***).*

Control experiments of the effect of application of the AMF on the viability of MCF-7 cells were not repeated as it was already shown it had no detrimental effect.

The relative cell viabilities 24 h after treatment were 70% ($p < 0.05$) for chemotherapy, 78% ($p < 0.05$) for hyperthermia and 53% ($p < 0.01$) for thermo-chemotherapy at 40 °C; 65% ($p < 0.01$) for hyperthermia and 47% ($p < 0.01$) for thermo-chemotherapy at 42 °C; 38% for hyperthermia ($p < 0.001$) and 14% ($p < 0.001$) for thermo-chemotherapy at 44 °C. 48 h after treatment, the relative cell viabilities were 45% ($p < 0.01$) for chemotherapy, 72% ($p < 0.05$) for hyperthermia and 28% ($p < 0.001$) for thermo-chemotherapy at 40 °C; 56% ($p < 0.01$) for hyperthermia and 30% ($p < 0.001$) for thermo-chemotherapy at 42 °C; 24% for hyperthermia ($p < 0.001$) and 6% ($p < 0.001$) for thermo-chemotherapy at 44 °C.

For each hyperthermia temperature, the cytotoxic effect of the combinatorial treatment achieved with the developed delivery system with the direct treatment method was found superior to each of the two treatments applied separately. For each hyperthermia temperature, the difference in cell death between hyperthermia and thermo-chemotherapy is higher 48 h after the treatment than 24 h after and translates into a decrease of p, while the difference in cell death between chemotherapy and thermo-chemotherapy is smaller

48 h after the treatment than 24 h after and translates into an increase of p. It is at mild hyperthermia temperature (40 °C) that the thermo-chemosensitisation effect is the biggest, followed by hyperthermia temperature at 44 °C. An evaluation of the combined effects using Valeriote's formula reflects this trend, as with increasing hyperthermia temperature (A)*(B)/100 decreases and becomes inferior to (A+B) at 42 °C and then becomes superior to (A+B) again at 44 °C (Table 5.6). As a consequence, the combined effects were found to be synergistic in nature at 40 °C and 44 °C, and sub-additive at 42 °C.

Table 5. 6 *Evaluation of the combined effects of the direct thermo-chemotherapy treatment with 5.25 µg of DOX at different hyperthermia temperatures for MCF-7 cells according to Valeriote's formula.*

			(A)*(B)/100 (%)	**(A+B)** (%)	**Effect**
MCF-7	**40 °C**	**24 h**	55	53	synergistic
		48 h	32	28	synergistic
	42 °C	**24 h**	46	47	sub-additive
		48 h	25	30	sub-additive
	44 °C	**24 h**	27	14	synergistic
		48 h	11	6	synergistic

The direct treatment method is quite effective on MCF-7 cells. The MCF-7 cells were shown to internalize the MNCs only in small quantity. This experiment shows that the combined therapy can be used using the direct treatment method and is effective on cells that do not internalize nanoparticles.

5.3.5.4 Comparison of the effects of the direct treatment on MCF-7 and U-87 cell lines

The direct treatment method was shown to be quite effective on both U-87 and MCF-7 cell lines for the thermo-chemotherapy treatment. Mild hyperthermia at 40 °C resulted in synergistic effects of the combined therapy for both U-87 and MCF-7 cell lines. Hyperthermia at 42 °C resulted in synergistic effects of the combined therapy for U-87 cell line, while for MCF-7 cell line, only and sub-additive effects were observed. Hyperthermia at 44 °C resulted in sub-additive effects of the combined therapy for U-87 cell line, while for MCF-7 cell line, synergistic effects were obtained again. These results indicate that the hyperthermia and DOX chemotherapy can have both synergistic and sub-additive effects on a same cell line depending on the applied hyperthermia temperature, and therefore an appropriate thermal dose is critical for the synergy of the combined therapy. Similar results

were reported *in vivo*, where the amount of intracellular DOX taken up by the tumour with 40 °C hyperthermia was increased by 80% relative to that at body temperature, but this effect was not observed at 43 °C hyperthermia.[346]

These experiments also emphasize the importance of studying a particular cell line for a particular purpose. Indeed, tumours cells from different cell lines might behave differently. In this case the thermo-chemosensitisation effect was the highest at 40 °C, 48 h after the treatment for both cell lines, however the effects of the combined therapy at 42 °C and 44 °C on MCF-7 cells are different from those obtained on U-87 cells. Depending on the cell line, the mechanisms responsible for the synergistic effect of the combined therapy might be more or less triggered at different applied hyperthermia temperature.

5.4 Conclusion

In summary, the MNCs were found to be biocompatible for concentrations up to 1 mg/mL. The quantification of MNCs cellular uptake with different cancer cell lines revealed significant variation of non-targeted cell loading. This affected the cytotoxicity of DOX-MNCs on those cell lines, as shown by the IC_{50} values for the DOX-MNCs. Unlike free DOX, the DOX-MNCs are taken up through endocytosis that results in slow DOX delivery to the nuclei. The main components of endocytic pathway have an acidic pH that facilitates the release of the DOX from the nanoparticles. The thermo-chemotherapy experiments performed with the developed delivery system showed that the combinatorial treatment was more effective than both chemotherapy or magnetic hyperthermia individual treatments applied separately. Two different methods of treatment were studied. The direct treatment method involves subjecting the cells to the hyperthermia treatment immediately after putting them in contact with the nanoparticles. There is no nanoparticle internalized by the cells and thus only the temperature of the surrounding medium is involved in the magnetic hyperthermia treatment. The treatment after internalisation consists in incubating the cells with the nanoparticles for 24 h and subsequent washing of the cells before subjecting the cells to an AMF. Only nanoparticles taken up by cells were involved in the hyperthermia treatment and this experiment revealed that the MNCs retain the capability to perform as heat vectors upon internalisation by the cells.

Cell death was found to be dependent on the method of treatment used. For a cell line that internalized the MNCs in a great extent such as the U-87 cell line, the thermo-chemotherapy applied through the treatment after internalisation was found to be more

effective, the combined effects were found to be synergistic in nature and an almost complete cell death was achieved. However, positive results were also obtained for the direct treatment method for both U-87 and MCF-7 cells. These findings demonstrate that it is not necessary for tumour cells to internalize the nanoparticles for an efficient therapy, but is preferable. The study of the direct thermo-chemotherapy treatment at different hyperthermia temperature revealed the importance of the applied thermal dose. Indeed, both synergistic and sub-additive effects of the combined therapy were observed for a same cell line depending on the applied hyperthermia temperature. However, synergistic and sub-additive effects were found at different hyperthermia temperature depending on the cell line and thus emphasize the necessity to study each cell line independently for a particular treatment. The mechanisms responsible for the synergistic effect of the combined therapy might be more or less triggered depending on both the applied hyperthermia temperature and the cell line.

Interestingly, the thermo-chemosensitisation effect was the highest at mild hyperthermia temperature of 40 °C for both cell lines. This result is of particular importance: if only a low hyperthermia temperature is necessary for the treatment, the quantity of nanoparticles necessary for the treatment can also remain low. The thermo-chemotherapy treatment allows for the reduction of both the chemotherapeutic dose and amount of nanoparticles needed which is a significant advantage for clinical use, in order to reduce toxicity and systemic effects to healthy tissues.

CHAPTER 6

CELLULAR STUDIES ON CHEMOTHERAPY, MAGNETIC HYPERTHERMIA AND COMBINED THERMO-CHEMOTHERAPY FOR THERAPEUTIC APPLICATIONS USING THE BIOLUMINESCENCE IMAGING METHOD

This work was performed during a short term scientific mission at the IMOTION laboratory (Imagerie Moléculaire et Thérapies Innovantes en Oncologie - Molecular Imaging and Innovative Therapies in Oncology), University of Bordeaux in collaboration with Dr. Franck Couillaud and Dr. Olivier Sandre. A grant obtained from the EU-COST (European Cooperation in Science and Technology) TD 1402 Multifunctional Nanoparticles for Magnetic Hyperthermia and Indirect Radiation Therapy (RADIOMAG) facilitated this study.

6.1 Introduction

In the previous chapter, the developed magnetic delivery system was tested for magnetic hyperthermia and drug delivery applications on two different human cancer cell lines. Overall, the MNCs developed in this work were found to have great potential for thermo-chemotherapy applications and synergistic effects of combinatorial treatment were obtained under different conditions. Differences in cellular uptake of the MNCs, drug sensitivity and effects of the combined therapy were observed depending on the cell line studied, emphasising the importance to study each cell line individually.

This chapter focuses on the suitability of the DOX-MNCs for the killing of another cell line by thermo-chemotherapy, a murine prostate cancer RM1 cell line model. This cell line was genetically modified to express the enzyme Firefly Luciferase, so that Luciferase activity could be used to evaluate the cell viability using the bioluminescence imaging method. The IC_{50} values of DOX-MNCs were evaluated on the RM1 cell line for different incubation times. The effect of magnetic hyperthermia, chemotherapy and the combinatorial treatment was assessed using the same two different treatment methods as in the previous chapter so that the effect of nanoparticle internalisation and hyperthermia temperature in the synergistic effect of the combined therapy for the new cell line could be studied. While in chapter 5 magnetic hyperthermia was experimented on adherent cells in suspension due to restrictions linked to the MACH setup, in this chapter, a new device was used to subject the cells to magnetic hyperthermia that allowed for treatment directly on cell monolayers, the natural state of adherent cells. The application of magnetic hyperthermia directly on cell culture is more representative of the reality and can greatly enhance the assessment of hyperthermia and thermo-chemotherapy treatments.

6.2 Bioluminescence imaging

Bioluminescence, the production and emission of light by a living organism is a naturally occurring phenomenon. It is a form of chemiluminescence where the light is emitted as a result of a chemical reaction. Bioluminescence is a biological process that occurs widely in marine vertebrates and invertebrates and may be considered one of the most widespread form of communication on the planet. Bioluminescence also occurs in some funghi, microorganisms including bacteria, and invertebrates such as the firefly. The main chemical reaction responsible for the production of light involves the substrate luciferin and the enzyme luciferase. Luciferases are a wide range of enzymes that catalyse the

oxidation of luciferins in the presence of adenosine triphosphate, Mg^{2+} and oxygen. The oxidation reaction yields non-reactive oxyluciferin and the release of photons of light of dispersed wavelengths.[347,348]

Bioluminescence imaging (BLI) is an optical imaging technique that is based on the sensitive detection of photons emitted during the bioluminescence reaction from bioreporter cells expressing luciferase. Currently, the firefly luciferase (LucF) and D-luciferin are the most widely used luciferase and substrate for BLI.[349] As of today, BLI has several limitations.[350] Absolute quantification of the photons is usually not possible, and therefore simple quantification of light emission may not provide a true representation of the biological process studied. Indeed, the bioluminescent signal is dependent on several factors such as D-luciferin and co-factors availability, signal depth, and tissue absorption. Indeed, if the luciferin substrate and the co-factors are not abundantly present, light emission may not be a true representation of luciferase activity. Moreover, BLI is only a two-dimensional imaging technique, which can result in inaccurate deep tumour localisation. Finally, for transmission of light through animal tissue, there is approximately a 10-fold loss of photon intensity for each centimeter of tissue depth.[351]

However, there are also many advantages to use LucF as a bioluminescent gene reporter. The inherent low background of bioluminescent markers as compared to fluorescent markers makes LucF a superior *in vivo* reporter.[349] LucF light production has the highest quantum efficiency known for any chemiluminescent reaction endowing BLI a high sensitivity.[352] The fast rate of LucF turnover in the presence of the D-luciferin substrate allows for real-time measurements, and the relationship between LucF concentration and photon emission *in vitro* is linear.[353] The high sensitivity and the minimal background noise makes BLI an ideal technique for the detection of minor events in living animals.
It is often used to study a wide range of molecular functions and ongoing biological processes *in vivo*, such as gene expression, cancer treatment, metastasis and disease progression.[347,354]

LucF requires D-luciferin to be injected into the subject prior to imaging. The peak emission wavelength is about 560 nm. While the total amount of light emitted from bioluminescence is typically small and not detected by the human eye, an ultra-sensitive CCD camera can image bioluminescence (Figure 6.1).

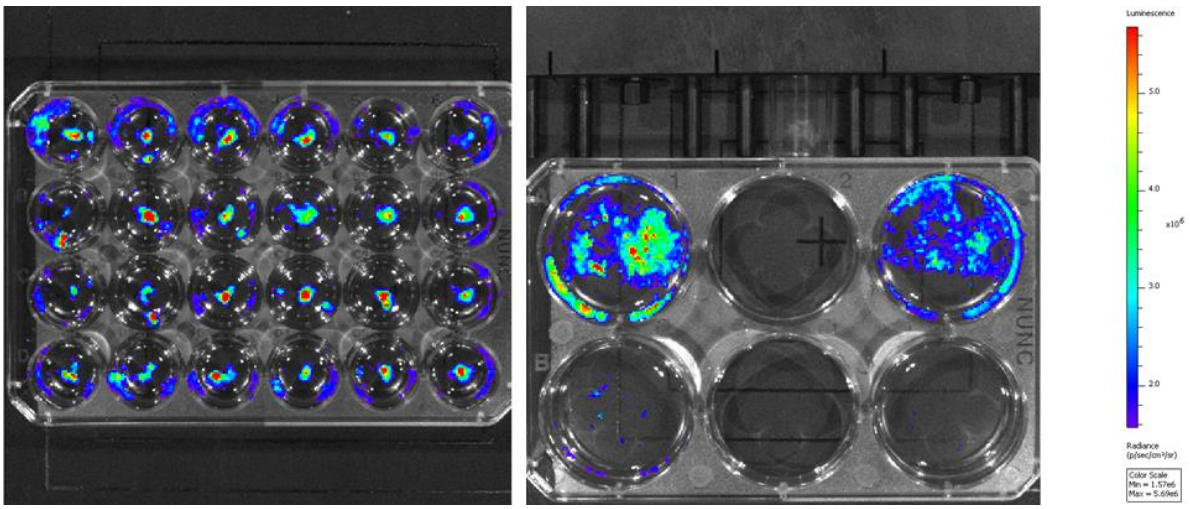

Figure 6. 1 *Examples of images obtained with the BLI method after subjecting cells genetically modified to express LucF to different treatments.*

6.3 Materials and methods

6.3.1 Reagents

Trypan blue solution (0.4%, sterile-filtered), was obtained from Sigma-Aldrich, France. Dulbecco's phosphate buffered saline (DPBS, no calcium, no magnesium, sterile) and trypsin (0.5%, with ethylenediaminetetraacetic acid, sterile) were obtained from Gibco by Thermo Fisher Scientific. D-luciferin was obtained from Promega.

Cell culture reagents: Dulbecco's modified Eagle's medium (DMEM, with 4.5 g/L D-glucose, 0.11 g/L sodium pyruvate, L-glutamine, sterile), Fetal Bovine Serum (FBS, sterile-filtered), and antibiotics Penicillin/Streptomycin (P/S, sterile) were obtained from Gibco by Thermo Fisher Scientific. Blasticidin was obtained from Euromedex.

Unless stated, all reagents were used as purchased, without any further modifications.

6.3.2 Cell culture media

DMEM was supplemented with 1% penicillin/streptomycin used to prevent bacterial contamination of cell culture and 10% FBS.

6.3.3 Experimental methods

6.3.3.1 In vitro hyperthermia of the magnetic nanocomposites

Magnetic heating measurements were performed to assess the heating performances of the MNCs using the DM3 hyperthermia system (nB nanoscale Biomagnetics, Spain). Samples made of 0.5 mL of MNCs dispersed in water with a concentration of 3 mg/mL were placed in the middle of the coil and subjected to an AMF. The increase in temperature was continuously logged using fibres optic probes centred in the suspension. Two probes were used in order to limit possible errors coming from a non-homogeneous spatial heating of the suspension. The measurement was started when the temperature of the suspension was stabilised to room temperature, and the measurement time was limited to 10 min. Different frequency and field amplitude conditions were tested (Table 6.1), for each conditions the SAR and ILP were calculated.

Table 6. 1 *Frequencies and amplitudes of AMF used for heating measurements using the DM3 instrument.*

Frequency (kHz)	146	217	344.5	473.5
Amplitude (kA/m)	20	20	16	13

6.3.3.2 Cell culture of RM1-CMV-LucF cell line

The murine prostate carcinoma cell line genetically modified to express the Luciferase Firefly (LucF) RM1-CMV-LucF was cultured in 20 mL of complete DMEM medium in a T-75 culture flask and incubated at 37 °C under 5% CO_2 in a humidified atmosphere. When the cells reached 80% – 90% confluence, adherent cells were detached by trypsinization (see section 6.2.3.3) and seeded on a new tissue culture plate for subculture or used directly for experiments.

6.3.3.3 Trypsinization of adherent cells

The cell culture medium was discarded and the cell layer washed with DPBS. 2 mL of pre-warmed trypsin at 37 °C was added to the cell layer. The culture flask was then returned to the incubator (37 °C, 5% CO_2) for 3 min. To inactivate the trypsin, 8 mL of complete medium was added for a T-75 culture flask. The cells, now suspended in the medium, were centrifuged at 1200 rpm for 3 min to obtain a cell pellet. The supernatant was discarded and the cells were redispersed in 5 mL of fresh medium. The average number of viable cells in suspension was determined with the aid of a Malassez counting chamber

and the trypan blue exclusion method. The cell viability should be at least 90% for a healthy log-phase culture. After determining the number of cells/mL, the cells were either passaged and used directly for experiments, or returned to culture in a new culture flask with approximately 6.10^5 cells in 20 mL of complete medium for a T-75 flask. 20 µL of blasticidin at 10 mg/mL was added to the new culture flask. Blasticidin is an antibiotic often used in genetic engineering, to select transformed cells in a mammalian cell line that have been engineered to be blasticidin-resistant. Blasticidin has a fast mode of action causing rapid cell death at low antibiotic concentration by inhibiting termination step of translation and peptide bond formation by the ribosome. In this case, the cells that have been genetically modified to carry the resistance gene to blastidicin have also been engineered to carry the LucF gene. Therefore, blasticidin is used as a selection antibiotic, to make sure that only cells expressing the LucF gene grow in the new culture.

6.3.3.4 Determination of the IC_{50} of DOX-MNCs in RM1-CMV-LucF by bioluminescence imaging

RM1-CMV-LucF cells were cultured as explained in section 6.2.3.2. After trypsinization, counting of the cells and confirmation that the cell viability was more than 90% by trypan blue exclusion as explained in section 6.2.3.3, cells suspended in 1 mL complete DMEM at a concentration of 2.5 10^4 cells/well were plated in 24 well, flat-bottomed culture plates. Cells were allowed to adhere and grow by incubation at 37 °C for 48 h before exposure to drug treatment. Briefly the medium was removed from each well, and the cells were exposed to 1 mL of complete DMEM containing various fixed concentration of DOX-MNCs for 24 h and 48 h at 37 °C in the 5% CO_2 incubator. At the end of incubation, the cell viability was determined using the BLI method. Culture medium was removed and cells were rinsed with DPBS. Luciferase activity was used to evaluate the cell viability, by briefly adding 100 µL of D-luciferin solution in DPBS at 6.10^{-4} mol/L to each well. After 5 min of luciferin treatment, images were acquired by BLI using a IVIS Lumina LT (Perkin Elmer Inc., USA). The bioluminescence signal was analyzed using Living Image software. The percentage of viable cells for each concentration of DOX was determined based on the bioluminescence readings, and expressed as a percentage of the vehicle control. All assays were performed in triplicate. Data obtained were subject to median effect analysis using the CompuSyn® software to determine the half maximal inhibitory concentration values of DOX-MNCs on both RM1-CMV-LucF cell line for each incubation period.

6.3.3.5 In vitro anticancer studies by bioluminescence imaging

For *in vitro* anticancer studies, the two same methods as in chapter 5 were employed: hyperthermia treatment after internalization of the nanoparticles in the cells and direct hyperthermia treatment.

6.3.3.5.1 Treatment after internalization

RM1-CMV-LucF cells were cultured, trypsinized and counted as explained in section 6.3.3.2 and 6.3.3.3. Cells suspended in 3 mL of complete medium were seeded in 35 mm culture dish at a density of 100,000 cells/dish. Cells were incubated at 37 °C for 48 h before replacing the medium from each well with 3 mL of fresh complete DMEM only or containing MNCs or DOX-MNCs. The cells were then incubated for an additional 24 h at 37 °C. Six groups were formed: control- (media only, no AMF), control+ (media only, AMF), MNCs- (media containing MNCs, no AMF), MNCs+ (media containing MNCs, AMF), DOX-MNCs- (media containing DOX-MNCs, no AMF) and DOX-MNCs+ (media containing DOX-MNCs, AMF). Therefore, the group MNCs+ corresponds to hyperthermia treatment, DOX-MNCs- corresponds to chemotherapy treatment, and DOX-MNCs+ corresponds to thermo-chemotherapy treatment. A nanoparticle concentration of 1 mg/mL was used for each group. After the 24 h incubation period, the three AMF positive groups (control+, MNCs+ and DOX-MNCs+ groups) were exposed to an AMF (H = 20.0 kA/m and f = 217 kHz) for 30 min using the DM3 instrument. To that aim, the supernatant in each well was discarded and replaced with 2 mL of fresh complete DMEM to keep only the nanoparticles internalized or adsorbed on the cell surface. The cells in the three AMF negative groups (control-, MNCs- and DOX-MNCs- groups) were subjected to the same protocol, without being subjected to an AMF, in order to remove any environmental effect on cell death. After hyperthermia treatment, the cell culture dish was incubated at 37 °C for 24 h. At the end of incubation, the cell viability was determined using the BLI method. Culture medium was removed and cells were rinsed with DPBS. Luciferase activity was used to evaluate the cell viability, by briefly adding 1 mL of D-luciferin solution in DPBS at 6.10^{-4} mol/L to each well. 5 min post-luciferin treatment, images were acquired by BLI using a Lumina LT (Perkin Elmer Inc., USA). The bioluminescence signal was analyzed using Living Image software. The percentage of viable cells for each concentration of DOX was determined based on the bioluminescence readings, and expressed as a percentage of the vehicle control. Experiments were repeated at least three times.

The combined effect of the thermo-chemotherapy treatment was evaluated by the Valeriote's method as described previously in section 5.2.4.11.1.

6.3.3.5.2 Direct treatment

RM1-CMV-LucF cells were cultured, trypsinized and counted as explained in section 6.3.3.2 and 6.3.3.3. Cells suspended in 200 µL of complete medium were seeded in 16 well, flat-bottomed culture plates, at a density of 2000 cells/well. These wells have the same size of the ones of 96 wells plate. These were chosen because they can fit in the DM3 setup and experiments can therefore be performed easily in triplicates. Cells were incubated at 37 °C for 48 h before replacing the medium from each well with 200 µL of fresh complete medium only or containing MNCs or DOX-MNCs. Again, six groups were formed as described in section 6.3.3.5.1. The concentration of nanoparticles in solution was chosen so that a temperature of 43 °C could be reached quickly (i.e. 0.5 mg/mL). The cells in culture plates were exposed to an AMF (f = 217 kHz) for 30 min using the DM3 instrument and the temperature (either 42°C or 43°C) was adjusted by tuning the field amplitude H of the AMF. The field amplitude H started at 20.0 kA/m and decreased as appropriate to maintain the desired temperature. The cells in the three AMF negative groups (control-, MNCs- and DOX-MNCs- groups) were subjected to the same protocol, without being subjected to an AMF, in order to remove any environmental effect on cell death. After hyperthermia treatment, the cell culture plates were incubated at 37 °C for 24 h. At the end of incubation, the cell viability was determined using the BLI method as described in section 6.3.3.5.1. Experiments were repeated at least three times.
The combined effect of the thermo-chemotherapy treatment was evaluated by the Valeriote's method as described previously in section 5.2.4.11.1.

6.3.3.6 Statistical analysis

Statistical analysis was performed using the Student's t-test for unpaired data and the results are presented as mean ± standard deviations. Statistical significance was accepted at a level of $p < 0.05$.

6.4 Results and discussion

6.4.1 Magnetic heating measurements – DM3

The field amplitude and frequency condition that gave the best heating potential were f = 217 kHz and H = 20 kA/m, with a temperature increase from 22 °C to 55 °C in 10 min (Figure 6.2). It translates into a SAR of 280 W/g, equivalent to an ILP of 3 nHm²/kg. It is

worth noting that the *Hf* factor, here equal to 4.34 x 10^9 $Am^{-1}s^{-1}$ is below the limit recommended for safe application of an AMF of 5 x 10^9 $Am^{-1}s^{-1}$.[65]

The staircase-like curve obtained is due to the DM3 software that did not save the temperature data with a decimal. This could not be fixed.

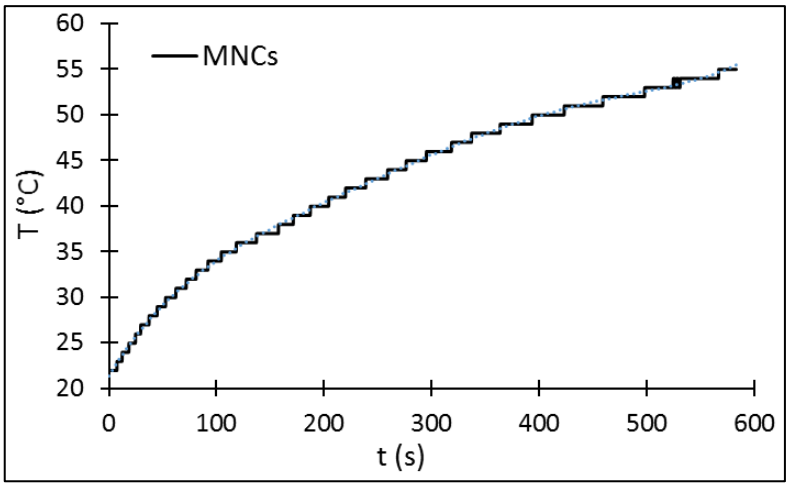

Figure 6. 2 *Typical heating curve of the MNCs dispersed in water with a concentration of 3 mg/mL and subjected to an AMF (f = 217 kHz and H = 20.0 kA/m) using the DM3 instrument.*

6.4.2 Determination of the IC_{50} of DOX-MNCs in RM1-CMV-LucF

The concentration effect of DOX-MNCs as well as the exposure time on the cell viability were investigated by monitoring LucF activity at incubation time points of 24 h and 48 h. For each condition, the IC_{50} values were determined by constructing a dose-response curve according to the results obtained from the bioluminescence signal (Figure 6.3).

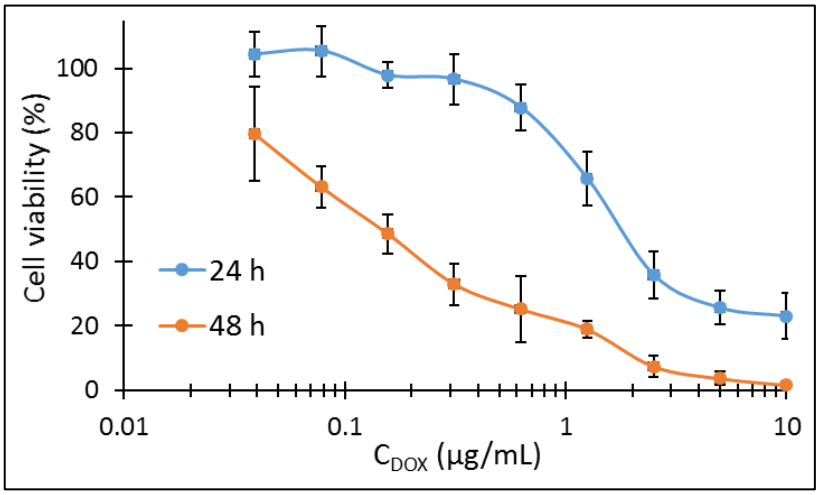

Figure 6. 3 *Dose response curves. Cell viability of RM1-CMV-LucF cells incubated with DOX concentrations DOX-MNCs for incubation period of 24 h and 48 h.*

The cytotoxicity of the DOX-MNCs is dependent on concentration and exposure time, and increased with increasing DOX concentration and incubation period. The IC_{50} values after 24 h and 48 h of incubation were found to be equivalent to a DOX concentration of 2.12 µg/mL and 0.16 µg/mL, respectively.

6.4.3 *In vitro* anticancer studies by bioluminescence imaging

6.4.3.1 Initial considerations and preliminary experiments

In this chapter, cell viability of a murine prostate carcinoma cell line genetically modified to express the luciferase firefly has been investigated by BLI. The two same methods of treatment as employed in Chapter 5 were also employed in this study: the direct treatment and treatment after internalization methods.

In the previous chapter, the hyperthermia experiments had to be conducted on MCF-7 and U-87 cells suspended in their culture medium. Cells had to be detached before being subjected to the hyperthermia treatment and then taken back to culture to study the delayed response at different time point. This strategy was chosen because the MACH setup does not allow for a petri dish to be placed in the coil, however it may not reflect the complete cell response. The metabolism of live adherent cells can be altered when in suspension by changes in temperature, pH and cell aggregation in suspension. Thanks to the DM3 setup, it was possible to perform the hyperthermia treatment directly on cell monolayers. This is an important consideration as it is the natural state of adherent cells. Thus, the application of magnetic hyperthermia directly on cell culture is more representative and can greatly enhance the assessment of hyperthermia treatments.

The same initials considerations as for U-87 and MCF-7 cells were made for RM1-CMV-LucF cells. Experiments with a lower DOX concentration were performed by mixing the MNCs with DOX-MNCs to obtain the desired nanoparticle concentration and the desired DOX concentration. Using the IC_{50} values of DOX-MNCs for RM1-CMV-LucF cells obtained from the dose-response curves determined by the BLI method in section 6.4.3 a DOX concentration of 0.18 µg/mL was chosen for the current study. At this concentration, cell viability was shown to remain above 90% 24 h after the treatment.

Preliminary experiments of hyperthermia, chemotherapy and the combined thermo-chemotherapy at different hyperthermia temperature using the direct treatment methods were realised on RM1-CMV-LucF cells. These experiments revealed that mild

hyperthermia temperature of 42 °C was more efficient for the combined therapy than hyperthermia at 40 °C or 44 °C for this specific cell line. As a consequence, hyperthermia temperatures of 42 °C and 43 °C were studied in this chapter.

6.4.3.2 In vitro anticancer studies, direct treatment and treatment after internalisation

Hyperthermia, chemotherapy and the combined thermo-chemotherapy using the direct treatment and the treatment after internalisation were experimented on RM1-CMV-LucF cells. The concentration in DOX was kept constant at 0.18 µg/mL by mixing MNCs and DOX-MNCs (ratio 399:1 w/w and 199:1 w/w for the treatment after internalisation and for the direct treatment, respectively) to obtained the desired final concentration in DOX and in nanoparticles. The obtained cell viabilities 24 h after treatment are presented in Figure 6.4.

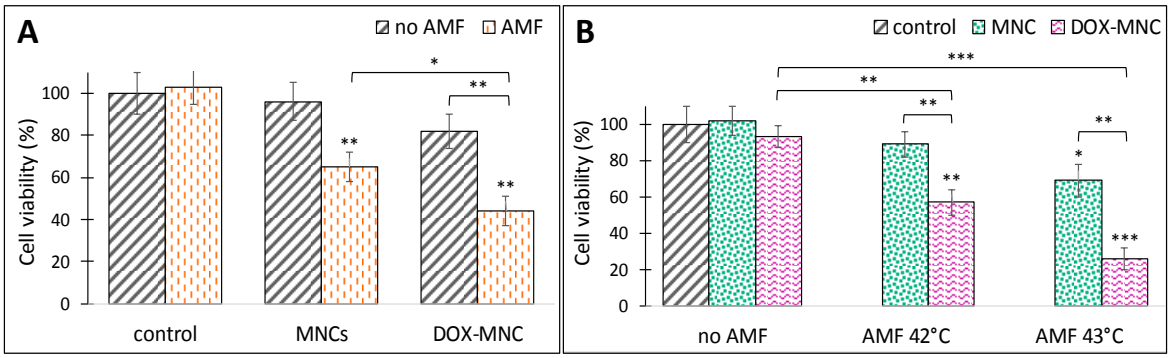

Figure 6. 4 *Cell viabilities of RM1-CMV-LucF cells 24 h following A) treatment after internalisation with or without a 30 min exposure to an AMF (f = 217 kHz and H = 20.0 kA/m) and B) direct treatment with or without a 30 min exposure to an AMF (f = 217 kHz and H varies to maintain the desired temperature, H_{max} = 20.0 kA/m) with media alone (control cells), MNCs or DOX-MNCs containing 0.18 µg of DOX. The asterisks refer to significant levels compared to the corresponding control experiment or the combined therapy; p < 0.05 (*), p < 0.01 (**) and p < 0.001 (***).*

The application of the AMF alone does not have any detrimental effect on the RM1-CMV-LucF viability. For the treatment after internalisation, the relative cell viabilities 24 h after treatment were 65% ($p < 0.01$) for hyperthermia, 82% for chemotherapy and 44% ($p < 0.01$) for thermo-chemotherapy. For the direct treatment, the relative cell viabilities 24 h after treatment were 93% for chemotherapy, 89% for hyperthermia and 57% ($p < 0.01$) for thermo-chemotherapy at 42 °C; 70% ($p < 0.05$) for hyperthermia and 26% ($p < 0.001$) for thermo-chemotherapy at 43 °C.

The RM1-CMV-LucF cell line is quite sensitive to heat released from nanoparticles internalised in the cells, as observed from the resulting cell viability of 65%, but is not too sensitive to the heating of the surrounding medium at temperature below 43 °C (cell viability of 89% 24 h after treatment at 42 °C).

Cell viabilities obtained 48 h after the different treatments are not shown. Indeed, one major problem encountered working with the RM1 cell line was a very important cell detachment, especially at high confluency. As a consequence, this phenomenon happened in a greater extent for control cells or cells that were not affected by the received treatment, and bioluminescence intensity values obtained could not be trusted to represent accurate values of the cell viabilities.

The cytotoxic effect of the combinatorial treatment achieved with the developed delivery system after cellular uptake of the nanoparticles was found superior to either hyperthermia ($p < 0.05$) or chemotherapy ($p < 0.01$) applied separately.

For each hyperthermia temperature, the cytotoxic effect of the combinatorial treatment achieved with the developed delivery system using the direct treatment method was also found superior to each of the two treatments applied separately.

For both methods, an evaluation using Valeriote's formula showed that the combined effects were synergistic in nature (Table 6.2).

Table 6. 2 *Evaluation of the combined effects of the thermo-chemotherapy treatment after nanoparticle internalisation and of the direct thermo-chemotherapy treatment at different hyperthermia temperatures with 0.18 µg of DOX for RM1-CMV-LucF cell line according to Valeriote's formula.*

		(A)*(B)/100 (%)	**(A+B)** (%)	**Effect**
Treatment after internalisation	/	53	44	Synergistic
Direct treatment	**42 °C**	83	59	Synergistic
	43 °C	64	27	Synergistic

6.5 Conclusion

In summary, the heating performance of the MNCs were assessed again with the DM3 machine and were found to yield an ILP of 3 nHm²/kg under the field conditions of f = 217

kHz and H = 20 kA/m. The IC_{50} values of the DOX-MNCs for the RM1-CMV-LucF cell line were evaluated for different incubation time before proceeding to the *in vitro* thermo-chemotherapy experiments.

Monitoring the luciferase activity by the BLI method was found to be a precise and simple tool for evaluation of the cell viability. Such as in chapter 5, cell death was found to be dependent on the method of treatment used. For both treatment methods, an evaluation using Valeriote's formula showed that the combined effects were synergistic in nature. However, while for the two cell lines studied in chapter 5 the thermo-chemosensitisation effect using the direct treatment method was the highest at mild hyperthermia temperature of 40 °C, it was found for the RM1 cell line to be more effective at hyperthermia temperature of 43 °C. This finding highlights again the cell line dependency and emphasizes the necessity to study each cell line independently for a particular treatment.

CHAPTER 7

CONCLUSIONS AND FUTURE WORK

CONCLUSION

Superparamagnetic iron oxides are the most commonly used nanoparticles for applications in biomedicine, because of their numerous advantages, but their heating potential for hyperthermia applications is limited because of their low saturation magnetisation and magnetic anisotropy. Pure metal nanoparticles such as iron have the highest saturation magnetisation, but have limited use in biomedical applications due to their inherent toxicity and poor chemical stability, mainly their quick oxidation process. A core/shell structure can be adopted with an appropriate coating able to prevent oxidation of the metallic core. Gold has been one of the most popular metallic coating materials for iron owing to its chemical inertness that protect iron against oxidation and its biocompatibility.[355] Similar to gold, bismuth is chemically inert and can be used as CT-imaging agent. Bismuth even possesses a larger X-ray attenuation coefficient, has low toxicity and is less expensive. For those reasons, bismuth was chosen as a coating for iron nanoparticles. Thermal decomposition of iron precursors followed by reduction of bismuth precursors was chosen as a synthetic route. As desired, iron nanoparticles were found to be highly magnetic. However, this caused issues in the stabilization of the nanoparticles due to strong magnetic interactions between the nanoparticles. Observation of the obtained nanoparticles with TEM was greatly hindered due to the highly aggregated state of the particles and made the interpretation of the results challenging. The stabilization of the particles could only be addressed by a long and tedious post-synthetic process with several cycles of oleylamine addition, sonication and washing of the particles. After stabilization and observation of well-separated particles on a TEM grid, only one type of core/shell nanoparticles could be observed. However, due to the grain size obtained from XRD patterns, EDS analyses and elemental mapping of single particle, it was concluded that bismuth did not seem to nucleate on the surface of the already formed iron nanoparticle but rather grow as separate particles. The bismuth nanoparticles might have been lost in the stabilization process. Despite different attempts varying the synthetic conditions, the separated growth of bismuth could not be suppressed and the synthesis of core@shell Fe@Bi nanoparticles was found unsuccessful.

As a consequence, core@shell Fe@Bi nanoparticles could not be used in the development of a magnetic nanocarrier for hyperthermia therapy and drug delivery applications. Iron oxide nanoparticles were chosen as substitute. Despite their lower saturation magnetisation, their ease of synthesis made them ideal candidates for investigation. Iron oxide nanoparticles were synthesised using a microwave-assisted co-precipitation method. This highly reproducible synthesis yielded highly crystalline naked

IONPs that were subsequently functionalised with a thermo-responsive polymer. The nanoparticles were superparamagnetic at room temperature with a high average saturation magnetisation of 78 emu/g. The thermo-responsive polymer p(DEGMA-co-PEGMA-b-[TMSPMA-co-VBA]), synthesized by RAFT polymerisation, was composed of four mains blocks each having a specific utility. The LCST, that could be tuned by varying the DEGMA:PEGMA molar ratio, was chosen around 40 °C to be above physiological temperature and easily reached via magnetic hyperthermia. Under appropriate conditions, the functionalisation of the nanoparticles resulted in highly stable aqueous suspensions exhibiting good heating performances with an ILP of 2.1 nHm^2/K, 3.5 nHm^2/K if only the mass of iron is considered.

High encapsulation of the anticancer drug DOX in the MNCs was achieved through formation of heat- and acid-labile Schiff base bonds. The dual temperature-and pH-responsive behaviour of the nanocarrier is an important feature that gives rise to spatial and temporal control over the release of the drug. High temperature and acidic pH were shown to act as triggers for the release of the drug. A burst release of the drug is achieved under application of an AMF and tumour acidic pH conditions, with almost 90% of drug being released after 1 h. At physiological pH and temperature, the amount of released drug is low; that is the DOX is correctly retained in the nanocarrier, which is desirable in clinical applications to limit distribution of the drug to healthy tissues and unwanted side effects.

The developed MNCs were then used for *in vitro* experiments on human glioma U-87 and breast cancer MCF-7 cell line models to demonstrate their potential as thermo-chemo therapeutic agent for the treatment of cancer. The MNCs were found to be non-toxic to cells at concentration up to 1 mg/mL. The cellular uptake of the MNCs was dependent on the nanoparticle concentration and the cell line. This cell line dependency was reflected in the study of DOX-MNCs cytotoxicity. U-87 cells internalised the MNCs in a great extent, which resulted in a more acute cytotoxicity of DOX-MNCs towards U-87 cells compared to MCF-7 cells. Study of drug intracellular distribution revealed the quick accumulation in the cell nuclei of free DOX through permeation of cellular and nuclear membrane by passive diffusion. In contrast, DOX-MNCs were shown to be taken up by malignant cells through endocytosis, followed by some extent of drug release in the cytoplasm due to acidic pH of endosomes/lysosomes organelles and subsequent DOX diffusion to the nucleus. Such a delivery system is particularly interesting to overcome drug resistance in drug resistant cancer and to reduce the amount of available drug molecules present in the extracellular environment therefore reducing unwanted side effects.

For thermo-chemotherapy experiments, two different methods of treatment were studied. The direct treatment method involved subjecting the cells to an AMF immediately after putting the nanoparticles together with the cells. There is no time for cell uptake of the particles and consequently only nanoparticles in the extracellular environment participate to the hyperthermia treatment. The treatment after internalisation consists in incubating the cells in culture with the nanoparticles for 24 h, and then remove the nanoparticles in the extracellular environment by replacing the media with fresh media before subjecting the cells to an AMF. Only nanoparticles internalised in the cells are involved in the hyperthermia treatment. This experiment revealed that the MNCs retain their heating capability in some extent upon internalisation by the cells. For both methods, the combinatorial treatment was more effective than chemotherapy or magnetic hyperthermia as individual treatments.

The method of treatment used was found to influence the resultant cell killing. For a cell line that internalized the MNCs in a great extent such as the U-87 cell line, the thermo-chemotherapy applied through the treatment after internalisation method was found to be more effective, the combined effects were found to be synergistic in nature and an almost complete cell death was achieved. However, encouraging results were also obtained for the direct treatment method for both U-87 and MCF-7 cells. These findings demonstrate that it is not necessary for tumour cells to internalize the nanoparticles for an efficient therapy, but is preferable. The importance of the applied thermal dose was emphasized through the study of the direct thermo-chemotherapy treatment at different hyperthermia temperature. Both synergistic and sub-additive effects of the combined therapy were observed depending on the applied hyperthermia temperature. However, synergistic and sub-additive effects were found at different hyperthermia temperature depending on the cell line which again showed the necessity to study each cell line independently for a particular treatment. The mechanisms responsible for the synergistic effect of the combined therapy might be more or less triggered depending on whether nanoparticles have been internalized, the applied hyperthermia temperature and the cell line. The mechanisms responsible for the synergy of the combined therapy generally involve an inhibition of DNA repair, acceleration of the cytotoxic chemical reaction rate and an improve intracellular uptake of nanoparticles or drug molecules in heated tumour as compared to non-heated tissues. The latter seems to be particularly relevant in the case of the direct treatment. Finally, because the MNCs are pH- and thermo-sensitive, a maximized drug release is obtained when both stimuli are applied at the same time, and therefore a better synergism of the combined therapy. This is the case for internalised DOX-MNCs. Nonetheless, *in vivo*, tumour extracellular environment is often more acidic than normal tissue, with a pH ranging from 5.7 to 7.8,[344] that would facilitate the release of

the drug from MNCs that have not been yet internalised, and subsequent quick accumulation of available released DOX molecules in the cell nuclei through cellular membrane diffusion.

Finally, monitoring the luciferase activity using the BLI method was used for the evaluation of the cell viability of a third cell line, a murine prostate carcinoma RM1 cell line genetically modified to express the Luciferase Firefly. It was found to be a simple but precise and reliable tool for the study of cell death after magnetic hyperthermia, chemotherapy or the combined treatment. The assessment of hyperthermia and thermo-chemotherapy treatments was enhanced as compared to the study carried out in chapter 5, because hyperthermia treatment could be applied directly on cell monolayers. For both treatment methods, the combined effects were found to be synergistic in nature.

To conclude, each cell line studied in this work was found to behave differently from one another and to respond differently to thermo-chemotherapy treatment, highlighting the necessity to study each cell line independently for a given treatment. However, the developed delivery system was shown to be an effective and promising tool for multi-modal cancer therapy, and especially for thermo-chemotherapy applications. Synergistic effects of the combinatorial treatment were observed for the three cell lines used in this work in almost every studied conditions. No matter the cell line, cell recovery 48 h after thermo-chemotherapy treatment was never observed, which is important to avoid tumour recurrence. This study also highlighted the difference in cell death that can be obtained depending on the method of treatment adopted for application of magnetic hyperthermia and thermo-chemotherapy, i.e. whether nanoparticles are situated in the intracellular or extracellular environment.

FUTURE WORK

The DOX-loaded dual pH- and thermo-responsive magnetic nanocarrier developed in this work as well as the *in vitro* studies constitute a step forward towards the generation of nanosystem that could be designed and envisioned for clinical applications. Next steps would involve more in depth *in vitro* studies such as cell death mechanisms (apoptosis or necrosis) depending on the method of treatment, chemotherapeutic and thermal dose applied. Investigating the effect of thermo-chemotherapy with the developed delivery system on a greater number of cell lines, including drug-resistance cell lines, would also be useful to provide a bank of results concerning both the response of a particular cell line to the combinatorial treatment and the compatibility of this particular developed delivery system for different type of cancer. Furthermore, it would be interesting to study and quantify the uptake of the MNCs by macrophages in order to evaluate whether the MNCs would be rapidly cleared by the reticulo-endothelial system or have a long blood circulation time.

Moreover, because *in vitro* studies showed the cell line dependency of cellular uptake of the non-targeted MNCs, and their different behaviour in response to thermo-chemotherapy treatment, further surface functionalisation of the MNCs for active targeting, improved specificity and therapeutic response with specific ligands or antibodies would be highly desirable. The carboxylic end group of the polymer offers an excellent platform for further functionalisation with targeting moieties.

Appendix I: Publications and participation to conferences

Publications

- A. Hervault and NTK. Thanh, Magnetic nanoparticle-based therapeutic agents for thermo-chemotherapy treatment of cancer, ***Nanoscale***, 2014, **6**, 11553-11573. Invited Featured article

- R. Hachani, M. Lowdell, M. Birchall, A. Hervault, D. Mertz, S. Bégin-Colin and NTK. Thanh, Polyol synthesis, functionalisation and biocompatibility studies of superparamagnetic iron oxide nanoparticles as potential MRI agents, ***Nanoscale***, 2016, **8**, 3278-3287.

- A. Hervault, A.E. Dunn, M. Lim, C. Boyer, D. Mott, S. Maenosono and NTK. Thanh, Doxorubicin loaded dual pH- and thermo-responsive magnetic nanocarrier for combined magnetic hyperthermia and targeted controlled drug delivery applications, ***Nanoscale***, 2016, **8**, 12152-12161. Cover paper

Conferences

- July 2014, UK colloids 2014, London (UK), *attendance only*

- September 2014, Faraday Discussion 175: Physical chemistry of functionalised biomedical nanoparticles, Bristol (UK). Poster presented by A. Hervault:

  A. Hervault and N.T.K. Thanh, Functionalisation and characterisation of magnetic nanoparticles for applications in thermo-chemotherapy of cancer.

- March 2015, The 95th annual meeting 2015 of Chemical Society of Japan, Tokyo (Japan). Talk presented by A. Hervault:

  A. Hervault, M. Lim, A. Dunn, C. Boyer, T. Taniike, D. Mott, S. Maenosono and N.T.K. Thanh, Functionalisation and characterisation of magnetic nanoparticles for applications in thermo-chemotherapy of cancer.

- September 2015, CSEJ 47th spring meeting, Kagoshima (Japan). Talk presented by A. Hervault:

  A. Hervault, M. Lim, A. Dunn, C. Boyer, T. Taniike, D. Mott, S. Maenosono and N.T.K. Thanh, Development of a dual pH- and thermo-responsive magnetic nanocarrier for application in thermo-chemotherapy of cancer.

- November 2015, 2015 EU-Japan collaborative workshop on Next-Generation Nanomagnetic Medicine, Kanazawa (Japan). Talk presented by A. Hervault:

  A. Hervault, M. Lim, A. Dunn, C. Boyer, T. Taniike, D. Mott, S. Maenosono and N.T.K. Thanh, Doxorubicin loaded dual pH- and thermo-responsive magnetic nanocarrier for application in thermo-chemotherapy of cancer.

- December 2015, PACIFICHEM The international chemical congress of Pacific Basin Societies 2015, Honolulu (Hawaii, USA). Talk and poster presented by A. Hervault:

  A. A. Hervault, M. Lim, A. Dunn, C. Boyer, T. Taniike, D. Mott, S. Maenosono and N.T.K. Thanh, Development of a dual pH- and thermo-responsive magnetic nanocarrier for application in thermo-chemotherapy of cancer (talk).
  B. A. Hervault, M. Lim, A. Dunn, C. Boyer, T. Taniike, D. Mott, S. Maenosono and N.T.K. Thanh, Synthesis and characterization of a composite magnetic nanosystem for application in thermo-chemotherapy of cancer (poster).

- April 2016, EU COST Meeting, Synthesis and functionalisation of magnetic nanoparticles for magnetic hyperthermia and radiotherapy, London, (UK). Talk presented by A. Hervault:

  A. Hervault, M. Lim, A. Dunn, C. Boyer, T. Taniike, D. Mott, S. Maenosono and N.T.K. Thanh, pH- and thermo-responsive magnetic nanocarrier for thermo-chemotherapy of cancer.

- May 2016, 2016 EU-Japan collaborative research on Next Generation Nanomagnetic Medicine, London (UK). *Attendance only.*

- June 2016, The 11th International Conference on the Scientific and Clinical Applications of Magnetic Carriers, Vancouver (Canada). Talk presented by A. Hervault:

  A. Hervault, M. Lim, A. Dunn, C. Boyer, T. Taniike, D. Mott, S. Maenosono and N.T.K. Thanh, Doxorubicin-loaded dual pH- and thermo-responsive magnetic nanocarrier for combined hyperthermia and controlled drug delivery applications.

References

1 Tiefenauer, L. X., Kuhne, G. & Andres, R. Y. ANTIBODY MAGNETITE NANOPARTICLES - IN-VITRO CHARACTERIZATION OF A POTENTIAL TUMOR-SPECIFIC CONTRAST AGENT FOR MAGNETIC-RESONANCE-IMAGING. *Bioconj. Chem.* **4**, 347-352, doi:10.1021/bc00023a007 (1993).

2 Hu, Y., Meng, L., Niu, L. & Lu, Q. Highly cross-linked and biocompatible polyphosphazene-coated superparamagnetic Fe3O4 nanoparticles for magnetic resonance imaging. *Langmuir* **29**, 9156-9163, doi:10.1021/la402119s (2013).

3 Jordan, A. *et al. Magnetic fluid hyperthermia (MFH)*. (1997).

4 Kallumadil, M. *et al.* Suitability of commercial colloids for magnetic hyperthermia. *Journal of Magnetism and Magnetic Materials* **321**, 1509-1513, doi:10.1016/j.jmmm.2009.02.075 (2009).

5 Banerjee, S. S. & Chen, D. H. Magnetic nanoparticles grafted with cyclodextrin for hydrophobic drug delivery. *Chem. Mater.* **19**, 6345-6349, doi:10.1021/cm702278u (2007).

6 Rahimi, M. *et al.* In vitro evaluation of novel polymer-coated magnetic nanoparticles for controlled drug delivery. *Nanomedicine-Nanotechnology Biology and Medicine* **6**, 672-680, doi:10.1016/j.nano.2010.01.012 (2010).

7 Wang, H. *et al.* Magnetic-Fe/Fe(3)O(4)-nanoparticle-bound SN38 as carboxylesterase-cleavable prodrug for the delivery to tumors within monocytes/macrophages. *Beilstein journal of nanotechnology* **3**, 444-455, doi:10.3762/bjnano.3.51 (2012).

8 Purushotham, S. *et al.* Thermoresponsive core-shell magnetic nanoparticles for combined modalities of cancer therapy. *Nanotechnology* **20**, 305101, doi:10.1088/0957-4484/20/30/305101 (2009).

9 Veiseh, O., Gunn, J. W. & Zhang, M. Design and fabrication of magnetic nanoparticles for targeted drug delivery and imaging. *Adv Drug Deliv Rev* **62**, 284-304, doi:10.1016/j.addr.2009.11.002 (2010).

10 Sanson, C. *et al.* Doxorubicin Loaded Magnetic Polymersomes: Theranostic Nanocarriers for MR Imaging and Magneto-Chemotherapy. *Acs Nano* **5**, 1122-1140, doi:10.1021/nn102762f (2011).

11 Lu, L. T. *et al.* Size and shape control for water-soluble magnetic cobalt nanoparticles using polymer ligands. *J. Mater. Chem.* **18**, 2453, doi:10.1039/b801800f (2008).

12 Guardia, P., Labarta, A. & Batlle, X. Tuning the Size, the Shape, and the Magnetic Properties of Iron Oxide Nanoparticles. *Journal of Physical Chemistry C* **115**, 390-396, doi:10.1021/jp1084982 (2011).

13 Narayanan, R. & El-Sayed, M. A. Catalysis with transition metal nanoparticles in colloidal solution: Nanoparticle shape dependence and stability. *Journal of Physical Chemistry B* **109**, 12663-12676, doi:10.1021/jp051066p (2005).

14 Gonzales-Weimuller, M., Zeisberger, M. & Krishnan, K. M. Size-dependant heating rates of iron oxide nanoparticles for magnetic fluid hyperthermia. *Journal of Magnetism and Magnetic Materials* **321**, 1947-1950, doi:10.1016/j.jmmm.2008.12.017 (2009).

15 Zhou, X. *et al.* Controllable synthesis, magnetic and biocompatible properties of Fe3O4 and alpha-Fe2O3 nanocrystals. *J. Solid State Chem.* **196**, 138-144, doi:10.1016/j.jssc.2012.05.025 (2012).

16 Atsumi, T., Jeyadevan, B., Sato, Y. & Tohji, K. Heating efficiency of magnetite particles exposed to AC magnetic field. *Journal of Magnetism and Magnetic Materials* **310**, 2841-2843, doi:10.1016/j.jmmm.2006.11.063 (2007).

17 Thuy, T. T., Maenosono, S. & Thanh, N. T. K. in *Magnetic Nanoparticles: From Fabrication to Clinical Applications* 99-126 (CRC Press, 2012).

18 Krishnan, K. M. Biomedical Nanomagnetics: A Spin Through Possibilities in Imaging, Diagnostics, and Therapy. *Ieee Transactions on Magnetics* **46**, 2523-2558, doi:10.1109/tmag.2010.2046907 (2010).

19 Moyer, H. R. & Delman, K. A. The role of hyperthermia in optimizing tumor response to regional therapy. *Int. J. Hyperthermia* **24**, 251-261, doi:10.1080/02656730701772480 (2008).

20 Baronzio, G. F. & Hager, E. D. *Hyperthermia in Cancer Treatment: A Primer*. pp Introduction (no page numbers) (Springer, 2006).

21 Cavaliere, R. *et al.* Selective heat sensibility of cancer cells. Biochemical and clinical studies. *Cancer* **20**, 1351-1381 (1967).
22 Gordon, R. T., Hines, J. R. & Gordon, D. INTRACELLULAR HYPERTHERMIA - BIOPHYSICAL APPROACH TO CANCER-TREATMENT VIA INTRACELLULAR TEMPERATURE AND BIOPHYSICAL ALTERATIONS. *Med. Hypotheses* **5**, 83-102, doi:10.1016/0306-9877(79)90063-x (1979).
23 Kerr, J. F. R., Winterford, C. M. & Harmon, B. V. APOPTOSIS - ITS SIGNIFICANCE IN CANCER AND CANCER-THERAPY. *Cancer* **73**, 2013-2026, doi:10.1002/1097-0142(19940415)73:8<2013::aid-cncr2820730802>3.0.co;2-j (1994).
24 Golstein, P. & Kroemer, G. Cell death by necrosis: towards a molecular definition. *Trends Biochem. Sci.* **32**, 37-43, doi:10.1016/j.tibs.2006.11.001 (2007).
25 Willingham, M. C. Cytochemical Methods for the Detection of Apoptosis. *J. Histochem. Cytochem.* **47**, 1101-1109, doi:10.1177/002215549904700901 (1999).
26 Hildebrandt, B. *et al.* The cellular and molecular basis of hyperthermia. *Critical Reviews in Oncology Hematology* **43**, 33-56, doi:10.1016/s1040-8428(01)00179-2 (2002).
27 Lepock, J. R. Cellular effects of hyperthermia: relevance to the minimum dose for thermal damage. *Int. J. Hyperthermia* **19**, 252-266, doi:10.1080/0265673031000065042 (2003).
28 Jain, R. K. Normalizing tumor vasculature with anti-angiogenic therapy: a new paradigm for combination therapy. *Nat. Med.* **7**, 987 (2001).
29 Song, C. W. Effect of Local Hyperthermia on Blood Flow and Microenvironment: A Review. *Cancer Res.* **44**, 4721s-4730s (1984).
30 Song, C. W., Rhee, J. G. & Levitt, S. H. BLOOD-FLOW IN NORMAL-TISSUES AND TUMORS DURING HYPERTHERMIA. *J. Natl. Cancer Inst.* **64**, 119-124 (1980).
31 Storm, F. K., Harrison, W. H., Elliott, R. S. & Morton, D. L. NORMAL TISSUE AND SOLID TUMOR EFFECTS OF HYPERTHERMIA IN ANIMAL-MODELS AND CLINICAL-TRIALS. *Cancer Res.* **39**, 2245-2251 (1979).
32 Siemann, D. W. The unique characteristics of tumor vasculature and preclinical evidence for its selective disruption by Tumor-Vascular Disrupting Agents. *Cancer Treat. Rev.* **37**, 63-74, doi:10.1016/j.ctrv.2010.05.001 (2011).
33 Dewhirst, M. W. *et al.* Morphologic and hemodynamic comparison of tumor and healing normal tissue microvasculature. *International Journal of Radiation Oncology*Biology*Physics* **17**, 91-99, doi:http://dx.doi.org/10.1016/0360-3016(89)90375-1 (1989).
34 Gerweck, L. E., Nygaard, T. G. & Burlett, M. RESPONSE OF CELLS TO HYPERTHERMIA UNDER ACUTE AND CHRONIC HYPOXIC CONDITIONS. *Cancer Res.* **39**, 966-972 (1979).
35 Song, C. W., Park, H. & Griffin, R. J. Improvement of tumor oxygenation by mild hyperthermia. *Radiat. Res.* **155**, 515-528, doi:10.1667/0033-7587(2001)155[0515:iotobm]2.0.co;2 (2001).
36 Wust, P. *et al.* Hyperthermia in combined treatment of cancer. *The Lancet Oncology* **3**, 487-497, doi:10.1016/s1470-2045(02)00818-5 (2002).
37 Maier-Hauff, K. *et al.* Efficacy and safety of intratumoral thermotherapy using magnetic iron-oxide nanoparticles combined with external beam radiotherapy on patients with recurrent glioblastoma multiforme. *J. Neurooncol.* **103**, 317-324, doi:10.1007/s11060-010-0389-0 (2011).
38 Maier-Hauff, K. *et al.* Intracranial thermotherapy using magnetic nanoparticles combined with external beam radiotherapy: results of a feasibility study on patients with glioblastoma multiforme. *J. Neurooncol.* **81**, 53-60, doi:10.1007/s11060-006-9195-0 (2007).
39 Manning, M. R. *et al.* CLINICAL HYPERTHERMIA - RESULTS OF A PHASE-I TRIAL EMPLOYING HYPERTHERMIA ALONE OR IN COMBINATION WITH EXTERNAL BEAM OR INTERSTITIAL RADIOTHERAPY. *Cancer* **49**, 205-216, doi:10.1002/1097-0142(19820115)49:2<205::aid-cncr2820490202>3.0.co;2-w (1982).
40 van der Zee, J. *et al.* Comparison of radiotherapy alone with radiotherapy plus hyperthermia in locally advanced pelvic tumours: a prospective, randomised, multicentre trial. *Lancet* **355**, 1119-1125, doi:10.1016/s0140-6736(00)02059-6 (2000).
41 Horsman, M. R. & Overgaard, J. Hyperthermia: a potent enhancer of radiotherapy. *Clin. Oncol.* **19**, 418-426, doi:10.1016/j.clon.2007.03.015 (2007).
42 van der Zee, J. Heating the patient: a promising approach? *Ann. Oncol.* **13**, 1173-1184, doi:10.1093/annonc/mdf280 (2002).

43 Issels, R. D. *et al.* Neo-adjuvant chemotherapy alone or with regional hyperthermia for localised high-risk soft-tissue sarcoma: a randomised phase 3 multicentre study. *Lancet Oncol.* **11**, 561-570, doi:10.1016/s1470-2045(10)70071-1 (2010).
44 Issels, R. D. *et al.* Neoadjuvant chemotherapy combined with regional hyperthermia (RHT) for locally advanced primary or recurrent high-risk adult soft-tissue sarcomas (STS) of adults: long-term results of a phase II study. *Eur. J. Cancer* **37**, 1599-1608, doi:10.1016/s0959-8049(01)00183-6 (2001).
45 Sugimachi, K. *et al.* CHEMOTHERAPY COMBINED WITH OR WITHOUT HYPERTHERMIA FOR PATIENTS WITH ESOPHAGEAL-CARCINOMA - A PROSPECTIVE RANDOMIZED TRIAL. *Int. J. Hyperthermia* **10**, 485-493, doi:10.3109/02656739409009352 (1994).
46 Issels, R. D. Hyperthermia adds to chemotherapy. *Eur. J. Cancer* **44**, 2546-2554, doi:10.1016/j.ejca.2008.07.038 (2008).
47 Chicheł, A., Skowronek, J., Kubaszewska, M. & Kanikowski, M. Hyperthermia – description of a method and a review of clinical applications. *Reports of Practical Oncology & Radiotherapy* **12**, 267-275, doi:http://dx.doi.org/10.1016/S1507-1367(10)60065-X (2007).
48 Falk, M. H. & Issels, R. D. Hyperthermia in oncology. *Int. J. Hyperthermia* **17**, 1-18, doi:10.1080/02656730150201552 (2001).
49 Otte, J. HYPERTHERMIA IN CANCER-THERAPY. *Eur. J. Pediatr.* **147**, 560-569, doi:10.1007/bf00442463 (1988).
50 Kurti, N. *Selected Works of Louis Neel*. (CRC Press, 1988).
51 Coey, J. M. *Magnetism and magnetic materials*. (Cambridge University Press, 2010).
52 Hergt, R., Dutz, S., Müller, R. & Zeisberger, M. Magnetic particle hyperthermia: nanoparticle magnetism and materials development for cancer therapy. *Journal of Physics: Condensed Matter* **18**, S2919-S2934, doi:10.1088/0953-8984/18/38/s26 (2006).
53 Cherukuri, P., Glazer, E. S. & Curley, S. A. Targeted hyperthermia using metal nanoparticles. *Adv Drug Deliv Rev* **62**, 339-345, doi:10.1016/j.addr.2009.11.006 (2010).
54 Fortin, J. P., Gazeau, F. & Wilhelm, C. Intracellular heating of living cells through Neel relaxation of magnetic nanoparticles. *European Biophysics Journal with Biophysics Letters* **37**, 223-228, doi:10.1007/s00249-007-0197-4 (2008).
55 Suto, M. *et al.* Heat dissipation mechanism of magnetite nanoparticles in magnetic fluid hyperthermia. *Journal of Magnetism and Magnetic Materials* **321**, 1493-1496, doi:10.1016/j.jmmm.2009.02.070 (2009).
56 Kotitz, R., Weitschies, W., Trahms, L. & Semmler, W. Investigation of Brownian and Neel relaxation in magnetic fluids. *Journal of Magnetism and Magnetic Materials* **201**, 102-104, doi:10.1016/s0304-8853(99)00065-7 (1999).
57 Kotitz, R., Fannin, P. C. & Trahms, L. TIME-DOMAIN STUDY OF BROWNIAN AND NEEL RELAXATION IN FERROFLUIDS. *Journal of Magnetism and Magnetic Materials* **149**, 42-46, doi:10.1016/0304-8853(95)00333-9 (1995).
58 Levy, M. *et al.* Magnetically induced hyperthermia: size-dependent heating power of gamma-Fe(2)O(3) nanoparticles. *Journal of physics. Condensed matter : an Institute of Physics journal* **20**, 204133, doi:10.1088/0953-8984/20/20/204133 (2008).
59 Rosensweig, R. E. Heating magnetic fluid with alternating magnetic field. *Journal of Magnetism and Magnetic Materials* **252**, 370-374, doi:10.1016/s0304-8853(02)00706-0 (2002).
60 Sharifi, I., Shokrollahi, H. & Amiri, S. Ferrite-based magnetic nanofluids used in hyperthermia applications. *Journal of Magnetism and Magnetic Materials* **324**, 903-915, doi:10.1016/j.jmmm.2011.10.017 (2012).
61 Habib, A. H., Ondeck, C. L., Chaudhary, P., Bockstaller, M. R. & McHenry, M. E. Evaluation of iron-cobalt/ferrite core-shell nanoparticles for cancer thermotherapy. *Journal of Applied Physics* **103**, 07A307, doi:10.1063/1.2830975 (2008).
62 Kappiyoor, R., Liangruksa, M., Ganguly, R. & Puri, I. K. The effects of magnetic nanoparticle properties on magnetic fluid hyperthermia. *Journal of Applied Physics* **108**, 094702, doi:10.1063/1.3500337 (2010).
63 Liu, X. L. *et al.* Optimization of surface coating on Fe3O4 nanoparticles for high performance magnetic hyperthermia agents. *J. Mater. Chem.* **22**, 8235, doi:10.1039/c2jm30472d (2012).

64 Hergt, R. *et al.* Enhancement of AC-losses of magnetic nanoparticles for heating applications. *Journal of Magnetism and Magnetic Materials* **280**, 358-368, doi:10.1016/j.jmmm.2004.03.034 (2004).
65 Hergt, R. & Dutz, S. Magnetic particle hyperthermia—biophysical limitations of a visionary tumour therapy. *Journal of Magnetism and Magnetic Materials* **311**, 187-192, doi:10.1016/j.jmmm.2006.10.1156 (2007).
66 Natividad, E., Castro, M. & Mediano, A. Accurate measurement of the specific absorption rate using a suitable adiabatic magnetothermal setup. *Applied Physics Letters* **92**, 093116, doi:10.1063/1.2891084 (2008).
67 Andreu, I. & Natividad, E. Accuracy of available methods for quantifying the heat power generation of nanoparticles for magnetic hyperthermia. *Int. J. Hyperthermia* **29**, 739-751, doi:10.3109/02656736.2013.826825 (2013).
68 Huang, S., Wang, S. Y., Gupta, A., Borca-Tasciuc, D. A. & Salon, S. J. On the measurement technique for specific absorption rate of nanoparticles in an alternating electromagnetic field. *Meas. Sci. Technol.* **23**, 035701, doi:10.1088/0957-0233/23/3/035701 (2012).
69 Zhai, Y., Xie, H. & Gu, H. C. Effects of hyperthermia with dextran magnetic fluid on the growth of grafted H22 tumor in mice. *Int. J. Hyperthermia* **25**, 65-71, doi:10.1080/02656730802363643 (2009).
70 Ito, A. *et al.* Complete regression of mouse mammary carcinoma with a size greater than 15 mm by frequent repeated hyperthermia using magnetite nanoparticles. *J. Biosci. Bioeng.* **96**, 364-369, doi:10.1016/s1389-1723(03)90138-1 (2003).
71 Johannsen, M. *et al.* Clinical hyperthermia of prostate cancer using magnetic nanoparticles: Presentation of a new interstitial technique. *Int. J. Hyperthermia* **21**, 637-647, doi:10.1080/02656730500158360 (2005).
72 Huang, H. S. & Hainfeld, J. F. Intravenous magnetic nanoparticle cancer hyperthermia. *International Journal of Nanomedicine* **8**, 2521-2532, doi:10.2147/ijn.s43770 (2013).
73 Kobayashi, H., Watanabe, R. & Choyke, P. L. Improving Conventional Enhanced Permeability and Retention (EPR) Effects; What Is the Appropriate Target? *Theranostics* **4**, 81-89, doi:10.7150/thno.7193 (2014).
74 Acharya, S. & Sahoo, S. K. PLGA nanoparticles containing various anticancer agents and tumour delivery by EPR effect. *Adv. Drug Del. Rev.* **63**, 170-183, doi:10.1016/j.addr.2010.10.008 (2011).
75 Matsumura, Y. & Maeda, H. A NEW CONCEPT FOR MACROMOLECULAR THERAPEUTICS IN CANCER-CHEMOTHERAPY - MECHANISM OF TUMORITROPIC ACCUMULATION OF PROTEINS AND THE ANTITUMOR AGENT SMANCS. *Cancer Res.* **46**, 6387-6392 (1986).
76 Maeda, H., Wu, J., Sawa, T., Matsumura, Y. & Hori, K. Tumor vascular permeability and the EPR effect in macromolecular therapeutics: a review. *J. Controlled Release* **65**, 271-284, doi:10.1016/s0168-3659(99)00248-5 (2000).
77 Maeda, H. in *Advances in Enzyme Regulation, Vol 41* Vol. 41 *Advances in Enzyme Regulation* (ed G. Weber) 189-207 (2001).
78 Iyer, A. K., Khaled, G., Fang, J. & Maeda, H. Exploiting the enhanced permeability and retention effect for tumor targeting. *Drug Discov. Today* **11**, 812-818, doi:10.1016/j.drudis.2006.07.005 (2006).
79 Fang, J., Nakamura, H. & Maeda, H. The EPR effect: Unique features of tumor blood vessels for drug delivery, factors involved, and limitations and augmentation of the effect. *Adv. Drug Del. Rev.* **63**, 136-151, doi:10.1016/j.addr.2010.04.009 (2011).
80 Maeda, H. Macromolecular therapeutics in cancer treatment: The EPR effect and beyond. *J. Controlled Release* **164**, 138-144, doi:10.1016/j.jconrel.2012.04.038 (2012).
81 Maeda, H., Nakamura, H. & Fang, J. The EPR effect for macromolecular drug delivery to solid tumors: Improvement of tumor uptake, lowering of systemic toxicity, and distinct tumor imaging in vivo. *Adv. Drug Del. Rev.* **65**, 71-79, doi:10.1016/j.addr.2012.10.002 (2013).
82 Jhaveri, A. M. & Torchilin, V. P. Multifunctional polymeric micelles for delivery of drugs and siRNA. *Front. Pharmacol.* **5**, 77 (2014).
83 Choi, H. S. *et al.* Renal clearance of quantum dots. *Nat. Biotechnol.* **25**, 1165-1170 (2007).
84 Longmire, M., Choyke, P. L. & Kobayashi, H. Clearance properties of nano-sized particles and molecules as imaging agents: considerations and caveats. (2008).

85 Saito, S. *et al.* Impact of surface coating and particle size on the uptake of small and ultrasmall superparamagnetic iron oxide nanoparticles by macrophages. *Int J Nanomedicine* **7**, 5415-5421, doi:10.2147/IJN.S33709 (2012).
86 Arruebo, M., Fernández-Pacheco, R., Ibarra, M. R. & Santamaría, J. Magnetic nanoparticles for drug delivery. *Nano Today* **2**, 22-32, doi:10.1016/s1748-0132(07)70084-1 (2007).
87 Saptarshi, S. R., Duschl, A. & Lopata, A. L. Interaction of nanoparticles with proteins: relation to bio-reactivity of the nanoparticle. *Journal of Nanobiotechnology* **11**, 26, doi:10.1186/1477-3155-11-26 (2013).
88 Gruttner, C. *et al.* Synthesis and antibody conjugation of magnetic nanoparticles with improved specific power absorption rates for alternating magnetic field cancer therapy. *Journal of Magnetism and Magnetic Materials* **311**, 181-186, doi:10.1016/j.jmmm.2006.10.1151 (2007).
89 Yang, H. C. *et al.* Enhancing the tumor discrimination using antibody-activated magnetic nanoparticles in ultra-low magnetic fields. *Applied Physics Letters* **102**, doi:10.1063/1.4774291 (2013).
90 Prantner, A. M., Nguyen, C. V. & Scholler, N. Facile Immunotargeting of Nanoparticles Against Tumor Antigens Using Site-Specific Biotinylated Antibody Fragments. *Journal of Biomedical Nanotechnology* **9**, 1686-1697, doi:10.1166/jbn.2013.1670 (2013).
91 Vigor, K. L. *et al.* Nanoparticles functionalised with recombinant single chain Fv antibody fragments (scFv) for the magnetic resonance imaging of cancer cells. *Biomaterials* **31**, 1307-1315, doi:10.1016/j.biomaterials.2009.10.036 (2010).
92 Kumar, M. *et al.* Cellular interaction of folic acid conjugated superparamagnetic iron oxide nanoparticles and its use as contrast agent for targeted magnetic imaging of tumor cells. *International Journal of Nanomedicine* **7**, 3503-3516, doi:10.2147/ijn.s32694 (2012).
93 Karmakar, A. *et al.* Radio-frequency induced in vitro thermal ablation of cancer cells by EGF functionalized carbon-coated magnetic nanoparticles. *J. Mater. Chem.* **21**, 12761-12769, doi:10.1039/c1jm10569h (2011).
94 Jie, L. Y. *et al.* Actively-targeted LTVSPWY peptide-modified magnetic nanoparticles for tumor imaging. *International Journal of Nanomedicine* **7**, 3981-3989, doi:10.2147/ijn.s33593 (2012).
95 Veiseh, O. *et al.* Chlorotoxin bound magnetic nanovector tailored for cancer cell targeting, imaging, and siRNA delivery. *Biomaterials* **31**, 8032-8042, doi:10.1016/j.biomaterials.2010.07.0126 (2010).
96 Lim, E. K. *et al.* Aptamer-conjugated magnetic nanoparticles enable efficient targeted detection of integrin alpha v beta 3 via magnetic resonance imaging. *Journal of Biomedical Materials Research Part A* **102**, 49-59, doi:10.1002/jbm.a.34678 (2014).
97 Yu, M. K. *et al.* Image-Guided Prostate Cancer Therapy Using Aptamer-Functionalized Thermally Cross-Linked Superparamagnetic Iron Oxide Nanoparticles. *Small* **7**, 2241-2249, doi:10.1002/smll.201100472 (2011).
98 Pala, K., Serwotka, A., Jelen, F., Jakimowicz, P. & Otlewski, J. Tumor-specific hyperthermia with aptamer-tagged superparamagnetic nanoparticles. *Int J Nanomedicine* **9**, 67-76, doi:10.2147/IJN.S52539 (2014).
99 Fortin-Ripoche, J. P. *et al.* Magnetic targeting of magnetoliposomes to solid tumors with MR imaging monitoring in mice: Feasibility. *Radiology* **239**, 415-424, doi:10.1148/radiol.2392042110 (2006).
100 Zulauf, G. D. *et al.* Targeting of systemically-delivered magnetic nanoparticle hyperthermia using a noninvasive, static, external magnetic field. *Energy-Based Treatment of Tissue and Assessment Vii* **8584**, doi:10.1117/12.2008816 (2013).
101 Jang, J. T. *et al.* Critical enhancements of MRI contrast and hyperthermic effects by dopant-controlled magnetic nanoparticles. *Angew. Chem. Int. Ed. Engl.* **48**, 1234-1238, doi:10.1002/anie.200805149 (2009).
102 Gruttner, C., Muller, K., Teller, J. & Westphal, F. Synthesis and functionalisation of magnetic nanoparticles for hyperthermia applications. *Int. J. Hyperthermia* **29**, 777-789, doi:10.3109/02656736.2013.835876 (2013).
103 Thanh, N. T. K. & Green, L. A. W. Functionalisation of nanoparticles for biomedical applications. *Nano Today* **5**, 213-230, doi:10.1016/j.nantod.2010.05.003 (2010).
104 Faraji, M., Yamini, Y. & Rezaee, M. Magnetic Nanoparticles: Synthesis, Stabilization, Functionalization, Characterization, and Applications. *Journal of the Iranian Chemical Society* **7**, 1-37 (2010).

105 Hao, R. *et al.* Synthesis, Functionalization, and Biomedical Applications of Multifunctional Magnetic Nanoparticles. *Advanced materials* **22**, 2729-2742, doi:10.1002/adma.201000260 (2010).
106 Kolhatkar, A. G., Jamison, A. C., Litvinov, D., Willson, R. C. & Lee, T. R. Tuning the Magnetic Properties of Nanoparticles. *International Journal of Molecular Sciences* **14**, 15977-16009, doi:10.3390/ijms140815977 (2013).
107 Carrey, J., Mehdaoui, B. & Respaud, M. Simple models for dynamic hysteresis loop calculations of magnetic single-domain nanoparticles: Application to magnetic hyperthermia optimization. *Journal of Applied Physics* **109**, doi:10.1063/1.3551582 (2011).
108 Sedlacik, M. *et al.* Correlation of structural and magnetic properties of Fe3O4 nanoparticles with their calorimetric and magnetorheological performance. *Journal of Magnetism and Magnetic Materials* **326**, 7-13, doi:10.1016/j.jmmm.2012.08.039 (2013).
109 Ma, M. *et al.* Size dependence of specific power absorption of Fe3O4 particles in AC magnetic field. *Journal of Magnetism and Magnetic Materials* **268**, 33-39, doi:10.1016/s0304-8853(03)00426-8 (2004).
110 Barati, M. R., Selomulya, C. & Suzuki, K. Particle size dependence of heating power in MgFe2O4 nanoparticles for hyperthermia therapy application. *Journal of Applied Physics* **115**, 17B522, doi:10.1063/1.4867751 (2014).
111 de la Presa, P. *et al.* Study of Heating Efficiency as a Function of Concentration, Size, and Applied Field in γ-Fe2O3Nanoparticles. *The Journal of Physical Chemistry C* **116**, 25602-25610, doi:10.1021/jp310771p (2012).
112 Song, M. *et al.* Influence of morphology and surface exchange reaction on magnetic properties of monodisperse magnetite nanoparticles. *Colloids and Surfaces a-Physicochemical and Engineering Aspects* **408**, 114-121, doi:10.1016/j.colsurfa.2012.05.039 (2012).
113 Hugounenq, P. *et al.* Iron Oxide Monocrystalline Nanoflowers for Highly Efficient Magnetic Hyperthermia. *The Journal of Physical Chemistry C* **116**, 15702-15712, doi:10.1021/jp3025478 (2012).
114 Larumbe, S., Gomez-Polo, C., Perez-Landazabal, J. I. & Pastor, J. M. Effect of a SiO2 coating on the magnetic properties of Fe3O4 nanoparticles. *Journal of physics. Condensed matter : an Institute of Physics journal* **24**, 266007, doi:10.1088/0953-8984/24/26/266007 (2012).
115 Shete, P. B. *et al.* Magnetic chitosan nanocomposite for hyperthermia therapy application: Preparation, characterization and in vitro experiments. *Applied Surface Science* **288**, 149-157, doi:10.1016/j.apsusc.2013.09.169 (2014).
116 Thorat, N. D. *et al.* Surface functionalized LSMO nanoparticles with improved colloidal stability for hyperthermia applications. *Journal of Physics D: Applied Physics* **46**, 105003, doi:10.1088/0022-3727/46/10/105003 (2013).
117 Barati, M. R., Suzuki, K., Selomulya, C. & Garitaonandia, J. S. New T-c-Tuned Manganese Ferrite-Based Magnetic Implant for Hyperthermia Therapy Application. *Ieee Transactions on Magnetics* **49**, 3460-3463, doi:10.1109/tmag.2013.2246860 (2013).
118 Natividad, E. *et al.* New insights into the heating mechanisms and self-regulating abilities of manganite perovskite nanoparticles suitable for magnetic fluid hyperthermia. *Nanoscale* **4**, 3954-3962, doi:10.1039/c2nr30667k (2012).
119 Yao, A. H., Ai, F. R., Wang, D. P., Huang, W. H. & Zhang, X. C. Synthesis, characterization and in vitro cytotoxicity of self-regulating magnetic implant material for hyperthermia application. *Materials Science & Engineering C-Materials for Biological Applications* **29**, 2525-2529, doi:10.1016/j.msec.2009.07.021 (2009).
120 Akin, Y., Obaidat, I. M., Issa, B. & Haik, Y. Ni1-xCrx alloy for self controlled magnetic hyperthermia. *Crystal Research and Technology* **44**, 386-390, doi:10.1002/crat.200800502 (2009).
121 Ferk, G. *et al.* Synthesis and characterization of Mg1+xFe2-2xTixO4 nanoparticles with an adjustable Curie point. *Journal of Magnetism and Magnetic Materials* **350**, 124-128, doi:10.1016/j.jmmm.2013.09.037 (2014).
122 Basel, M. T. *et al.* Cell-delivered magnetic nanoparticles caused hyperthermia-mediated increased survival in a murine pancreatic cancer model. *International Journal of Nanomedicine* **7**, 297-306, doi:10.2147/ijn.s28344 (2012).

123 Lin, M. *et al.* The anti-hepatoma effect of nanosized Mn-Zn ferrite magnetic fluid hyperthermia associated with radiation in vitro and in vivo. *Nanotechnology* **24**, 255101, doi:10.1088/0957-4484/24/25/255101 (2013).
124 Araya, T. *et al.* Antitumor effects of inductive hyperthermia using magnetic ferucarbotran nanoparticles on human lung cancer xenografts in nude mice. *Onco Targets Ther.* **6**, 237-242, doi:10.2147/OTT.S42815 (2013).
125 Shetake, N. G. *et al.* Magnetic nanoparticle-mediated hyperthermia therapy induces tumour growth inhibition by apoptosis and Hsp90/AKT modulation. *Int. J. Hyperthermia* **31**, 909-919, doi:10.3109/02656736.2015.1075072 (2015).
126 Kossatz, S. *et al.* High Therapeutic Efficiency of Magnetic Hyperthermia in Xenograft Models Achieved with Moderate Temperature Dosages in the Tumor Area. *Pharm. Res.* **31**, 3274-3288, doi:10.1007/s11095-014-1417-0 (2014).
127 Thiesen, B. & Jordan, A. Clinical applications of magnetic nanoparticles for hyperthermia. *Int. J. Hyperthermia* **24**, 467-474, doi:10.1080/02656730802104757 (2008).
128 Zhao, L.-Y. *et al.* Magnetic-mediated hyperthermia for cancer treatment: Research progress and clinical trials. *Chinese Physics B* **22**, 108104, doi:10.1088/1674-1056/22/10/108104 (2013).
129 May, J. P. & Li, S.-D. Hyperthermia-induced drug targeting. *Expert Opinion on Drug Delivery* **10**, 511-527, doi:10.1517/17425247.2013.758631 (2013).
130 Rao, W., Deng, Z.-S. & Liu, J. A Review of Hyperthermia Combined With Radiotherapy/Chemotherapy on Malignant Tumors. *Crit. Rev. Biomed. Eng.* **38**, 101-116 (2010).
131 Urano, M., Kuroda, M. & Nishimura, Y. For the clinical application of thermochemotherapy given at mild temperatures. *Int. J. Hyperthermia* **15**, 79-107, doi:10.1080/026567399285765 (1999).
132 Bull, J. M. C. AN UPDATE ON THE ANTICANCER EFFECTS OF A COMBINATION OF CHEMOTHERAPY AND HYPERTHERMIA. *Cancer Res.* **44**, 4853-4856 (1984).
133 Itoh, Y., Yamada, Y., Kazaoka, Y., Ishiguchi, T. & Honda, N. Combination of chemotherapy and mild hyperthermia enhances the anti-tumor effects of cisplatin and adriamycin in human bladder cancer T24 cells in vitro. *Exp. Ther. Med.* **1**, 319-323, doi:10.3892/etm_00000049 (2010).
134 Siddik, Z. H. Cisplatin: mode of cytotoxic action and molecular basis of resistance. *Oncogene* **22**, 7265-7279, doi:10.1038/sj.onc.1206933 (2003).
135 Thorn, C. F. *et al.* Doxorubicin pathways: pharmacodynamics and adverse effects. *Pharmacogenet. Genomics* **21**, 440-446, doi:10.1097/FPC.0b013e32833ffb56 (2011).
136 Wu, Y. N., Mikulski, S. M., Ardelt, W., Rybak, S. M. & Youle, R. J. A CYTOTOXIC RIBONUCLEASE - STUDY OF THE MECHANISM OF ONCONASE CYTOTOXICITY. *J. Biol. Chem.* **268**, 10686-10693 (1993).
137 Saxena, A., Saxena, S. K. & Shogen, K. Effect of Onconase on Double-stranded RNA In Vitro. *Anticancer Res.* **29**, 1067-1071 (2009).
138 Halicka, H. D., Ardelt, B., Shogen, K. & Darzynkiewicz, Z. Mild hyperthermia predisposes tumor cells to undergo apoptosis upon treatment with onconase. *Int. J. Oncol.* **30**, 841-847 (2007).
139 Urano, M. & Ling, C. C. Thermal enhancement of melphalan and oxaliplatin cytotoxicity in vitro. *Int. J. Hyperthermia* **18**, 307-315, doi:10.1080/02656730210123534 (2002).
140 Nakao, K. *et al.* The synergistic effects of hyperthermia and anticancer drugs on induction of apoptosis. *Med. Electron Microsc.* **33**, 44-50, doi:10.1007/s007950000007 (2000).
141 Petryk, A. A., Giustini, A. J., Gottesman, R. E., Kaufman, P. A. & Hoopes, P. J. Magnetic nanoparticle hyperthermia enhancement of cisplatin chemotherapy cancer treatment. *Int. J. Hyperthermia* **29**, 845-851, doi:10.3109/02656736.2013.825014 (2013).
142 Tofilon, P. J., Dasilva, V., Gutin, P. H. & Deen, D. F. EFFECTS OF HYPERTHERMIA ON DNA INTERSTRAND CROSSLINKING AFTER TREATMENT WITH BCNU IN 9L RAT-BRAIN TUMOR-CELLS. *Radiat. Res.* **103**, 373-382, doi:10.2307/3576759 (1985).
143 Gabano, E., Colangelo, D., Ghezzi, A. R. & Osella, D. The influence of temperature on antiproliferative effects, cellular uptake and DNA platination of the clinically employed Pt(II)-drugs. *J. Inorg. Biochem.* **102**, 629-635, doi:10.1016/j.jinorgbio.2007.10.006 (2008).
144 Komatsu, K., Miller, R. C. & Hall, E. J. THE ONCOGENIC POTENTIAL OF A COMBINATION OF HYPERTHERMIA AND CHEMOTHERAPY AGENTS. *Br. J. Cancer* **57**, 59-63, doi:10.1038/bjc.1988.9 (1988).

145 Miller, R. C., Richards, M., Baird, C., Martin, S. & Hall, E. J. INTERACTION OF HYPERTHERMIA AND CHEMOTHERAPY AGENTS - CELL LETHALITY AND ONCOGENIC POTENTIAL. *Int. J. Hyperthermia* **10**, 89-99, doi:10.3109/02656739409009335 (1994).
146 Tang, R. *et al.* The impact of hyperthermic chemotherapy on human gastric cancer cell lines: Preliminary results. *Oncol. Rep.* **16**, 631-641 (2006).
147 Timko, B. P., Dvir, T. & Kohane, D. S. Remotely Triggerable Drug Delivery Systems. *Advanced materials* **22**, 4925-4943, doi:10.1002/adma.201002072 (2010).
148 Mahmoudi, M., Sant, S., Wang, B., Laurent, S. & Sen, T. Superparamagnetic iron oxide nanoparticles (SPIONs): Development, surface modification and applications in chemotherapy. *Adv. Drug Del. Rev.* **63**, 24-46, doi:10.1016/j.addr.2010.05.006 (2011).
149 Bawa, P., Pillay, V., Choonara, Y. E. & du Toit, L. C. Stimuli-responsive polymers and their applications in drug delivery. *Biomedical Materials* **4**, 022001, doi:10.1088/1748-6041/4/2/022001 (2009).
150 Cho, K., Wang, X., Nie, S., Chen, Z. G. & Shin, D. M. Therapeutic nanoparticles for drug delivery in cancer. *Clin. Cancer. Res.* **14**, 1310-1316, doi:10.1158/1078-0432.CCR-07-1441 (2008).
151 Bibi, S., Lattmann, E., Mohammed, A. R. & Perrie, Y. Trigger release liposome systems: local and remote controlled delivery? *J. Microencaps.* **29**, 262-276, doi:10.3109/02652048.2011.646330 (2012).
152 Ward, M. A. & Georgiou, T. K. Thermoresponsive Polymers for Biomedical Applications. *Polymers* **3**, 1215-1242, doi:10.3390/polym3031215 (2011).
153 Theato, P., Sumerlin, B. S., O'Reilly, R. K. & Epps, T. H. Stimuli responsive materials. *Chem. Soc. Rev.* **42**, 7055-7056, doi:10.1039/c3cs90057f (2013).
154 Alarcon, C. D. H., Pennadam, S. & Alexander, C. Stimuli responsive polymers for biomedical applications. *Chem. Soc. Rev.* **34**, 276-285, doi:10.1039/b406727d (2005).
155 Kumar, C. S. & Mohammad, F. Magnetic nanomaterials for hyperthermia-based therapy and controlled drug delivery. *Adv Drug Deliv Rev* **63**, 789-808, doi:10.1016/j.addr.2011.03.008 (2011).
156 Klibanov, A. L., Maruyama, K., Torchilin, V. P. & Huang, L. AMPHIPATHIC POLYETHYLENEGLYCOLS EFFECTIVELY PROLONG THE CIRCULATION TIME OF LIPOSOMES. *FEBS Lett.* **268**, 235-237, doi:10.1016/0014-5793(90)81016-h (1990).
157 Faria, M. R. *et al.* Synthesis and characterization of magnetoliposomes for MRI contrast enhancement. *Int. J. Pharm.* **446**, 183-190, doi:10.1016/j.ijpharm.2013.02.025 (2013).
158 Qiu, D., An, X. Q., Chen, Z. Y. & Ma, X. Y. Microstructure study of liposomes decorated by hydrophobic magnetic nanoparticles. *Chem. Phys. Lipids* **165**, 563-570, doi:10.1016/j.chemphyslip.2012.06.004 (2012).
159 Ponce, A. M., Vujaskovic, Z., Yuan, F., Needham, D. & Dewhirst, M. W. Hyperthermia mediated liposomal drug delivery. *Int. J. Hyperthermia* **22**, 205-213, doi:10.1080/02656730600582956 (2006).
160 Landon, C. D., Park, J. Y., Needham, D. & Dewhirst, M. W. Nanoscale drug delivery and hyperthermia: The materials design and preclinical and clinical testing of low temperature-sensitive liposomes used in combination with mild hyperthermia in the treatment of local cancer. *Open Nanomedicine Journal* **3**, 38-64 (2011).
161 Ta, T. & Porter, T. M. Thermosensitive liposomes for localized delivery and triggered release of chemotherapy. *J. Control. Release* **169**, 112-125, doi:10.1016/j.jconrel.2013.03.036 (2013).
162 Qiu, D. & An, X. Controllable release from magnetoliposomes by magnetic stimulation and thermal stimulation. *Colloids and Surfaces B-Biointerfaces* **104**, 326-329, doi:10.1016/j.colsurfb.2012.11.033 (2013).
163 Kulshrestha, P., Gogoi, M., Bahadur, D. & Banerjee, R. In vitro application of paclitaxel loaded magnetoliposomes for combined chemotherapy and hyperthermia. *Colloids and Surfaces B-Biointerfaces* **96**, 1-7, doi:10.1016/j.colsurfb.2012.02.029 (2012).
164 Wei, H., Zhuo, R. X. & Zhang, X. Z. Design and development of polymeric micelles with cleavable links for intracellular drug delivery. *Progress in Polymer Science* **38**, 503-535, doi:10.1016/j.progpolymsci.2012.07.002 (2013).
165 Gong, J., Chen, M. W., Zheng, Y., Wang, S. P. & Wang, Y. T. Polymeric micelles drug delivery system in oncology. *J. Controlled Release* **159**, 312-323, doi:10.1016/j.jconrel.2011.12.012 (2012).

166 Talelli, M. & Hennink, W. E. Thermosensitive polymeric micelles for targeted drug delivery. *Nanomedicine* **6**, 1245-1255, doi:10.2217/nnm.11.91 (2011).
167 McDaniel, J. R., Dewhirst, M. W. & Chilkoti, A. Actively targeting solid tumours with thermoresponsive drug delivery systems that respond to mild hyperthermia. *Int. J. Hyperthermia* **29**, 501-510, doi:10.3109/02656736.2013.819999 (2013).
168 Kim, H. C. *et al.* Magnetic nanoparticle-conjugated polymeric micelles for combined hyperthermia and chemotherapy. *Nanoscale* **7**, 16470-16480, doi:10.1039/c5nr04130a (2015).
169 Deng, L. *et al.* Magnetothermally responsive star-block copolymeric micelles for controlled drug delivery and enhanced thermo-chemotherapy. *Nanoscale* **7**, 9655-9663, doi:10.1039/c5nr00642b (2015).
170 Elsabahy, M. & Wooley, K. L. Design of polymeric nanoparticles for biomedical delivery applications. *Chem. Soc. Rev.* **41**, 2545-2561, doi:10.1039/c2cs15327k (2012).
171 Balasubramanian, S. *et al.* Curcumin and 5-Fluorouracil-loaded, folate- and transferrin-decorated polymeric magnetic nanoformulation: a synergistic cancer therapeutic approach, accelerated by magnetic hyperthermia. *Int J Nanomedicine* **9**, 437-459, doi:10.2147/IJN.S49882 (2014).
172 Wang, Y. *et al.* A facile concentric-layered magnetic chitosan hydrogel with magnetic field remote stimulated drug release. *Journal of controlled release : official journal of the Controlled Release Society* **172**, e90, doi:10.1016/j.jconrel.2013.08.182 (2013).
173 Jaiswal, M. K., Pradhan, A., Banerjee, R. & Bahadur, D. Dual pH and Temperature Stimuli-Responsive Magnetic Nanohydrogels for Thermo-Chemotherapy. *Journal of Nanoscience and Nanotechnology* **14**, 4082-4089, doi:10.1166/jnn.2014.8662 (2014).
174 Jaiswal, M. K. *et al.* Magneto-thermally responsive hydrogels for bladder cancer treatment: Therapeutic efficacy and in vivo biodistribution. *Colloids and Surfaces B-Biointerfaces* **136**, 625-633, doi:10.1016/j.colsurfb.2015.09.058 (2015).
175 Kumar, S. K., Jouault, N., Benicewicz, B. & Neely, T. Nanocomposites with Polymer Grafted Nanoparticles. *Macromolecules* **46**, 3199-3214, doi:10.1021/ma4001385 (2013).
176 Majeed, M. I. *et al.* Highly water-soluble magnetic iron oxide (Fe3O4) nanoparticles for drug delivery: enhanced in vitro therapeutic efficacy of doxorubicin and MION conjugates. *Journal of Materials Chemistry B* **1**, 2874-2884, doi:10.1039/c3tb20322k (2013).
177 Taratula, O. *et al.* Multifunctional nanomedicine platform for concurrent delivery of chemotherapeutic drugs and mild hyperthermia to ovarian cancer cells. *Int. J. Pharm.* **458**, 169-180, doi:10.1016/j.ijpharm.2013.09.032 (2013).
178 Kumar, S., Daverey, A., Sahu, N. K. & Bahadur, D. In vitro evaluation of PEGylated mesoporous MgFe2O4 magnetic nanoassemblies (MMNs) for chemo-thermal therapy. *Journal of Materials Chemistry B* **1**, 3652-3660, doi:10.1039/c3tb20429d (2013).
179 Barick, K. C. *et al.* pH-Responsive Peptide Mimic Shell Cross-Linked Magnetic Nanocarriers for Combination Therapy. *Advanced Functional Materials* **22**, 4975-4984, doi:10.1002/adfm.201201140 (2012).
180 Yao, A. H., Chen, Q., Ai, F. R., Wang, D. P. & Huang, W. H. Preparation and characterization of temperature-responsive magnetic composite particles for multi-modal cancer therapy. *Journal of Materials Science-Materials in Medicine* **22**, 2239-2247, doi:10.1007/s10856-011-4413-5 (2011).
181 N'Guyen, T. T. T. *et al.* Functional Iron Oxide Magnetic Nanoparticles with Hyperthermia-Induced Drug Release Ability by Using a Combination of Orthogonal Click Reactions. *Angew. Chem.-Int. Edit.* **52**, 14152-14156, doi:10.1002/anie.201306724 (2013).
182 Creixell, M., Bohorquez, A. C., Torres-Lugo, M. & Rinaldi, C. EGFR-Targeted Magnetic Nanoparticle Heaters Kill Cancer Cells without a Perceptible Temperature Rise. *Acs Nano* **5**, 7124-7129, doi:10.1021/nn201822b (2011).
183 Kozissnik, B., Bohorquez, A. C., Dobson, J. & Rinaldi, C. Magnetic fluid hyperthermia: advances, challenges, and opportunity. *Int. J. Hyperthermia* **29**, 706-714, doi:10.3109/02656736.2013.837200 (2013).
184 Kabb, C. P., Carmean, R. N. & Sumerlin, B. S. Probing the surface-localized hyperthermia of gold nanoparticles in a microwave field using polymeric thermometers. *Chemical Science* **6**, 5662-5669, doi:10.1039/c5sc01535a (2015).
185 Dai, Y. *et al.* Near-IR-induced dissociation of thermally-sensitive star polymers. *Chemical Science* (2017).

186 Saint-Cricq, P., Deshayes, S., Zink, J. I. & Kasko, A. M. Magnetic field activated drug delivery using thermodegradable azo-functionalised PEG-coated core-shell mesoporous silica nanoparticles. *Nanoscale* **7**, 13168-13172, doi:10.1039/c5nr03777h (2015).
187 Riedinger, A. *et al.* Subnanometer Local Temperature Probing and Remotely Controlled Drug Release Based on Azo-Functionalized Iron Oxide Nanoparticles. *Nano Lett.* **13**, 2399-2406, doi:10.1021/nl400188q (2013).
188 Ruiz-Hernandez, E., Baeza, A. & Vallet-Regi, M. Smart Drug Delivery through DNA/Magnetic Nanoparticle Gates. *Acs Nano* **5**, 1259-1266, doi:10.1021/nn1029229 (2011).
189 Derfus, A. M. *et al.* Remotely triggered release from magnetic nanoparticles. *Advanced materials* **19**, 3932-+, doi:10.1002/adma.200700091 (2007).
190 Zhao, Z. *et al.* Magnetite nanoparticles as smart carriers to manipulate the cytotoxicity of anticancer drugs: magnetic control and pH-responsive release. *J. Mater. Chem.* **22**, 15717-15725, doi:10.1039/c2jm31692g (2012).
191 Chang, Y. L. *et al.* Novel water-soluble and pH-responsive anticancer drug nanocarriers: Doxorubicin-PAMAM dendrimer conjugates attached to superparamagnetic iron oxide nanoparticles (IONPs). *J. Colloid Interface Sci.* **363**, 403-409, doi:10.1016/j.jcis.2011.06.086 (2011).
192 Chang, Y. L. *et al.* Synthesis and characterization of DOX-conjugated dendrimer-modified magnetic iron oxide conjugates for magnetic resonance imaging, targeting, and drug delivery. *J. Mater. Chem.* **22**, 9594-9601, doi:10.1039/c2jm16792a (2012).
193 Li, D. *et al.* Doxorubicin-Conjugated Mesoporous Magnetic Colloidal Nanocrystal Clusters Stabilized by Polysaccharide as a Smart Anticancer Drug Vehicle. *Small* **8**, 2690-2697, doi:10.1002/smll.201200272 (2012).
194 Chang, Y. L. *et al.* Dendrimer functionalized water soluble magnetic iron oxide conjugates as dual imaging probe for tumor targeting and drug delivery. *Polymer Chemistry* **4**, 789-794, doi:10.1039/c2py20740k (2013).
195 Luo, Z. *et al.* Redox-Responsive Molecular Nanoreservoirs for Controlled Intracellular Anticancer Drug Delivery Based on Magnetic Nanoparticles. *Advanced materials* **24**, 431-435, doi:10.1002/adma.201103458 (2012).
196 Balendiran, G. K., Dabur, R. & Fraser, D. The role of glutathione in cancer. *Cell Biochem. Funct.* **22**, 343-352, doi:10.1002/cbf.1149 (2004).
197 Wang, Y. C., Wang, F., Sun, T. M. & Wang, J. Redox-Responsive Nanoparticles from the Single Disulfide Bond-Bridged Block Copolymer as Drug Carriers for Overcoming Multidrug Resistance in Cancer Cells. *Bioconj. Chem.* **22**, 1939-1945, doi:10.1021/bc200139n (2011).
198 Gao, F. P., Yan, Z. X., Zhou, J., Cai, Y. Y. & Tang, J. T. Methotrexate-conjugated magnetic nanoparticles for thermochemotherapy and magnetic resonance imaging of tumor. *Journal of Nanoparticle Research* **14**, 1160, doi:10.1007/s11051-012-1160-6 (2012).
199 Yoo, D., Jeong, H., Noh, S. H., Lee, J. H. & Cheon, J. Magnetically Triggered Dual Functional Nanoparticles for Resistance-Free Apoptotic Hyperthermia. *Angew. Chem.-Int. Edit.* **52**, 13047-13051, doi:10.1002/anie.201306557 (2013).
200 Carper, S. W., Duffy, J. J. & Gerner, E. W. HEAT-SHOCK PROTEINS IN THERMOTOLERANCE AND OTHER CELLULAR PROCESSES. *Cancer Res.* **47**, 5249-5255 (1987).
201 Li, T. J. *et al.* In vivo anti-cancer efficacy of magnetite nanocrystal-based system using locoregional hyperthermia combined with 5-fluorouracil chemotherapy. *Biomaterials* **34**, 7873-7883, doi:10.1016/j.biomaterials.2013.07.012 (2013).
202 Wang, L. *et al.* A study on the thermochemotherapy effect of nanosized As2O3/MZF thermosensitive magnetoliposomes on experimental hepatoma in vitro and in vivo. *Nanotechnology* **22**, doi:10.1088/0957-4484/22/31/315102 (2011).
203 Lin, W. *et al.* Thermosensitive magnetic liposomes with doxorubicin cell-penetrating peptides conjugate for enhanced and targeted cancer therapy. *Drug Deliv.* **23**, 3436-3443, doi:10.1080/10717544.2016.1189983 (2016).
204 Lu, T., Lokerse, W. J. M., Seynhaeve, A. L. B., Koning, G. A. & ten Hagen, T. L. M. Formulation and optimization of idarubicin thermosensitive liposomes provides ultrafast triggered release at mild hyperthermia and improves tumor response. *J. Controlled Release* **220**, 425-437, doi:10.1016/j.jconrel.2015.10.056 (2015).

205 Dou, Y. N. *et al.* Thermosensitive liposomal cisplatin in combination with local hyperthermia results in tumor growth delay and changes in tumor microenvironment in xenograft models of lung carcinoma. *J. Drug Targeting* **24**, 865-877, doi:10.1080/1061186x.2016.1191079 (2016).
206 Jenkins, A. D., Kratochvil, P., Stepto, R. F. T. & Suter, U. W. Glossary of basic terms in polymer science. *Pure Appl. Chem.* **68**, 2287-2311, doi:10.1351/pac199668122287 (1996).
207 Penczek, S. & Moad, G. GLOSSARY OF TERMS RELATED TO KINETICS, THERMODYNAMICS, AND MECHANISMS OF POLYMERIZATION (IUPAC Recommendations 2008). *Pure Appl. Chem.* **80**, 2163-2193, doi:10.1351/pac200880102163 (2008).
208 Jenkins, A. D., Jones, R. G. & Moad, G. Terminology for reversible-deactivation radical polymerization previously called "controlled" radical or "living" radical polymerization (IUPAC Recommendations 2010). *Pure Appl. Chem.* **82**, 483-491, doi:10.1351/pac-rep-08-04-03 (2010).
209 Keddie, D. J. A guide to the synthesis of block copolymers using reversible-addition fragmentation chain transfer (RAFT) polymerization. *Chem. Soc. Rev.* **43**, 496-505, doi:10.1039/c3cs60290g (2014).
210 Ozturk, T., Goktas, M. & Hazer, B. Synthesis and Characterization of Poly(methyl methacrylate-block-ethylene glycol-block-methyl methacrylate) Block Copolymers by Reversible Addition-Fragmentation Chain Transfer Polymerization. *Journal of Macromolecular Science Part a-Pure and Applied Chemistry* **48**, 65-72, doi:10.1080/10601325.2011.528310 (2011).
211 Hong, C. Y., You, Y. Z., Liu, J. & Pan, C. Y. Dendrimer-star polymer and block copolymer prepared by reversible addition-fragmentation chain transfer (RAFT) polymerization with dendritic chain transfer agent. *Journal of Polymer Science Part a-Polymer Chemistry* **43**, 6379-6393, doi:10.1002/pola.21098 (2005).
212 Mayadunne, R. T. A., Jeffery, J., Moad, G. & Rizzardo, E. Living free radical polymerization with reversible addition-fragmentation chain transfer (RAFT polymerization): Approaches to star polymers. *Macromolecules* **36**, 1505-1513, doi:10.1021/ma021219w (2003).
213 Zheng, G. H. & Pan, C. Y. Preparation of star polymers based on polystyrene or polystyrene-b-N-isopropyl acrylamide) and divinylbenzene via reversible addition-fragmentation chain transfer polymerization. *Polymer* **46**, 2802-2810, doi:10.1016/j.polymer.2005.01.071 (2005).
214 Li, C. Z. & Benicewicz, B. C. Synthesis of well-defined polymer brushes grafted onto silica nanoparticles via surface reversible addition-fragmentation chain transfer polymerization. *Macromolecules* **38**, 5929-5936, doi:10.1021/ma050216r (2005).
215 Xu, G. Y. *et al.* Constructing polymer brushes on multiwalled carbon nanotubes by in situ reversible addition fragmentation chain transfer polymerization. *Polymer* **47**, 5909-5918, doi:10.1016/j.polymer.2006.06.027 (2006).
216 Matyjaszewski, K. & Spanswick, J. Controlled/living radical polymerization. *Materials Today* **8**, 26-33, doi:10.1016/s1369-7021(05)00745-5 (2005).
217 Grubbs, R. B. Nitroxide-Mediated Radical Polymerization: Limitations and Versatility. *Polymer Reviews* **51**, 104-137, doi:10.1080/15583724.2011.566405 (2011).
218 Le Droumaguet, B. & Nicolas, J. Recent advances in the design of bioconjugates from controlled/living radical polymerization. *Polymer Chemistry* **1**, 563-598, doi:10.1039/b9py00363k (2010).
219 Matyjaszewski, K. & Xia, J. H. Atom transfer radical polymerization. *Chem. Rev.* **101**, 2921-2990, doi:10.1021/cr940534g (2001).
220 Matyjaszewski, K. Atom Transfer Radical Polymerization (ATRP): Current Status and Future Perspectives. *Macromolecules* **45**, 4015-4039, doi:10.1021/ma3001719 (2012).
221 di Lena, F. & Matyjaszewski, K. Transition metal catalysts for controlled radical polymerization. *Progress in Polymer Science* **35**, 959-1021, doi:10.1016/j.progpolymsci.2010.05.001 (2010).
222 Semsarilar, M. & Perrier, S. 'Green' reversible addition-fragmentation chain-transfer (RAFT) polymerization. *Nat. Chem.* **2**, 811-820, doi:10.1038/nchem.853 (2010).
223 Le, T. P. T., Moad, G., Rizzardo, E. & Thang, S. H. Polymerization with living characteristics. . WO 98/01478 (1998).

224 Chiefari, J. *et al.* Living free-radical polymerization by reversible addition-fragmentation chain transfer: The RAFT process. *Macromolecules* **31**, 5559-5562, doi:10.1021/ma9804951 (1998).
225 Mayadunne, R. T. A. *et al.* Living radical polymerization with reversible addition-fragmentation chain transfer (RAFT polymerization) using dithiocarbamates as chain transfer agents. *Macromolecules* **32**, 6977-6980, doi:10.1021/ma9906837 (1999).
226 Hawthorne, D. G., Moad, G., Rizzardo, E. & Thang, S. H. Living radical polymerization with reversible addition-fragmentation chain transfer (RAFT): Direct ESR observation of intermediate radicals. *Macromolecules* **32**, 5457-5459, doi:10.1021/ma990316v (1999).
227 Chong, Y. K., Le, T. P. T., Moad, G., Rizzardo, E. & Thang, S. H. A more versatile route to block copolymers and other polymers of complex architecture by living radical polymerization: The RAFT process. *Macromolecules* **32**, 2071-2074 (1999).
228 Moad, G. *et al.* Living free radical polymerization with reversible addition-fragmentation chain transfer (the life of RAFT). *Polym. Int.* **49**, 993-1001, doi:10.1002/1097-0126(200009)49:9<993::aid-pi506>3.0.co;2-6 (2000).
229 Corpart, P., Charmot, D., Zard, S., Franck, X. & Bouhadir, G. Method for block polymer synthesis by controlled radical polymerisation from dithiocarbamate compounds. . WO 99/35177 (1999).
230 Charmot, D. *et al.* Controlled radical polymerization in dispersed media. *Macromolecular Symposia* **150**, 23-32, doi:10.1002/1521-3900(200002)150:1<23::aid-masy23>3.0.co;2-e (2000).
231 Moad, G., Chong, Y. K., Postma, A., Rizzardo, E. & Thang, S. H. Advances in RAFT polymerization: the synthesis of polymers with defined end-groups. *Polymer* **46**, 8458-8468, doi:10.1016/j.polymer.2004.12.061 (2005).
232 Hill, M. R., Carmean, R. N. & Sumerlin, B. S. Expanding the Scope of RAFT Polymerization: Recent Advances and New Horizons. *Macromolecules* **48**, 5459-5469, doi:10.1021/acs.macromol.5b00342 (2015).
233 Moad, G., Rizzardo, E. & Thang, S. H. in *Fundamentals of Controlled/Living Radical Polymerization RSC Polymer Chemistry Series* (eds B. Z. Tang, N. V. Tsarevsky, & B. S. Sumerlin) Ch. 6, 226 (2013).
234 Boyer, C., Stenzel, M. H. & Davis, T. P. Building Nanostructures Using RAFT Polymerization. *Journal of Polymer Science Part a-Polymer Chemistry* **49**, 551-595, doi:10.1002/pola.24482 (2011).
235 Moad, G., Rizzardo, E. & Thang, S. H. Living radical polymerization by the RAFT process - A first update. *Aust. J. Chem.* **59**, 669-692, doi:10.1071/ch06250 (2006).
236 Smith, A. E., Xu, X. & McCormick, C. L. Stimuli-responsive amphiphilic (co)polymers via RAFT polymerization. *Progress in Polymer Science* **35**, 45-93, doi:10.1016/j.progpolymsci.2009.11.005 (2010).
237 Paulus, R. M., Becer, C. R., Hoogenboom, R. & Schubert, U. S. High Temperature Initiator-Free RAFT Polymerization of Methyl Methacrylate in a Microwave Reactor. *Aust. J. Chem.* **62**, 254-259, doi:10.1071/ch09064 (2009).
238 Li, M., Li, H., De, P. & Sumerlin, B. S. Thermoresponsive Block Copolymer-Protein Conjugates Prepared by Grafting-from via RAFT Polymerization. *Macromolecular Rapid Communications* **32**, 354-359, doi:10.1002/marc.201000619 (2011).
239 Li, H., Li, M., Yu, X., Bapat, A. P. & Sumerlin, B. S. Block copolymer conjugates prepared by sequentially grafting from proteins via RAFT. *Polymer Chemistry* **2**, 1531-1535, doi:10.1039/c1py00031d (2011).
240 Lowe, A. B. & McCormick, C. L. Reversible addition-fragmentation chain transfer (RAFT) radical polymerization and the synthesis of water-soluble (co)polymers under homogeneous conditions in organic and aqueous media. *Progress in Polymer Science* **32**, 283-351, doi:10.1016/j.progpolymsci.2006.11.003 (2007).
241 Boyer, C. *et al.* Bioapplications of RAFT Polymerization. *Chem. Rev.* **109**, 5402-5436, doi:10.1021/cr9001403 (2009).
242 Wang, A. R. & Zhu, S. P. Modeling the reversible addition-fragmentation transfer polymerization process. *Journal of Polymer Science Part a-Polymer Chemistry* **41**, 1553-1566, doi:10.1002/pola.10701 (2003).
243 Chong, Y. K. *et al.* Thiocarbonylthio compounds S=C(Ph)S-R in free radical polymerization with reversible addition-fragmentation chain transfer (RAFT polymerization). Role of the free-radical leaving group (R). *Macromolecules* **36**, 2256-2272, doi:10.1021/ma020882h (2003).

244 Chiefari, J. *et al.* Thiocarbonylthio compounds (S=C(Z)S-R) in free radical polymerization with reversible addition-fragmentation chain transfer (RAFT polymerization). Effect of the activating group Z. *Macromolecules* **36**, 2273-2283, doi:10.1021/ma020883+ (2003).
245 Keddie, D. J., Moad, G., Rizzardo, E. & Thang, S. H. RAFT Agent Design and Synthesis. *Macromolecules* **45**, 5321-5342, doi:10.1021/ma300410v (2012).
246 Moad, G., Rizzardo, E. & Thang, S. H. Living Radical Polymerization by the RAFT Process - A Second Update. *Aust. J. Chem.* **62**, 1402-1472, doi:10.1071/ch09311 (2009).
247 Moad, G., Rizzardo, E. & Thang, S. H. Living Radical Polymerization by the RAFT Process - A Third Update. *Aust. J. Chem.* **65**, 985-1076, doi:10.1071/ch12295 (2012).
248 Moad, G., Rizzardo, E. & Thang, S. H. Living radical polymerization by the RAFT process. *Aust. J. Chem.* **58**, 379-410, doi:10.1071/ch05072 (2005).
249 Moseley, H. G. XCIII. The high-frequency spectra of the elements. *The London, Edinburgh, and Dublin Philosophical Magazine and Journal of Science* **26**, 1024-1034 (1913).
250 Bunaciu, A. A., Udriştioiu, E. g. & Aboul-Enein, H. Y. X-ray diffraction: instrumentation and applications. *Crit. Rev. Anal. Chem.* **45**, 289-299 (2015).
251 Jenkins, R. & Snyder, R. *Introduction to X-ray powder diffractometry*. Vol. 267 (John Wiley & Sons, 2012).
252 Göbel, E. O. & Siegner, U. Superconductivity, Josephson Effect, and Flux Quanta. *Quantum Metrology: Foundation of Units and Measurements*, 61-102 (2015).
253 Zappe, H. A single flux quantum Josephson junction memory cell. *Applied Physics Letters* **25**, 424-426 (1974).
254 Bean, C. P. MAGNETIZATION OF HARD SUPERCONDUCTORS. *Phys. Rev. Lett.* **8**, 250-&, doi:10.1103/PhysRevLett.8.250 (1962).
255 Iwasa, Y. Magnetization of Hard Superconductors. *Case Studies in Superconducting Magnets: Design and Operational Issues*, 163-202 (1994).
256 Hattersley, S. R., Southern, P., Pankhurst, Q. A. & Kallumadil, M. (Google Patents, 2010).
257 Callaghan, P. T. *Principles of nuclear magnetic resonance microscopy*. (Oxford University Press on Demand, 1993).
258 Shapiro, H. M. *Practical flow cytometry*. (John Wiley & Sons, 2005).
259 Dettmeyer, R. B. in *Forensic Histopathology* 17-35 (Springer, 2011).
260 Ferguson, P. M. Iron Nanoparticles as Magnetic Resonance Imaging Contrast Agents. (2011).
261 Veintemillas-Verdaguer, S. *et al.* Bismuth labeling for the CT assessment of local administration of magnetic nanoparticles. *Nanotechnology* **26**, 135101, doi:10.1088/0957-4484/26/13/135101 (2015).
262 Andrés-Vergés, M., del Puerto Morales, M., Veintemillas-Verdaguer, S., Palomares, F. J. & Serna, C. J. Core/Shell Magnetite/Bismuth Oxide Nanocrystals with Tunable Size, Colloidal, and Magnetic Properties. *Chem. Mater.* **24**, 319-324, doi:10.1021/cm202949q (2012).
263 Lacroix, L. M. *et al.* Stable single-crystalline body centered cubic Fe nanoparticles. *Nano Lett.* **11**, 1641-1645, doi:10.1021/nl200110t (2011).
264 Mai, N. T., Mott, D., Thuy, N. T. B., Osaka, I. & Maenosono, S. Study on formation mechanism and ligand-directed architectural control of nanoparticles composed of Bi, Sb and Te: towards one-pot synthesis of ternary (Bi,Sb)(2)Te-3 nanobuilding blocks. *Rsc Advances* **1**, 1089-1098, doi:10.1039/c1ra00069a (2011).
265 Thomas, F., Bialek, B. & Hensel, R. Medical Use of Bismuth: the Two Sides of the Coin. *J Clinic Toxicol S* **3**, 2161-0495 (2012).
266 Crangle, J. & Goodman, G. in *Proceedings of the Royal Society of London A: Mathematical, Physical and Engineering Sciences.* 477-491 (The Royal Society).
267 Wu, W. *et al.* One-pot reaction and subsequent annealing to synthesis hollow spherical magnetite and maghemite nanocages. *Nanoscale research letters* **4**, 926 (2009).
268 Mohammad, F., Balaji, G., Weber, A., Uppu, R. M. & Kumar, C. S. S. R. Influence of Gold Nanoshell on Hyperthermia of Superparamagnetic Iron Oxide Nanoparticles. *Journal of Physical Chemistry C* **114**, 19194-19201, doi:10.1021/jp105807r (2010).
269 Bach, L. G., Rafiqul Islam, M., Kim, J. H., Kim, H. G. & Lim, K. T. Synthesis and characterization of poly(2-hydroxyethyl methacrylate)-functionalized Fe-Au/core-shell nanoparticles. *J. Appl. Polym. Sci.*, n/a-n/a, doi:10.1002/app.35530 (2011).

270 Cho, S. J. *et al.* Growth mechanisms and oxidation resistance of gold-coated iron nanoparticles. *Chem. Mater.* **17**, 3181-3186, doi:10.1021/cm0500713 (2005).
271 Zhou, W. L. *et al.* Nanostructures of gold coated iron core-shell nanoparticles and the nanobands assembled under magnetic field. *European Physical Journal D* **16**, 289-292, doi:10.1007/s100530170112 (2001).
272 Robinson, I., Tung le, D., Maenosono, S., Walti, C. & Thanh, N. T. Synthesis of core-shell gold coated magnetic nanoparticles and their interaction with thiolated DNA. *Nanoscale* **2**, 2624-2630, doi:10.1039/c0nr00621a (2010).
273 Anderson, B. D. & Tracy, J. B. Nanoparticle conversion chemistry: Kirkendall effect, galvanic exchange, and anion exchange. *Nanoscale* **6**, 12195-12216, doi:10.1039/c4nr02025a (2014).
274 Xia, X. H., Wang, Y., Ruditskiy, A. & Xia, Y. N. 25th Anniversary Article: Galvanic Replacement: A Simple and Versatile Route to Hollow Nanostructures with Tunable and Well-Controlled Properties. *Advanced materials* **25**, 6313-6333, doi:10.1002/adma.201302820 (2013).
275 Dunn, A. E. *et al.* Spatial and temporal control of drug release through pH and alternating magnetic field induced breakage of Schiff base bonds. *Polymer Chemistry* **5**, 3311, doi:10.1039/c4py00150h (2014).
276 Blanco-Andujar, C., Ortega, D., Southern, P., Pankhurst, Q. A. & Thanh, N. T. K. High performance multi-core iron oxide nanoparticles for magnetic hyperthermia: microwave synthesis, and the role of core-to-core interactions. *Nanoscale* **7**, 1768-1775, doi:10.1039/c4nr06239f (2015).
277 Zambito, Y., Pedreschi, E. & Di Colo, G. Is dialysis a reliable method for studying drug release from nanoparticulate systems?-A case study. *Int. J. Pharm.* **434**, 28-34, doi:10.1016/j.ijpharm.2012.05.020 (2012).
278 Modi, S. & Anderson, B. D. Determination of Drug Release Kinetics from Nanoparticles: Overcoming Pitfalls of the Dynamic Dialysis Method. *Mol. Pharm.* **10**, 3076-3089, doi:10.1021/mp400154a (2013).
279 D'Souza, S. A Review of In Vitro Drug Release Test Methods for Nano-Sized Dosage Forms. *Advances in Pharmaceutics* **2014** (2014).
280 Gupta, P. K., Hung, C. T. & Perrier, D. G. Quantitation of the release of doxorubicin from colloidal dosage forms using dynamic dialysis. *J. Pharm. Sci.* **76**, 141-145, doi:10.1002/jps.2600760211 (1987).
281 Dash, S., Murthy, P. N., Nath, L. & Chowdhury, P. KINETIC MODELING ON DRUG RELEASE FROM CONTROLLED DRUG DELIVERY SYSTEMS. *Acta Pol. Pharm.* **67**, 217-223 (2010).
282 Gref, R. *et al.* THE CONTROLLED INTRAVENOUS DELIVERY OF DRUGS USING PEG-COATED STERICALLY STABILIZED NANOSPHERES. *Adv. Drug Del. Rev.* **16**, 215-233, doi:10.1016/0169-409x(95)00026-4 (1995).
283 Lee, H. *et al.* Antibiofouling polymer-coated superparamagnetic iron oxide nanoparticles as potential magnetic resonance contrast agents for in vivo cancer imaging. *J. Am. Chem. Soc.* **128**, 7383-7389, doi:10.1021/ja061529k (2006).
284 Haynes, W. M. *CRC handbook of chemistry and physics*. (CRC press, 2014).
285 Thanh, N. T. *Magnetic nanoparticles: from fabrication to clinical applications*. (CRC press, 2012).
286 Osterholtz, F. D. & Pohl, E. R. KINETICS OF THE HYDROLYSIS AND CONDENSATION OF ORGANOFUNCTIONAL ALKOXYSILANES - A REVIEW. *Journal of Adhesion Science and Technology* **6**, 127-149, doi:10.1163/156856192x00106 (1992).
287 Minko, S. in *Polymer surfaces and interfaces* 215-234 (Springer, 2008).
288 de Gennes, P. Conformations of polymers attached to an interface. *Macromolecules* **13**, 1069-1075 (1980).
289 Jokerst, J. V., Lobovkina, T., Zare, R. N. & Gambhir, S. S. Nanoparticle PEGylation for imaging and therapy. *Nanomedicine* **6**, 715-728 (2011).
290 Naahidi, S. *et al.* Biocompatibility of engineered nanoparticles for drug delivery. *J. Controlled Release* **166**, 182-194 (2013).
291 Liu, G. & Zhang, G. in *QCM-D Studies on Polymer Behavior at Interfaces* 9-31 (Springer, 2013).
292 Zhang, J. L., Boyd, C. & Luo, W. L. Two mechanisms and a scaling relation for dynamics in ferrofluids. *Phys. Rev. Lett.* **77**, 390-393, doi:10.1103/PhysRevLett.77.390 (1996).

293 Salas, G. *et al.* Modulation of Magnetic Heating via Dipolar Magnetic Interactions in Monodisperse and Crystalline Iron Oxide Nanoparticles. *Journal of Physical Chemistry C* **118**, 19985-19994, doi:10.1021/jp5041234 (2014).
294 Landi, G. T. Role of dipolar interaction in magnetic hyperthermia. *Physical Review B* **89**, doi:10.1103/PhysRevB.89.014403 (2014).
295 Coral, D. F. *et al.* Effect of Nanoclustering and Dipolar Interactions in Heat Generation for Magnetic Hyperthermia. *Langmuir* **32**, 1201-1213, doi:10.1021/acs.langmuir.5b03559 (2016).
296 Cabrera, D., Camarero, J., Ortega, D. & Teran, F. J. Influence of the aggregation, concentration, and viscosity on the nanomagnetism of iron oxide nanoparticle colloids for magnetic hyperthermia. *Journal of Nanoparticle Research* **17**, doi:10.1007/s11051-015-2921-9 (2015).
297 Guibert, C., Dupuis, V., Peyre, V. & Fresnais, J. Hyperthermia of Magnetic Nanoparticles: Experimental Study of the Role of Aggregation. *Journal of Physical Chemistry C* **119**, 28148-28154, doi:10.1021/acs.jpcc.5b07796 (2015).
298 Hervault, A. & Thanh, N. T. K. Magnetic nanoparticle-based therapeutic agents for thermo-chemotherapy treatment of cancer. *Nanoscale* **6**, 11553-11573, doi:10.1039/c4nr03482a (2014).
299 van Landeghem, F. K. *et al.* Post-mortem studies in glioblastoma patients treated with thermotherapy using magnetic nanoparticles. *Biomaterials* **30**, 52-57, doi:10.1016/j.biomaterials.2008.09.044 (2009).
300 Johannsen, M. *et al.* Thermotherapy of prostate cancer using magnetic nanoparticles: feasibility, imaging, and three-dimensional temperature distribution. *Eur. Urol.* **52**, 1653-1662 (2007).
301 Wu, W., He, Q. G. & Jiang, C. Z. Magnetic Iron Oxide Nanoparticles: Synthesis and Surface Functionalization Strategies. *Nanoscale Research Letters* **3**, 397-415, doi:10.1007/s11671-008-9174-9 (2008).
302 Wu, W., Wu, Z. H., Yu, T., Jiang, C. Z. & Kim, W. S. Recent progress on magnetic iron oxide nanoparticles: synthesis, surface functional strategies and biomedical applications. *Science and Technology of Advanced Materials* **16**, doi:10.1088/1468-6996/16/2/023501 (2015).
303 Hansen, M. F. & Morup, S. Estimation of blocking temperatures from ZFC/FC curves. *Journal of Magnetism and Magnetic Materials* **203**, 214-216, doi:10.1016/s0304-8853(99)00238-3 (1999).
304 Topkaya, R. *et al.* Surface spin disorder and spin-glass-like behaviour in manganese-substituted cobalt ferrite nanoparticles. *Journal of Nanoparticle Research* **14**, doi:10.1007/s11051-012-1156-2 (2012).
305 Wood, M. J., Irwin, W. J. & Scott, D. K. PHOTODEGRADATION OF DOXORUBICIN, DAUNORUBICIN AND EPIRUBICIN MEASURED BY HIGH-PERFORMANCE LIQUID-CHROMATOGRAPHY. *J. Clin. Phar. Ther.* **15**, 291-300, doi:10.1111/j.1365-2710.1990.tb00387.x (1990).
306 Allwood, M., Stanley, A. & Wright, P. *The Cytotoxics Handbook*. (CRC Press, 2002).
307 Tomlinson, E. & Malspeis, L. Concomitant adsorption and stability of some anthracycline antibiotics. *J. Pharm. Sci.* **71**, 1121-1125 (1982).
308 Wood, M. J., Irwin, W. J. & Scott, D. K. STABILITY OF DOXORUBICIN, DAUNORUBICIN AND EPIRUBICIN IN PLASTIC SYRINGES AND MINIBAGS. *J. Clin. Phar. Ther.* **15**, 279-289, doi:10.1111/j.1365-2710.1990.tb00386.x (1990).
309 Carvalho, C. *et al.* Doxorubicin: The Good, the Bad and the Ugly Effect. *Curr. Med. Chem.* **16**, 3267-3285 (2009).
310 Nitiss, J. L. Targeting DNA topoisomerase II in cancer chemotherapy. *Nature Reviews Cancer* **9**, 338-350, doi:10.1038/nrc2607 (2009).
311 Cutts, S. M., Nudelman, A., Rephaeli, A. & Phillips, D. R. The power and potential of doxorubicin-DNA adducts. *Iubmb Life* **57**, 73-81, doi:10.1080/15216540500079093 (2005).
312 Kim, D. H. *et al.* Stimuli-Responsive Magnetic Nanomicelles as Multifunctional Heat and Cargo Delivery Vehicles. *Langmuir* **29**, 7425-7432, doi:10.1021/la3044158 (2013).
313 Valeriote, F. & Lin, H. Synergistic interaction of anticancer agents: a cellular perspective. *Cancer chemotherapy reports* **59**, 895 (1975).

314 Pradhan, P. *et al.* Targeted temperature sensitive magnetic liposomes for thermo-chemotherapy. *J. Control. Release* **142**, 108-121, doi:10.1016/j.jconrel.2009.10.002 (2010).
315 Li, X., Wang, L., Fan, Y., Feng, Q. & Cui, F.-z. Biocompatibility and toxicity of nanoparticles and nanotubes. *Journal of Nanomaterials* **2012**, 6 (2012).
316 Kobayashi, K., Wei, J., Iida, R., Ijiro, K. & Niikura, K. Surface engineering of nanoparticles for therapeutic applications. *Polymer Journal* **46**, 460-468 (2014).
317 Gautam, A. & van Veggel, F. C. Synthesis of nanoparticles, their biocompatibility, and toxicity behavior for biomedical applications. *Journal of Materials Chemistry B* **1**, 5186-5200 (2013).
318 Alcantar, N. A., Aydil, E. S. & Israelachvili, J. N. Polyethylene glycol-coated biocompatible surfaces. *J. Biomed. Mater. Res.* **51**, 343-351 (2000).
319 Conner, S. D. & Schmid, S. L. Regulated portals of entry into the cell. *Nature* **422**, 37-44 (2003).
320 Sahay, G., Alakhova, D. Y. & Kabanov, A. V. Endocytosis of nanomedicines. *J. Controlled Release* **145**, 182-195, doi:10.1016/j.jconrel.2010.01.036 (2010).
321 Zhang, S., Gao, H. & Bao, G. Physical principles of nanoparticle cellular endocytosis. *ACS nano* **9**, 8655-8671 (2015).
322 Mayor, S. & Pagano, R. E. Pathways of clathrin-independent endocytosis. *Nature reviews Molecular cell biology* **8**, 603-612 (2007).
323 Fröhlich, E. The role of surface charge in cellular uptake and cytotoxicity of medical nanoparticles. *Int J Nanomedicine* **7**, 5577-5591 (2012).
324 Treuel, L., Jiang, X. & Nienhaus, G. U. New views on cellular uptake and trafficking of manufactured nanoparticles. *Journal of The Royal Society Interface* **10**, 20120939 (2013).
325 Zhao, F. *et al.* Cellular uptake, intracellular trafficking, and cytotoxicity of nanomaterials. *Small* **7**, 1322-1337 (2011).
326 Mustafa, T. *et al.* Impact of Gold Nanoparticle Concentration on their Cellular Uptake by MC3T3-E1 Mouse Osteocytic Cells as Analyzed by Transmission Electron Microscopy. *Journal of Nanomedicine & Nanotechnology* **2011** (2012).
327 Li, Y., Kröger, M. & Liu, W. K. Shape effect in cellular uptake of pegylated nanoparticles: comparison between sphere, rod, cube and disk. *Nanoscale* **7**, 16631-16646 (2015).
328 Dasgupta, S., Auth, T. & Gompper, G. Shape and orientation matter for the cellular uptake of nonspherical particles. *Nano Lett.* **14**, 687-693 (2014).
329 Sahay, G., Kim, J. O., Kabanov, A. V. & Bronich, T. K. The exploitation of differential endocytic pathways in normal and tumor cells in the selective targeting of nanoparticulate chemotherapeutic agents. *Biomaterials* **31**, 923-933 (2010).
330 Gao, Z. B., Zhang, L. N. & Sun, Y. J. Nanotechnology applied to overcome tumor drug resistance. *J. Controlled Release* **162**, 45-55, doi:10.1016/j.jconrel.2012.05.051 (2012).
331 Zeng, X. H., Morgenstern, R. & Nystrom, A. M. Nanoparticle-directed sub-cellular localization of doxorubicin and the sensitization breast cancer cells by circumventing GST-Mediated drug resistance. *Biomaterials* **35**, 1227-1239, doi:10.1016/j.biomaterials.2013.10.042 (2014).
332 Upadhyay, K. K. *et al.* The intracellular drug delivery and anti tumor activity of doxorubicin loaded poly(gamma-benzyl L-glutamate)-b-hyaluronan polymersomes. *Biomaterials* **31**, 2882-2892, doi:10.1016/j.biomaterials.2009.12.043 (2010).
333 Heibein, A. D., Guo, B. Q., Sprowl, J. A., MacLean, D. A. & Parissenti, A. M. Role of aldo-keto reductases and other doxorubicin pharmacokinetic genes in doxorubicin resistance, DNA binding, and subcellular localization. *BMC Cancer* **12**, doi:10.1186/1471-2407-12-381 (2012).
334 Tomankova, K. *et al.* In vitro cytotoxicity analysis of doxorubicin-loaded/superparamagnetic iron oxide colloidal nanoassemblies on MCF7 and NIH3T3 cell lines. *International Journal of Nanomedicine* **10**, 949-961, doi:10.2147/ijn.s72590 (2015).
335 Rittierodt, M. & Harada, K. Repetitive doxorubicin treatment of glioblastoma enhances the PGP expression–a special role for endothelial cells. *Exp. Toxicol. Pathol.* **55**, 39-44 (2003).
336 Amin, M. L. P-glycoprotein inhibition for optimal drug delivery. *Drug target insights* **7**, 27 (2013).
337 Callaghan, R., Luk, F. & Bebawy, M. Inhibition of the multidrug resistance P-glycoprotein: time for a change of strategy? *Drug Metab. Disposition* **42**, 623-631 (2014).

338 Kossatz, S. *et al.* Efficient treatment of breast cancer xenografts with multifunctionalized iron oxide nanoparticles combining magnetic hyperthermia and anti-cancer drug delivery. *Breast Cancer Res.* **17**, doi:10.1186/s13058-015-0576-1 (2015).
339 Quinto, C. A., Mohindra, P., Tong, S. & Bao, G. Multifunctional superparamagnetic iron oxide nanoparticles for combined chemotherapy and hyperthermia cancer treatment. *Nanoscale* **7**, 12728-12736, doi:10.1039/c5nr02718g (2015).
340 Aljarrah, K. *et al.* Magnetic nanoparticles sensitize MCF-7 breast cancer cells to doxorubicin-induced apoptosis. *World J. Surg. Oncol.* **10**, doi:10.1186/1477-7819-10-62 (2012).
341 Blanco-Andujar, C. *et al.* Real-time tracking of delayed-onset cellular apoptosis induced by intracellular magnetic hyperthermia. *Nanomedicine* **11**, 121-136 (2016).
342 Fang, K. *et al.* Magnetic field activated drug release system based on magnetic PLGA microspheres for chemo-thermal therapy. *Colloids and Surfaces B-Biointerfaces* **136**, 712-720, doi:10.1016/j.colsurfb.2015.10.014 (2015).
343 He, X., Li, J., An, S. & Jiang, C. pH-sensitive drug-delivery systems for tumor targeting. *Ther. Deliv.* **4**, 1499-1510, doi:10.4155/tde.13.120 (2013).
344 Liu, J. *et al.* pH-Sensitive nano-systems for drug delivery in cancer therapy. *Biotechnol. Adv.* **32**, 693-710 (2014).
345 Peller, M. *et al.* Surrogate MRI markers for hyperthermia-induced release of doxorubicin from thermosensitive liposomes in tumors. *J. Controlled Release* **237**, 138-146, doi:10.1016/j.jconrel.2016.06.035 (2016).
346 Nagaoka, S., Kawasaki, S., Karino, Y., Hiraki, Y. & Nakanishi, T. In vivo effects of hyperthermia on the cellular uptake of adriamycin. *J. Radiat. Res.* **28**, 262-267 (1987).
347 Greer, L. F. & Szalay, A. A. Imaging of light emission from the expression of luciferases in living cells and organisms: a review. *Luminescence* **17**, 43-74, doi:10.1002/bio.676 (2002).
348 Germain-Genevois, C., Garandeau, O. & Couillaud, F. Detection of brain tumors and systemic metastases using NanoLuc and Fluc for dual reporter imaging. *Mol. Imag. Biol.* **18**, 62-69 (2016).
349 Contag, P. R., Olomu, I. N., Stevenson, D. K. & Contag, C. H. Bioluminescent indicators in living mammals. *Nat. Med.* **4**, 245-247, doi:10.1038/nm0298-245 (1998).
350 Badr, C. E. in *Bioluminescent Imaging: Methods and Protocols* Vol. 1098 *Methods in Molecular Biology* (ed C. E. Badr) 1-18 (2014).
351 Tarantal, A. F. & Lee, C. C. I. Long-Term Luciferase Expression Monitored by Bioluminescence Imaging After Adeno-Associated Virus-Mediated Fetal Gene Delivery in Rhesus Monkeys (Macaca mulatta). *Hum. Gene Ther.* **21**, 143-148, doi:10.1089/hum.2009.126 (2010).
352 Wood, K. Firefly luciferase: A new tool for molecular biologists. *Promega Notes* **28**, 2 (1990).
353 Genevois, C., Loiseau, H. & Couillaud, F. In Vivo Follow-up of Brain Tumor Growth via Bioluminescence Imaging and Fluorescence Tomography. *International journal of molecular sciences* **17**, 1815 (2016).
354 Badr, C. E. & Tannous, B. A. Bioluminescence imaging: progress and applications. *Trends Biotechnol.* **29**, 624-633, doi:10.1016/j.tibtech.2011.06.010 (2011).
355 Wang, J. & Zeng, X. in *Nanoscale Magnetic Materials and Applications* 35-65 (Springer, 2009).